

AD-A252 663



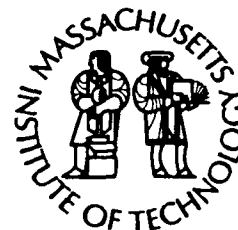
WHOI-92-13

(1)

Woods Hole Oceanographic Institution Massachusetts Institute of Technology

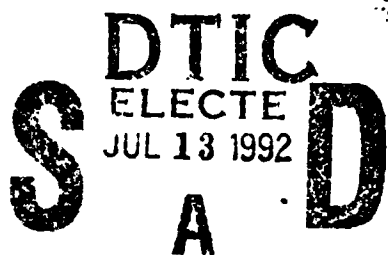


Joint Program
in Oceanography/
Applied Ocean Science
and Engineering



DOCTORAL DISSERTATION

Laboratory Measurements of the Sound
Generated by Breaking Waves



by

Mark R. Loewen

December 1991

This document has been approved
for public release and sale; its
distribution is unlimited.

92-18220



92

1.2

DISCLAIMER NOTICE



THIS DOCUMENT IS BEST QUALITY AVAILABLE. THE COPY FURNISHED TO DTIC CONTAINED A SIGNIFICANT NUMBER OF COLOR PAGES WHICH DO NOT REPRODUCE LEGIBLY ON BLACK AND WHITE MICROFICHE.

WHOI-92-13

Laboratory Measurements of the Sound
Generated by Breaking Waves

by

Mark R. Loewen

Woods Hole Oceanographic Institution
Woods Hole, Massachusetts 02543

and

The Massachusetts Institute of Technology
Cambridge, Massachusetts 02139

December 1991

DOCTORAL DISSERTATION

Reproduction in whole or in part is permitted for any purpose of the United States
Government. This thesis should be cited as: Mark R. Loewen, 1992.
Laboratory Measurements of the Sound Generated by Breaking Waves. Ph.D.
Thesis. MIT/WHOI, WHOI-92-13.

Approved for publication; distribution unlimited.

Approved for Distribution:

Albert J. Williams 3rd

Albert J. Williams 3rd, Chairman
Department of Applied Ocean Physics and Engineering

John W. Farrington

John W. Farrington
Dean of Graduate Studies

Accession For	
NTIS	CRA&I
DTIC	TAB
Unannounced	
Justification	
By	
Distribution/	
Availability Codes	
Dist	Avail and/or Special
A-1	

LABORATORY MEASUREMENTS OF THE SOUND
GENERATED BY BREAKING WAVES

by

Mark Richard Loewen

B.Sc. Civil Engineering
(1983)

M.Sc. Civil Engineering
(1984)

University of Alberta

SUBMITTED IN PARTIAL FULFILLMENT OF THE
REQUIREMENTS FOR THE DEGREE OF

DOCTOR OF PHILOSOPHY

at the

MASSACHUSETTS INSTITUTE OF TECHNOLOGY

and the

WOODS HOLE OCEANOGRAPHIC INSTITUTION

December 1991

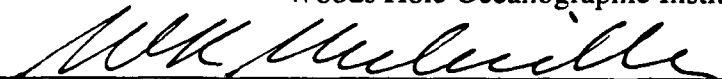
© Massachusetts Institute of Technology and
Woods Hole Oceanographic Institution, 1991

Signature of Author



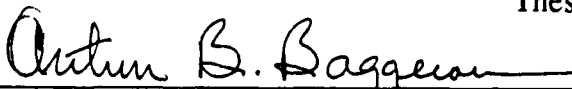
Joint Program in Oceanographic Engineering
Massachusetts Institute of Technology
Woods Hole Oceanographic Institution

Certified by



Professor W. Kendall Melville
Thesis Supervisor

Accepted by



Professor Arthur B. Baggeroer, Chairman
Joint Committee for Oceanographic Engineering
Massachusetts Institute of Technology
Woods Hole Oceanographic Institution

LABORATORY MEASUREMENTS OF THE SOUND
GENERATED BY BREAKING WAVES

by

Mark Richard Loewen

Submitted to the Department of Civil Engineering
on December 16, 1991 in partial fulfillment of the
requirements for the Degree of Doctor of Philosophy
in Oceanographic Engineering

ABSTRACT

Breaking waves dissipate energy, transfer momentum from the wind to surface currents and breaking enhances the transfer of gas and mass across the air-sea interface. Breaking waves are believed to be the dominant source of sea surface sound at frequencies greater than 500 Hz and the presence of breaking waves on the ocean surface has been shown to enhance the scattering of microwave radiation. Previous studies have shown that breaking waves can be detected by measuring the microwave backscatter and acoustic radiation from breaking waves. However, these techniques have not yet proven effective for studying the dynamics of breaking. The primary motivation for the research presented in this thesis was to determine whether measurements of the sound generated by breaking waves could be used to quantitatively study the dynamics of the breaking process.

Laboratory measurements of the microwave backscatter and acoustic radiation from two-dimensional breaking waves are described in Chapter 2. The major findings of this Chapter are: 1) the mean square acoustic pressure and backscattered microwave power correlate with the wave slope and dissipation for waves of moderate slope, 2) the mean square acoustic pressure and backscattered microwave power correlate strongly with each other, and 3) the amount of acoustic energy radiated by an individual breaking event scaled with the amount of mechanical energy dissipated by breaking. The observed correlations with the mean square acoustic pressure are only relevant for frequencies greater than 2200 Hz because lower frequencies were below the first acoustic cut-off frequency of the wave channel.

In order to study the lower frequency sound generated by breaking waves another series of two-dimensional breaking experiments was conducted. Sound at frequencies as low as 20 Hz was observed and the mean square acoustic pressure in the frequency band from 20 Hz-1 kHz correlated strongly with the wave slope and dissipation. A characteristic low frequency signal was observed immediately following the impact of the plunging wave crest. The origin of this low frequency signal was found to be the pulsating cylinders of air which are entrained by the plunging waves. The pulsation frequency correlated with both the wave slope and dissipation. Following the characteristic constant frequency signal, approximately 0.25 s after the initial impact of

the plunging crest, another low frequency signal was typically observed. These signals were generally lower in frequency initially and then increased in frequency as time progressed.

To determine if three-dimensional effects were important in the sound generation process and to measure the sound beneath larger breaking waves a series of experiments was conducted in a large multi-paddle wave basin. Three-dimensional breaking waves were generated and the sound produced by breaking was measured in the frequency range from 10 Hz to 20 kHz. The observed sound spectra showed significant increases in level across the entire bandwidth from 10 Hz to 20 kHz and the spectra sloped at -5 to -6 dB per octave at frequencies greater than 1 kHz. The mean square acoustic pressure in the frequency band from 10 Hz to 150 Hz correlated with the wave amplitude similar to the results obtained in the two-dimensional breaking experiments. Large amplitude low frequency spectral peaks were observed approximately 0.75 s after the initial impact of the plunging crests.

It was postulated that the low frequency signals observed some time after the initial impact of the plunging crests for both the two and three-dimensional breakers were caused by the collective oscillation of bubble clouds. Void fraction measurements taken by Eric Lamarre were available for five breaking events and therefore the average sound speed inside the bubble clouds and their radii were known. Using this information the resonant frequencies of a two-dimensional cylindrical bubble cloud of equal radius and sound speed were calculated. The frequencies of the observed signals matched closely with the calculated resonant frequencies of the first and second mode of the two-dimensional cylindrical bubble cloud. The close agreement supports the hypothesis that the low frequency signals were produced by the collective oscillation of bubble clouds.

In Chapter 4 a model of the sound produced by breaking waves is presented which uses the sound radiated by a single bubble oscillating at its linear resonant frequency and the bubble size distribution to estimate the sound spectrum. The model generates a damped sinusoidal pulse for every bubble formed, as calculated from the bubble size distribution. If the range to the receiver is known then the only unknown parameters are ϵ , the initial fractional amplitude of the bubble oscillation and L , the dipole moment arm or twice the depth of the bubble below the free surface. It was found that if the product $\epsilon \times L$ is independent of the bubble radius the model reproduces the shape and magnitude of the observed sound spectrum accurately. The success of the model implies that it may be possible to calculate the bubble size distribution from the sound spectrum. The model was validated using data from experiments where the breaking events were small scale gently spilling waves (Medwin and Daniel, 1990).

Thesis Supervisor: W. Kendall Melville

Title: Professor of Civil Engineering

Acknowledgements

I would like to acknowledge and thank the people who assisted and encouraged me during my time at the Parsons Lab.

My thesis supervisor Ken Melville provided the resources and direction which made this work possible. Ken introduced me to the topic of breaking waves and taught me how to conduct experimental research. I would like to thank my thesis committee; Mike Buckingham, Ira Dyer and Sandy Williams for their help and support.

I received a great deal of encouragement and assistance from my fellow graduate students within the "Melville group". First, I would like to thank Jun Zhang who worked with me when I first arrived at MIT and taught me how to operate the wave maker system. My work on radar backscatter from breaking waves would not have been possible without the help of Andy Jessup. Francis Felizardo worked with me during the combined microwave and acoustic experiments. Eric Lamarre and I worked together on the OTRC experiment and his void fraction measurements from there and at MIT have been invaluable to me. Anatol Rozenberg suggested that I listen to the sound radiated by breaking with a microphone in the air and this was very helpful in the 2D breaking experiments.

I have enjoyed my time at the Parsons Lab and this is largely due to the many friends I have made during my time there. Gunnar Tomasson arrived at the lab at the same time as me, in September 1986, and we have experienced the trials and tribulations of completing a Ph.D. together. I thank my colleagues Andy, Eric, Francis, Anatol, Anne, Ge and Analia for their friendship. A special thanks to Pat Dixon who is always willing to listen and who makes everyone feel welcome at the lab.

Finally, I thank my wife Cheryl who has always believed in me and encouraged me to pursue my dreams. Without her love and support I would not have been able to complete this thesis.

This research was funded by grants from the MIT Sloan Basic Research Fund, the National Science Foundation and the Office of Naval Research (Ocean Acoustics and Physical Oceanography).

Table of Contents

List of Figures.....	8
List of Tables	29
Chapter 1: Introduction and Literature Review.....	31
1.1 Ambient Sound Measurements.....	33
1.2 Sound Produced by Oscillating Air Bubbles.....	37
1.3 Measurements of the Sound Generated by Breaking Waves	39
1.4 Collective Bubble Cloud Oscillations.....	51
1.5 Models of the Sound Generated by Breaking Waves	57
1.6 Outline of Experimental Objectives	64
Chapter 2: Microwave and Acoustic Experiment.....	67
2.1 Literature Review: Microwave Backscatter	67
2.2 Experimental Procedure.....	69
2.2.1 Wave Generation	69
2.2.2 Surface Displacement Measurements	78
2.2.3 Acoustic Measurements	79
2.2.4 Microwave Measurements	83
2.3 Results	87
2.3.1 Wave Dissipation.....	87
2.3.2 Microwave Scattering.....	94
2.3.3 Acoustic Radiation.....	103
2.3.4 Empirical Scaling and Correlations.....	114
2.4 Discussion.....	120

Chapter 3: Measurements of the Sound Generated by Two and Three-	
Dimensional Breaking Waves	132
3.1 Experimental Procedure: Two-Dimensional breaking	133
3.1.1 Surface Displacement Measurements	136
3.1.2 Sound Measurements	136
3.1.3 Video Measurements	140
3.2 Two-Dimensional Breaking: Results	143
3.2.1 Wave Dissipation.....	143
3.2.2 Sound	146
3.3 Experimental Procedure: Three-Dimensional breaking	167
3.3.1 Surface Displacement Measurements	170
3.3.2 Video Measurements	171
3.3.3 Sound Measurements.....	171
3.4 Three-Dimensional Breaking: Results	172
3.4.1 Surface Displacement	172
3.4.2 Sound	178
3.5 Discussion.....	206
3.5.1 Volume of Entrained Air	206
3.5.2 Low Frequency Spectral Peaks	209
3.5.3 Pulsating Cylinder	220
3.5.4 Bubble Cloud Resonance`	237
3.5.5 Comparison of Two and Three-Dimensional Results	257
Chapter 4: A Model Of the Sound Generated by Gently Breaking Waves	262
4.1 Introduction	262
4.2 Formulation	266
4.3 Results	272
4.4 Discussion.....	279

Chapter 5: Summary and Conclusions.....	282
References	293
Appendix A: Chapter 2 Programs.....	299
Appendix B: Chapter 3 Programs.....	312
Appendix C: The Effect of Noncircular Cylinder Shape.....	333
Appendix D: Chapter4 Programs.....	339

List of Figures

	<u>page</u>
Figure 1.1 Frequency spectra of ambient noise in the ocean. (from Wenz, 1962).	34
Figure 1.2 Spectrum level of ambient sound as a function of the windspeed class from data gathered in the North Sea (from Carey et al 1990).	36
Figure 1.3 An example of the sound spectrum level as a function of time in three frequency bands measured beneath a breaking wave in the ocean (from Farmer and Vagle, 1989).	41
Figure 1.4 Ambient sound spectrum level of a breaking wave at sea. The spectra are plotted for three different time intervals during the event. The upper spectrum represents the background sound spectrum prior to breaking and is shown in the lower plots as a dashed line. The lower two spectra correspond to times during active breaking (from Farmer and Vagle, 1989).	42
Figure 1.5 Spectrograph of the sound generated by breaking ocean waves. The grey scale indicates the spectral level above the background f^2 spectrum. There is energy in the spectra down to frequencies as low as 60 Hz. (from Vagle, 1989).	44
Figure 1.6 The pressure spectrum level of the sound as a function of time sampled by an upward looking directional hydrophone mounted on the ocean floor in 80 meters of water in five 2 kHz wide frequency bands from 10 kHz to 50 kHz (from Crowther, 1988).	45
Figure 1.7 Typical sound pulse emitted by an oscillating air bubble entrained by a gently spilling breaking wave in a laboratory wave channel (from Medwin and Beaky, 1989).	48
Figure 1.8 Typical sound pulse radiated by an oscillating air bubble beneath a gently spilling breaking wave at sea (from Updegraff and Anderson, 1991).	50
Figure 1.9 Total damping constant for a 1 mm radius air bubble in water. \circ , marks the location of resonance (from Prosperetti, 1984).	54

Figure 1.10	Theoretically predicted resonant frequencies of a spherical and cylindrical bubble cloud as a function of the void fraction and radius (from Carey et al, 1990).	56
Figure 1.11	Frequency of oscillation of substructures as a function of the volume of water released from a cylinder. The large symbols correspond to data from a large tank and the smaller symbols to data from a smaller tank (from Kolaini et al 1991).	58
Figure 1.12	Modeled sound spectra of the noise generated by breaking waves (from Crowther, 1988).	61
Figure 2.1	Schematic drawing of the wave channel and the arrangement of the experimental equipment.	73
Figure 2.2	(a) The amplitude transfer function of the wavemaker system $H(f)$ (cm/volt) as a function of frequency f (Hz). (b) The phase transfer function $\Phi(f)$ (radians) as a function of the frequency f (Hz).	74
Figure 2.3	The upper plot is a typical frequency response of a B&K model 8105 spherical hydrophone. The lower plot is the typical frequency response of a B&K model 2635 charge amplifier. The curve marked acceleration is for the mode of operation used in these experiments.	80
Figure 2.4	The background ambient noise spectrum in the wave channel $G(f)$ in dB re $1 \mu\text{Pa}^2/\text{Hz}$.	84
Figure 2.5	The radar calibration data, received power P_r in volts ² as a function of σ/R^4 , σ is the radar cross section in m ² and R is the range in m.	88
Figure 2.6	The surface displacement variance $\overline{\eta^2}$ normalized by the reference upstream surface displacement variance η_o^2 plotted versus the dimensionless distance along the wave channel, x is the distance along the channel measured from the mean position of the wave paddle, x_b is the theoretical focal point and k_c is the wavenumber of the wave packet center component. Data is for wave packet P_1 : ∇ , $S=0.226$; \bullet , $S=0.254$; \circ , $S=0.263$.	90

- Figure 2.7 The surface displacement variance $\overline{\eta^2}$ normalized by the reference upstream surface displacement variance η_0^2 plotted versus the dimensionless distance along the wave channel, x is the distance along the channel measured from the mean position of the wave paddle, x_b is the theoretical focal point and k_c is the wavenumber of the wave packet center component. Data is for wave packet P_2 : ∇ , $S=0.221$; \bullet , $S=0.244$; \circ , $S=0.312$. 91
- Figure 2.8 The surface displacement variance $\overline{\eta^2}$ normalized by the reference upstream surface displacement variance η_0^2 plotted versus the dimensionless distance along the wave channel, x is the distance along the channel measured from the mean position of the wave paddle, x_b is the theoretical focal point and k_c is the wavenumber of the wave packet center component. Data is for wave packet P_3 : ∇ , $S=0.218$; \bullet , $S=0.240$; \circ , $S=0.320$. 92
- Figure 2.9 The fractional dissipation of wave packet energy as a function of the slope parameter S : \circ , P_1 ; \bullet , P_2 ; Δ , P_3 . The variability of the data was typically less than the symbol size. 93
- Figure 2.10 (a) Time series of the radar signal band pass filtered from 1-250 Hz for packet P_1 with $S = 0.254$. (b) Power spectrum of time series in (a). 95
- Figure 2.11 Radar Doppler spectra at various x -locations for packet P_1 with $S = 0.254$, the radar time series were band pass filtered from 1-250 Hz. 96
- Figure 2.12 Bottom trace is a hydrophone time series band pass filtered in the range 500 Hz-10 kHz, upper traces are radar time series at various x -locations, band pass filtered in the range 50-250 Hz, for packet P_1 with $S = 0.254$. The \blacktriangledown mark the times corresponding to the photographs in figure 2.13. 97
- Figure 2.13 Photographs of a breaking wave matching the data in figure 2.12. Each photograph corresponds to one radar time series and the time the photograph was taken is marked in figure 2.12 with a \blacktriangledown above the matching radar time series. 99

Figure 2.14	(a) Time averaged radar cross-section as a function of x . (b) Peak frequency (Hz) of the radar Doppler spectrum as a function of x . \circ , P_1 , $S = 0.254$; \bullet , P_3 , $S = 0.385$; $-\circ-$ and $-\bullet-$ on (b) denote the center component phase speeds for P_1 and P_3 respectively. Each data point is averaged from 3 runs at each location; radar data were band pass filtered in the range 50-250 Hz. The typical variability of the data between runs is shown by the scatter bars.	102
Figure 2.15	Vertical eigenfunction shapes; m is the vertical mode number.	104
Figure 2.16	Horizontal eigenfunction shapes; n is the horizontal mode number.	105
Figure 2.17	Upper curve is the acoustic spectrum for packet P_1 with $S = 0.254$; lower curve is the spectrum of the background noise. \blacktriangle , mark locations of the cutoff frequencies.	107
Figure 2.18	Coherence $\gamma_{xv}^2(f)$ of two hydrophone signals, $S = 0.263$ and the separation distance between the hydrophones $\Delta x = 1.15$ m.	109
Figure 2.19	Phase spectrum $\theta_{xv}(f)$ of two hydrophone signals, $S = 0.263$ and the separation distance between the hydrophones $\Delta x = 1.15$ m.	110
Figure 2.20	Solid curves show equation 2.23, the theoretical values for the group velocities of the acoustic modes in the wave channel; \bullet , estimates of the group	112
Figure 2.21	Mean square acoustic pressure as a function of x . All data are for P_1 : \circ , $S = 0.286$; \bullet , $S = 0.274$; Δ , $S = 0.263$; \blacktriangle , $S = 0.254$; \square , $S = 0.249$; \blacksquare , $S = 0.247$; ∇ , $S = 0.244$; \blacktriangledown , $S = 0.241$; \diamond , $S = 0.237$; \blacklozenge , $S = 0.226$. Each data point is the average of 5 runs and the typical variability of the data between runs is shown by the scatter bars.	113
Figure 2.22	Dimensionless radar cross-section σk_c^2 as a function of the slope parameter S : \circ , P_1 ; \bullet , P_2 ; Δ , P_3 .	116

Figure 2.23	Dimensionless mean square acoustic pressure P_d as a function of the slope parameter, S : \circ , P_1 ; \bullet , P_2 ; Δ , P_3 .	117
Figure 2.24	Correlation between the dimensionless radar cross-section σk_c^2 and the dimensionless mean square acoustic pressure P_d : \circ , P_1 ; \bullet , P_2 ; Δ , P_3 .	118
Figure 2.25	Correlation of the dimensionless radar cross-section σk_c^2 with the fractional dissipation D . For $\sigma k_c^2 > 0.15$ the data are independent of D and fall within the range marked — . \circ , P_1 ; \bullet , P_2 ; Δ , P_3 .	119
Figure 2.26	Correlation of the dimensionless mean square acoustic pressure P_d with the fractional dissipation D . For $P_d > 10^{-8}$ the data are independent of D and fall within the range marked — . \circ , P_1 ; \bullet , P_2 ; Δ , P_3 .	121
Figure 2.27	Correlation of the dimensionless radar cross-section σk_c^2 and the dimensionless hydrophone signal duration T_c . \circ , P_1 ; \bullet , P_2 ; Δ , P_3 .	122
Figure 2.28	Correlation of the dimensionless mean square acoustic pressure P_d with the dimensionless hydrophone signal duration T_c . \circ , P_1 ; \bullet , P_2 ; Δ , P_3 .	123
Figure 2.29	Variation of the bandwidth with x , the distance along the channel. \circ , P_1 , $S = 0.254$. Data correspond to the spectra in figure 2.11.	125
Figure 2.30	(a) Variation of $\overline{p^2}$ in the wave channel with the transverse coordinate, z . (b) Variation of $\overline{p^2}$ in the wave channel with the vertical coordinate, y .	128
Figure 2.31	The mean square acoustic pressure, $\overline{p^2}$ measured upstream and downstream of the breaking location. Theoretical breaking location is at $(x-x_b)/k_c = 0$.	130
Figure 2.32	Correlation between the estimated radiated acoustic energy E_a scaled by $(k_c h)^{-2}$ and the energy dissipated by the breaking wave E_L . \circ , P_1 ; \bullet , P_2 ; Δ , P_3 .	131

Figure 3.1	Schematic drawing of an elevation view (top) and plan view (bottom) of the $25\text{ m} \times 0.76\text{ m} \times 0.60\text{ m}$ wave channel at MIT. The configuration of the experimental equipment is also illustrated.	134
Figure 3.2	The upper plot is the amplitude transfer function $H(f)$ (cm/volt) for the $25\text{ m} \times 0.76\text{ m} \times 0.60\text{ m}$ wave channel as a function of frequency, f (Hz). The lower plot is the phase transfer function $\Phi(f)$ (radians) as a function of frequency, f (Hz) (E. Lamarre, 1991).	135
Figure 3.3	A plot of the typical frequency response of an ITC 1089E hydrophone.	137
Figure 3.4	The upper plot is a typical frequency response of a Shure SM81 microphone. The curve labelled flat corresponds to the setting used in these experiments. The lower plots are typical polar plots of the directional characteristics of a SM81 microphone at various frequencies.	141
Figure 3.5	The fractional dissipation D as a function of the wave slope parameter, S . \circ , W_1 ; \bullet , W_2 ; ∇ , W_3 .	144
Figure 3.6	The frequency spectrum of wave packet W_1 . The units of the spectral density are arbitrary. \times marks the location of the centroid of the spectrum.	145
Figure 3.7	The fractional dissipation D scaled by k_{cd} the wavenumber of the centroidal component and the water depth, h as a function of the slope parameter, S . \circ , W_1 ; \bullet , W_2 ; ∇ , W_3 .	147
Figure 3.8	The upper plot is a time series of the upstream hydrophone signal band pass filtered from 20 Hz to 10 kHz for packet W_2 with $S = 0.544$. The lower plot is a spectrograph of the time series in the upper plot. 48 spectra with a bandwidth resolution of 39 Hz are shown plotted. They were computed by dividing the time series into 144-512 point segments which overlapped 171 points, windowing with a Blackman-Harris window and computing FFT's which were averaged over every 3 segments. Each color corresponds to a 5 dB re $1\text{ }\mu\text{Pa}^2$ increment in spectral level.	148

- Figure 3.9 The upper plot is a time series of a microphone signal band pass filtered from 20 Hz to 10 kHz for packet W_2 with $S = 0.544$. The lower plot is a spectrograph of the time series in the upper plot. 48 spectra with a bandwidth resolution of 39 Hz are shown plotted. They were computed by dividing the time series into 144-512 point segments which overlapped 171 points, windowing with a Blackman-Harris window and computing FFT's which were averaged over every 3 segments. Each color corresponds to a 5 dB re $1 \mu\text{Pa}^2$ increment in spectral level. 149
- Figure 3.10 Frequency spectra of the signal from the upstream hydrophone for wave packet W_1 with slope, S increasing from 0.288 to 0.512 in 0.032 increments. Pressure spectrum level, PSL in dB re $1 \mu\text{Pa}^2/\text{Hz}$. Each spectrum is the average of 5 repeats and was smoothed in the frequency domain with a 9 point Bartlett window to produce an estimate with 80 degrees of freedom. 152
- Figure 3.11 Frequency spectra of the signal from the downstream hydrophone for wave packet W_1 with slope, S increasing from 0.288 to 0.512 in 0.032 increments. Pressure spectrum level, PSL in dB re $1 \mu\text{Pa}^2/\text{Hz}$. Each spectrum is the average of 5 repeats and was smoothed in the frequency domain with a 9 point Bartlett window to produce an estimate with 80 degrees of freedom. 153
- Figure 3.12 Frequency spectra of the signal from the microphone for wave packet W_1 with slope, S increasing from 0.288 to 0.512 in 0.032 increments. Pressure spectrum level, PSL in dB re $1 \mu\text{Pa}^2/\text{Hz}$. Each spectrum is the average of 5 repeats and was smoothed in the frequency domain with a 9 point Bartlett window to produce an estimate with 80 degrees of freedom. 154

Figure 3.13 The pressure spectrum level PSL (dB re $1\mu\text{Pa}^2/\text{Hz}$) of the signal from the upstream hydrophone in two frequency bands as a function of time for packet W_1 . Each data point is the average of 5 repeats of the event. (a) $S = 0.288$ (b) $S = 0.320$ (c) $S = 0.352$ (d) $S = 0.384$ (e) $S = 0.416$ (f) $S = 0.448$ (g) $S = 0.480$ (h) $S = 0.512$. \circ , 20Hz-1 kHz; \bullet , 1-10 kHz. 157

Figure 3.14 The pressure spectrum level PSL (dB re $1\mu\text{Pa}^2/\text{Hz}$) of the signal from the downstream hydrophone in two frequency bands as a function of time for packet W_2 . Each data point is the average of 5 repeats of the event. (a) $S = 0.288$ (b) $S = 0.320$ (c) $S = 0.352$ (d) $S = 0.384$ (e) $S = 0.416$ (f) $S = 0.448$ (g) $S = 0.480$ (h) $S = 0.512$. \circ , 20Hz-1 kHz; \bullet , 1-10 kHz. 158

Figure 3.15 The pressure spectrum level PSL (dB re $1\mu\text{Pa}^2/\text{Hz}$) of the signal from the microphone in two frequency bands as a function of time for packet W_3 . Each data point is the average of 5 repeats of the event. (a) $S = 0.288$ (b) $S = 0.320$ (c) $S = 0.352$ (d) $S = 0.384$ (e) $S = 0.416$ (f) $S = 0.448$ (g) $S = 0.480$ (h) $S = 0.512$. \circ , 20Hz-1 kHz; \bullet , 1-10 kHz. 159

Figure 3.16 The mean square acoustic pressure $\overline{p^2}$ (Pa^2) of the signal from the upstream hydrophone calculated over the entire signal duration in two frequency bands as a function of the slope parameter S . The upper plot is for the frequency band 0-1 kHz and the lower plot for the band 1-10 kHz. Each data point is the average of 5 repeats of the measurement and the error bars indicate the 95% confidence limits. \circ , W_1 ; \bullet , W_2 ; ∇ , W_3 . 160

Figure 3.17 The mean square acoustic pressure $\overline{p^2}$ (Pa^2) of the signal from the downstream hydrophone calculated over the entire signal duration in two frequency bands as a function of the slope parameter S . The upper plot is for the frequency band 0-1 kHz and the lower plot for the band 1-10 kHz. Each data point is the average of 5 repeats of the measurement and the error bars indicate the 95% confidence limits. \circ , W_1 ; \bullet , W_2 ; ∇ , W_3 . 161

- Figure 3.18 The mean square acoustic pressure $\overline{p^2}$ (Pa²) of the signal from the microphone calculated over the entire signal duration in two frequency bands as a function of the slope parameter S. The upper plot is for the frequency band 0-1 kHz and the lower plot for the band 1-10 kHz. Each data point is the average of 5 repeats of the measurement and the error bars indicate the 95% confidence limits. \circ , W₁; \bullet , W₂; ∇ , W₃. 162
- Figure 3.19 The mean square acoustic pressure $\overline{p^2}$ (Pa²) of the signal from the upstream hydrophone calculated over the entire signal duration in two frequency bands as a function of the fractional dissipation D. The upper plot is for the frequency band 0-1 kHz and the lower plot for the band 1-10 kHz. Each data point is the average of 5 repeats of the measurement and the error bars indicate the 95% confidence limits. \circ , W₁; \bullet , W₂; ∇ , W₃. 164
- Figure 3.20 The mean square acoustic pressure $\overline{p^2}$ (Pa²) of the signal from the downstream hydrophone calculated over the entire signal duration in two frequency bands as a function of the fractional dissipation D. The upper plot is for the frequency band 0-1 kHz and the lower plot for the band 1-10 kHz. Each data point is the average of 5 repeats of the measurement and the error bars indicate the 95% confidence limits. \circ , W₁; \bullet , W₂; ∇ , W₃. 165
- Figure 3.21 The mean square acoustic pressure $\overline{p^2}$ (Pa²) of the signal from the microphone calculated over the entire signal duration in two frequency bands as a function of the fractional dissipation D. The upper plot is for the frequency band 0-1 kHz and the lower plot for the band 1-10 kHz. Each data point is the average of 5 repeats of the measurement and the error bars indicate the 95% confidence limits. \circ , W₁; \bullet , W₂; ∇ , W₃. 166
- Figure 3.22 A drawing of a plan (top plot) and elevation view (bottom plot) of the three-dimensional wave channel at the Offshore Technology Research Center at Texas A&M University. The layout of some of the experimental equipment is also shown. 168

Figure 3.23	A schematic of the experimental equipment set-up and the wavemaker control system.	169
Figure 3.24	A schematic of the three signal conditioning configurations used in the three-dimensional breaking experiments.	173
Figure 3.25	Time series of the surface displacement $\eta(t)$ (cm) for a three-dimensional breaking wave with a gain, $A = 0.70$, along the centerline of the channel at six locations. The wave paddles are located at $x = 0$ m and breaking occurs at 18.6 m: (a) 12.5 m (b) 15.5 m (c) 18.6 m (d) 21.6 m (e) 24.7 m (f) 27.7 m.	174
Figure 3.26	Frequency spectra of the surface displacement data plotted in figure 3.25. The dotted line in figure (b) to (f) is the reference upstream spectrum at 18.6 m: (a) 12.5 m (b) 15.5 m (c) 18.6 m (d) 21.6 m (e) 24.7 m (f) 27.7 m.	176
Figure 3.27	Contour plot of the surface displacement variance (cm^2) averaged over the entire signal duration. The x axis is the distance along the channel from the wave paddles and the y axis is the distance across the channel. $y = 0$ is the centerline of the channel and the wave paddles are located at $x = 0$ m. Waves propagated from left to right in this coordinate system.	177
Figure 3.28	The upper plot is a time series of the acoustic pressure from the downstream hydrophone for a three-dimensional breaking wave with gain, $A = 0.70$. The signal was conditioned with set-up I shown in figure 3.24. The lower plot is a spectrograph of the time series in the upper plot. 52 spectra with a bandwidth resolution of 78 Hz are plotted. They were computed by dividing the time series into 416-512 point segments which overlapped 128 points, windowing with a Blackman-Harris window and computing FFT's which were averaged over every 8 segments. Each color corresponds to a 5 dB re $1 \mu\text{Pa}^2$ increment in spectral level.	180

- Figure 3.29 The upper plot is a time series of the acoustic pressure from the upstream hydrophone for a three-dimensional breaking wave with gain, $A = 0.70$. The signal was conditioned with set-up I shown in figure 3.24. The lower plot is a spectrograph of the time series in the upper plot. 52 spectra with a bandwidth resolution of 78 Hz are plotted. They were computed by dividing the time series into 416-512 point segments which overlapped 128 points, windowing with a Blackman-Harris window and computing FFT's which were averaged over every 8 segments. Each color corresponds to a 5 dB re $1 \mu\text{Pa}^2$ increment in spectral level. 181
- Figure 3.30 The upper plot is a time series of the acoustic pressure from the microphone for a three-dimensional breaking wave with gain, $A = 0.70$. The signal was conditioned with set-up I shown in figure 3.24. The lower plot is a spectrograph of the time series in the upper plot. 52 spectra with a bandwidth resolution of 78 Hz are plotted. They were computed by dividing the time series into 416-512 point segments which overlapped 128 points, windowing with a Blackman-Harris window and computing FFT's which were averaged over every 8 segments. Each color corresponds to a 5 dB re $1 \mu\text{Pa}^2$ increment in spectral level. 182
- Figure 3.31 Frequency spectra of the signal from the downstream hydrophone conditioned using set-up I (see figure 3.24) for the three-dimensional breaking events with gains, $A = 0.24, 0.40, 0.475, 0.55, 0.675$ and 0.70 . Pressure spectrum level PSL in dB re $1 \mu\text{Pa}^2/\text{Hz}$. Each spectrum was averaged over 5 repeats of the same event and was then smoothed with a 9 point Bartlett window to produce an estimate with 80 degrees of freedom. 184

- Figure 3.32 Frequency spectra of the signal from the upstream hydrophone conditioned using set-up I (see figure 3.24) for the three-dimensional breaking events with gains, $A = 0.24, 0.40, 0.475, 0.55, 0.675$ and 0.70 . Pressure spectrum level PSL in dB re $1 \mu\text{Pa}^2/\text{Hz}$. Each spectrum was averaged over 5 repeats of the same event and was then smoothed with a 9 point Bartlett window to produce an estimate with 80 degrees of freedom. 185
- Figure 3.33 Frequency spectra of the signal from the microphone conditioned using set-up I (see figure 3.24) for the three-dimensional breaking events with gains, $A = 0.24, 0.40, 0.475, 0.55, 0.675$ and 0.70 . Pressure spectrum level PSL in dB re $1 \mu\text{Pa}^2/\text{Hz}$. Each spectrum was averaged over 5 repeats of the same event and was then smoothed with a 9 point Bartlett window to produce an estimate with 80 degrees of freedom. 186
- Figure 3.34 The pressure spectrum level PSL (dB re $1 \mu\text{Pa}^2/\text{Hz}$) of the signal from the downstream hydrophone as a function of time in two frequency bands for the three-dimensional breaking events. Each data point is the average of at least 3 repeats of the event. (a) $A = 0.24$ (b) $A = 0.40$ (c) $A = 0.475$ (d) $A = 0.55$ (e) $A = 0.625$ (f) $A = 0.70$. \circ , 10Hz-1 kHz; \bullet , 1-20 kHz. 189
- Figure 3.35 The pressure spectrum level PSL (dB re $1 \mu\text{Pa}^2/\text{Hz}$) of the signal from the upstream hydrophone as a function of time in two frequency bands for the three-dimensional breaking events. Each data point is the average of at least 3 repeats of the event. (a) $A = 0.24$ (b) $A = 0.40$ (c) $A = 0.475$ (d) $A = 0.55$ (e) $A = 0.625$ (f) $A = 0.70$. \circ , 10Hz-1 kHz; \bullet , 1-20 kHz. 190
- Figure 3.36 The pressure spectrum level PSL (dB re $1 \mu\text{Pa}^2/\text{Hz}$) of the signal from the microphone as a function of time in two frequency bands for the three-dimensional breaking events. Each data point is the average of at least 3 repeats of the event. (a) $A = 0.24$ (b) $A = 0.40$ (c) $A = 0.475$ (d) $A = 0.55$ (e) $A = 0.625$ (f) $A = 0.70$. \circ , 10Hz-1 kHz; \bullet , 1-20 kHz. 191

- Figure 3.37 The pressure spectrum level PSL (dB re $1\mu\text{Pa}^2/\text{Hz}$) of the signal from the downstream hydrophone as a function of time in two lower frequency bands for the three-dimensional breaking events. Each data point is the average of at least 3 repeats of the event. (a) $A = 0.24$ (b) $A = 0.40$ (c) $A = 0.475$ (d) $A = 0.55$ (e) $A = 0.625$ (f) $A = 0.70$. \circ , 10-150 Hz; \bullet , 150-500 Hz. 192
- Figure 3.38 The pressure spectrum level PSL (dB re $1\mu\text{Pa}^2/\text{Hz}$) of the signal from the upstream hydrophone as a function of time in two lower frequency bands for the three-dimensional breaking events. Each data point is the average of at least 3 repeats of the event. (a) $A = 0.24$ (b) $A = 0.40$ (c) $A = 0.475$ (d) $A = 0.55$ (e) $A = 0.625$ (f) $A = 0.70$. \circ , 10-150 Hz; \bullet , 150-500 Hz. 193
- Figure 3.39 The pressure spectrum level PSL (dB re $1\mu\text{Pa}^2/\text{Hz}$) of the signal from the microphone as a function of time in two lower frequency bands for the three-dimensional breaking events. Each data point is the average of at least 3 repeats of the event. (a) $A = 0.24$ (b) $A = 0.40$ (c) $A = 0.475$ (d) $A = 0.55$ (e) $A = 0.625$ (f) $A = 0.70$. \circ , 10-150 Hz; \bullet , 150-500 Hz. 194
- Figure 3.40 Mean square acoustic pressure $\overline{p^2}$ (Pa^2) of the two hydrophone signals calculated over the entire signal duration in two frequency bands plotted as a function of the gain A . The data in the upper plot is for the frequency band 0-1 kHz and the lower plot for 1-20 kHz. Each data point is the average of at least 3 repeats of the same event and the error bars indicate the 95% confidence limits of the data. \bullet , downstream hydrophone; \circ , upstream hydrophone. 196
- Figure 3.41 Mean square acoustic pressure $\overline{p^2}$ (Pa^2) of the two hydrophone signals calculated over the entire signal duration in two lower frequency bands plotted as a function of the gain A . The data in the upper plot is for the frequency band 0-150 Hz and the lower plot for 150-500 Hz. Each data point is the average of at least 4 repeats of the same event and the error bars indicate the 95% confidence limits of the data. \bullet , downstream hydrophone; \circ , upstream hydrophone. 197

Figure 3.42	Mean square acoustic pressure $\overline{p^2}$ (Pa ²) of the microphone signal calculated over the entire signal duration in two frequency bands plotted as a function of the gain A. The data in the upper plot is for the frequency band 0-1 kHz and the lower plot for 1-20 kHz. Each data point is the average of at least 5 repeats of the same event and the error bars indicate the 95% confidence limits of the data.	198
Figure 3.43	Plan view of the whitecap generated by the three-dimensional breaking event with A = 0.40. The time is referenced to plot (a) for which t = 0 s (b) t = 0.2 s (c) t = 0.47 s (d) t = 0.67 s.	200
Figure 3.44	Plan view of the whitecap generated by the three-dimensional breaking event with A = 0.475. The time is referenced to plot (a) for which t = 0 s (b) t = 0.27 s (c) t = 0.53 s (d) t = 0.8 s.	201
Figure 3.45	Plan view of the whitecap generated by the three-dimensional breaking event with A = 0.55. The time is referenced to plot (a) for which t = 0 s (b) t = 0.27 s (c) t = 0.53 s (d) t = 0.8 s.	202
Figure 3.46	Plan view of the whitecap generated by the three-dimensional breaking event with A = 0.625. The time is referenced to plot (a) for which t = 0 s (b) t = 0.27 s (c) t = 0.7 s (d) t = 1.0 s.	203
Figure 3.47	Plan view of the whitecap generated by the three-dimensional breaking event with A = 0.70. The time is referenced to plot (a) for which t = 0 s (b) t = 0.27 s (c) t = 0.53 s (d) t = 0.8 s.	204
Figure 3.48	The integrated area (ft. ²), defined as sum of the area of the whitecap at the four times corresponding to the four frames plotted in figures 3.43 to 3.47, for each breaking event and the maximum area (ft. ²), defined as the maximum whitecap area observed for each breaking event, as a function of gain. ○, integrated area; ●, maximum area.	205

- Figure 3.49 The volume of air in the cylinder V (cm^3) formed by the plunging wave crest versus the slope parameter for the 3 wave packets in the two-dimensional breaking experiments. \circ , W_1 ; \bullet , W_2 ; ∇ , W_3 . 207
- Figure 3.50 The fractional dissipation D as a function of the cylinder volume V (cm^3). \circ , W_1 ; \bullet , W_2 ; ∇ , W_3 . 208
- Figure 3.51 The mean square acoustic pressure $\overline{p^2}$ (Pa^2) of the signal from the upstream hydrophone calculated over the entire signal duration in two frequency bands as a function of the volume of the cylinder V (cm^3). The upper plot is for the frequency band 20 Hz-1 kHz and the lower plot for the band 1-10 kHz. Each data point is the average of 5 repeats of the measurement and the error bars indicate the 95% confidence limits. \circ , W_1 ; \bullet , W_2 ; ∇ , W_3 . 210
- Figure 3.52 The mean square acoustic pressure $\overline{p^2}$ (Pa^2) of the signal from the downstream hydrophone calculated over the entire signal duration in two frequency bands as a function of the volume of the cylinder V (cm^3). The upper plot is for the frequency band 20 Hz-1 kHz and the lower plot for the band 1-10 kHz. Each data point is the average of 5 repeats of the measurement and the error bars indicate the 95% confidence limits. \circ , W_1 ; \bullet , W_2 ; ∇ , W_3 . 211
- Figure 3.53 The mean square acoustic pressure $\overline{p^2}$ (Pa^2) of the signal from the microphone calculated over the entire signal duration in two frequency bands as a function of the volume of the cylinder V (cm^3). The upper plot is for the frequency band 20 Hz-1 kHz and the lower plot for the band 1-10 kHz. Each data point is the average of 5 repeats of the measurement and the error bars indicate the 95% confidence limits. \circ , W_1 ; \bullet , W_2 ; ∇ , W_3 . 212

- Figure 3.54 Spectrographs of signals from the microphone (top plot) and the upstream hydrophone (bottom plot) for the two-dimensional breaking event packet W_3 with $S = 0.48$. The spectra were averaged over 5 repeats of the event and were calculated for 32-2048 point segments overlapped by 512 points and windowed with a Blackman-Harris window. The bandwidth resolution is 9.8 Hz. Each color corresponds to a 5 dB re 1 μPa^2 increment in spectral level. 214
- Figure 3.55 Spectrographs of signals from the microphone (top plot) and the upstream hydrophone (bottom plot) for the two-dimensional breaking event packet W_1 with $S = 0.416$. The spectra were averaged over 5 repeats of the event and were calculated for 32-2048 point segments overlapped by 512 points and windowed with a Blackman-Harris window. The bandwidth resolution is 9.8 Hz. Each color corresponds to a 5 dB re 1 μPa^2 increment in spectral level. 215
- Figure 3.56 The characteristic frequency f (Hz) of (a) the microphone signal and (b) the hydrophone signal for the two-dimensional breaking events plotted versus the slope parameter S . \circ , W_1 ; \bullet , W_2 ; ∇ , W_3 . 217
- Figure 3.57 The characteristic frequency f (Hz) of (a) the microphone signal and (b) the hydrophone signal for the two-dimensional breaking events plotted versus the fractional dissipation, D . \circ , W_1 ; \bullet , W_2 ; ∇ , W_3 . 218
- Figure 3.58 Frequency spectra (pressure spectrum level PSL in dB re 1 $\mu\text{Pa}^2/\text{Hz}$) of the signal from the downstream hydrophone for the three-dimensional breaking events. The gain $A = 0.24, 0.40, 0.475, 0.55, 0.625$ and 0.70 . The spectra were computed from data conditioned using set-up III and decimated to a sampling rate of 1 kHz. The data was divided into 17-256 point segments, windowed using a Blackman-Harris window, overlapped by 64 points and averaged over 5 repeats of the events. The estimated spectra have 10 degrees of freedom and a bandwidth resolution of 3.9 Hz. \blacktriangledown mark the shifting low frequency spectral peaks. 219

Figure 3.59 A series of photographs showing the formation and subsequent break-up of the cylinder of air formed by a plunging breaker for wave packet W_2 with $S = 0.544$. Frame (23) $t = 0.322$ s, prior to the impact of the plunging crest, the free surface is visible as a horizontal line across the middle of the photograph and the plunging wave crest is visible above the free surface. Frame (24) $t = 0.465$ s, the crest has just impacted the free surface. Frame (25) $t = 0.532$ s, the smooth-walled cylinder of air is partially visible, the lower edge of the cylinder is the horizontal line slightly above the centerline of the frame. Frame (26) $t = 0.599$ s, the smooth-walled cylinder fills the upper half of the frame. Frame (27) $t = 0.665$ s, the cylinder is becoming unstable, waves can be seen forming along the lower portion of the cylinder. Frame (28) $t = 0.699$ s (29) $t = 0.732$ s (30) $t = 0.766$ s, the break-up of the cylinder into a cloud of small bubbles continues, the waves visible in frame (27) develop into periodic bubble cloud substructures most clearly visible in frame (29). Frame (31) $t = 0.799$ s (32) $t = 0.866$ s, the structure of the bubble cloud becomes finer as the bubbles break-up into progressively smaller sizes.

222

Figure 3.60 A series of photographs showing a view from the side of the cylinder formation for packet W_2 with $S = 0.544$. Frame (34) $t = 0.266$ s, the wave crest has just begun to plunge forward. Frame (35) $t = 0.333$ s, the crest has curled over and the cylinder is partially formed, this frame matches the time of frame (23) in figure 3.59. Frame (36) $t = 0.466$ s, the wave crest has just impacted the free surface and the cylinder is fully formed, this frame matches the time of frame (24) in figure 3.59.

224

Figure 3.61 Geometry of the problem of an oscillating air cylinder located close to a pressure release surface.

226

Figure 3.62	The resonant frequency f_c (Hz) of a cylinder of air oscillating near a pressure release surface as given by equation 3.19, evaluated for various values of L/a_0 , the ratio of twice the distance between the cylinder center and the free surface to the cylinder radius, plotted as a function of the cylinder radius a_0 (m).	231
Figure 3.63	The resonant frequency f_c (Hz) a cylinder of air oscillating near a pressure release surface as given by equation 3.19 plotted as a function of the cylinder radius a_0 (m) compared to the observed oscillation frequencies and radii of the cylinders of air produced by the two-dimensional breaking waves. \circ , W_1 ; \bullet , W_2 ; ∇ , W_3 .	232
Figure 3.64	Trace of the geometry of the free surface and the air cylinder for packet W_2 with $S = 0.544$. The cross hatched region is the measured mass.	234
Figure 3.65	Observations of the oscillation frequencies and radii of the cylinders of air produced by the two-dimensional breaking waves compared to equation 3.20. \circ , W_1 ; \bullet , W_2 ; ∇ , W_3 .	236
Figure 3.66	Typical plot of the magnitude of the resonant amplification factor A_n as a function of frequency f (Hz) for the first three modes for which $n = 0, 1$ and 2 .	239
Figure 3.67	Theoretical predictions of the resonant frequencies f (Hz) of the first 4 modes ($n = 0, 1, 2$ and 3) of a cylindrical bubble cloud as a function of time for the two-dimensional packet W_2 with $S = 0.384$.	244
Figure 3.68	Theoretical predictions of the resonant frequencies f (Hz) of the first 4 modes ($n = 0, 1, 2$ and 3) of a cylindrical bubble cloud as a function of time for the two-dimensional packet W_2 with $S = 0.448$.	245
Figure 3.69	Theoretical predictions of the resonant frequencies f (Hz) of the first 4 modes ($n = 0, 1, 2$ and 3) of a cylindrical bubble cloud as a function of time for the two-dimensional packet W_2 with $S = 0.544$.	246

- Figure 3.70 Theoretical predictions of the resonant frequencies f (Hz) of the first 4 modes ($n = 0, 1, 2$ and 3) of a cylindrical bubble cloud as a function of time for the three-dimensional packet with gain $A = 0.40$. 247
- Figure 3.71 Theoretical predictions of the resonant frequencies f (Hz) of the first 4 modes ($n = 0, 1, 2$ and 3) of a cylindrical bubble cloud as a function of time for the three-dimensional packet with gain $A = 0.70$. 248
- Figure 3.72 Spectrograph of the signal from the upstream hydrophone for the two-dimensional breaking event packet W_2 with $S = 0.384$. The theoretical resonant frequencies of a cylindrical bubble cloud computed using the void fraction data are marked with Δ for mode 0 in the upper plot and for mode 1 in the lower plot. The spectra were averaged over 5 repeats of the event and were calculated for 32-2048 point segments overlapped by 512 points and windowed with a Blackman-Harris window. The bandwidth resolution is 9.8 Hz. Each color corresponds to a 5 dB re $1 \mu\text{Pa}^2$ increment in spectral level. 249
- Figure 3.73 Spectrograph of the signal from the microphone for the two-dimensional breaking event packet W_2 with $S = 0.384$. The theoretical resonant frequencies of a cylindrical bubble cloud computed using the void fraction data are marked with Δ for mode 0 in the upper plot and for mode 1 in the lower plot. The spectra were averaged over 5 repeats of the event and were calculated for 32-2048 point segments overlapped by 512 points and windowed with a Blackman-Harris window. The bandwidth resolution is 9.8 Hz. Each color corresponds to a 5 dB re $1 \mu\text{Pa}^2$ increment in spectral level. 250

- Figure 3.74 Spectrograph of the signal from the downstream hydrophone 253
for the three-dimensional breaking event with $A = 0.70$. The theoretical resonant frequencies of a cylindrical bubble cloud computed using the void fraction data are marked with Δ for mode 0 in the upper plot and for mode 1 in the lower plot. The spectra were averaged over 5 repeats of the event and were calculated for 52-4096 point segments overlapped by 1024 points and windowed with a Blackman-Harris window. The bandwidth resolution is 9.8 Hz. Each color corresponds to a 5 or 3 dB re $1 \mu\text{Pa}^2$ increment in spectral level.
- Figure 3.75 Spectrograph of the signal from the upstream hydrophone 254
for the three-dimensional breaking event with $A = 0.40$. The theoretical resonant frequencies of a cylindrical bubble cloud computed using the void fraction data are marked with Δ for mode 0 in the upper plot and for mode 1 in the lower plot. The spectra were averaged over 5 repeats of the event and were calculated for 52-4096 point segments overlapped by 1024 points and windowed with a Blackman-Harris window. The bandwidth resolution is 9.8 Hz. Each color corresponds to a 5 or 3 dB re $1 \mu\text{Pa}^2$ increment in spectral level.
- Figure 3.76 Time series of the sound spectrum level, SSL (same as PSL) 259
in dB re $1 \mu\text{Pa}^2/\text{Hz}$ in three frequency bands centered at 1 kHz, 10 kHz and 18 kHz when an ocean surface wave is breaking overhead of the sampling hydrophone (Farmer and Vagle, 1989).
- Figure 4.1 Peak pressures (\times) (Pa) of the bubble oscillation pulses 264
observed by Updegraff and Anderson (1991) as a function of the oscillation frequency. The * symbols joined by the solid line are the mean of the peak pressures in a frequency bandwidth 1 kHz wide centered at the symbol locations.
- Figure 4.2 $N(a)$ the number of bubbles per wave in the radius interval 265
from $(a_i + a_{i-1})/2$ to $(a_{i+1} + a_i)/2$ centered at a_i , (Medwin and Daniel, 1990).
- Figure 4.3 Measured sound power spectrum averaged over six gently 267
spilling waves (Medwin and Daniel, 1990).

Figure 4.4 Sketch of the geometry of the problem and definitions of some of the parameters.	268
Figure 4.5 The power spectrum of an individual bubble pulse $g(\omega; \omega_b)$ as given by equation 4.4.	270
Figure 4.6 A comparison of the sound spectrum calculated using the analytic spectrum model, plotted with the bold line, and the Monte Carlo model, plotted with the thin line.	273
Figure 4.7 The bold line is the mean spectrum averaged from ten spectra generated by the analytic spectrum model. The upper and lower lines are the 95% confidence limits.	274
Figure 4.8 Sketch of the formation of bubbles at the toe of the spilling region in a gently spilling wave.	276
Figure 4.9 Comparison of a sound spectrum from the Monte Carlo model with $\epsilon = 0.005-0.025$ and $L = 0.01-0.03$ m and the measured sound spectrum of Medwin and Daniel (1990), plotted with a bold line. The bars indicate the 95% confidence limits of the modeled spectrum.	277
Figure 4.10 Comparison of a sound spectrum from the analytic spectrum model with $\epsilon = 0.015$ and $L = 0.02$ m and the measured sound spectrum of Medwin and Daniel (1990), plotted with a bold line. The bars indicate the 95% confidence limits of the modeled spectrum.	278

List of Tables

	<u>page</u>
Table 2.1 Computer programs used to obtain the transfer function of the wave maker system. Listings of these programs can be found in appendix A.	75
Table 2.2 Computer programs used to generate the wave packets. See appendix A for complete listings.	77
Table 2.3 Wave packet characteristics; $\Delta f/f_c = 0.73$ and $x_b k_c = 28.3$ for all wave packets	78
Table 2.4 Specifications of a B&K 8105 spherical hydrophone.	81
Table 2.5 Specifications of a B&K 2635 charge amplifier.	82
Table 2.6 Kustom Electronics radar model MR7/9 characteristics.	85
Table 2.7 Acoustic modes and their theoretical cutoff frequencies	106
Table 3.1 Wave packet characteristics; $\Delta f/f_c = 1.0$ and $x_b k_c = 24.6$ for all wave packets.	136
Table 3.2 The frequency response and output characteristics of the Wilcoxon model AM-5 amplifiers.	138
Table 3.3 Specifications of 844P8B-5 low pass and the 874P8B-3 highpass filters	139
Table 3.4 The specifications of the Symetrix model SX202 microphone pre-amplifier.	142
Table 3.5 Acoustic modes and their theoretical cut-off frequencies for the 0.76 m wide 0.6 m deep wave tank.	150
Table 3.6 Results from analysis of traces of the free surface geometry and cylinder. The measured mass was obtained from the traces, the theoretical mass from equation 3.12, with $L/a_0 = 2$, and the correction factor equals $\sqrt{(\text{theoretical mass} / \text{measured mass})}$.	235
Table 3.7 The maximum mean void fraction and maximum bubble cloud radius for the five breaking events for which void fraction measurements are available.	241

Table 3.8 A comparison of the predicted resonant frequency of the lowest mode of a two-dimensional bubble cloud, f_o (calculated from the magnitude of A_n given by equation 3.22) and the predicted resonant frequency of the lowest mode of a spherical bubble cloud of equal volume, f_{os} (calculated from equation 3.24). a_o is the radius of the observed bubble cloud, r_o is the radius of a spherical bubble cloud of equal volume and α is the mean void fraction of the observed bubble cloud.

242

Chapter 1: Introduction and Literature Review

Deep-water breaking waves occur on the ocean surface in all but the lightest winds. Breaking occurs over a wide range of scales, from gently spilling waves only centimeters long to energetic plunging breakers tens of meters in length. Plunging breakers are generally steep, very energetic and are characterized by a wave crest which plunges forward and impacts the free surface ahead of the wave. Spilling breakers are less energetic events in which the wave begins to break at the crest and forms a whitecap which rides down the forward face of the wave (Longuet-Higgins and Turner, 1974).

Breaking is considered to be the dominant mechanism responsible for limiting the height of waves and for dissipating energy (Phillips, 1977). Breaking waves are believed to be the primary mechanism for the transfer of momentum from the wind to surface currents (Longuet-Higgins, 1969). Wave breaking is known to enhance the transfer of gas across the air-sea interface and it may play an important role in the transfer of anthropogenic CO₂ from the atmosphere to the oceans (Watson et al, 1991). The presence of breaking waves on the ocean surface has been shown to enhance the scattering of microwaves and breaking waves are believed to be the dominant source of sea surface sound in the ocean at frequencies greater than 500 Hz (Kwoh and Lake, 1981, Melville et al, 1988, Farmer and Vagle, 1988 and Jessup et al, 1990).

Breaking clearly has a great influence on the dynamics of the atmosphere and oceans. Detecting breaking waves on the ocean surface is possible using remote sensing techniques such as microwave backscatter and passive acoustics (Keller et al, 1981, Jessup et al, 1990 Crowther, 1988 and Farmer and Vagle, 1988). These techniques provide valuable information on the statistics and kinematics of breaking waves but they have not yet proven effective for studying the dynamics of breaking. A common measure of breaking is the whitecap coverage, which is defined as the fraction of the sea

surface which is covered with whitecaps. Whitecap coverage has been correlated with wind speed and atmospheric stability but such correlations are of limited usefulness because they are indirectly related to the dynamics of breaking (Monahan and O'Muirheartaigh, 1986). Attempts have been made to detect breaking waves using a jump meter (Longuet-Higgins and Smith, 1983). The jump meter identified breaking by using the amplitude of the time derivative of the surface displacement elevation as measured by a wave gauge. This technique proved to be unreliable because it depended on the assumption that all waves with local slopes greater than a critical value were about to break or were breaking. At the present time there is no proven method for quantitatively studying the dynamics of breaking waves in the ocean.

Much of our current understanding of the dynamics of breaking waves has been gained by studying them in the laboratory. In the laboratory it is possible to control and systematically vary the important dynamical variables associated with breaking; the wave slope and energy dissipation. It was first shown by Melville and Rapp (1985) that the amount of energy dissipated by breaking correlated with the pre-breaking wave slope. They found that up to 40% of the pre-breaking wave energy could be dissipated by a steep plunging breaker. Melville et al (1988) observed that the acoustic energy radiated and the microwave power backscattered by breaking waves in the laboratory correlated with the wave slope and the energy dissipation. This was the first conclusive evidence that measurements of the sound and backscattered microwave power produced by breaking waves could be used to quantitatively study the dynamics of breaking waves.

The laboratory experiments described in this thesis were motivated by the fact that these preliminary experiments described above demonstrated that the simple averaged acoustic and microwave measurements were correlated with the dynamics of breaking. Prior to these measurements it was known that the microwave power backscattered from the ocean surface and the oceanic ambient sound levels varied as a function of the windspeed (Wenz, 1962 and Ulaby, Moore and Fung, 1986, p.859).

Correlations of the backscattered microwave power and ambient sound levels with the windspeed are useful tools if the goal is to use remote sensing to estimate the windspeed over the oceans. However, if the goal is to use these remote sensing techniques to obtain a deeper understanding of the dynamics of breaking waves and their role in air-sea interaction then more detailed studies which relate the dynamics of breaking directly to the sound levels and backscattered microwave power are required.

1.1 Ambient Sound Measurements

Ambient sound in the ocean has been a subject of interest to oceanographers for many years. In 1948 Knudsen et al found that spectral levels of "ambient noise from water motion" decreased with increasing frequency at a rate of 5 to 6 dB per octave in the frequency range 100 Hz to 25 kHz and that the sound levels increased with increasing windspeeds. Breaking waves at the sea surface were cited as a possible source of this sound. In 1962 Wenz did an extensive review of the available oceanic ambient sound data and found the same -5 to -6 dB spectral slope as Knudsen et al (1948) had observed. Shown in figure 1.1 is a composite plot of his ambient sound spectra. He also found that the sound spectrum levels increased with windspeed. From 500 Hz to 20 kHz the wind dependence was described by the following empirical rule; with each doubling of the windspeed from 2.5 to 40 knots the spectrum levels increase by 5dB. Wenz concluded that this data supported the hypothesis that oscillating gas bubbles, cavitation and spray at the sea surface were the sources of sound in the 100 Hz to 20 kHz frequency range.

More recently Kerman et al (1983) using data from previous studies (Pigott 1964, Crouch and Burt 1971, Cato 1976, Shaw et al 1978 and Shooter and Gentry 1981) found that the ambient sound intensity was correlated with the windspeed but that the slope of the correlation changed at a windspeed of approximately 5 m/s. For windspeed

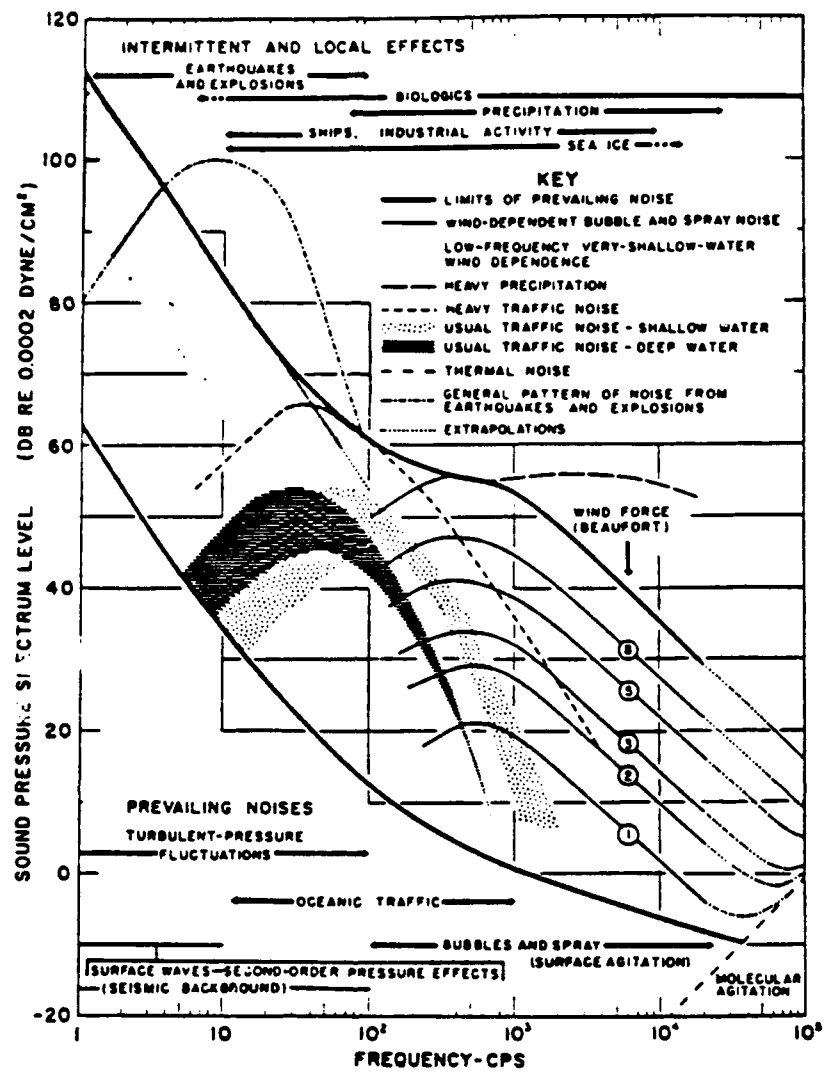


Figure 1.1 Frequency spectra of ambient noise in the ocean. (from Wenz, 1962).

$U < 5$ m/s the sound intensity was proportional to U^3 and for $U > 5$ m/s it was proportional to U^2 . Kerman (1984) attributes this change in slope to either a change in a single mechanism associated with breaking waves or to two different mechanisms being responsible for the generation of the sound. Farmer and Lemon (1984) correlated the NSL (noise spectrum level) in frequency bands centered at 4.3, 8.0, 14.5 and 25.0 kHz with windspeed. They observed that the spectrum levels at 14.5 and 25.0 kHz did not increase as rapidly with windspeed as those at 4.3 kHz. The effect was more pronounced at higher windspeeds. They attributed this effect to the bubbly layer generated by breaking waves at higher windspeeds. The bubbly layer attenuates the sound produced by breaking waves at the sea surface. The attenuation is more pronounced at higher frequencies hence the reduced spectral levels at 14.5 and 25 kHz. Vagle et al (1990) observed that the NSL was lower than that predicted for steady winds when the windspeed was increasing and when the windspeed was decreasing, it was higher. They suggest that this is due to disequilibrium of the surface wave field when the windspeed is changing.

Carey et al (1990) examined ambient sound data over a range of frequencies from 50 Hz to 20 kHz. In figure 1.2 a plot of the sound spectrum level (SSL) at various frequencies as a function of the windspeed for ambient sound data from the North Sea is shown. At 20 kHz the SSL increases with the windspeed from 4 m/s to 12 m/s and then decreases for higher windspeeds. This decrease is attributed to bubble absorption and trapping of the sound in the near surface bubbly layer. At very low frequencies 50 Hz to 600 Hz the SSL is constant for windspeeds less than 6 m/s and increases with windspeed at speeds greater than 6 m/s.

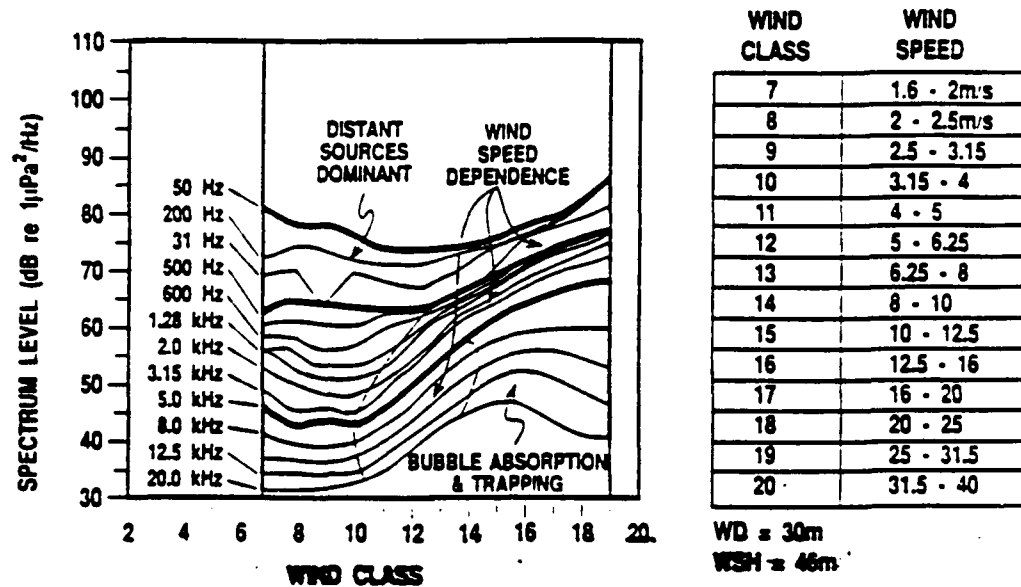


Figure 1.2 Spectrum level of ambient sound as a function of the windspeed class from data gathered in the North Sea (from Carey et al 1990).

1.2 Sound Produced by Oscillating Air Bubbles

Minnaert (1933) studied the oscillation of air bubbles released from an underwater nozzle. He calculated the kinetic energy of the liquid surrounding the bubble and the potential energy of the gas inside the bubble and obtained an equation for the resonant frequency of the lowest mode of bubble oscillation. The radian frequency of the lowest mode (volume pulsations) is given by,

$$\omega_b = \left(\frac{1}{a_o} \right) \left[\frac{3\kappa P_o}{\rho} \right]^{1/2} \quad 1.1$$

where ω_b is the resonant radian frequency, a_o is the equilibrium radius of the bubble, κ is the polytropic index of the bubble gas, P_o is the ambient pressure at the bubble and ρ is the density of water. If it is assumed that the bubble compression is adiabatic, as Minnaert (1933) did, then $\kappa = \gamma = 1.4$ the ratio of the specific heats. At resonance the adiabatic assumption is valid; however, at lower frequencies oscillating bubbles behave isothermally and $\kappa = 1$ (Prosperetti 1984).

The effect of nonspherical bubble shape on the resonant frequency was found by Strasberg (1953) to be quite small. He modeled the shape of nonspherical bubbles as a family of oblate spheroids. When the ratio of the major to minor axis was equal to 3 the resonant frequency was 5% higher than that of an equal volume spherical bubble.

If the bubble is oscillating near a free surface, as is often the case for bubbles beneath breaking waves, then the resonant frequency is altered. For sound waves in water incident on a free surface with air, the surface acts as a pressure release surface. The impedance, ρc , (where ρ is the density of the fluid or gas and c is the velocity of sound in the fluid or gas) of the water is much greater than that of the air. Therefore the pressure reflection coefficient, defined as the ratio of the amplitude of the reflected

pressure wave to that of the incident pressure wave, equals minus one and the pressure transmission coefficient, defined as the ratio of the amplitude of the pressure wave transmitted into the air to that of the incident pressure wave, equals zero. The acoustic energy is totally reflected but with a phase shift of π and the amplitude of the acoustic pressure field transmitted into the air is negligible (Dowling and Ffowcs Williams, 1983). The effect of the pressure release surface is to cause the oscillating bubble which radiates sound as a monopole source when it is located far from any boundaries to radiate sound as a dipole. This is evident from the fact that the radiated pressure field from a bubble located at a distance $L/2$ beneath a free surface is equal to that of an oscillating bubble radiating as a monopole plus the pressure field from an image bubble located a distance $L/2$ above the free surface and oscillating 180° out of phase with the real bubble. The sum of these two pressure fields meets the pressure release boundary condition at the free surface and produces a dipole radiation pattern (Clay and Medwin, 1977, p.452). It can be shown that when the ratio of the bubble radius to the distance between the free surface and the bubble is small, $a_0 / L \ll 1$, the resonant frequency can be approximated by,

$$\omega_s = \omega_b (1 + a_0 / L)^{1/2} \quad 1.2$$

where ω_s is the resonant frequency including free surface effects, ω_b is given by equation 1.1 and L is twice the distance from the bubble center to the free surface (Longuet-Higgins, 1990). If we take $a_0 / L = 0.2$ (the bubble is 5 radii away from the free surface) then eq. 1.2 gives $\omega_s = 1.10 \omega_b$, an increase of 10%.

Franz (1959) investigated the sound produced by the impact of solid bodies and water drops on a free surface. He conducted a series of experiments using high speed photography and sound measurements to study the impact and splashes produced by rigid bodies and water drops. He found that the sound was due to; 1) the initial impact and

passage of the body or drop through the free surface, 2) the resonant vibrations of the rigid body, and 3) the volume oscillations of air bubbles in the water. More recently Pumphrey and his co-workers (Pumphrey et al 1989 and Pumphrey and Crum 1990) have studied the problem of sound from drop impact and rainfall in detail. They observed that every drop produces sound due to its impact but that only some of the drops produce sound due to the formation of an air bubble. It was discovered that for drops falling at their terminal velocities only a narrow range of drop sizes, 0.8 to 1.1 mm, entrained bubbles. The acoustic signals radiated by the oscillating bubbles were damped sinusoids and the frequency of oscillation was well predicted by Minnaert's formula, equation 1.1 . The pressure radiation pattern was consistent with the assumption that the bubbles radiate as dipoles due to their close proximity to the free surface.

1.3 Measurements of the Sound Generated by Breaking Waves

Breaking waves were first suggested as a source of the wind dependence of oceanic ambient sound by Knudsen et al in 1948. More recently Kerman (1984), Farmer and Vagle (1988) and Pumphrey and Ffowcs Williams (1990) have also concluded that the wind dependence of ambient sound in the ocean at frequencies greater than several hundred Hz is caused by the increasing density and frequency of occurrence of breaking waves . Farmer and Vagle (1988) sampled the sound produced by breaking waves in the ocean in three frequency bands centered at 4.3, 14.5 and 25 kHz with three hydrophones located at depths of 1, 10 and 40m. They used the data from the 4.3 kHz band to infer information about the surface wave field. A peak at one-half the frequency of the dominant waves was observed in the acoustic spectra . This is consistent with the observation that waves tend to break at one-half the frequency of the dominant waves (Donelan et al 1972). They concluded that the variability of the acoustic signal is

governed by; 1) the mean spacing of the breaking events, 2) the duration of the events, 3) the tendency of the breaking events to occur at twice the dominant wave period, and 4) the larger scale "groupiness" of the wave field. They used a model to quantitatively estimate the wave field parameters from the acoustic time series. Increasing windspeeds were found to produce increases in; 1) the dominant wave period, 2) the mean breaker spacing, and 3) the acoustic strength of the events. These results were significant because they demonstrated that measurements of the sound generated by breaking waves could be used to study the kinematics and statistics of breaking waves.

In another field experiment Farmer and Vagle (1989) sampled the sound generated by breaking waves in the frequency range 40 Hz to 20,000 Hz. Plots of the sound spectrum level in three frequency bands showed that the signal level in all three bands rise simultaneously and then decay gradually. An example of the sound spectrum level as a function of time in the three bands for a typical breaking event is shown plotted in figure 1.3. They observed that the acoustic spectra had well defined peaks which remained generally consistent from one breaking event to the next, but which changed significantly from storm to storm. The fine structure of the observed spectra remained coherent throughout a breaking event and was similar from one event to the next. This can be seen in figure 1.4 where three of their sound spectra are plotted showing the background level prior to breaking in the upper plot and two spectra at different times during the breaking event in the lower two plots. They state that the coherent fine structure evident in the lower two spectra was typical of their complete data set. They do not believe that this coherent structure is due to coherent features in the sound generation mechanism or the hydrodynamics of the breaking process but rather is due to the effects of waveguide propagation of the sound through the ocean-surface bubble layer.

Farmer and Vagle (1989) investigated this hypothesis by estimating sound speed anomaly profiles from bubble populations which were obtained from multi-frequency inverted echo sounder data. The profiles were then used to calculate the modal cut off

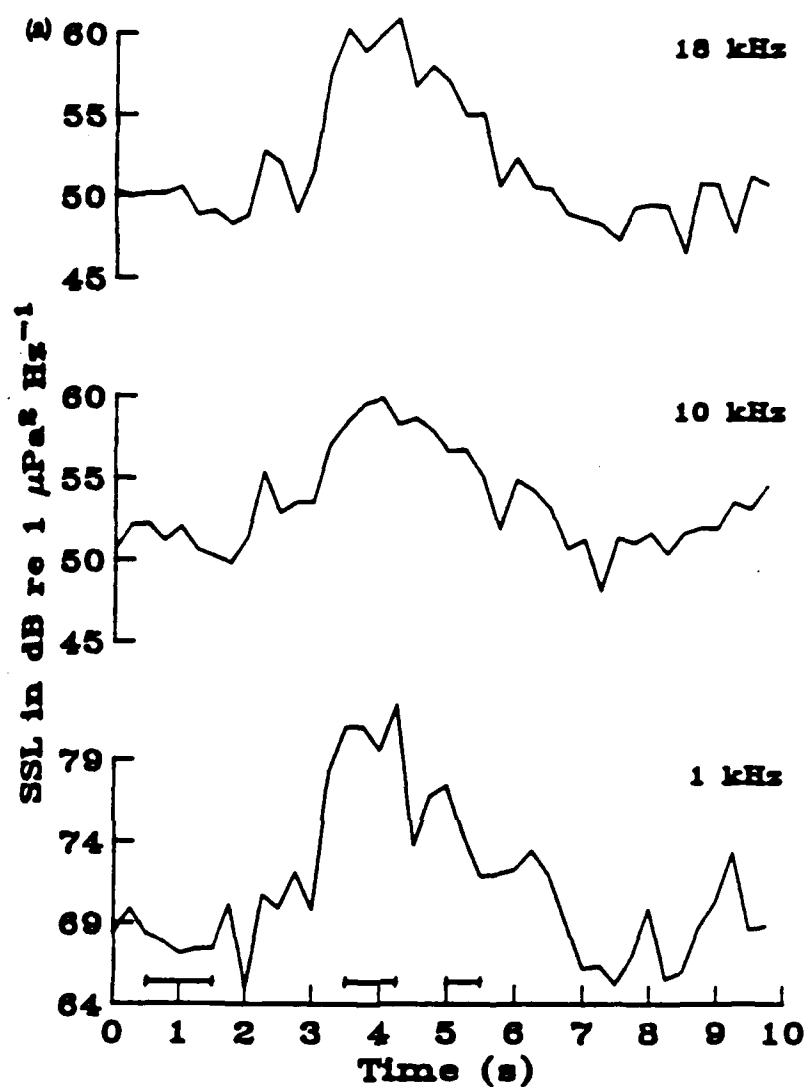


Figure 1.3 An example of the sound spectrum level as a function of time in three frequency bands measured beneath a breaking wave in the ocean (from Farmer and Vagle, 1989).

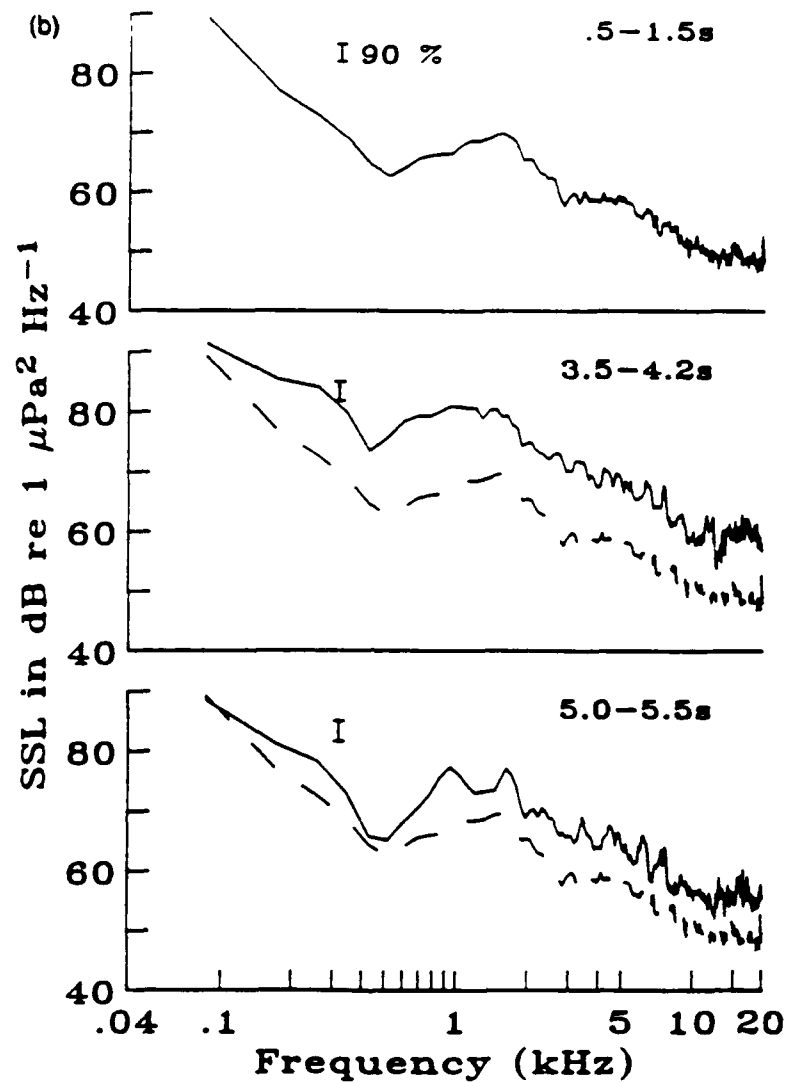


Figure 1.4 Ambient sound spectrum level of a breaking wave at sea. The spectra are plotted for three different time intervals during the event. The upper spectrum represents the background sound spectrum prior to breaking and is shown in the lower plots as a dashed line. The lower two spectra correspond to times during active breaking (from Farmer and Vagle, 1989).

frequencies of the acoustic waveguide formed by the bubbly layer. The predicted cut-off frequencies were in reasonable agreement with the observed peaks in the acoustic spectra. From this they concluded that the observed coherent structure of the sound spectra was caused by the propagation of the received signals through the waveguide formed by the surface bubble layer. These results are important because they demonstrate that not only can the sound generated by breaking be used to infer information about the kinematics and statistics of breaking waves but it can also be used to quantify the effect breaking waves have on the ocean surface layer.

Farmer and Vagle (1989) also concluded from their data that breaking waves produce sound at low frequencies, in the range 50 Hz to 500 Hz. Vagle (1989), referring to the same data set, concludes that breaking waves contribute to the ambient sound field at frequencies as low as 50 Hz. Figure 1.5, reproduced from Vagle (1989), shows the sound spectra from four breaking events where the background f^{-2} trend has been removed. Low frequency ambient sound is clearly evident at frequencies as low as 60 Hz.

Crowther (1988, 1989) used a bottom mounted directional hydrophone at a depth of 65 m to 80 m to study the sound from breaking waves in the frequency range from 10 kHz to 50 kHz. He observed that fluctuations in the hydrophone signal caused by breaking waves could be as large as 20 dB. In figure 1.6, reproduced from Crowther (1988), a plot of the pressure spectrum level in five frequency bands 2 kHz wide and centered at frequencies from 10 kHz to 50 kHz is shown. The large fluctuations in the signal correspond to the passage of breaking waves above the upward looking hydrophone. The signals from the various bands are remarkably similar although the fluctuations in the signal centered at 10 kHz are not as large as in the other bands. This is likely due to the fact that the hydrophone beamwidth was much larger at 10 kHz and therefore the signal is averaged over a much larger area of the ocean surface. The sound was measured for windspeeds in the range 3 m/s to 20 m/s. He found that the horizontal

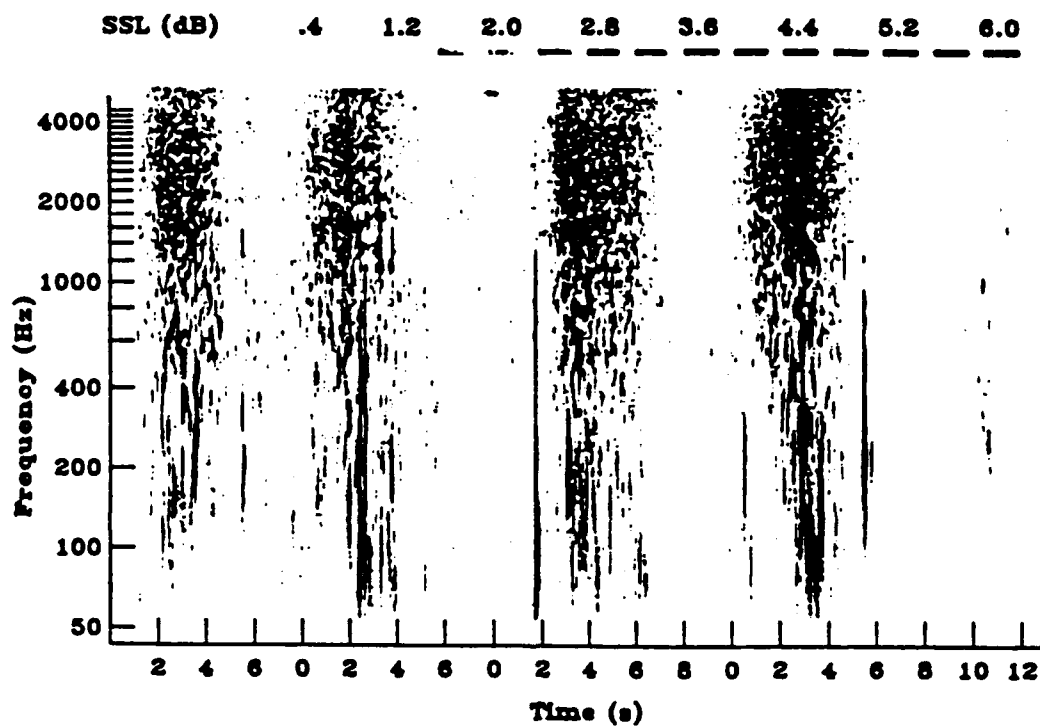


Figure 1.5 Spectrogram of the sound generated by breaking ocean waves. The grey scale indicates the spectral level above the background f^{-2} spectrum. There is energy in the spectra down to frequencies as low as 60 Hz. (from Vagle, 1989).

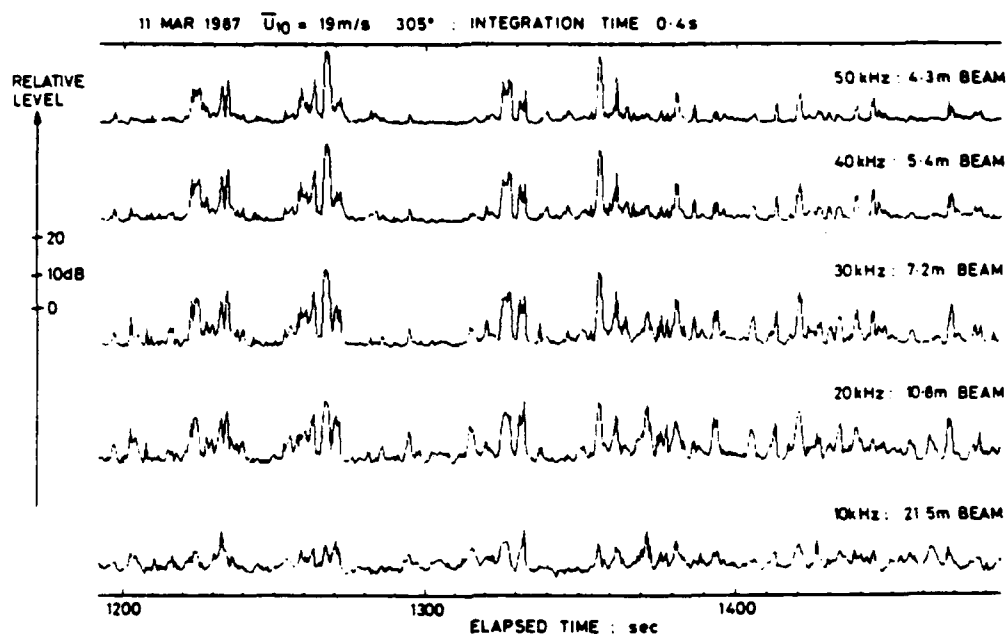


Figure 1.6 The pressure spectrum level of the sound as a function of time sampled by an upward looking directional hydrophone mounted on the ocean floor in 80 meters of water in five 2 kHz wide frequency bands from 10 kHz to 50 kHz (from Crowther, 1988).

speed of the sound sources beneath breaking waves was approximately equal to one-half the windspeed in well developed seas.

Hollet (1989) used a vertical array of hydrophones to form an end-fire beam which received the sound from a patch of the ocean surface directly above the array. Strong bursts of sound were observed which correlated with visual observations of whitecaps directly above the array. During the breaking events significant low frequency sound at frequencies as low as 200 Hz was observed.

Banner and Cato (1988) used simultaneous sound measurements and high speed photography to study the mechanism of sound generation beneath a laboratory model of a breaking wave. They generated a quasi-steady stationary breaking wave by submerging a hydrofoil in a steady flow. The acoustic signal was found to be composed of "discrete tone bursts" which were associated with the formation of bubbles at the leading edge of the breaker and with the splitting and coalescence of bubbles. They concluded that the character of the observed sound suggested that its source was the damped resonant oscillation of air bubbles in water. Bubbles bursting at the free surface did not appear to produce significant sound energy and no sound was observed to correlate with the large deformations of bubbles as they were swept downstream through the wave.

Pumphrey and Ffowcs Williams (1990) studied the generation of sound beneath a "rather crude model of a breaking wave". Breaking was modeled in a channel using the steady flow of water over a small weir. They made simultaneous sound measurements and high speed cinematographic photographs of the flow. It was found that the beginning of sound production coincided with the formation of bubbles as they detached from the free surface. The measured frequency of oscillation agreed well with the theoretically predicted values (see equation 1.1) for air bubbles oscillating at their resonant frequency.

Some of the strongest experimental evidence to date in support of the hypothesis that newly created bubbles oscillating at their linear resonant frequency are the dominant source of sound beneath gently breaking waves has been provided by Medwin and his co-workers (Medwin and Beaky, 1989 and Medwin and Daniel, 1990). The experiments were conducted in the Ocean Acoustic Wave Facility at the Naval Postgraduate school which consists of a wave channel 17 m long , 1.2 m wide and 1.2 m deep which terminates in a 3 m deep, 3m square anechoic chamber. A wedge shaped plunger wavemaker was used to generate a steady train of 1.4 Hz surface waves which broke approximately 1 m after entering the anechoic chamber. The sound was measured using two hydrophones mounted at 12 and 24 cm below the free surface. The acoustic time series were found to be composed of a number of damped sinusoidal pulses.

Medwin and Beaky (1989) studied over 2000 sound pulses and classified them according to the shape of the pulse. Type A1 (simply damped, spherical bubble) and A2 (doubly damped, spherical bubble) occurred approximately 65% of the time. A typical type A bubble oscillation time series is shown in figure 1.7 . Type A1 bubbles are damped sinusoidal pulses characterized by a single damping rate which agreed well with theoretically predicted damping rates for air bubbles in water. Type A2 bubbles are damped sinusoidal pulses characterized by two damping rates. Initially the damping is twice as large as theoretically predicted and the final damping rate equals the predicted values. They attribute the higher damping to non-linear dissipation mechanisms such as bubble interaction with the ocean surface or acoustic streaming. The remaining 35% of the bubbles are classified as type B, damped oscillation with spin-off bubbles, type C, near surface moving bubbles, and type D, amplitude-modulated bubbles. The slope of the observed acoustic spectra was approximately -5 dB per octave in agreement with the observations of Knudsen et al (1948) and Wenz (1962). Medwin and Beaky (1989) conclude that ambient sound in the ocean in the frequency range 1 kHz to 20 kHz is due to the oscillating air bubbles produced by spilling breakers. They also state that sea

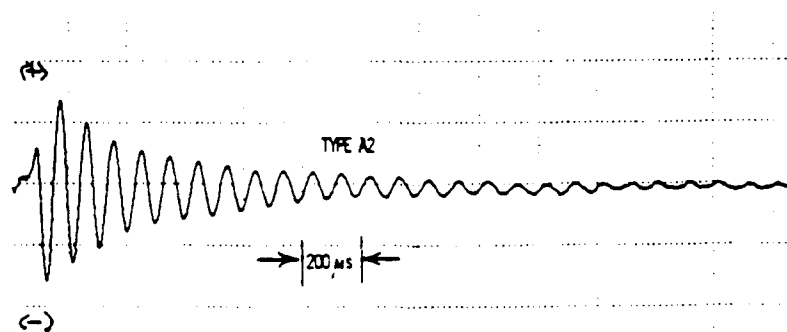


Figure 1.7 Typical sound pulse emitted by an oscillating air bubble entrained by a gently spilling breaking wave in a laboratory wave channel (from Medwin and Beaky, 1989).

surface sound does not depend on the number of "senile" bubbles which may be observed as whitecap coverage or bubble clouds on inverted echo sounders.

Medwin and Daniel (1990), utilizing the same experimental set-up as Medwin and Beaky (1989), identified the radius, position and time of creation of several hundred bubbles beneath gently spilling waves. The bubble sizes observed ranged from 50 μm to 7.4 mm with the peak in the bubble size spectrum occurring at 150 μm . They found that bubble production decreases exponentially with time and that 97% of the bubbles were produced in the first 500 ms after the initiation of breaking. They calculated the volume of air encapsulated by bubbles per square meter of water surface as a function of the bubble radius and concluded that the largest bubbles contributed the majority of the volume even though there were relatively few of them.

Updegraff and Anderson (1991) gathered measurements of the sound radiated by gently spilling breaking waves using a floating submerged instrument called the synoptic surface noise instrument (SSNI). The instrument was used to take simultaneous video and hydrophone measurements at a depth of approximately 1 m in the open ocean. The instrument was deployed only during periods of low windspeed, 1 m/s to 2.1 m/s, in order to study the sound generated by "micro-breaking". They found that the acoustic spectrum from a small spilling wave had a slope of -5 dB per octave and that the time series was composed of a series of damped sinusoidal pulses. A plot of a typical pulse observed by them is shown in figure 1.8. They note that their data "bears a striking acoustical resemblance to the artificial wave breaks described by Medwin and Beaky (1989)". It was also observed that the peak pressures of the damped sinusoidal pulses were scattered between 0.2 and 1.2 Pa and showed no dependence on frequency. They compared the decay rates of the observed pulses with Strasberg's (1956) empirical formula for the damping of pulsating air bubbles in water and the agreement was reasonable. They concluded that the sound under gently spilling waves was due to the oscillation of air bubbles with radii of approximately 1 mm.

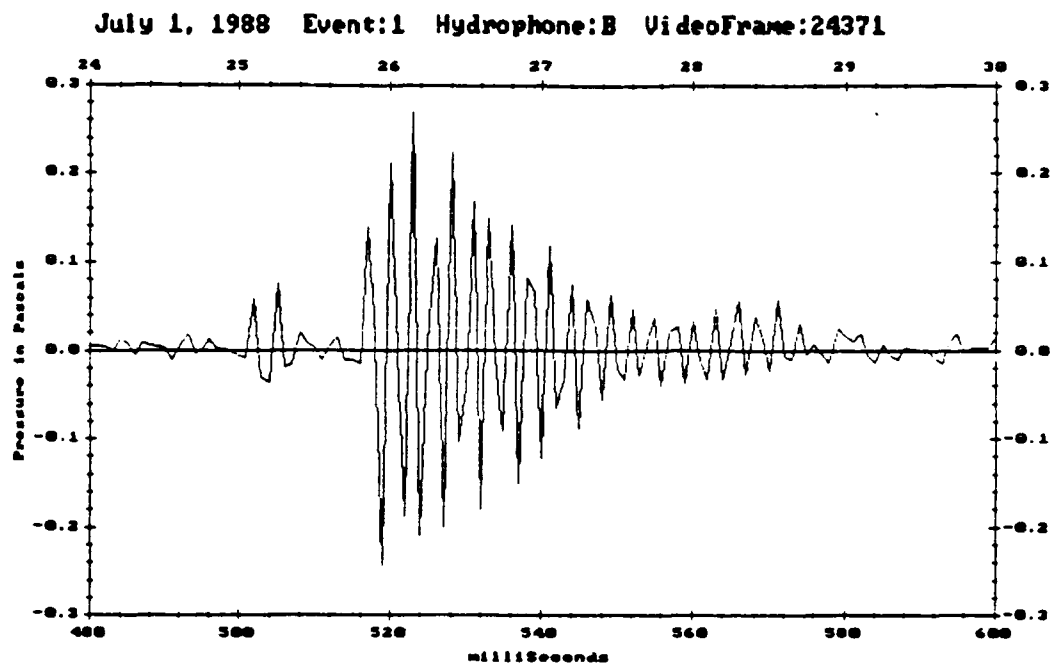


Figure 1.8 Typical sound pulse radiated by an oscillating air bubble beneath a gently spilling breaking wave at sea (from Updegraff and Anderson, 1991).

1.4 Collective Bubble Cloud Oscillations

The collective oscillation of bubble clouds beneath breaking waves has been cited by several investigators as a possible source of low frequency sound (Prosperetti 1988, Carey et al, 1990, Lu et al 1990, Yoon et al 1991 and Kolaini et al 1991). Prosperetti (1988) argues that at frequencies below 500 Hz single bubble oscillations are an unlikely source of sound because bubble sizes of O(1 cm) are required and the available data indicate that very few bubbles of this size are generated. This argument is not convincing given the fact that Medwin and Daniel (1990) observed bubbles with radii up to 7.4 mm under very small breaking waves. An oscillating bubble of radius 7.4 mm radiates sound at 440 Hz and even though Medwin and Daniel observed very few bubbles larger than 3 mm they still saw a broad maximum in the sound spectrum at approximately 1 kHz. Whether or not Prosperetti's argument that single bubble oscillations are unimportant below 500 Hz is valid, it is still an unresolved issue as to whether collective bubble cloud oscillations occur beneath breaking waves and, if they do, does this mechanism produce significant amounts of sound.

Prosperetti (1988) postulates that a cloud of bubbles will behave like a system of coupled oscillators, pulsating according to collective modes. To first order the lowest resonant frequency of oscillation, f_{min} , of a bubble cloud is approximately c_m/L where c_m is the speed of sound in the bubbly mixture and L is the linear dimension of the cloud. The sound speed of a bubbly mixture is given by,

$$c_m = \sqrt{\frac{P}{\rho\alpha(1 - \alpha)}} \quad 1.3$$

where P is the pressure in the mixture equal to the atmospheric pressure P_o for bubble clouds close to the ocean surface, ρ is the density of pure water, 1000 kg/m^3 and α is the void fraction defined as the volume of air divided by the total volume (Carey and Browning, 1988). Equation 1.3 is valid for, $0.002 < \alpha < 0.94$. If the term of order $(\alpha)^2$ is ignored in equation 1.3 then the equation for f_{\min} becomes,

$$f_{\min} = \frac{1}{L} \sqrt{\frac{P_o}{\rho \alpha}} . \quad 1.4$$

If the bubble cloud is spherically shaped and contains N bubbles of equal radius a_o the void fraction is given by,

$$\alpha = \left(\frac{a_o}{L} \right)^3 N . \quad 1.5$$

Using these results and equation 1.1 for the resonant frequency of a single bubble, f_b , the ratio of the resonant frequency of the bubble cloud, f_{\min} , to f_b , the resonant frequency of a single bubble is,

$$\frac{f_{\min}}{f_b} \sim \alpha^{-1/6} N^{-1/3} . \quad 1.6$$

For example a spherical bubble cloud with $\alpha = 0.1$, $L = 0.1 \text{ m}$ and $a_o = 1 \text{ mm}$ equation 1.5 gives $N = 10^5$ and equation 1.6 predicts that the cloud would oscillate at a frequency of 103 Hz, or 0.032 times the resonant frequency, 3.26 kHz, of an individual 1 mm radius bubble.

The damping constant for each bubble in a bubble cloud is approximately equal to the value for a single isolated bubble oscillating at the natural frequency of the collective mode (Prosperetti, 1988). The damping constant is a strong function of frequency with a minimum value at the resonant frequency. In figure 1.9 (Prosperetti 1984, figure 3) the total damping constant for a 1 mm radius air bubble in water is shown. It is evident from figure 1.9 that at frequencies well below resonance the damping is greatly increased. The effect of this increased damping is less when the bubble cloud is made up of larger diameter bubbles (Prosperetti 1988). Therefore Prosperetti concludes that if the collective oscillation of bubble clouds is to have any significance the clouds must consist of bubbles of radii > 1 mm .

Carey et al (1990) calculated the resonant frequencies of a bubbly spherical volume immersed in an infinite fluid. They assumed the bubbly region was acoustically compact, $kr_0 \ll 1$, where k is the acoustic wavenumber and r_0 is the radius of the bubbly region. The bubble cloud was assumed to be made up of small bubbles whose resonant frequencies were much higher than the excitation frequency. Buoyancy and surface tension forces were neglected. The properties of the bubbly region were given by the sound speed of the bubbly mixture as given by equation 1.3 and the mixtures density, ρ_m . They assumed the cloud was excited by a plane acoustic wave and the boundary conditions enforced at the edge of the bubbly region were the continuity of the pressure and the velocity. The solutions for the scattered pressure field and the pressure field inside the volume lead to an expression for the resonant frequency of the lowest mode of the bubble cloud, f_0 . The equation is,

$$f_0 = \frac{1}{2\pi r_0} \sqrt{\frac{3\gamma P}{\rho \alpha}} \quad 1.7$$

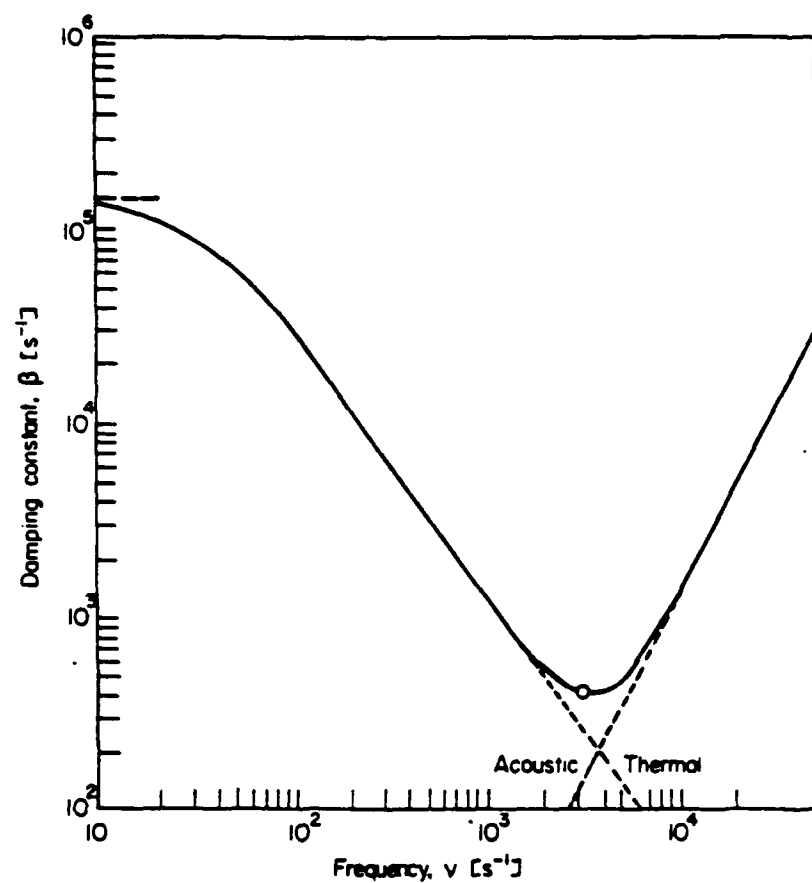


Figure 1.9 Total damping constant for a 1 mm radius air bubble in water. ○, marks the location of resonance (from Prosperetti, 1984).

where γ is the ratio of the specific heats, $\gamma = 1$ for isothermal conditions, ρ is the density of the fluid and α is the void fraction. The same formulation was used to solve for the resonant frequencies of a long cylindrical bubbly region. In figure 1.10 the resonant frequency of a spherical bubble cloud as given by equation 1.7 for various values of the void fraction is shown plotted as a function of the cloud radius. Also shown plotted is the resonant frequency of the cylindrical bubble cloud. For a spherical cloud of radius 20 cm and a void fraction of 1% the resonant frequency is approximately 150 Hz. For a cylindrical region with a radius of 20 cm and a void fraction of 1% the resonant frequency is approximately 40 Hz.

Yoon et al (1991) reported on an experimental investigation of the collective oscillations of a cylindrical bubble cloud. The cloud was generated by the steady injection of air through a series of hypodermic needles located at the bottom of a tank of fresh water. The measured acoustic spectra showed low frequency peaks from 260 to 550 Hz. Lu et al (1990) used averaged equations based on the assumption that the bubbly cloud is a continuum described by effective bulk properties to calculate the modes of oscillation of cylindrical bubble clouds. Yoon et al (1991) compared the observed frequencies to theoretically predicted values using the results of Lu et al (1990). The agreement between the experimental and theoretical results was excellent. They conclude that their results support the hypothesis that most of the observed oceanic ambient sound at frequencies below 1 kHz may be due to the collective oscillation of bubble clouds produced by breaking waves. However, the authors themselves state that their experimental geometry is not of direct relevance to oceanic conditions. Therefore it still remains to be shown that the collective oscillation of bubble clouds is a source of significant sound in the ocean.

Kolaini et al (1991) studied the sound generated by bubble clouds produced when a fixed cylindrical volume of water is dropped onto a still water surface. The characteristics of the bubble cloud were varied by changing the height from which the

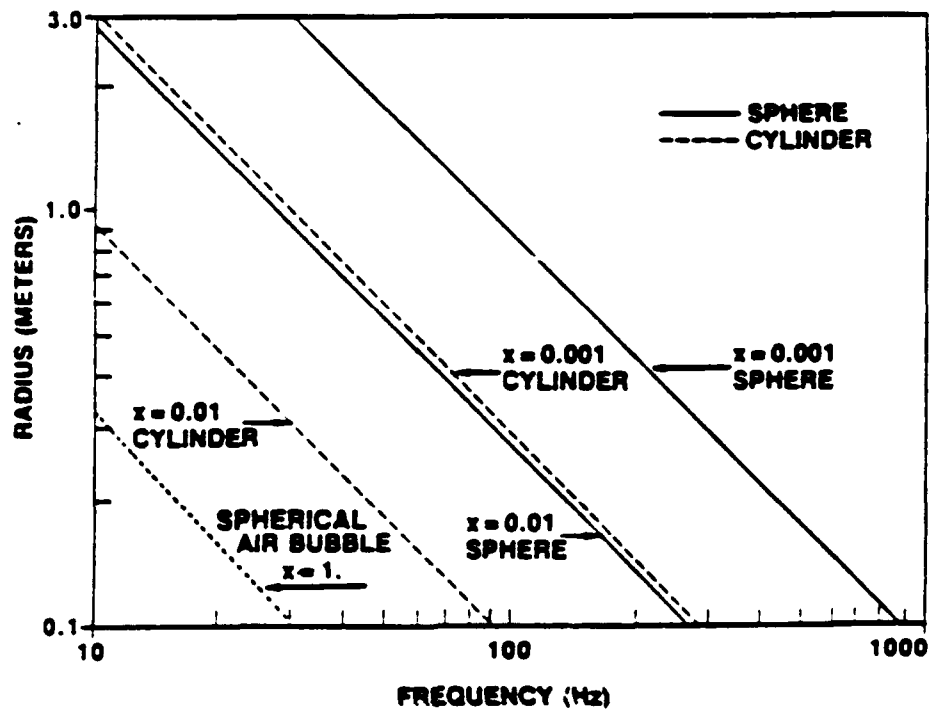


Figure 1.10 Theoretically predicted resonant frequencies of a spherical and cylindrical bubble cloud as a function of the void fraction and radius (from Carey et al, 1990).

cylinder of water was dropped and by changing the volume of water dropped. They found that the frequency generated when a "substructure" detaches from the rest of the cloud correlated with the volume of the dropped water. This can be seen in figure 1.11 (Kolaini et al 1991) where the frequency is plotted versus the volume of water dropped. The detached substructures were observed to oscillate at frequencies as low as tens of Hz. They state that if their observations are duplicated in the ocean, then a mechanism for low frequency sound generation by breaking waves may have been discovered.

1.5 Models of the Sound Generated by Breaking Waves

Kerman (1984) presented one of the first models of the underwater sound generated by breaking waves. The model predicted a sound intensity proportional to the wind friction velocity raised to the $3/2$ power in agreement with Perrone's (1969) data. The mechanism of sound generation was assumed to be large amplitude, nonlinear bubble oscillations induced by turbulent pressure fluctuations. He argued that bubbles with radii comparable to the Kolmogorov scale would produce the most intense sound.

More recently Guo (1987) and Ffowcs Williams and Guo (1988) use Lighthill's (1952) analogy and the results of Crighton and Ffowcs Williams (1969) to investigate the sound generation mechanisms beneath breaking waves. They concluded that the dominant mechanism of sound generation under breaking waves is splashing water sprays. The unsteady momentum fluctuations caused by water sprays were shown to produce a dipole sound field. Sound production from the forced oscillation of air bubbles by turbulence was shown to be negligible. They did not consider the free oscillations of newly created air bubbles as a source of sound and therefore they failed to recognize that this is likely the dominant mechanism of sound generation beneath breaking waves.

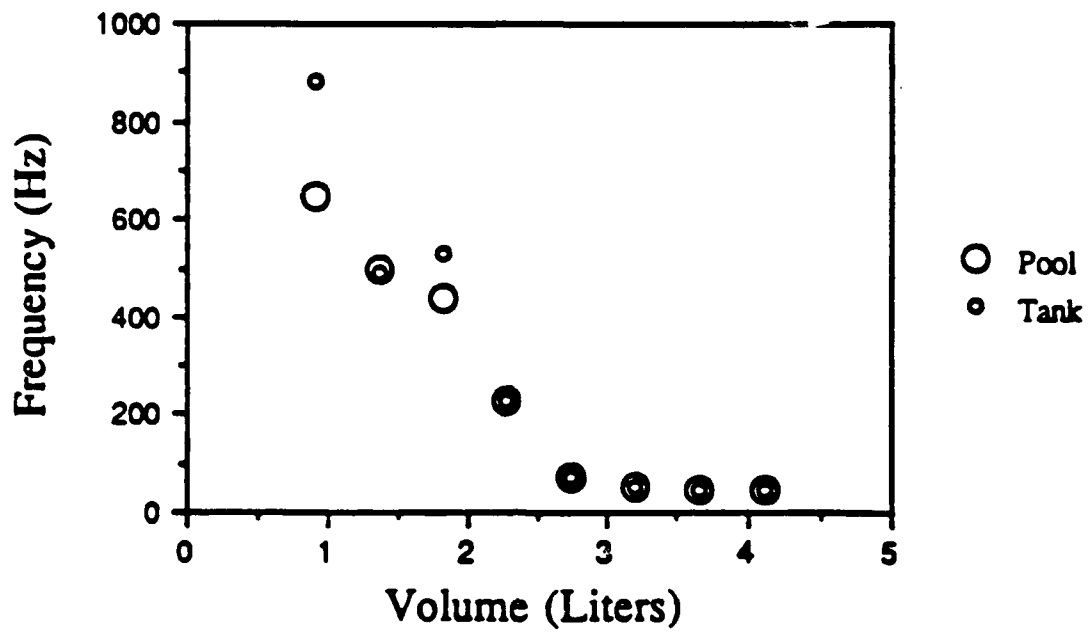


Figure 1.11 Frequency of oscillation of substructures as a function of the volume of water released from a cylinder. The large symbols correspond to data from a large tank and the smaller symbols to data from a smaller tank (from Kolaini et al 1991).

Prosperetti and Lu (1988) examined the sound generation mechanisms of cavitation-like bubble collapse (similar to the mechanism proposed by Kerman, 1984) and the bursting of air bubbles at the free surface. Using a simplified Rayleigh-Plessett equation they show that the magnitude of the pressure fluctuations required to promote a violent collapse of the bubble are unlikely to occur in the ocean. They therefore concluded that the cavitation-like collapse of bubbles is unimportant as a source of sound in the ocean. The bursting of floating air bubbles was analyzed by assuming that the pressure disturbances generated in the water when the bubbles burst were proportional to, σ / a_0 , where σ is the surface tension of water and a_0 is the bubble radius. They calculated that the number of bursting bubbles required to produce an intensity of 50 dB re $1 \mu\text{Pa}^2/\text{Hz}$ in the water would be $48 \times 10^6 / (\text{sec cm}^2)$. They state that most of the acoustic energy associated with the bursting bubble is radiated into the air due to the large impedance mismatch between air and water. Their conclusion was that this mechanism contributes a negligible amount of sound to the ocean.

Hollett and Heitmeyer (1988) reported on a model of the high frequency sound generated by breaking waves in which the mechanism of sound production was assumed to be the linear oscillation of newly formed air bubbles. They postulated that the bubble oscillations were excited by either a sudden change in the external pressure at the instant of bubble formation or by the initial rate of change of the bubble volume. They used the whitecap coverage data of Ross and Cardone (1974) to obtain a breaking wave occurrence rate and a model proposed by Crowther (1980) to obtain the surface generation rate of bubbles at the ocean surface. The sound spectra computed using the sudden pressure change excitation hypothesis agreed approximately with the corresponding Wenz spectrum.

Crowther (1988) also modeled the sound from breaking waves by assuming that the linear oscillations of newly created bubbles was the dominant mechanism. He obtained a bubble creation rate by fitting the data of Johnson and Cooke (1979) with a

power law relationship proportional to the windspeed cubed, U_{10}^3 , and the inverse of the bubble radius cubed, a^{-3} . The computed spectra, shown in figure 1.12, matched the slope of the Wenz spectra but the computed levels were 10 dB higher than the observed levels. There was a great deal of uncertainty associated with the calculation of the bubble creation rate and this may have been what caused the model to predict sound levels an order of magnitude higher than the observed sound spectra. Crowther also postulates that because wave breaking is confined to a small area, the bubble clouds are very dense and many bubbles which normally would radiate sound are masked by the surrounding bubbles.

Prosperetti (1988) examined the generation of sound at the sea surface caused by three mechanisms; 1) the amplification of water turbulence noise in the frequency range up to 100 Hz to 200 Hz, 2) the oscillation of newly formed bubbles for frequencies > 1 kHz to 2 kHz, and 3) the collective oscillation of bubble clouds for frequencies from 200 Hz to 1 kHz. Turbulence in the absence of air bubbles radiates sound as a quadrupole distribution and therefore is relatively inefficient (Lighthill 1952). The presence of air bubbles in the turbulent region greatly enhances the acoustic efficiency because the bubbles respond to the turbulent pressure fluctuations by oscillating volumetrically as monopoles (Crighton and Ffowcs Williams 1969). Prosperetti (1988) used an approach similar to that of Lighthill's (1952) to formulate the problem and then estimated the surface source spectral density due to this mechanism. He took the average lifetime of a turbulent spot to be 100 s, the vertical extent to be 1 m, the turbulent velocity fluctuations to be 0.15 m/s and the void fraction to be 5%. Using these parameters he calculated a surface source spectral level of 67.2 dB re $1 \mu\text{Pa}^2/\text{Hz}$ for a frequency of 50 Hz. This estimate was comparable to Wilson's (1983) estimates of the source level at 50 Hz which were 55.4 dB re $1 \mu\text{Pa}^2/\text{Hz}$ at a windspeed of 7.5 m/s and 72.0 dB re $1 \mu\text{Pa}^2/\text{Hz}$ at a windspeed of 20 m/s. However Prosperetti appears to have overestimated the significance of this mechanism. By assuming that the lifetime of the turbulent spot is

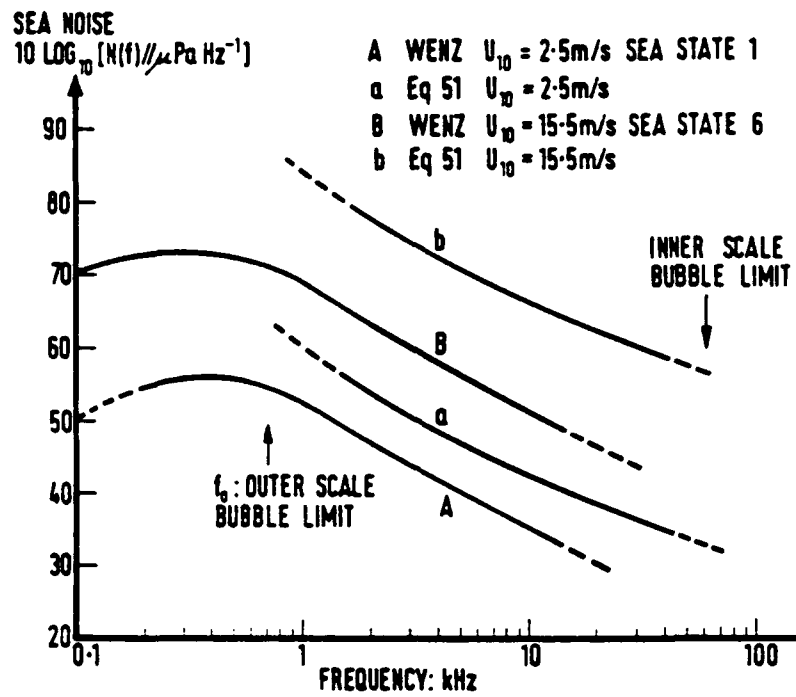


Figure 1.12 Modeled sound spectra of the noise generated by breaking waves (from Crowther, 1988).

100 s and the void fraction is 5% he is assuming that the void fraction could have an average value of 5% for up to 100 s. Lamarre and Melville (1990) have shown that the average void fraction under laboratory breaking waves can remain above 1% for up to one wave period. If we assume a wave period of 6 s then Prosperetti's estimated surface source spectral level drops to 55 dB re 1 $\mu\text{Pa}^2/\text{Hz}$ a decrease of over one order of magnitude. There is no experimental evidence which supports the hypothesis that this mechanism is a significant source of sea surface sound. Order of magnitude estimates such as Prosperetti's are useful for encouraging discussion about possible sources of sea surface sound but the large uncertainty associated with such estimates must be taken into account.

Using the same formulation as described above Prosperetti (1988) derived an equation for the surface source spectral density due to the oscillation of newly formed bubbles. The surface source spectral density was found to be ,

$$S(\omega_o) \sim \frac{\rho \alpha^2 X_o^2 V \delta^3 \omega_o^4}{T c^3 b^2 \Theta^2} \quad 1.8$$

where $S(\omega_o)$ is the surface source spectral density, ρ is the density of water, α is the average void fraction, X_o is the initial fractional amplitude of oscillation (i.e. $X(t) = a(t) / a_o$), V is the volume of the bubble cloud, δ is the depth of the cloud, ω_o is the radian frequency of oscillation, T is the averaging time, c is the speed of sound, b is the damping constant and Θ is the period of the breaking wave. Taking $V = 0.01 \text{ m}^3$, $\alpha = 10\%$, $T = 1 \text{ s}$, $X_o = 0.1$, $\delta = 0.1 \text{ m}$ and $b = 271 \text{ Hz}$ for a 1mm radius bubble he obtains a surface source spectral density of 95.9 dB re 1 $\mu\text{Pa}^2/\text{Hz}$. This result is 20 to 30 dB higher than observed sound levels. However, this estimate is for a single bubble cloud entrained by a breaking wave and will be reduced considerably if it is multiplied by the percentage of the ocean surface which is covered by breaking waves. Taking this into

account Prosperetti concludes that his order of magnitude estimate gives intensity levels comparable to the observed levels.

Longuet-Higgins (1989a,b) proposed a theory which suggests that the shape oscillations of bubbles can resonate (at second order) with the volume or breathing mode and produce significant sound levels. The resonance occurs only for specific bubble sizes when the natural frequency of the volume mode equals twice the resonant frequency of the shape oscillations. The resonant frequency of the volume mode is given by equation 1.1 and the resonant frequencies of the shape oscillations are given by,

$$\sigma_n = (n-1)(n+1)(n+2)(\sigma/a_0^3) \quad 1.9$$

where n is the degree of the spherical harmonic S_n (Lamb 1932). There is some indication that this mechanism has been observed in measurements of oceanic sound (Longuet-Higgins 1990) but more concrete experimental evidence is required to confirm that this mechanism is important.

Pumphrey and Ffowcs Williams (1990) concluded from experimental results that most of the sound generated by breaking waves is due to the free oscillations of air bubbles. They then examined the possible mechanisms by which newly formed bubbles are excited. Four mechanisms were considered; 1) the surface tension or Laplace pressure as the bubble is formed, 2) surface waves or shape oscillations, 3) the initial volume velocity, and 4) the hydrostatic pressure. The Laplace and hydrostatic pressures were found to produce weak oscillation pressures, approximately 5% of the observed values, and therefore these mechanisms were dismissed. A simple estimate was made of the significance of Longuet-Higgins' (1989a,b) theory that the shape oscillations transfer energy to the volume mode. A single spherical bubble was assumed to be distorted until it was nearly broken into two smaller spherical bubbles enclosing the same volume as the single bubble. Then all the increased bubble energy was assumed to be transferred

instantly to the volume mode. This analysis predicted oscillation pressures of 0.13 Pa for a bubble of radius 1 mm located 2 mm below the free surface. They point out that this value is at the lower limit of the observed experimental values and that their simplified analysis probably overestimated the oscillation pressure. Therefore they concluded that the coupling of the shape oscillations to the volume mode is probably not a significant sound generation mechanism.

The effect of the initial volume velocity of a bubble at the instant of closure was examined with the aid of high speed photography. The rate of growth of an air bubble beneath a small laboratory waterfall was measured from successive frames of a high speed film. The volume velocity U was found to be 0.23 ± 0.1 m/s for this single bubble. This gave a dipole strength D of 1.3 ± 0.6 Pa m, in agreement with the experimental values observed by Medwin and Beaky (1989). From these results they concluded that the initial volume velocity of the bubbles is the mechanism which is responsible for imparting the initial energy which drives the subsequent bubble oscillations.

1.6 Outline of Experimental Objectives

As the preceding literature review demonstrates, there has been a great renewal of interest in breaking waves and sea surface sound in recent years. Substantial progress has been made towards understanding the mechanisms which generate sea surface sound and the dominant role breaking waves play in this process. It has been shown that the dynamics of breaking are related to the averaged acoustic measures such as the mean square acoustic pressure (Melville et al 1988). It has also been shown that the acoustic signals generated by breaking waves can be used to infer information about the kinematics and statistics of breaking waves (Crowther, 1988 and Farmer and Vagle, 1988). Conclusive experimental evidence has been presented which demonstrates that

the source of sound beneath gently spilling breaking waves is individual oscillating air bubbles (Medwin and Beaky, 1989 and Updegraff and Anderson, 1991).

However, there is still a great deal about the sound generated by breaking waves which is not well understood. For example, it is not clear that the dominant source of sound beneath larger scale, energetic, plunging breaking waves is the oscillation of individual air bubbles. Whereas, there is some evidence that the collective oscillations of bubble clouds may be an important source of low frequency sound beneath more energetic breaking waves, no convincing experimental evidence has yet been presented which shows definitively that this is the case (Yoon et al, 1991). In addition, it remains to be shown that more than just the averaged acoustic measures are correlated with the dynamics of breaking. More detailed studies of the sound radiated by breaking may show that the spectral content of the acoustic signals is related to the dynamics of breaking or that the time evolution of the acoustic pressure is closely linked to the hydrodynamics of the breaking process.

The following chapters present the results from a series of laboratory experiments in which the sound produced by two- and three-dimensional breaking waves was measured. The correlation of the averaged acoustic measurements with the dynamical variables and the scaling of these correlations with the wave packet wavelength will be examined. A more detailed analysis of the sound generation process and its coupling to the dynamics of air entrainment and energy dissipation will be discussed. A comparison will be made of the sound generated by two- and three-dimensional breaking waves. Observations of low frequency sound generated by breaking waves will be presented and the possible sources of these low frequency signals will be examined in detail. Finally, an analytic model of the sound produced by gently spilling waves will be presented and discussed.

The primary objectives of the research are as follows:

- 1) to determine whether the averaged acoustic and microwave measurements correlate with the dynamics of breaking waves over a range of wave packet scales;
- 2) to investigate in greater detail the relationship between the sound generation process and the dynamics of breaking;
- 3) to discover whether significant low frequency sound can be detected beneath breaking waves;
- 4) to investigate the mechanisms which cause the generation of low frequency sound when waves break;
- 5) to determine whether the sound produced by gently spilling breakers can be modeled simply and accurately.

Chapter 2: Microwave and Acoustic Experiment

This chapter reports on a laboratory experimental study of both the microwave backscatter and the sound produced by breaking waves. A large portion of this chapter is taken from, "Microwave backscatter and acoustic radiation from breaking waves", M.R. Loewen and W.K. Melville, J. Fluid Mech., 224, 601-623, 1991. The research was motivated by the fact that preliminary measurements by Melville, Loewen, Felizardo, Jessup and Buckingham (1988) demonstrated that both the microwave power backscattered and the sound radiated by breaking waves correlated with the dynamics of breaking. Specifically, they found that the mean square acoustic pressure and the backscattered microwave correlated with the fractional energy dissipation. The preliminary experiments were conducted using a single wave packet with a center frequency of 0.88 Hz and the results were significant because they showed that dynamical information, such as the amount of energy dissipated due to breaking, could be inferred from the acoustic or microwave signal. In order to extend the measurements simultaneous microwave, acoustic and surface displacement measurements of three wave packets of center frequencies 0.88, 1.08 and 1.28 Hz have been carried out.

2.1 Literature Review: Microwave Backscatter

Several studies of radar return at grazing angles have shown that large fluctuations in the radar cross section, commonly referred to as "sea spikes" are associated with breaking waves. Lewis and Olin (1980) took simultaneous radar backscatter measurements and video recordings to show that sea spikes were correlated with whitecaps. Ewell, Tuley and Horne (1984) tracked sea spikes on the ocean surface,

and observed that they moved with a speed approximately equal to the phase speed of the dominant surface waves.

Recent work by Jessup, Melville and Keller (1991a,b) has demonstrated that microwave backscatter measurements at moderate incidence angles (20° to 70°) can be used to quantitatively study breaking waves. They observed that the majority of sea spikes associated with breaking occurred when the steep forward face of a wave passed through the radar illumination area and then subsequently broke. The contribution to the radar cross section from sea spikes and the number of sea spikes were both found to be approximately proportional to u_*^3 in agreement with Phillip's (1988) model. The friction velocity u_* is equal to $\sqrt{\tau/\rho}$ where τ is the shear stress and ρ is the density of air. The average radar cross section of an individual sea spike was found to be independent of u_* . They also observed that the bandwidth of the Doppler spectrum was greatly increased during breaking similar to the observations of Keller, Plant and Valenzuela (1981).

Jessup, Keller and Melville (1991a) used a detection threshold based on the amplitude of the radar cross section and the size of the Doppler spectrum bandwidth to identify breaking waves. Simultaneous video recordings confirmed that this technique detected 70% of the breaking waves. Keller, Plant and Valenzuela (1981) observed that the speed of the scatterers increased and approached the phase speed of the dominant ocean waves during breaking. Jessup, Melville and Keller (1991b) found that the maximum mean Doppler velocities associated with the detected breaking events was approximately equal to 25% of the phase speed of the dominant waves.

There is considerable disagreement in the literature over which scattering mechanism produces the sea spikes. Alpers, Ross and Rufenach (1981) suggest that sea spikes are due to the spontaneous generation of Bragg waves at the steep crests of breaking waves. Kwoh and Lake (1981) studied the microwave backscatter from laboratory breaking waves and concluded that the backscatter could be separated into specular and non-specular components. The specular component was attributed to either

the turbulent wake of the breaking wave or the capillary waves generated on the forward face of the steep wave. The non-specular component was attributed to wedge-like diffraction from the sharp crested breaking wave, at or near breaking. Banner and Fooks (1985) made laboratory radar measurements of a quasi-steady stationary breaking wave. They found that the backscatter was due to Bragg scattering from the hydrodynamic disturbances, which were generated just downstream of the breaking crest.

Phillips (1988) used an approach which did not attempt to characterize the detailed scattering mechanism. He describes the backscatter from breaking waves as the overall contribution from the family of surface configurations that are present throughout the breaking process. The contribution to the normalized radar cross-section from sea spikes and the frequency of occurrence of sea spikes are both predicted to be proportional to u_*^3 .

2.2 Experimental Procedure

2.2.1 Wave Generation

The experiments were conducted in a steel-framed glass wave channel 25m long and 0.38m wide at the R.M. Parsons Laboratory, MIT. The wave channel was filled with fresh water to a depth of 0.38 m for these experiments. A computer-controlled piston wave generator was programmed to focus a dispersive wave packet at a point x_0 down the channel. The wave packets were synthesized from N sinusoidal components of constant slope ak , where a is the component amplitude and k is the component wavenumber. This technique has been used previously to study the energy dissipation and wave forces produced by deep water breaking waves (Chan and Melville, 1988 and Rapp and Melville, 1990). The method and the formulation are presented in detail by

Rapp and Melville (1990). The following description is a summary of their work and is included here for completeness.

The linear dispersion relation for finite amplitude surface waves is,

$$\frac{(2\pi f_n)^2}{g} = k_n \tanh(k_n h) \quad 2.1$$

where $2\pi f_n = \omega_n$ is the radian frequency of the n th component, k_n is the wavenumber, g is the acceleration due to gravity and h is the water depth (Mei, 1983). For this work the number of components N was held constant at 32 and they were spread evenly over a frequency bandwidth, Δf defined by,

$$\Delta f = f_N - f_1 \quad 2.2$$

the center frequency of the packet is given by,

$$f_c = \frac{1}{2}(f_N + f_1) . \quad 2.3$$

The free surface displacement at any time, t and position, x along the wave channel can be written as,

$$\eta(x,t) = \sum_{n=1}^N a_n \cos(k_n x - 2\pi f_n t - \phi_n) \quad 2.4$$

where a_n is the amplitude and ϕ_n is the phase of the n th component. The basic principle of this method of generating breaking waves is that the phase of each component is

adjusted such that according to linear theory the wave crest of each component arrives at point x_b simultaneously. This is accomplished by enforcing the following relationship,

$$\cos(k_n x_b - 2\pi f_n t_b - \phi_n) = 1 \quad 2.5$$

where t_b is the theoretical time of focusing. From eq. 2.5 we can calculate the phase of each component,

$$\phi_n = k_n x_b - 2\pi f_n t_b . \quad 2.6$$

The mean position of the wave maker paddle is at $x=0$, and therefore the surface displacement at the paddle is,

$$\eta(0,t') = \sum_{n=1}^N a_n \cos(-k_n x_b - 2\pi f_n t') \quad 2.7$$

where $t' = t - t_b$. The packet may be advanced or delayed by varying t_b without changing its form or the theoretical breaking location x_b .

In this study the slope of each of the 32 packet components was held constant and therefore the slope of the wave packet is given by,

$$S = G N a k \quad 2.8$$

where G is a gain factor, $N = 32$ and ak is a constant equal to the slope of the components. The slope of the wave packets was varied by increasing or decreasing the gain factor, G .

The wave packets were generated by using an IBM XT computer to convert digital data to an analog voltage signal which was then fed to the wave maker system. In order to produce the desired surface displacement at the paddle, given by eq. 2.7, it was necessary to account for the complex transfer function of the wave maker system. The transfer function can be written as,

$$H(f) = A(f)e^{j\phi(f)} \quad 2.9$$

where $A(f)$ is the amplitude transfer function and $\phi(f)$ is the phase transfer function. The complete wave maker system, shown in figure 2.1, was comprised of a Metrabyte DAS-16 multifunction board (used for digital to analog conversion), a Model 107 precision buck and gain amplifier (manufactured by Michael Head Designs), the servo control valve and electronics, the hydraulic system and the wave paddle apparatus. The buck and gain amplifier was required because the DAS-16 board digital to analog output varied from 0 to 5 volts and the wave maker required a ± 5 volt signal. The buck and gain amplifier was set to buck (offset) the signal by 2.5 volts and the gain was set at 2 to produce a ± 5 volt signal.

The transfer function of the complete system was measured by generating small amplitude sinusoidal waves of different frequencies and amplitudes and then measuring the surface displacement amplitude and phase at a distance 2 m downstream of the paddle. Measurements were made with waves of frequency 0.4 to 2 Hz and amplitudes 1 to 4 mm to match the frequencies and amplitudes of the wave packet components used. The measured amplitude and phase transfer functions are shown plotted in figure 2.2, the solid lines are smooth cubic spline curves fitted to the data. In table 2.1 the computer programs used to determine the transfer function are listed.

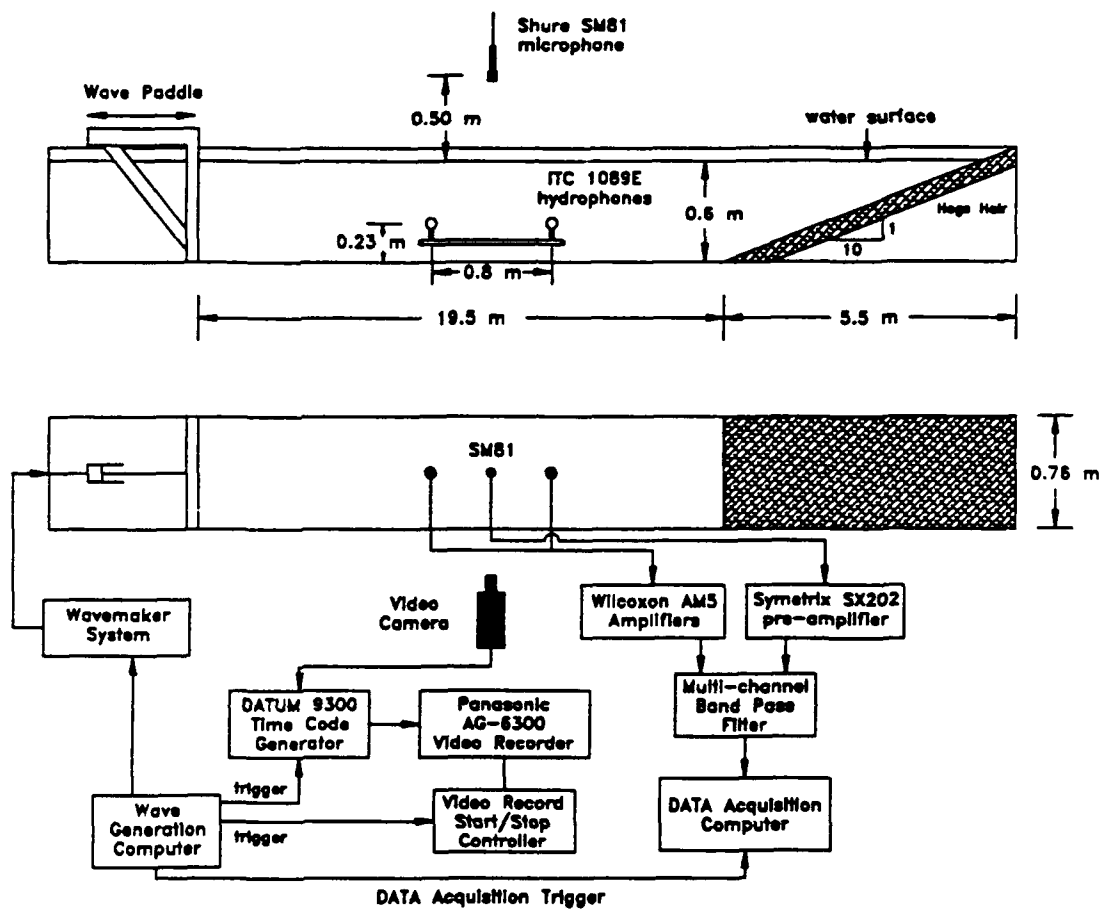


Figure 2.1 Schematic drawing of the wave channel and the arrangement of the experimental equipment.

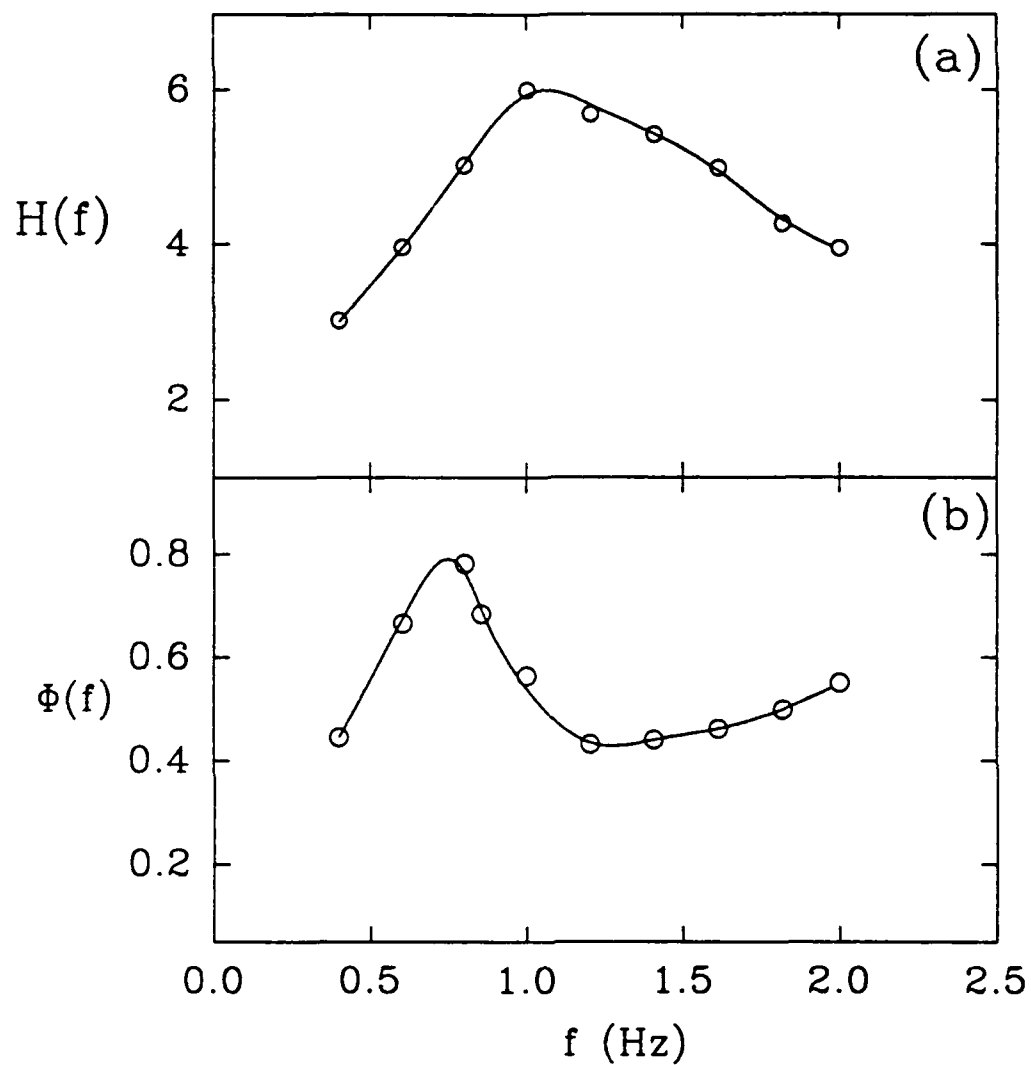


Figure 2.2 (a) The amplitude transfer function of the wavemaker system $H(f)$ (cm/volt) as a function of frequency f (Hz). (b) The phase transfer function $\Phi(f)$ (radians) as a function of the frequency f (Hz).

PROGRAM	PROGRAM FUNCTION
WAVES2.FOR	Used on the XT computer which controlled the wave maker, generated sinusoidal surface waves and triggered data acquisition computer.
MADTES2.FOR	Used on AT data acquisition computer, began data acquisition after receiving trigger, sampled the wave gauge signal and the signal produced by the XT computer.
WAVAMP6.FOR	Used to analyze the amplitude data, removes the D.C. and finds the maxima and minima and calculates the amplitude.
PHCOMP.FOR	Used to calculate the phase data, measures the phase lag between the maxima in the two time series of the surface displacement and the XT output signal.
SPLINE2.FOR	Program which fits a cubic spline to the transfer function amplitude and phase data.

Table 2.1 Computer programs used to obtain the transfer function of the wave maker system. Listings of these programs can be found in appendix A.

The programs used to generate the wave packets used the spline curves shown in figure 2.2 to compensate for the transfer function. The phase of each component adjusted for the transfer function is given by,

$$\phi_n = k_n x_b - 2\pi f_n t_b + \phi(f_n) \quad 2.10$$

where $\varphi(f_n)$ is obtained from the cubic spline equations. The amplitude of each component was adjusted so that each component had a constant slope equal to $a_c k_c$, the slope of the center component. The amplitude of each component was calculated from,

$$a_n = \frac{a_c A(f_c) k_c}{A(f_n) k_n} \quad 2.11$$

where a_c is the amplitude of the center component, $A(f_c)$ is the value of the cubic spline equation for the amplitude transfer function data at the center frequency and $A(f_n)$ is the value at the component frequency. The final signal produced by the XT computer was of the following form,

$$\eta(0,t) = G \sum_{n=1}^N a_n \cos(-k_n x_b - 2\pi f_n t' - \varphi(f_n)) \quad 2.12$$

where a_n is given by eq. 2.11 . The computer programs used to generate the wave packets are listed in table 2.2 .

PROGRAM	PROGRAM FUNCTION
GENPACK2.FOR	Program to generate a raw wave packet signal for viewing on the oscilloscope. The wave maker system transfer function is implemented and the slope of each frequency component is held constant. The program outputs analog data through D/A channel 1 for viewing the raw packet data on the oscilloscope.
SEND4.FOR	Uses the data produced by genpack2.for as input and tapers the packet data with a cosine function at both ends.
WAVREP3.FOR	Program which converts the digital wave packet data to an analog voltage signal which is sent to the buck and gain amplifier and then to the wave maker electronics. It also sends a trigger to the data acquisition computers.

Table 2.2 Computer programs used to generate the wave packets. See appendix A for complete listings.

It has been shown that deep water breaking is a function of three dimensionless parameters; a bandwidth parameter $\Delta f/f_c$, a phase parameter $x_b k_c$ and a slope parameter S , (Melville and Rapp, 1985; Rapp, 1986). The earlier experiments showed that the dependence on $\Delta f/f_c$ and $x_b k_c$ was weak and that the dissipation due to wave breaking depended most strongly on the slope parameter S . In the present experiments, $\Delta f/f_c$ and $x_b k_c$ were held constant at 0.73 and 28.5 respectively, and S was varied. Table 2.3 lists the characteristics of the three wave packets used in these experiments.

Wave packet	P_1	P_2	P_3
Center frequency, f_c (Hz)	0.88	1.08	1.28
Theoretical break point, x_b (m)	8.0	5.79	4.27
Center component wavenumber, k_c	3.56	4.92	6.68
Center component phase speed, c_c (m/s)	1.55	1.38	1.20

Table 2.3 Wave packet characteristics; $\Delta f/f_c = 0.73$ and $x_b k_c = 28.3$ for all wave packets

2.2.2 Surface Displacement Measurements

The surface displacement was measured with a set of resistance wire wave gauges and sampled at a rate of 100 Hz using a Metrabyte DAS-16 data acquisition board installed in an XT computer. The gauges were constructed at MIT and the electronic circuitry was supplied by the Danish Hydraulic Institute, model 80-74G. The sensing wires were two 0.127 mm (0.005 inch) diameter Nichrome 80 wire mounted 4 mm apart. The wire was purchased from the Pelican Wire Company, Naples, Florida. The supporting frame was made of 0.25 inch stainless steel tubing and pierced the surface 15 cm away from the wires to minimize the disturbance to the flow. An AC excitation (3 kHz) is transmitted through the wires and then amplified, demodulated and filtered to produce a DC signal proportional to the submerged depth of the wires.

Acetone was used to clean the wave gauges prior to each calibration and the offset and gain on the wave gauge amplifiers was adjusted to give ± 5 volts at ± 10 cm and 0 volts at 0 cm. The wave gauges were then calibrated (see program GCAL.FOR appendix XX) by sampling the still water level voltage for 8 seconds, as the gauge was moved in 2 cm increments from +12cm to -10cm. A third order polynomial was fitted to

the average voltage at each amplitude to give a calibration equation relating voltage to wave amplitude. The standard error of the fit of the equation to the data was calculated, and the calibration was accepted if the error was less than 0.04cm.¹

Prior to each run the still water level was sampled for 20 seconds and this DC value was used as the zero order term in the calibration equations to remove the effect of any DC drift. Runs were separated by a minimum of 10 minutes to allow the surface oscillations in the channel to decay to negligible amplitudes. Rapp (1986) found that the variation in the linear term of the calibration equation was less than 1% over 8 hours. In order to minimize the errors due to variations in wave gauge calibration each wave gauge was calibrated every 4 hours.

The repeatability of the wave packets was monitored by measuring the position of the wave paddle. The wave maker system included a position transducer which produced an analog signal proportional to the linear position of the paddle. This signal was sampled at 100 Hz along with the wave gauge signals and the variance was checked to ensure that repeated runs of the same wave packet slope produced identical variances.

2.2.3 Acoustic Measurements

The acoustic measurements were made with an omnidirectional B&K model 8105 spherical hydrophone and a B&K 2635 charge amplifier. The frequency response of the hydrophone and amplifier system was constant to within ± 2 dB from 2Hz to 20kHz. Typical frequency response curves for both the 8105 and 2635 are shown in figure 2.3 and the specifications are listed in tables 2.4 and 2.5 . The hydrophone signal was

¹ At one time during the experiments a small amount of hydraulic oil leaked out of the wave maker system into the tank and this made it impossible to accurately calibrate the wave gauges. After skimming the water surface for 24 hours to remove all of the oil the gauges calibrated with acceptable errors. Following this episode a drip pan was installed to contain any future oil leaks.

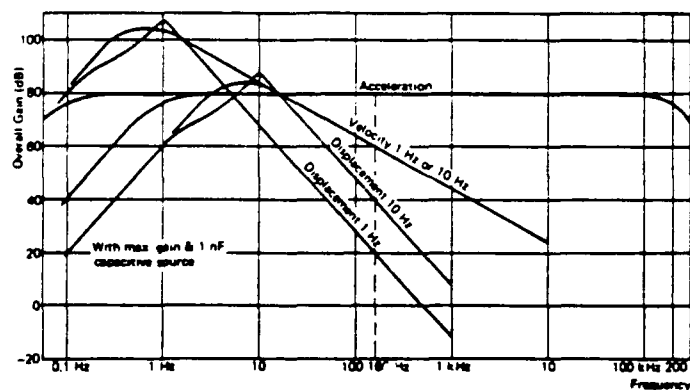
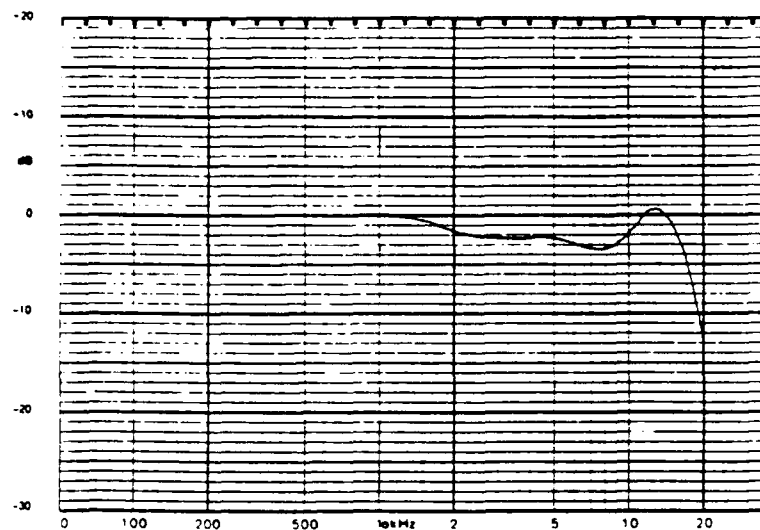


Figure 2.3 The upper plot is a typical frequency response of a B&K model 8105 spherical hydrophone. The lower plot is the typical frequency response of a B&K model 2635 charge amplifier. The curve marked acceleration is for the mode of operation used in these experiments.



Calibration Chart for
Hydrophone Type 8105

Brüel & Kjær

Serial No. 1390689

Reference Sensitivity at 250 Hz at 23 °C
including 10 m integral cable

Cable Capacitance 150 pF/m typical

Open Circuit Sensitivity:

Voltage Sensitivity:

-205.5 dB re 1 V/μPa** or 53.1 μV/Pa

Charge Sensitivity: 400 · 10⁻³ pC/Pa

Capacitance (including 10 m cable) 7540 pF

Leakage Resistance: 7.1 · 10⁹ MΩ at 23 °C

Frequency Response:

Individual Free Field Frequency Response Curve
attached

Date 83.10.29 Signature J. D.

Summarized Specifications:

Usable Frequency Range: 0.1 Hz to 160 kHz ±2 dB
-10 dB

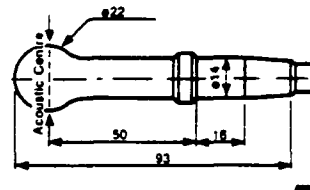
Linear Frequency Range: 0.1 Hz to 100 kHz ±0.5 dB
-4 dB

Horizontal Directivity 100 kHz:
(XY-plane) typical ±2 dB

Vertical Directivity 100 kHz (270°):
(XZ-plane) typical ±2 dB

BC 0177-12

Physical (mm):



Operating Temperature Range:

Short term -40 °C to +120 °C
Continuous -40 °C to +80 °C

Change of Sensitivity with Temperature:

Charge 0 to 0.03 dB/°C
Voltage 0 to -0.03 dB/°C

Change of Sensitivity with Static Pressure:

0 to -3 × 10⁻³ dB/Pa
(0 to -0.03 dB/atm)

Allowable Total Radiation Dose: 5 × 10⁷ Rad

Maximum Operating Static Pressure:

9.8 × 10⁶ Pa (100 atm)

Cable:

Two conductors shielded low noise
Waterblocked to MIL-815

Weight including 10 m cable: 1.6 kg

For further information see instruction manual

* Traceable to NBS

** 1 Pascal = 1 N/m² = 10⁻⁵ bar

Table 2.4 Specifications of a B&K 8105 spherical hydrophone.

Specifications 2635

<p>CHARGE INPUT: Via 10-32 NF and BNC coaxial socket Max. input: -10^6 pC</p> <p>SENSITIVITY CONDITIONING: 3 digit dial-in of transducer sensitivity from 0.1 to 10.99 pC/ms²</p> <p>AMPLIFIER SENSITIVITY: 0.01 mV to 10 V/pC corresponding to -40 to +80 dB with transducer capacitance of 1 nF</p> <p>CALIBRATED OUTPUT RATINGS: Selectable in 10 dB steps Acceleration: 0.1 mV to 1 V/ms² Velocity: 10 mV to 100 V/ms¹ Displacement: 0.1 mV to 10 V/mm</p> <p>SIGNAL OUTPUT: Via 10-32 NF and BNC coaxial socket Max. Output: 8 V (8 mA) peak Output impedance: $<1 \Omega$ DC Offset: $< \pm 50$ mV</p> <p>FREQUENCY RANGE: Acceleration*: Switchable 0.2 or 2 Hz to 100 kHz Velocity: Switchable 1 or 10 Hz to 10 kHz Displacement: Switchable 1 or 10 Hz to 1 kHz -10% limits quoted — see Fig. 3</p>	<p>LOW-PASS FILTER: Switchable -10% frequency limits of 100 Hz, 1 kHz, 3 kHz, 10 kHz, 30 kHz and >100 kHz with attenuation ~ 20 dB/decade</p> <p>INHERENT NOISE (2 Hz to 22 kHz) $5 \cdot 10^{-3}$ pC referred to input with maximum sensitivity and 1 nF transducer capacitance</p> <p>TEST OSCILLATOR: 160 Hz ($\omega = 1000$ rad/s) sinusoid, factory pre-set for test level of 1 V</p> <p>OVERLOAD INDICATOR: Overload LED lights when input or output of amplifier is overloaded by signals of 100 high a peak level</p> <p>RISE TIME: ~ 2.5 V/μs</p> <p>ENVIRONMENTAL CONDITIONS: Temperature Range: -10 to $+55^\circ\text{C}$ ($+14$ to 131°F) Humidity: 0 to 90% RH (non-condensing). For use in high humidities a 3 W heater may be fitted on special order</p> <p>POWER REQUIREMENTS: Int. Battery: Three 1.5 V Alkaline Cells QB 0004 (IEC LR20). Provide approximately 100 hours use</p>	<p>Ext. Source: $+6$ to $+28$ V (55 mA) single or ± 14 V (14 mA) dual polarity DC</p> <p>DIMENSIONS: Height: 132.6 mm (5.22 in) Width: 69.5 mm (2.74 in) Depth: 200 mm (7.87 in) B & K module cassette KK 0022, 2/12 of 19 in rack</p> <p>WEIGHT: 1.45 kg (3.2 lb) including batteries</p> <p>ACCESSORIES INCLUDED: 3 x 1.5 V Alkaline Cells.....QB 0004 1 x 7-pin DIN plug.....JP 0703 2 x Overlays.....SC 0418</p> <p>ACCESSORIES AVAILABLE: Rechargeable Ni-Cd Cells.....3 x QB 0008 Battery Charger.....ZC 0113 Power Supply.....Type 2805 7-pin Plug for Preamp. Input of B & K Measuring Amplifiers and Analyzers.....JP 0701</p> <p><small>*The Acceleration mode 0.2 and 2 Hz -10% limits correspond to 0.1 and 1 Hz -3 dB limits</small></p>
--	--	--

Table 2.5 Specifications of a B&K 2635 charge amplifier.

bandpass filtered from 500 Hz to 10 kHz and sampled at 20 kHz with a Metrabyte DAS-16F data acquisition board installed in an IBM AT computer. The low frequency cut-off at 500 Hz was used to remove the background noise of the wavemaker hydraulic system. The ambient sound spectrum from 0 to 1000 Hz is shown in figure 2.4 . There are large peaks at 28 and 56 Hz which are likely caused by machinery generated structural vibration. The peak at 235 Hz is the fundamental frequency of the wave maker hydraulic system, its first harmonic is evident at 470 Hz. The peak at 400 Hz is due to the noise from the cooling fan. At frequencies > 500 Hz the ambient noise spectrum is white.

The hydrophone was located vertically at mid-depth and transversely at the center of the channel, mounted on an L-shaped bracket pointing upstream towards the breaking event. The bracket was supported from an overhead carriage which was set on rollers allowing the hydrophone to be moved easily along the channel. This configuration made it necessary to keep the hydrophone at least 2m downstream of the breaking event to avoid vibrations caused by the surface waves striking the bracket during sampling.

Measurements of the sound produced by breaking waves in laboratory wave tanks may be difficult to interpret because of reverberation. If the wave tank is highly reverberant, absolute sound levels are difficult to measure because the sound is recorded more than once as it reflects back and forth past the hydrophone. We studied this problem in detail for our wave tank, and found that the sound measured was predominantly radiated away from the breaking region with negligible reflections from the endwalls of the tank. These results are discussed in section 2.3.

2.2.4 Microwave Measurements

The microwave backscatter was measured with a modified X-band CW Doppler radar model MR7/9 manufactured by Kustom Electronics. The characteristics of the radar are summarized in table 2.6 .

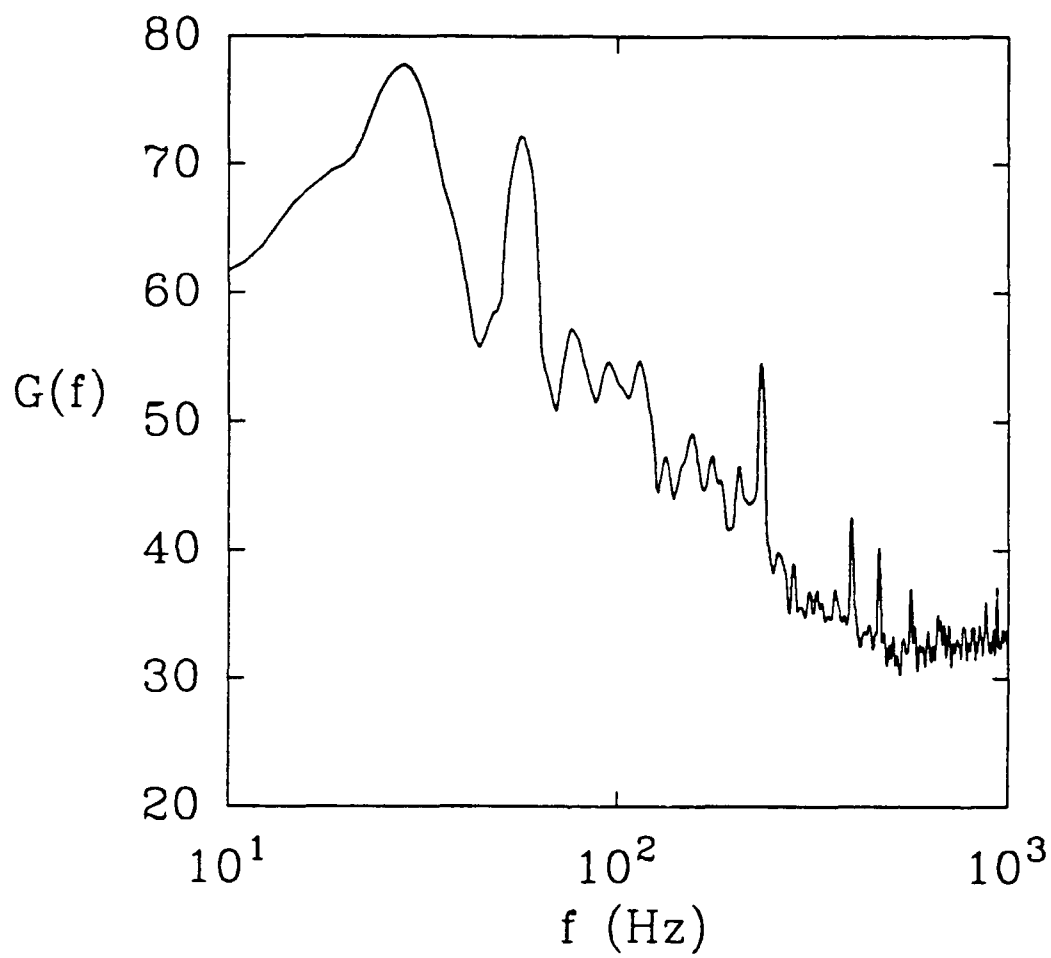


Figure 2.4 The background ambient noise spectrum in the wave channel $G(f)$ in dB re $1 \mu\text{Pa}^2/\text{Hz}$.

RF source	Gunn effect diode in a temperature compensated tuned cavity, 10 VDC at 0.3 to 0.5 amps.
Transmit frequency	10.525 Ghz \pm 25 Mhz
Transmitted power	50 mW typical
Antenna type	Circularly polarized horn, 22 dB gain.
Power requirements	11 to 15 VDC at 1.8 A max.
Operating ambient temperature	0°C to 60°C .
Mixer assembly	Cartridge Schottky-Barrier mixer diode mounted in a terminated wave guide.

Table 2.6 Kustom Electronics radar model MR7/9 characteristics.

The radar was modified by the addition of an HP model X383A variable attenuator and a new amplifier and filter circuit. The manufacturers circuits included a 100 Hz highpass filter and because the signals of interest included frequencies below 100 Hz we replaced the manufacturers circuits with a new amplifier and filter circuit. The circuit included an Analog Devices AD524 instrumentation amplifier chip and a Frequency Devices 711H4B highpass filter. The gain of the amplifier was set at 100 and the highpass filter had a 3 dB cut-off frequency of 1 Hz.

The radar signal was bandpassed from 1-250 Hz and sampled at 500 Hz with the same data acquisition system used to sample the wave gauges. The circularly polarized radar had a 15 cm aperture conical horn, was mounted 71 cm above the still water surface pointing in the upstream direction (looking into the advancing waves) at an incidence angle of 65°, and produced a 3 dB spot size of 1 m at the water surface. The far-field of the aperture defined by the criterion, $R \gg 2d^2 / \lambda$, is 1.53 m, where d is the

diameter of the horn (Ulaby et al, 1981). The centerline range was 1.68 m and the range variation over the 3dB spot was 1.42 m to 2.08 m to the still water surface.

The transmitted power of the radar was monitored during each run with a HP 432A power meter and a X486A temperature compensated thermistor mount. There were no significant variations observed in the transmitted power. To avoid unwanted returns from the downward pointing sidelobes of the radar, a panel of 40 dB radar absorbing material was placed beneath the horn. Absorbing material was also used to block reflections from the wave gauge mounting frame of the wave gauge placed upstream of the radar.

The linearity of the radar system was tested using a set of three metal spheres of diameters 15 cm, 30 cm and 44 cm as targets. The spheres were suspended on nylon string from overhead and swung as pendulums to provide moving targets of known radar cross-section. The radar was mounted horizontally, aimed at the centerline of the spheres at the lowest point in their trajectories. Panels of radar absorbing material were mounted to cover the wave channel and shield each side of the swinging spheres to minimize the effect of multipath reflections. The procedure was based on the well known equation for a monostatic radar,

$$P_r = \frac{P_t G^2 \lambda^2 \sigma}{(4\pi)^3 R^4} \quad 2.13$$

where P_r is the received power, P_t the transmitted power, G is the antenna gain and σ is the radar scattering cross-section (Ulaby et al, 1981). In this case P_t , G and σ are constants and therefore, $\log P_r = \log 4(\sigma / R^4) + \text{constant}$. We varied the range R , from 2 m to 16 m and the radar cross-section σ had three values of 0.018 m², 0.073 and 0.16 m², corresponding to the areas of the three metal spheres.

At each value of R and σ , three runs were performed by swinging the spheres and sampling the data on a HP 3561A signal analyzer. The returned power was taken as the average over the three runs. The calibration data are shown in figure 2.5 where $10 \log(P_r)$ is plotted versus $10 \log(\sigma/R^4)$. The data agree with the radar equation, eq. 2.13, for $\sigma/R^4 > -45$ with scatter of ± 2 dB. At larger ranges the scatter increases because of the effect of multipath reflections which could not be avoided because it became impractical to shield a large enough area of the laboratory with absorbing material. The data follow the radar equation for received voltage amplitudes from 20 mV to 320 mV. The lower limit was due to the effect of multipath reflections at larger ranges and the upper limit was due to the practical limit on the radar cross-section (i.e. larger spheres than the 44.4 cm diameter one used were not practical within our laboratory set-up). At larger voltage amplitudes (up to 4 volts) the radar frequency response was found to be uniform from 1 Hz to 2 kHz. The backscattered radar signals, during the breaking experiments, were typically in the range ± 2 volts and the largest voltage amplitudes observed were 4 volts. Therefore, we concluded that the radar behavior was linear over the range of signal amplitudes observed during the experiments.

2.3 Results

2.3.1 Wave Dissipation

The surface displacement was measured with an array of resistance wire wave gauges, positioned upstream and downstream of the breaking event. Rapp and Melville (1990) have demonstrated that when the surface displacement variance is used to estimate the momentum flux of weakly non-linear, slowly varying, two-dimensional, deep water waves, errors of the order of 5% are incurred. We would expect errors of

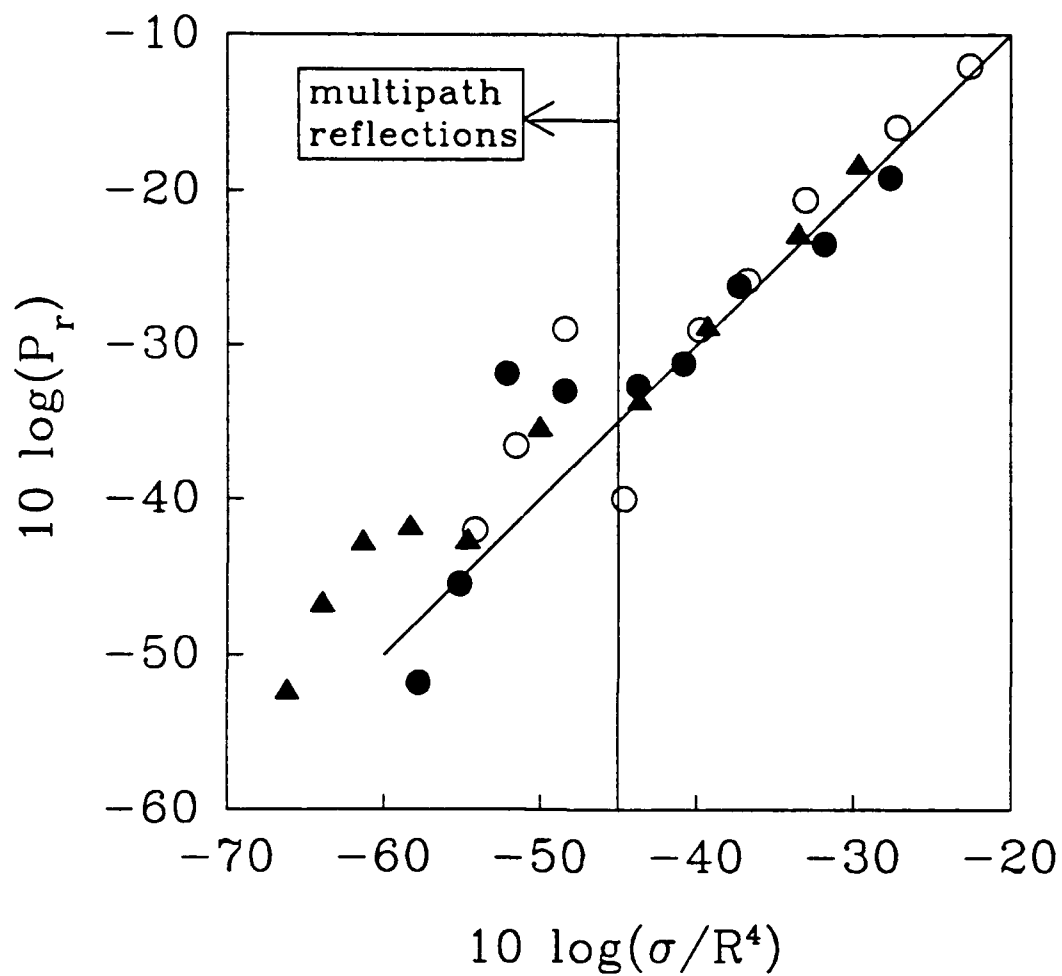


Figure 2.5 The radar calibration data, received power P_r in volts² as a function of σ/R^4 , σ is the radar cross section in m² and R is the range in m.

similar magnitude in these experiments because our wave packet parameters are very similar to theirs. The center frequencies and bandwidths were the same but in our work the water depth was 0.38m compared to their depth of 0.6m. The surface displacement variance $\overline{\eta^2}$ is given by,

$$\overline{\eta^2} = \frac{1}{T} \int_0^T \eta^2(t) dt \quad 2.14$$

where $\eta(t)$ is the surface displacement and T is the length of the sampling interval.

Plots of the dimensionless wave height variance, $\overline{\eta^2} / \overline{\eta_0^2}$ versus the dimensionless distance $(x-x_b)k_c$ for the three wave packets are shown in figures 2.6, 2.7 and 2.8 . The three plots each show the incipient breaking event, an event with an intermediate slope corresponding to either a small plunging or spilling breaker and a steep event corresponding to a large plunging wave. The incipient events slope almost uniformly because of losses due to friction. The steeper events show rapid decreases in the dimensionless variance near the theoretical break point.

The fractional dissipation D due to breaking, is given by,

$$D = \frac{\overline{\Delta\eta^2}}{\overline{\eta_0^2}} = \left[\frac{\overline{\eta_0^2} - \overline{\eta_f^2}}{\overline{\eta_0^2}} \right] \quad 2.15$$

where $\overline{\eta_0^2}$ and $\overline{\eta_f^2}$ are the surface displacement variances upstream and downstream of the event. Figure 2.9 shows the dissipation D , as a function of the wave slope parameter S . The data collapse onto a single curve similar to the data presented by Melville and Rapp (1985). There is a threshold at $S = 0.23$, below which no breaking occurs. In the range, $S = 0.23-0.28$, the dissipation increases rapidly reaching a plateau at

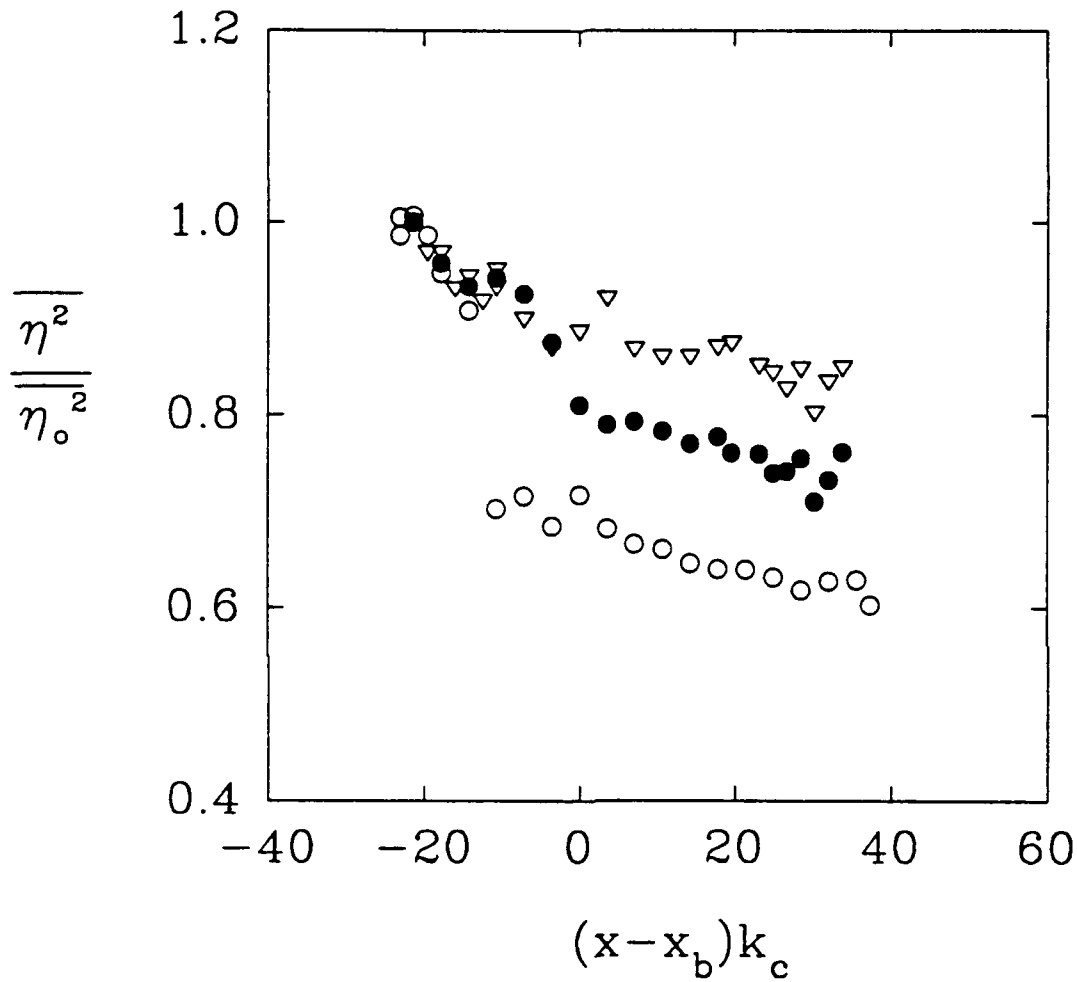


Figure 2.6 The surface displacement variance $\overline{\eta^2}$ normalized by the reference upstream surface displacement variance $\overline{\eta_o^2}$ plotted versus the dimensionless distance along the wave channel, x is the distance along the channel measured from the mean position of the wave paddle, x_b is the theoretical focal point and k_c is the wavenumber of the wave packet center component. Data is for wave packet P_1 : ▽, $S=0.226$; ●, $S=0.254$; ○, $S=0.263$.

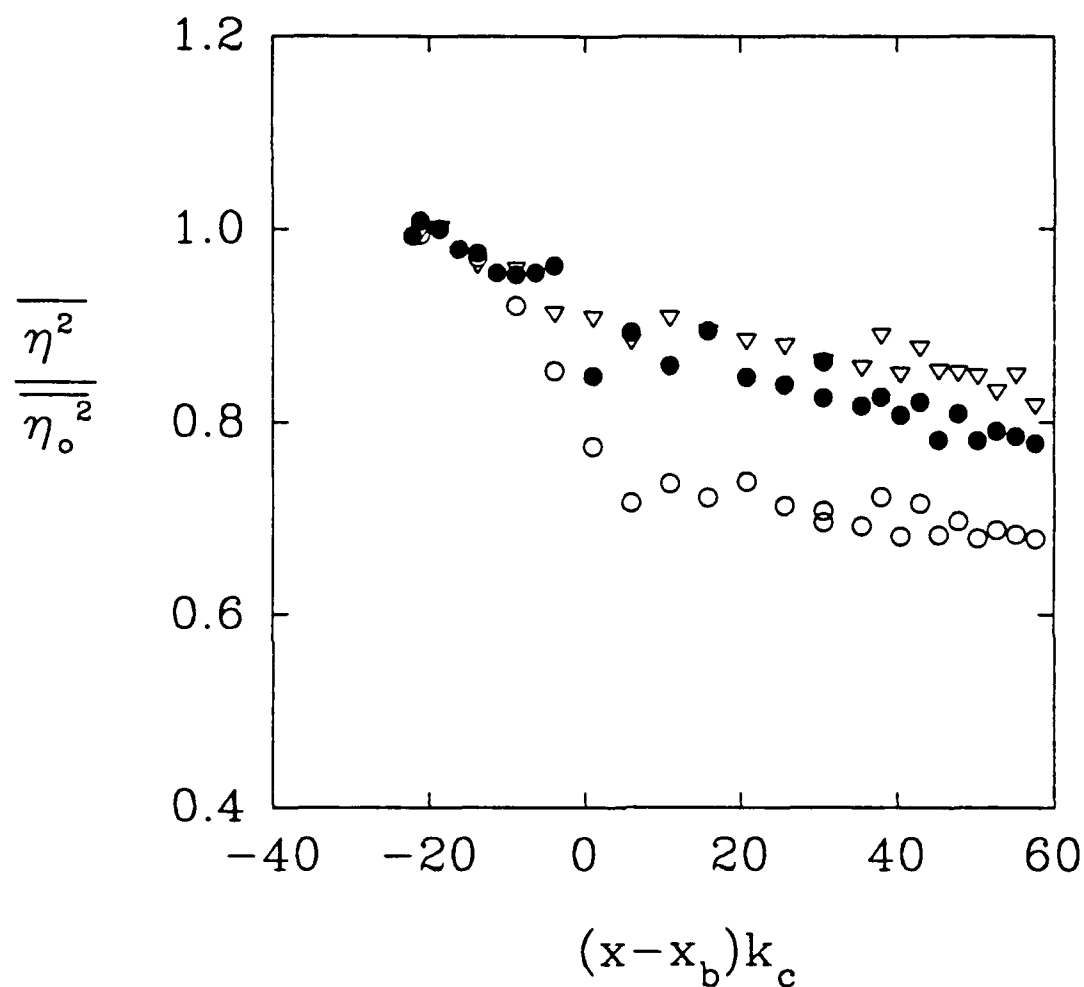


Figure 2.7 The surface displacement variance $\overline{\eta^2}$ normalized by the reference upstream surface displacement variance $\overline{\eta_o^2}$ plotted versus the dimensionless distance along the wave channel, x is the distance along the channel measured from the mean position of the wave paddle, x_b is the theoretical focal point and k_c is the wavenumber of the wave packet center component. Data is for wave packet P_2 : ∇ , $S=0.221$; \bullet , $S=0.244$; \circ , $S=0.312$.

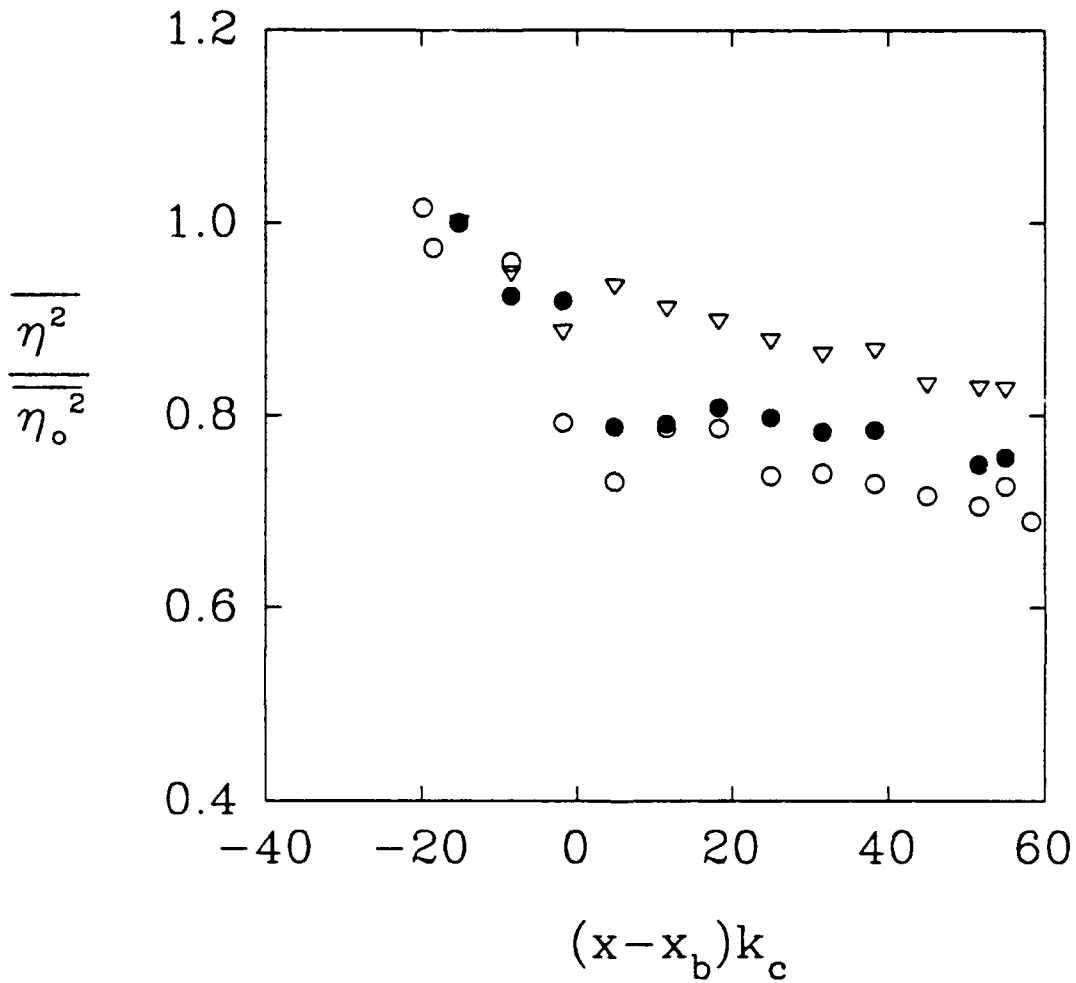


Figure 2.8 The surface displacement variance $\overline{\eta^2}$ normalized by the reference upstream surface displacement variance $\overline{\eta_o^2}$ plotted versus the dimensionless distance along the wave channel, x is the distance along the channel measured from the mean position of the wave paddle, x_b is the theoretical focal point and k_c is the wavenumber of the wave packet center component. Data is for wave packet P_3 : ∇ , $S=0.218$; \bullet , $S=0.240$; \circ , $S=0.320$.

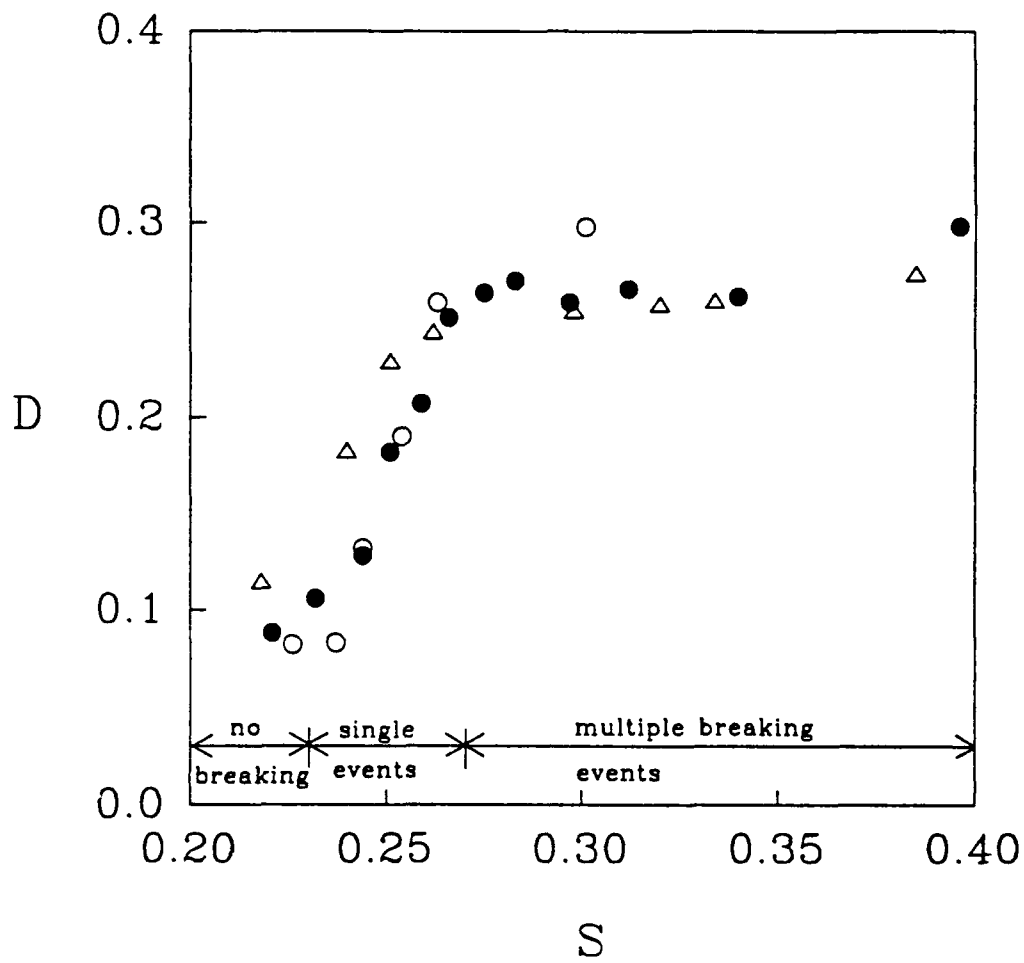


Figure 2.9 The fractional dissipation of wave packet energy as a function of the slope parameter S : ○, P_1 ; ●, P_2 ; △, P_3 . The variability of the data was typically less than the symbol size.

$D \cong 0.30$ and then remains approximately constant for $S > 0.28$. For values of $S < 0.23$ the dissipation is approximately constant at 0.10, consistent with theoretically predicted losses due to friction (Rapp and Melville, 1990).

2.3.2 Microwave Scattering

A typical radar time series and the corresponding Doppler spectrum are shown in figure 2.10. The breaking events were found to be associated with the higher frequency components of the signal, which in figure 2.10a occur in the interval 2.5s - 3.2s. The spectrum in figure 2.10b has a well defined minimum at 50 Hz which was typical for all events observed. In figure 2.11 a set of radar spectra, for time series bandpass filtered from 1-250 Hz and sampled at different locations along the channel are shown.

In figure 2.11 the spectra at 9.5m, 10m and 10.5m have considerable energy above the ambient levels for frequencies < 50 Hz. This energy is not associated with the breaking wave because it was also observed at these locations for lower amplitude non-breaking waves. Similar behavior was observed for the two other wave packets as well, which led us to conclude that for the wave frequencies used in these experiments, the backscattered microwave power due to breaking corresponded to frequencies in the range 50-250 Hz. The energy below 50 Hz is likely due to the backscatter from the orbital motions of the waves or from capillary waves near the crest of steep but unbroken wave.

In figure 2.12 a set of radar time series, bandpass filtered from 50-250 Hz and a matching hydrophone time series, bandpass filtered from 500-10,000 Hz, are displayed. In figure 2.13 a series of photographs, matching the radar and acoustic time series of

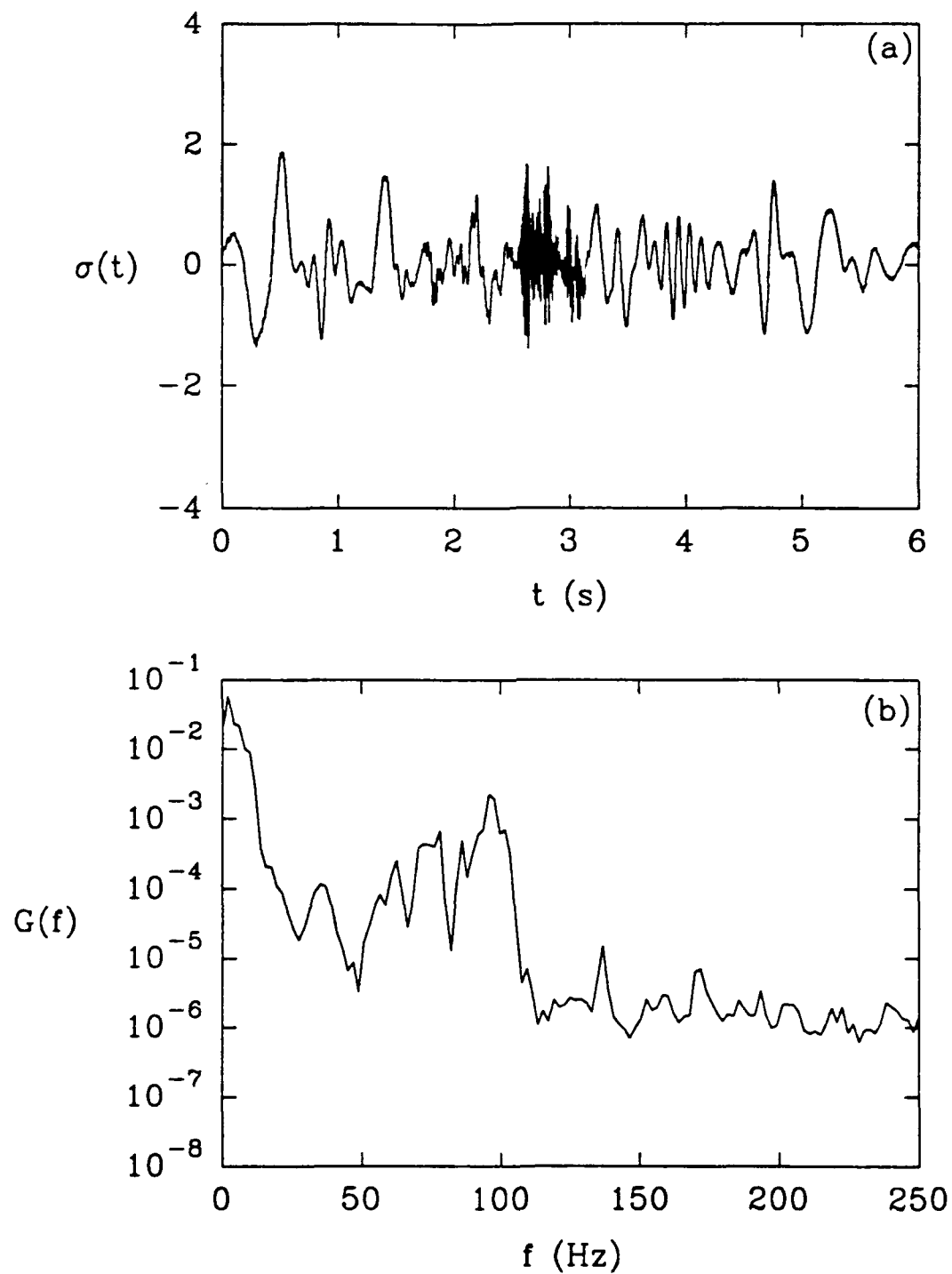


Figure 2.10 (a) Time series of the radar signal band pass filtered from 1-250 Hz for packet P_1 with $S = 0.254$. (b) Power spectrum of time series in (a).

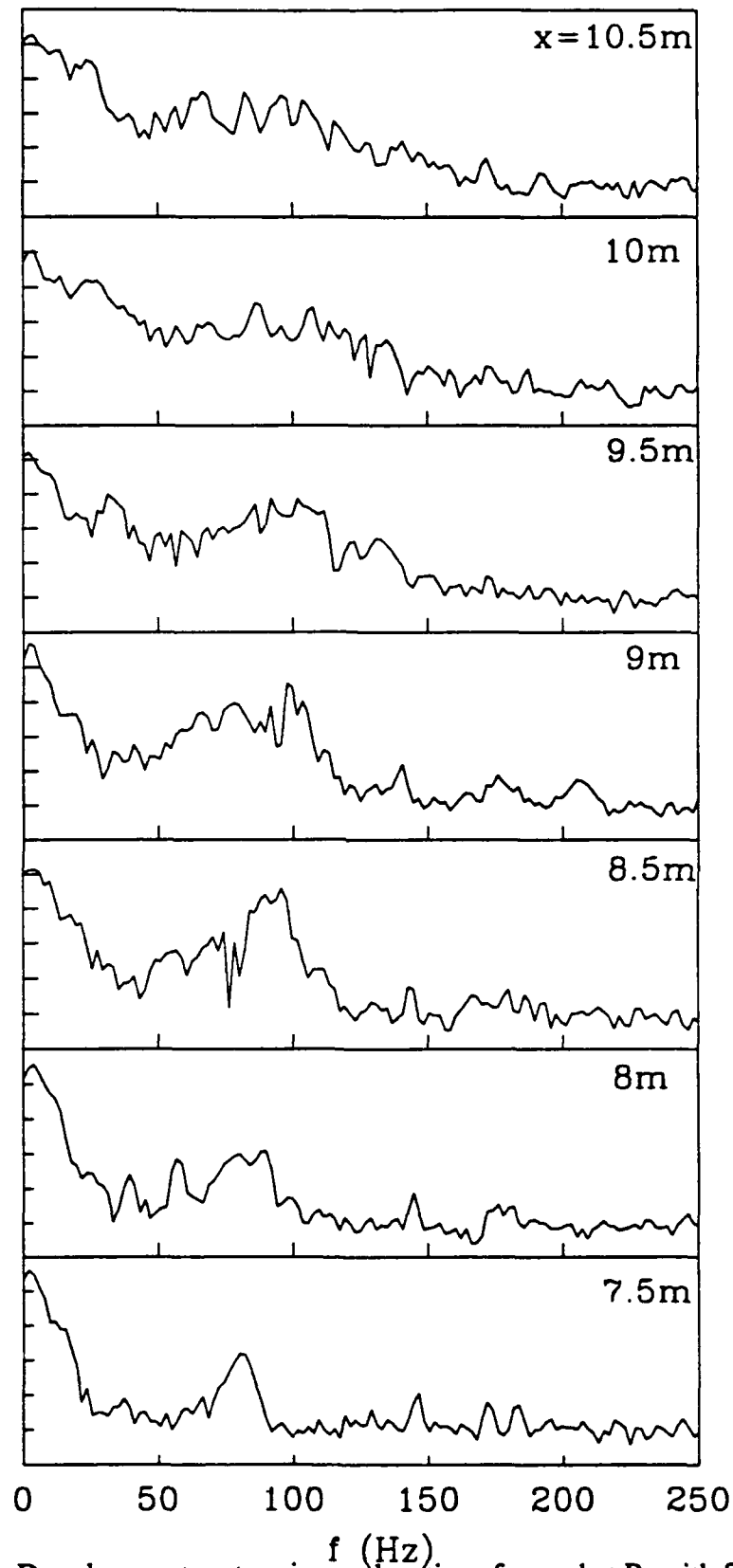


Figure 2.11 Radar Doppler spectra at various x-locations for packet P_1 with $S = 0.254$, the radar time series were band pass filtered from 1-250 Hz.

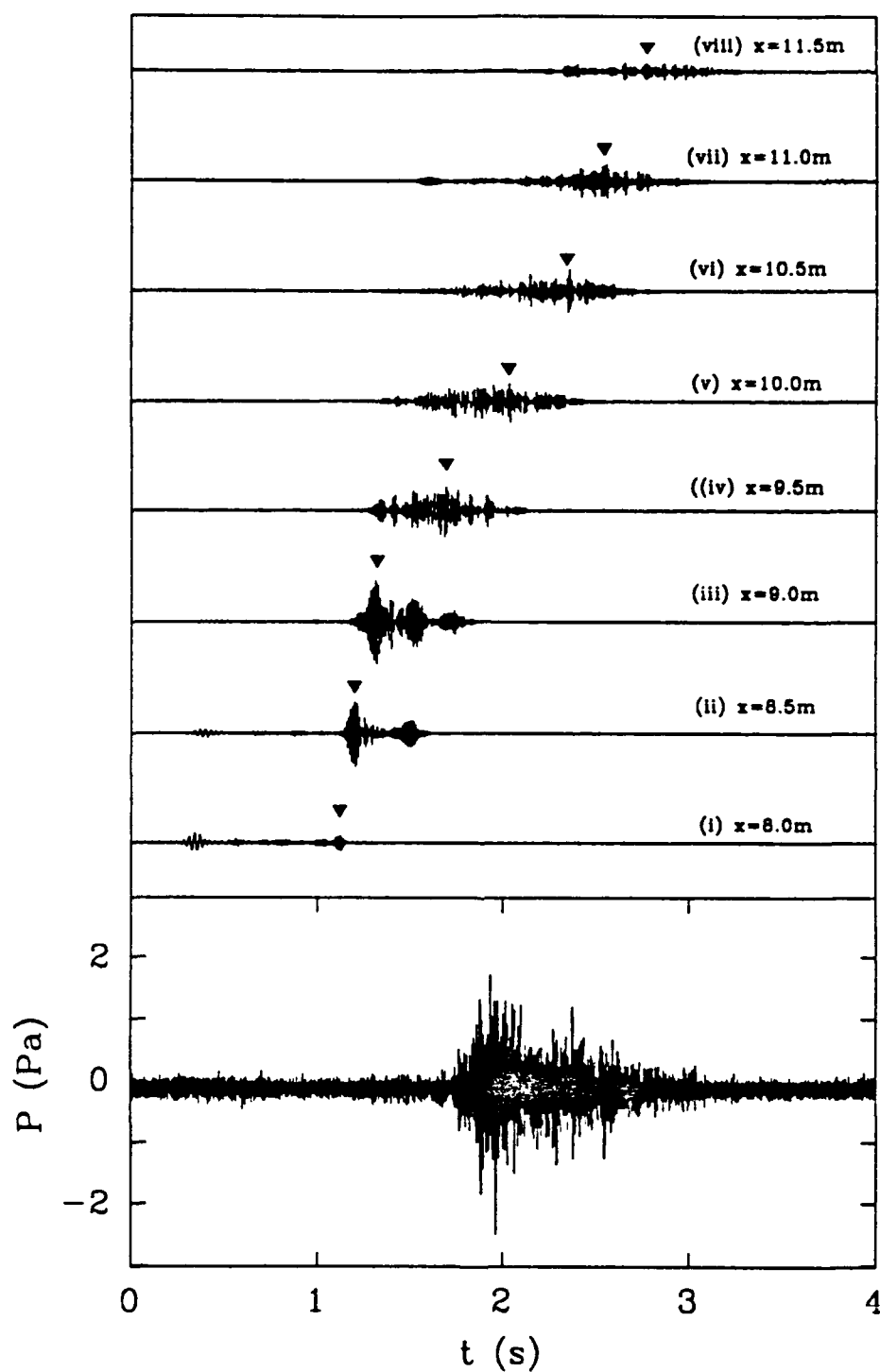


Figure 2.12 Bottom trace is a hydrophone time series band pass filtered in the range 500 Hz-10 kHz, upper traces are radar time series at various x -locations, band pass filtered in the range 50-250 Hz, for packet P_1 with $S = 0.254$. The ▼ mark the times corresponding to the photographs in figure 2.13.

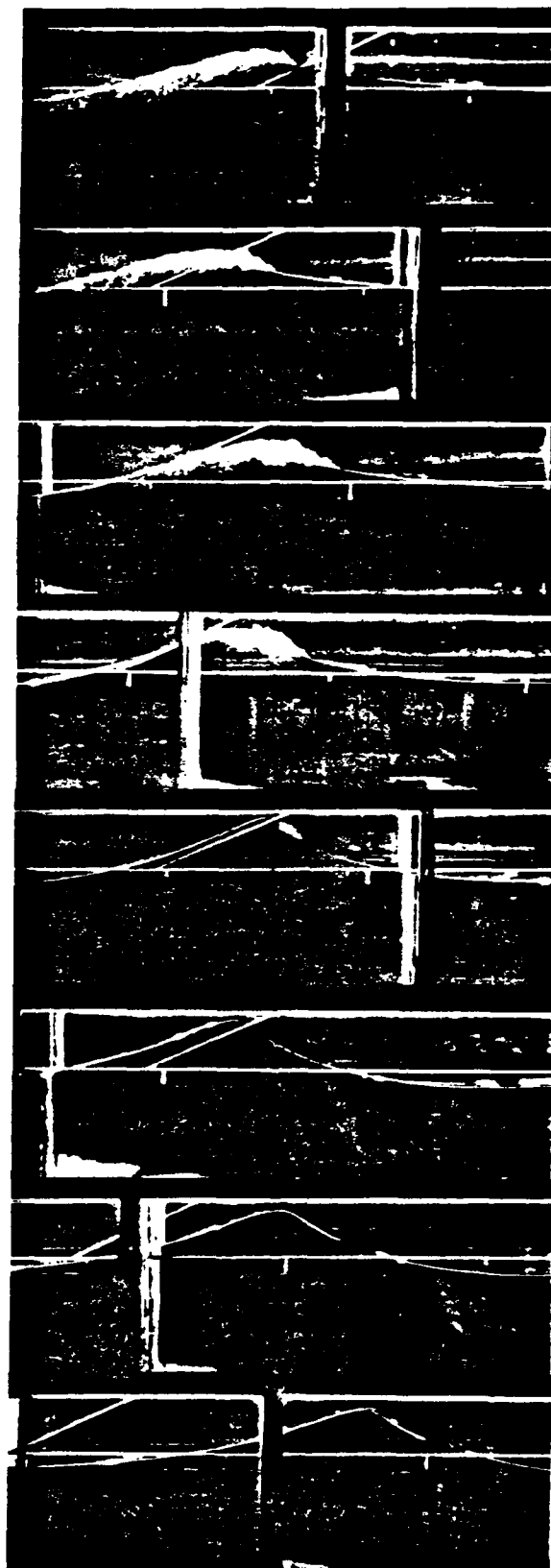
figure 2.12, show the evolution of a breaking wave with time ². The mean water surface elevation is marked by the horizontal tape and the tick marks denote 0.5m intervals. The centerline of the radar antenna pattern is marked by the angled tape above the mean water level.

In figure 2.13, photograph I ($x=8\text{m}$, $t=1.12\text{s}$), the unbroken wave crest is downstream of the radar centerline, there is no acoustic signal and the amplitude of the radar signal is very small. In II ($x=8.5\text{m}$, $t=1.2\text{s}$) the unbroken crest is slightly downstream of the radar centerline, there is still no acoustic signal and the radar signal amplitude is large. The large backscattered signal is probably due to specular reflection from the steep forward face of the wave which is located just downstream of the center of the beam but still within the 3dB beamwidth. The wave is still unbroken and no sound has been produced in III ($x=9\text{m}$, $t=1.32\text{s}$), the steep forward face of the wave is directly in line with the centerline of the radar beam and the radar signal amplitude is at a maximum. The beginning of sound production coincides with IV ($x=9.5\text{m}$, $t=1.69\text{s}$), the wave has begun to break, the crest is in line with the center of the radar beam and the radar signal amplitude has begun to decrease. The wave is breaking vigorously in V ($x=10\text{m}$, $t=2.03\text{s}$) and the acoustic signal amplitude is large. In photographs VI, VII and VIII the wave is actively breaking and both the radar and acoustic signal amplitudes are decreasing with time. In VII the crest is at the centerline of the radar beam, the acoustic signal amplitude has decreased to 50% of the maximum and the radar signal amplitude is 35% of its maximum.

These photographs and time series clearly show that a large portion of the backscattered microwave power associated with breaking is due to scattering from the

² The data in figure 2.12 and the photographs in figure 2.13 were taken with a water depth of 0.364m compared to 0.38m which was used for the bulk of the experiments. This was necessary because at a depth of 0.38m the wave crest was hidden from view behind the upper steel beam of the wave tank. We observed no significant differences between the radar and acoustic signals at the two depths.

Figure 2.13 Photographs of a breaking wave matching the data in figure 2.12 . Each photograph corresponds to one radar time series and the time the photograph was taken is marked in figure 2.12 with a ▼ above the matching radar time series.



(viii) $x = 11.5$ m
 $t = 2.72$ s

(vii) $x = 11.0$ m
 $t = 2.54$ s

(vi) $x = 10.5$ m
 $t = 2.34$ s

(v) $x = 10.0$ m
 $t = 2.03$ s

(iv) $x = 9.5$ m
 $t = 1.69$ s

(iii) $x = 9.0$ m
 $t = 1.32$ s

(ii) $x = 8.5$ m
 $t = 1.2$ s

(i) $x = 8.0$ m
 $t = 1.12$ s

steep forward face of the wave prior to the start of active breaking and sound generation. They also show that the majority of the sound energy produced by breaking occurs during the early stages of active breaking, see figure 2.13 V. In the latter stages, figure 2.13, VII and VIII, the bubble cloud is still clearly visible but sound amplitudes have decreased significantly.

The more energetic breaking events covered an area larger than the area illuminated by the radar. In order to obtain a single measure of the backscattered power from each event and to eliminate the influence of the antenna, it was necessary to take radar measurements at a number of positions along the channel. At each location the time averaged radar cross-section $\overline{\sigma}(x)$ was calculated from,

$$\overline{\sigma}(x) = \frac{1}{T} \int_0^T \tilde{\sigma}(x,t) dt \quad 2.16$$

where T is the length of the sample and $\tilde{\sigma}(x,t)$ is the time series of the radar cross-section as a function of both x and t . Two examples of the time averaged radar cross-section as a function of position along the channel are shown in figure 2.14a. Both events shown are typical, with $\overline{\sigma}(x)$ increasing from zero to a well defined peak and then decaying towards zero as x increases.

The peak frequency is defined as the frequency of the maximum value of the Doppler spectrum. It is a measure of the velocity of the dominant scatterers present in the illuminated area during the sampling interval. In figure 2.14b the peak frequency, corresponding to the data in figure 2.14a, is plotted. It was calculated from the Doppler spectrum of the radar signal bandpassed from 50-250 Hz. The maximum peak frequencies for the two events plotted in figure 2.14b are close to the phase velocities of the center components for their respective wave packets, see Table 2.3.

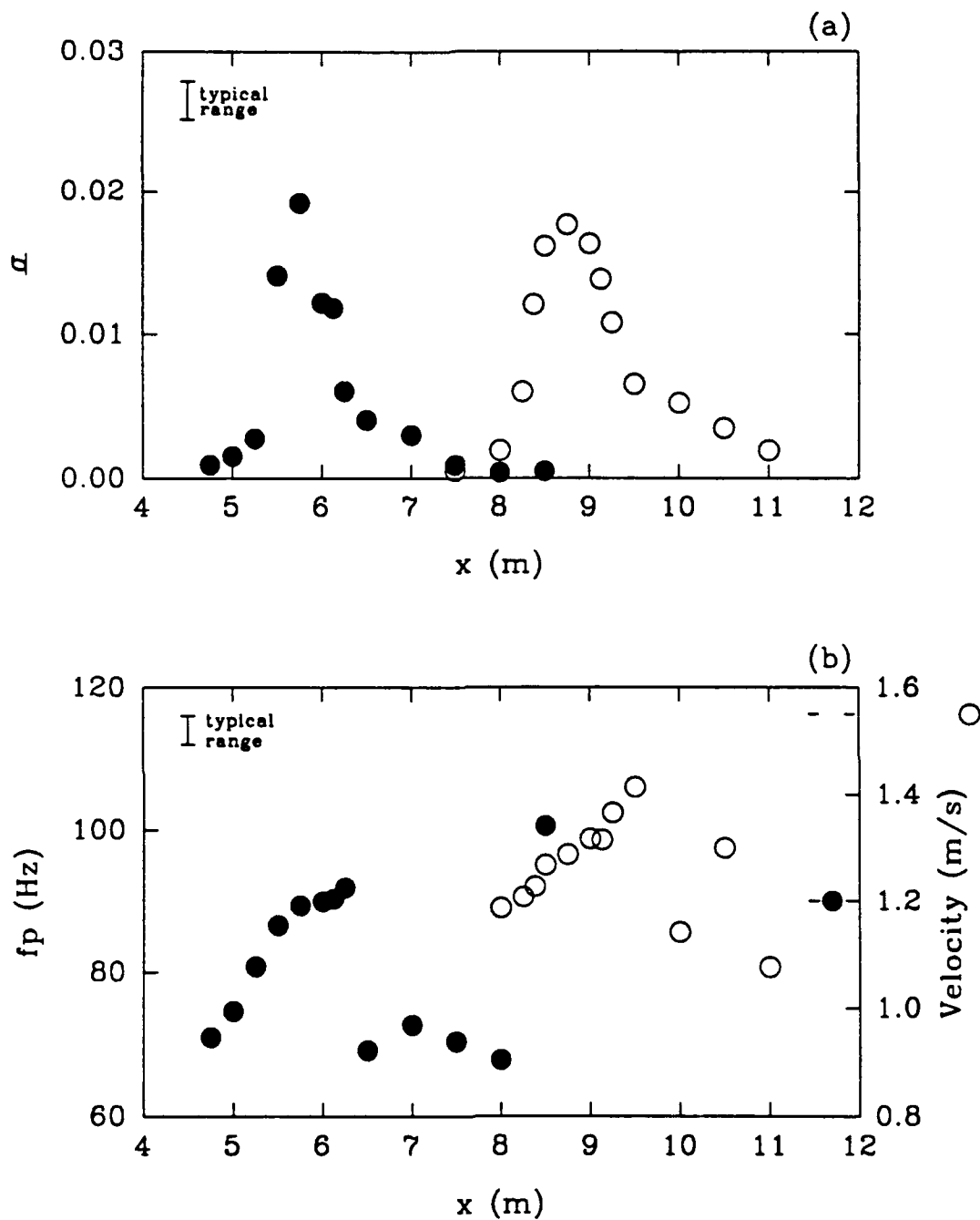


Figure 2.14 (a) Time averaged radar cross-section as a function of x . (b) Peak frequency (Hz) of the radar Doppler spectrum as a function of x . ○, P_1 , $S = 0.254$; ●, P_3 , $S = 0.385$; -○- and -●- on (b) denote the center component phase speeds for P_1 and P_3 respectively. Each data point is averaged from 3 runs at each location; radar data were band pass filtered in the range 50-250 Hz. The typical variability of the data between runs is shown by the scatter bars.

2.3.3 Acoustic Radiation

The acoustic field is dominated by the modal structure present in the wave tank. If the tank sidewalls and bottom are assumed to be rigid and the free surface a pressure release surface the mode shapes are given by,

$$\phi_m^v(z) = \sin \left[\frac{(2m-1)\pi z}{2H} \right] \quad m = 1, 2, \dots, \infty \quad 2.17$$

$$\phi_n^h(y) = \cos \left[\frac{n\pi y}{W} \right] \quad n = 0, 1, \dots, \infty \quad 2.18$$

where $\phi_m^v(z)$ is the vertical eigenfunction, z is the vertical coordinate, m is the water depth, $\phi_n^h(y)$ is the horizontal eigenfunction, y is the transverse coordinate and W is the tank width (Brekhovskikh and Lysanov, 1982). The mode shapes are composed of combinations of one horizontal and one vertical eigenfunction. The first six vertical and horizontal eigenfunctions are illustrated in figures 2.15 and 2.16. The cut-off frequencies of the modes are given by,

$$F_c = \frac{c}{2\pi} (k_z^2 + k_y^2)^{1/2} \quad 2.19$$

where F_c is the cut-off frequency in Hz, k_z is the vertical wavenumber and k_y is the transverse wavenumber. In table 2.7 the modes with cut-off frequencies less than 10 kHz are listed.

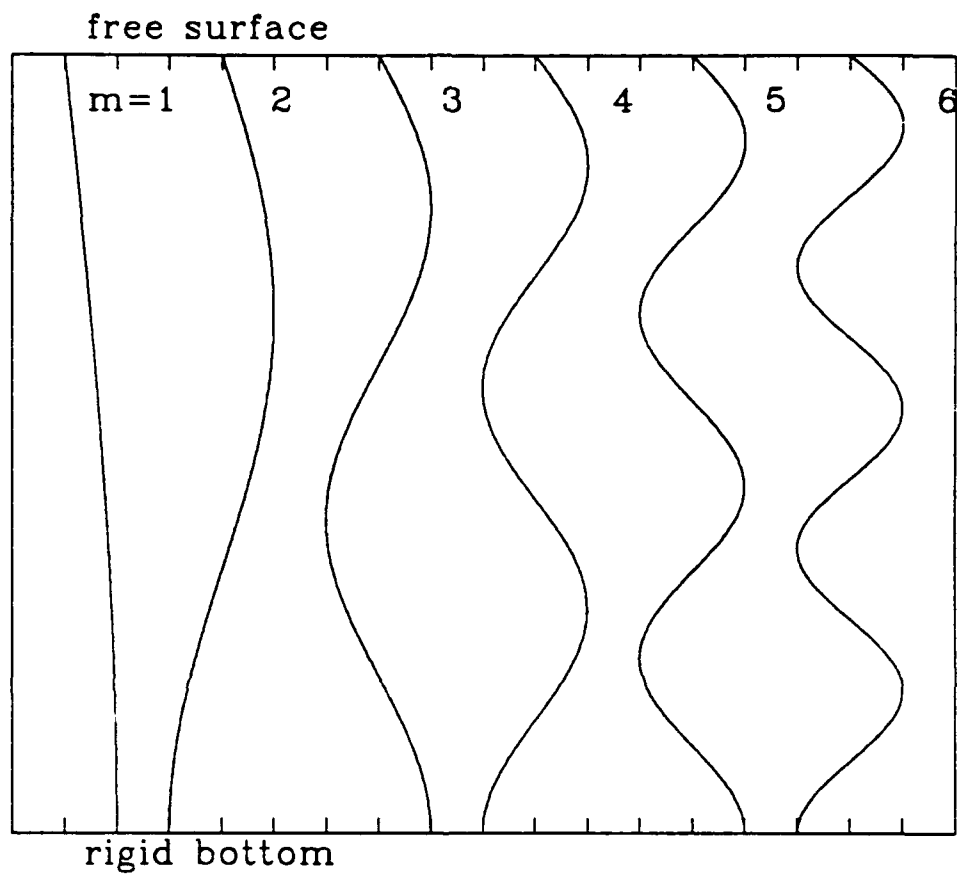


Figure 2.15 Vertical eigenfunction shapes; m is the vertical mode number.

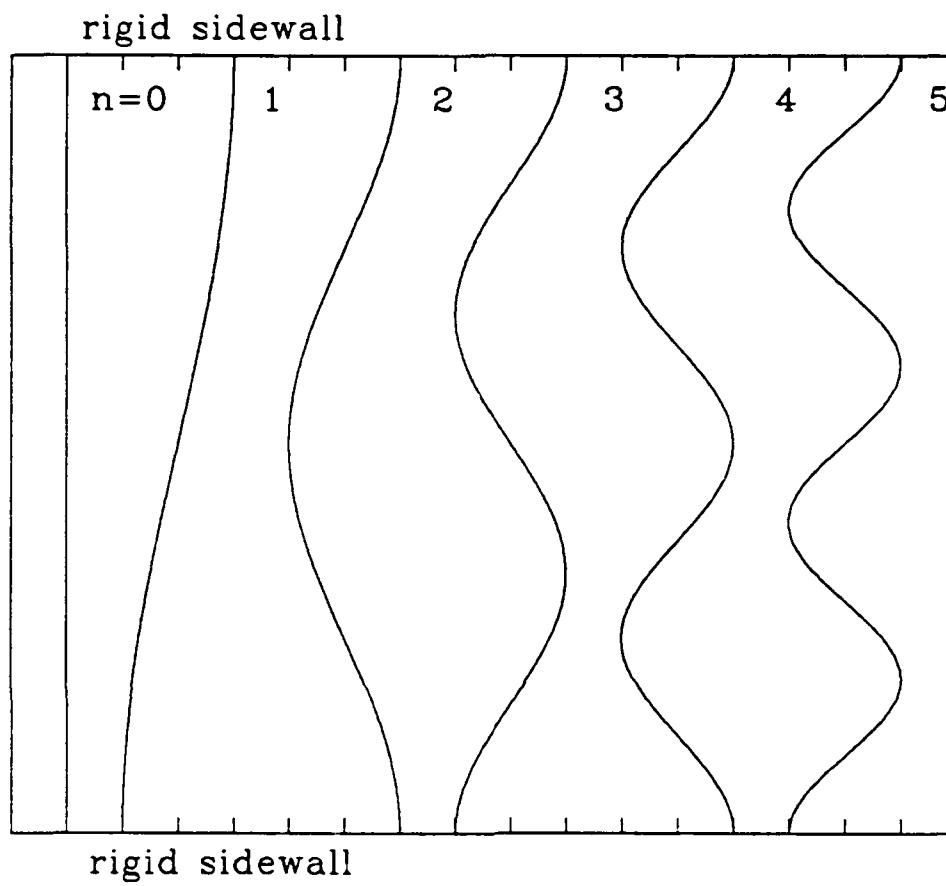


Figure 2.16 Horizontal eigenfunction shapes; n is the horizontal mode number.

Horizontal mode number n	Vertical mode number m	Theoretical cutoff frequency (Hz)
0	1	990
0	2	2960
0	3	4930
0	4	6910
0	5	8880
1	1	2210
1	2	3560
1	3	5310
1	4	7190
1	5	9100
2	1	4070
2	2	4940
2	3	6320
2	4	7960
2	5	9720
3	1	6010
3	2	6630
3	3	7710
3	4	9100
4	1	7960
4	2	8430
4	3	9310
5	1	9920

Table 2.7 Acoustic modes and their theoretical cutoff frequencies

A typical acoustic spectrum for a breaking wave and the spectrum of the background noise are shown in figure 2.17. There is energy above the background levels across the entire spectrum, but the majority of the energy is between 2200 Hz and 4500 Hz. The cut-off at 2200 Hz is most prominent and was clearly evident in the spectra of all events. It is not clear why the lowest order mode with $m = 1$, $n = 0$ and a cut-off frequency of 990 Hz is not observed.

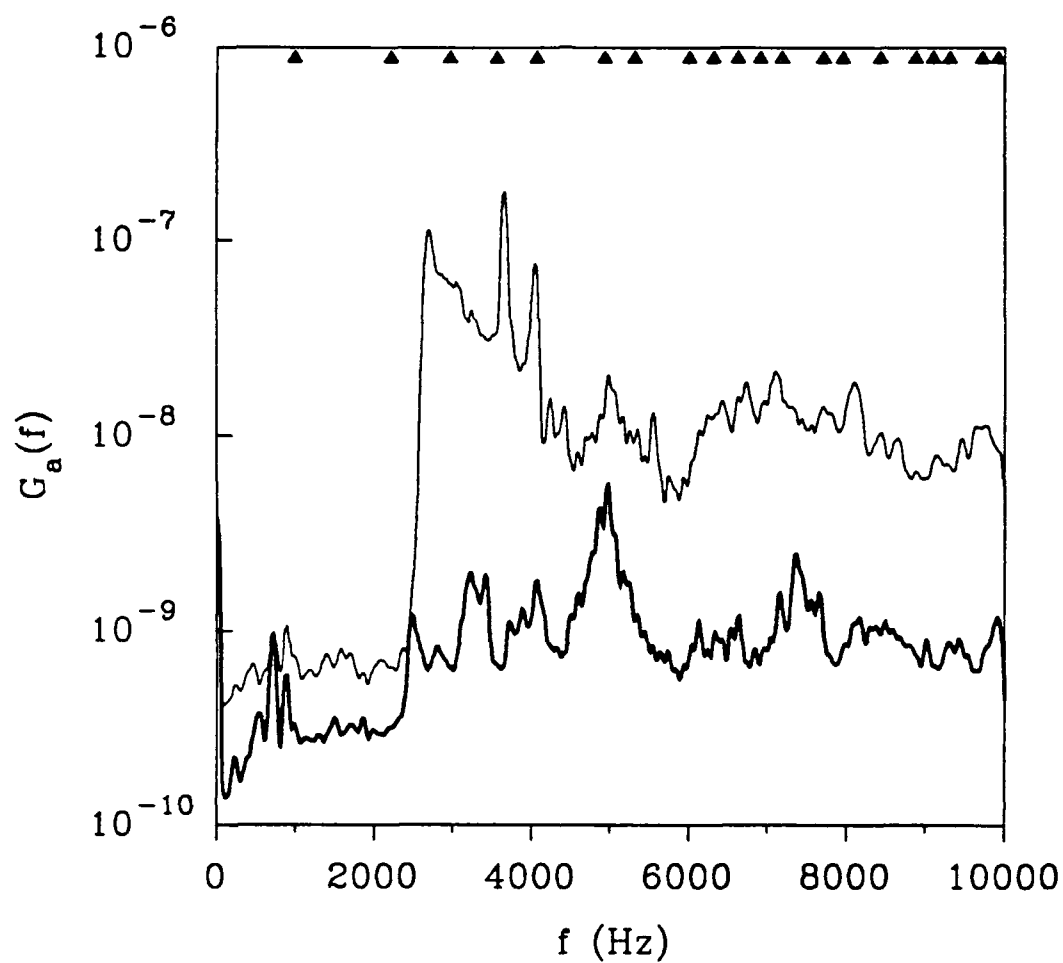


Figure 2.17 Upper curve is the acoustic spectrum for packet P_1 with $S = 0.254$; lower curve is the spectrum of the background noise. ▲, mark locations of the cutoff frequencies.

We investigated the influence of reverberation on the acoustic measurements. Two hydrophones were positioned at mid-depth in the tank, several meters downstream of the breaking location, separated by a distance Δx in the longitudinal direction. The acoustic signal from a breaking wave was then recorded simultaneously using both hydrophones and the phase and time delay between them was calculated.

In figure 2.18 and 2.19 the coherence, $\gamma_{xy}^2(f)$, and the phase spectrum, $\theta_{xy}(f)$, for a run with $S=0.263$ and $\Delta x=1.15\text{m}$ are shown. The coherence is defined by,

$$\gamma_{xy}^2(f) = \frac{|G_{xy}(f)|^2}{G_{xx}(f) G_{yy}(f)} \quad 2.20$$

where $G_{xy}(f)$ is the cross-spectral density function of the two time series $x(t)$ and $y(t)$, $G_{xx}(f)$ and $G_{yy}(f)$ are the autospectral density functions of $x(t)$ and $y(t)$ respectively. The phase spectrum is given by,

$$\theta_{xy}(f) = \tan^{-1} \left[\frac{Q_{xy}(f)}{C_{xy}(f)} \right] \quad 2.21$$

where $Q_{xy}(f)$ the quad-spectrum and $C_{xy}(f)$, the co-spectrum are defined by,

$$G_{xy}(f) = C_{xy}(f) - jQ_{xy}(f) \quad 2.22$$

(Bendat and Piersol, 1986). From figure 2.18 it is seen that where the coherence is high the phase spectrum is ordered and continuous. The positive slope of $\theta_{xy}(f)$ indicates that $y(t)$, which corresponds to the hydrophone closest to the event, leads $x(t)$ which is consistent with the acoustic energy propagating downstream away from the breaking location.

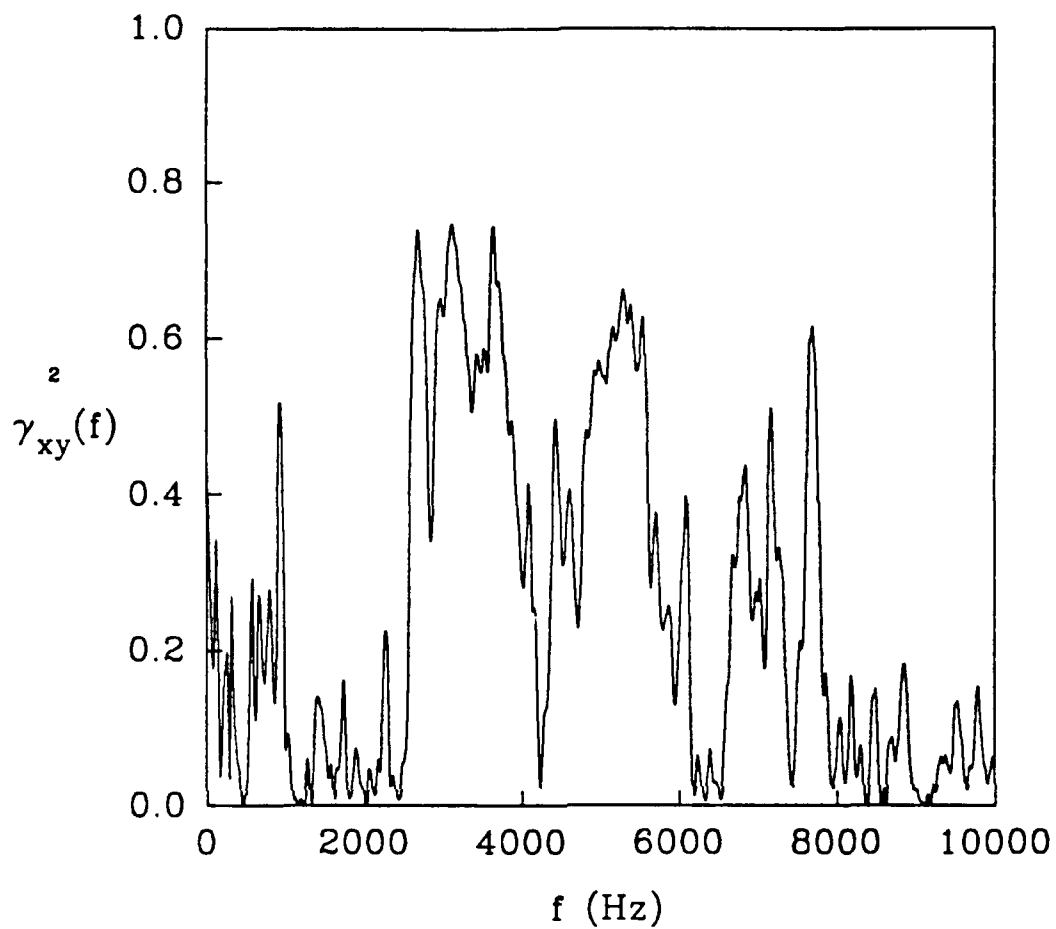


Figure 2.18 Coherence $\gamma_{xy}^2(f)$ of two hydrophone signals, $S = 0.263$ and the separation distance between the hydrophones $\Delta x = 1.15$ m.

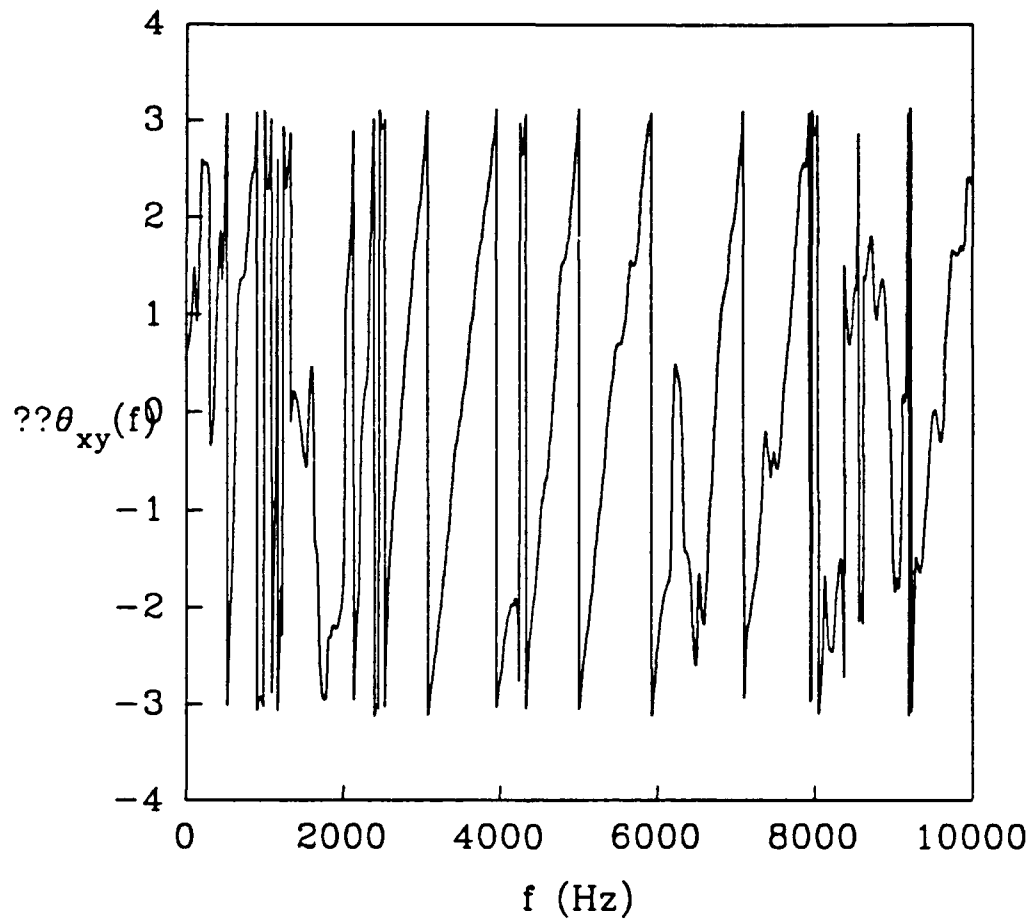


Figure 2.19 Phase spectrum $\theta_{xy}(f)$ of two hydrophone signals, $S = 0.263$ and the separation distance between the hydrophones $\Delta x = 1.15 \text{ m}$.

The data from the pair of hydrophones was digitally processed to obtain the time delay between the two signals. The processing consisted of bandpassing the two signals in a narrow band over which the coherence was high and then rectifying and lowpassing to obtain the envelopes of the two signals. The two envelopes were then cross-correlated and the time delay found by locating the maximum in the cross-correlation sequence. Using the time delay and the distance Δx between the two hydrophones the group velocity was calculated. The group velocities for the modes of the wave tank can be computed using the following equation:

$$C_g = C (1.0 - (F_c/f)^2)^{1/2} \quad 2.23$$

where C_g is the group velocity, C the phase speed, F_c the cut-off frequency (cf. eq. 2.19) and f the frequency (Brekhovskikh and Lysanov, 1982). In figure 2.20 the theoretical curves given by eq. 2.23 and the group velocities obtained from the time delay estimates are compared. Except for the one outlier at 5500 Hz the agreement is good and the time delays obtained showed that the signal from the hydrophone closer to the breaking event leads the other signal as expected. The data points estimated using the time delay technique were at frequencies where the two signals were significantly correlated, that is had a coherence exceeding 0.5.

To study the acoustic attenuation along the channel, hydrophone measurements were taken at a number of positions downstream of the breaking event. Figure 2.21 shows a set of data from our earlier experiments, which were reported in Melville et al (1988), showing the attenuation of the mean square acoustic pressure, $\overline{p^2}(x)$, where

$$\overline{p^2}(x) = \frac{1}{T} \int_0^T p(x,t)^2 dt \quad 2.24$$

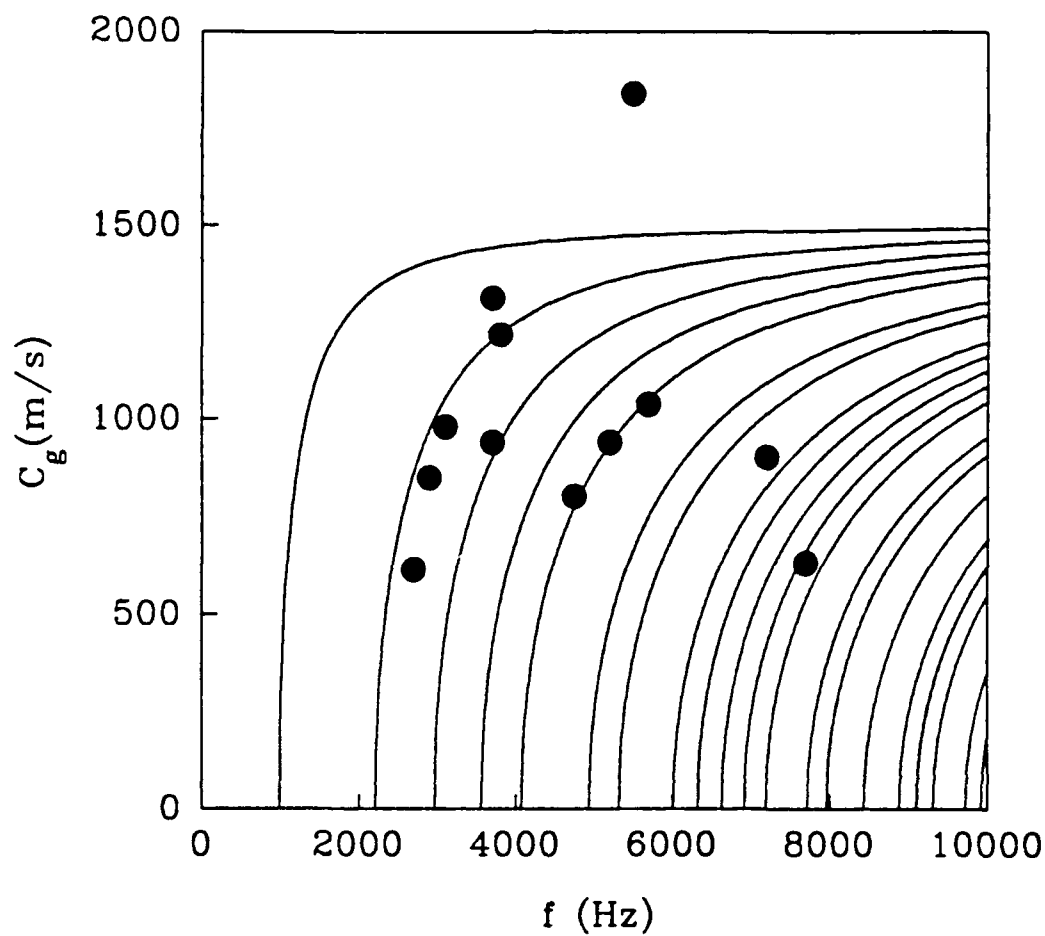


Figure 2.20 Solid curves show equation 2.23, the theoretical values for the group velocities of the acoustic modes in the wave channel; •, estimates of the group

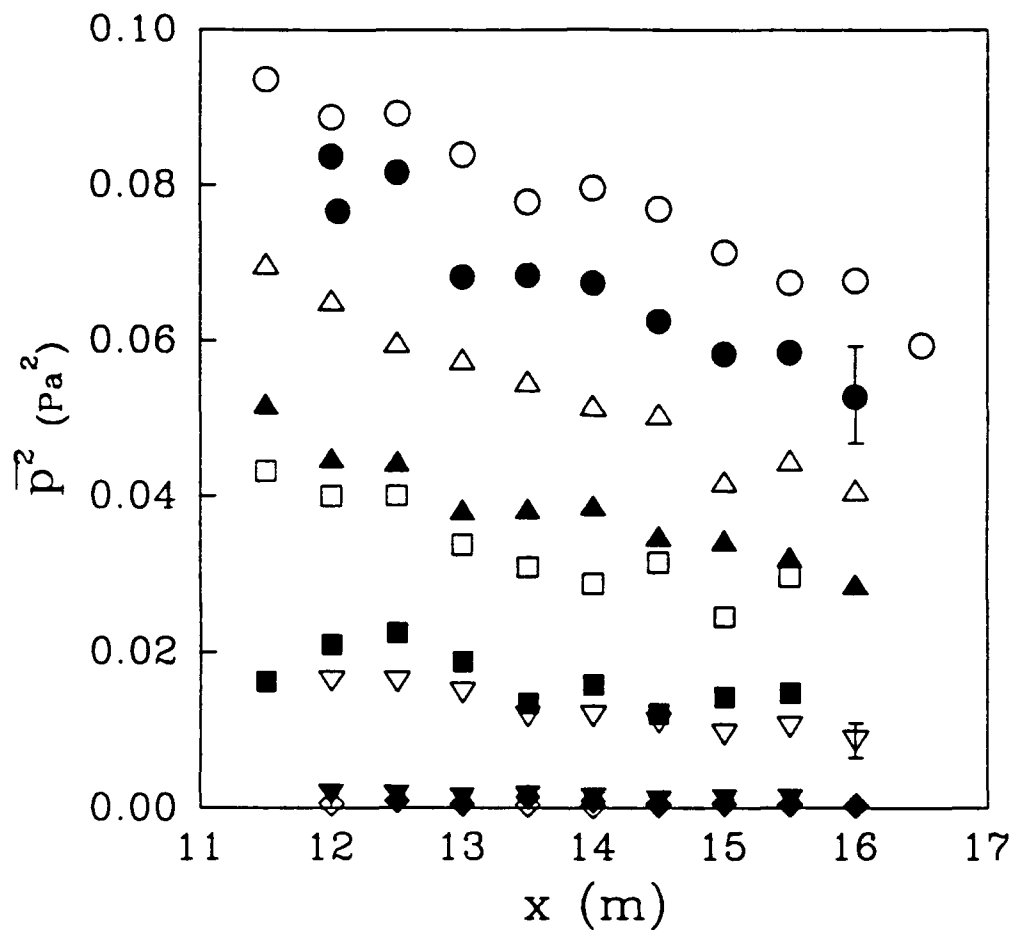


Figure 2.21 Mean square acoustic pressure as a function of x . All data are for P_1 : \circ , $S = 0.286$; \bullet , $S = 0.274$; \triangle , $S = 0.263$; \blacktriangle , $S = 0.254$; \square , $S = 0.249$; \blacksquare , $S = 0.247$; ∇ , $S = 0.244$; \blacktriangledown , $S = 0.241$; \diamond , $S = 0.237$; \blacklozenge , $S = 0.226$. Each data point is the average of 5 runs and the typical variability of the data between runs is shown by the scatter bars.

where $p(x,t)$ is the acoustic pressure, and T is the duration of the sampling interval. The attenuation rate is approximately constant for a given slope, S , and at a given x location the mean square pressure increases with increasing S . In the present study hydrophone measurements were taken over a range of 4m in the x direction for one third of the events, and over a range of 2 m for the remaining events. Extrapolating over twice the distance from the sampling location of the hydrophone to the wavemaker paddle or to the endwall showed that the sound had decayed to negligible levels before returning to the hydrophone location.

The results for the attenuation of the acoustic signal along the tank, the slope of the phase spectrum and the sign and magnitude of the group velocity results all demonstrate that the acoustic measurements were not corrupted significantly by reflections or excessive reverberation. The relative phase of the two signals at frequencies at which the coherence is high and the time delay estimates for the entire signals confirm that the acoustic energy was propagating away from the breaking location.

2.3.4 Empirical Scaling and Correlations

A single measure of the backscattered microwave power was obtained by integrating the time averaged radar cross-section $\overline{\sigma}(x)$, along the channel in x . Defining the radar cross-section as,

$$\sigma = \frac{1}{L_e} \int_0^{L_e} \overline{\sigma}(x) dx \quad 2.25$$

where L_e is the length of the longest event measured, T is the sampling time and $\overline{\sigma}(x)$ is the time averaged radar cross-section. The radar cross-section has units of length squared and is most naturally scaled by the wave packet center component wavenumber, k_c . In figure 2.22 the scaled radar cross-section σk_c^2 , is plotted as a function of the slope parameter, S . The data collapses onto a single curve and there is a linear correlation between the dimensionless radar cross-section and the wave slope.

A dimensionless mean square pressure can be defined by scaling with $(\rho c_c^2)^2$,

$$P_d = \frac{\overline{p^2}(x)}{(\rho c_c^2)^2} \quad 2.26$$

where ρ is the density of water and c_c is the phase speed of the center frequency component. We chose to use $\overline{p^2}(x)$ measured at 7m downstream from the breaking location in calculating P_d . In figure 2.23 the dimensionless mean square pressure, P_d , is shown as a function of the slope parameter, S . The data falls onto a single curve and a linear correlation is again evident.

It was of interest to see if the radar and hydrophone signals were correlated. The dimensionless radar cross-section, σk_c^2 , and the dimensionless mean square pressure, P_d , are plotted in figure 2.24. A strong correlation is evident except for one outlying point which remains unexplained. The experimental data for this outlier at $P_d = 10^{-8}$ and $\sigma k_c^2 = 0.5$ has been verified by repeating the complete experimental run for this data point.

The microwave and acoustic signals were observed to correlate with the dissipation. In figure 2.25 the dimensionless radar cross-section is plotted as a function of dissipation. It increases linearly as D varies from 0.10 to 0.25 and is independent of D for $\sigma k_c^2 > 0.15$, with the data falling between 0.25 and 0.30. The dimensionless mean square pressure is plotted as a function of D in figure 2.26, it increases linearly as D

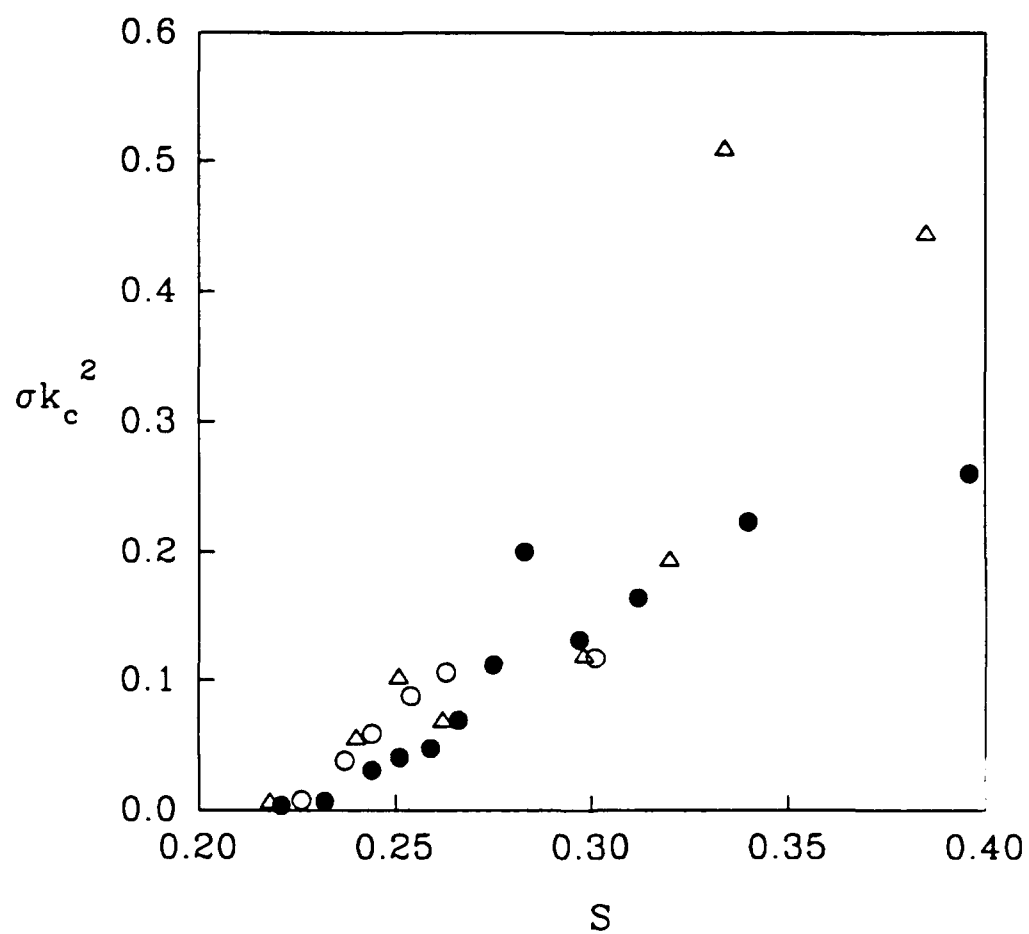


Figure 2.22 Dimensionless radar cross-section σk_c^2 as a function of the slope parameter S: \circ , P_1 ; \bullet , P_2 ; Δ , P_3 .

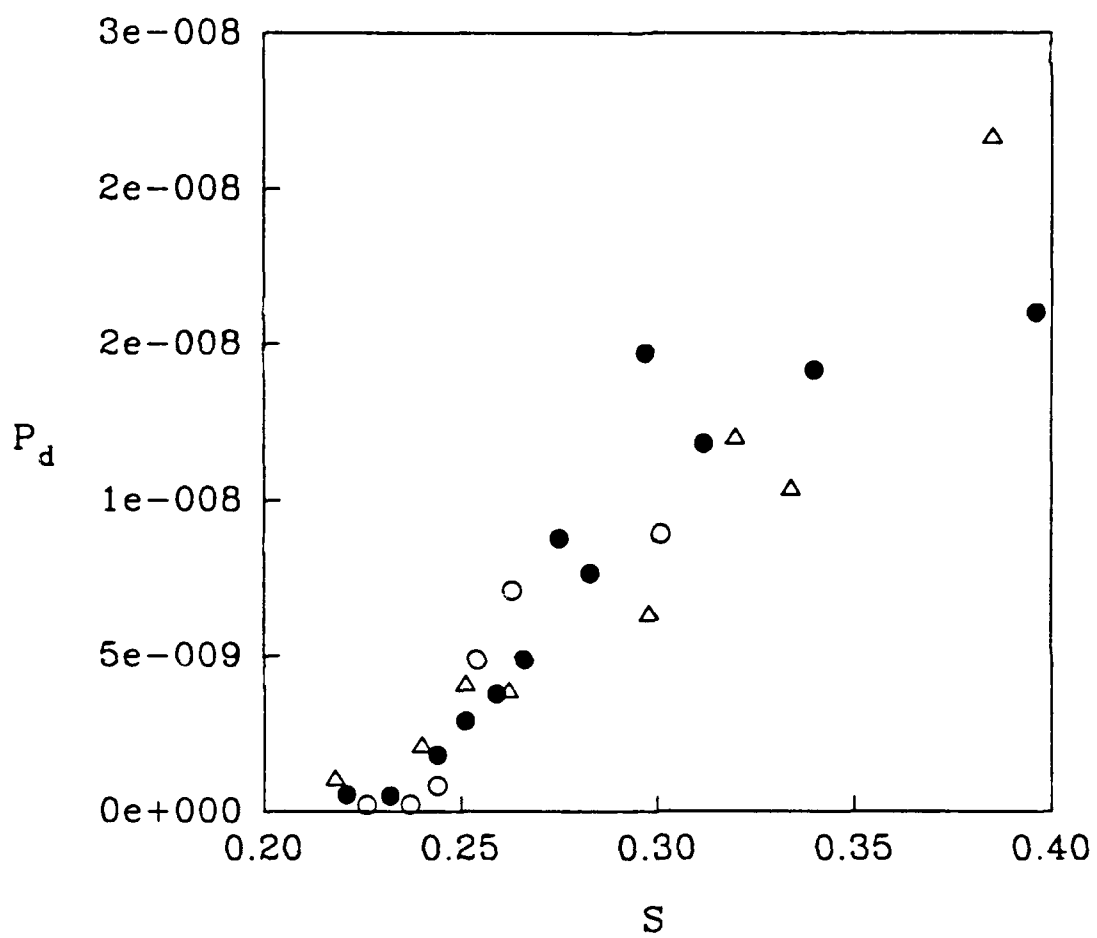


Figure 2.23 Dimensionless mean square acoustic pressure P_d as a function of the slope parameter, S : ○, P_1 ; ●, P_2 ; △, P_3 .

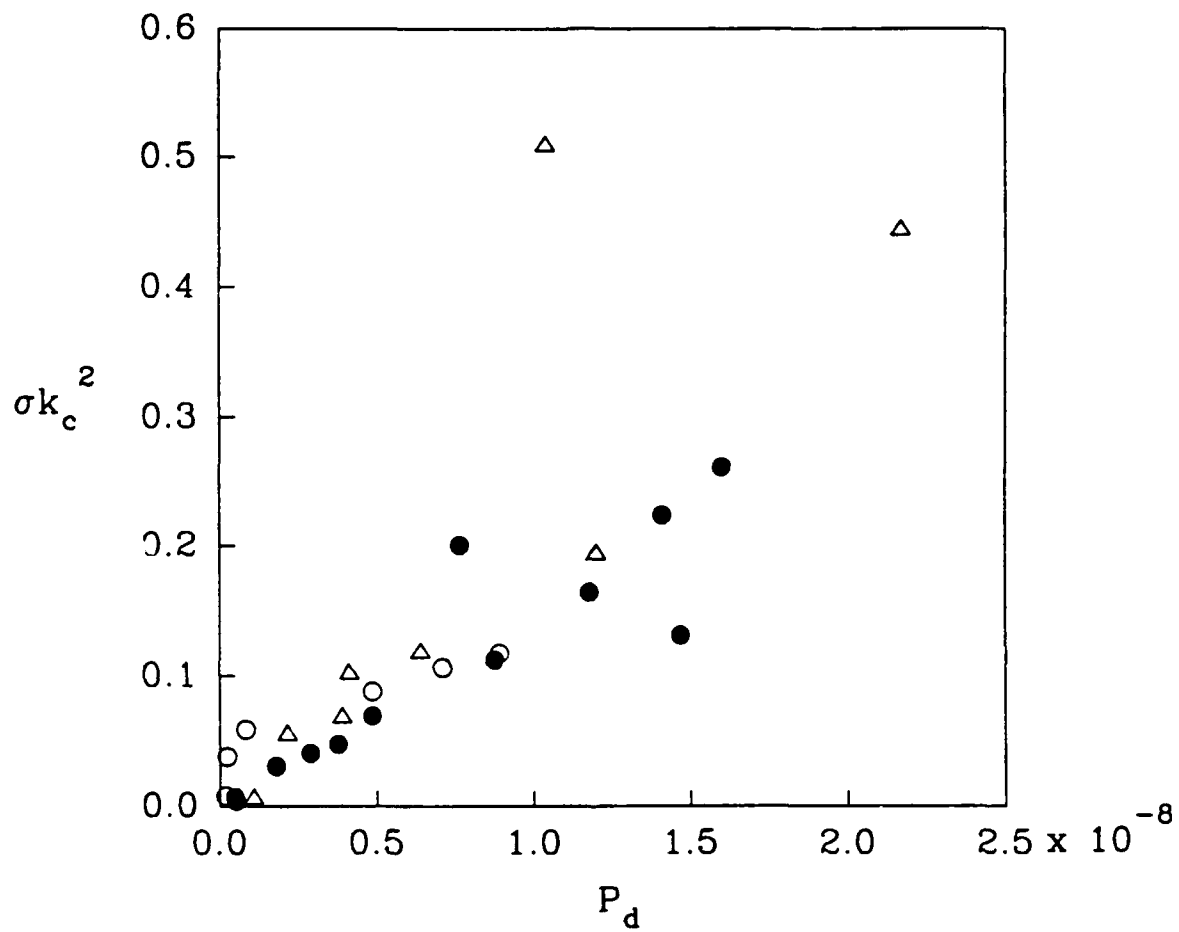


Figure 2.24 Correlation between the dimensionless radar cross-section σk_c^2 and the dimensionless mean square acoustic pressure P_d : \circ , P_1 ; \bullet , P_2 ; Δ , P_3 .

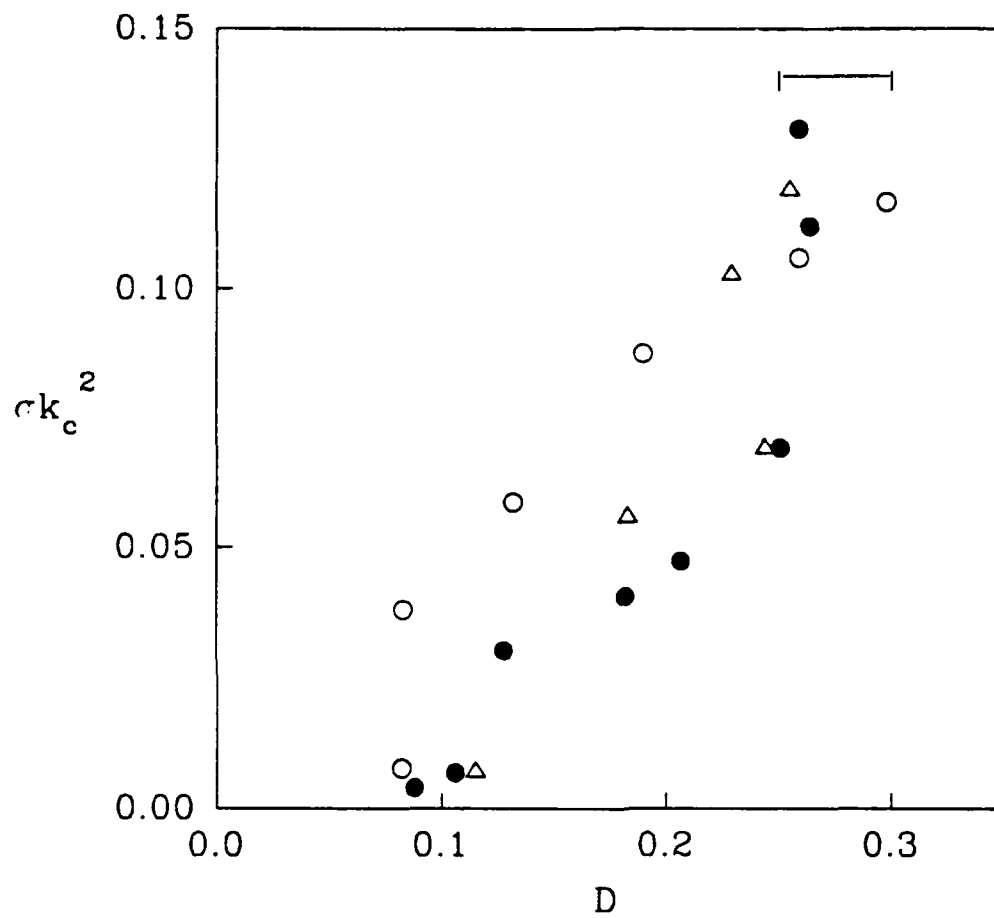


Figure 2.25 Correlation of the dimensionless radar cross-section σk_c^2 with the fractional dissipation D . For $\sigma k_c^2 > 0.15$ the data are independent of D and fall within the range marked |—|. \circ , P_1 ; \bullet , P_2 ; Δ , P_3 .

increases from 0.10 to 0.25 and it is independent of D for $P_d > 10^{-8}$, with the data falling between 0.25 and 0.30

The duration of the hydrophone signal was measured by visually determining the beginning and end of sound production from the acoustic time series. The measurements were converted to a dimensionless time scale, T_c , by multiplying by the radian frequency of the center component of the wave packet. The correlations of the mean square pressure and the radar cross-section with the duration are shown in figures 2.27 and 2.28. There is some scatter in the data but, with the exception of one or two outlying points, the dimensionless radar cross section and the dimensionless mean square pressure are approximately proportional to the dimensionless duration.

2.4 Discussion

The results presented above show that the backscattered microwave power and the radiated acoustic energy correlate with the wave slope and the energy dissipation due to breaking over a range of wave parameters. The correlation is strongest at wave slopes within the range commonly observed in ocean waves, $S < 0.30$. We also found that the backscattered microwave power and the radiated acoustic energy were correlated.

The observation that a large portion of the backscattered microwave power precedes the onset of sound production and visible breaking has several implications. One is that the backscatter from breaking is strongly influenced by the geometry of the wave prior to breaking. If, following Phillips (1988), we consider the backscatter as the overall contribution from the family of surface configurations present during breaking, we note that the configurations occurring just prior to breaking may be the dominant ones. Another implication is that the unsteadiness of the breaking process is important

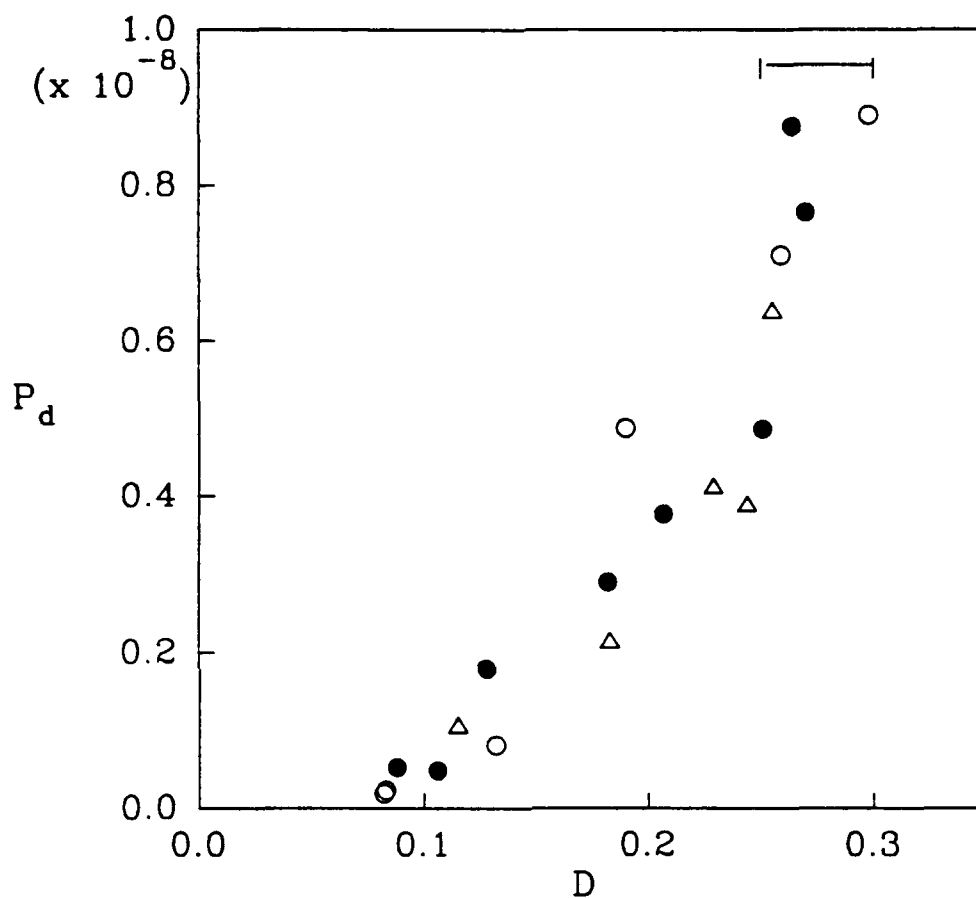


Figure 2.26 Correlation of the dimensionless mean square acoustic pressure P_d with the fractional dissipation D . For $P_d > 10^{-8}$ the data are independent of D and fall within the range marked |——|. \circ , P_1 ; \bullet , P_2 ; Δ , P_3 .

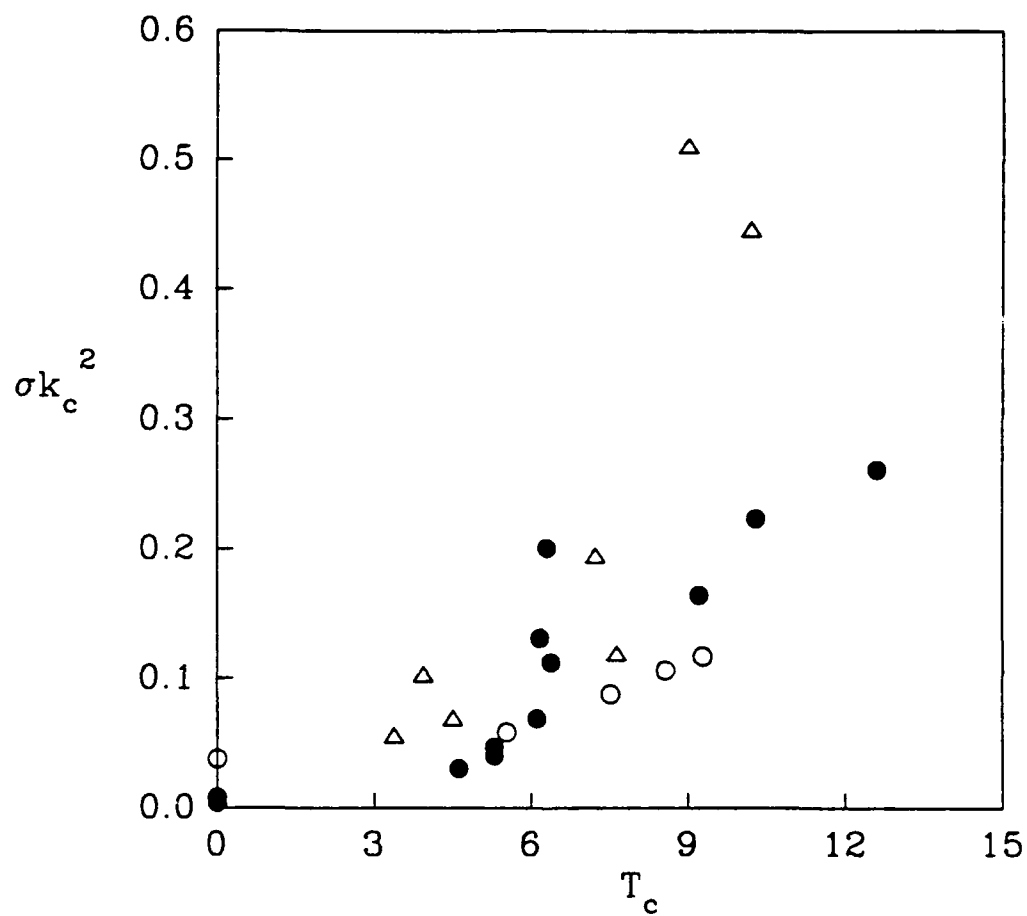


Figure 2.27 Correlation of the dimensionless radar cross-section σk_c^2 and the dimensionless hydrophone signal duration T_c . \circ , P_1 ; \bullet , P_2 ; Δ , P_3 .

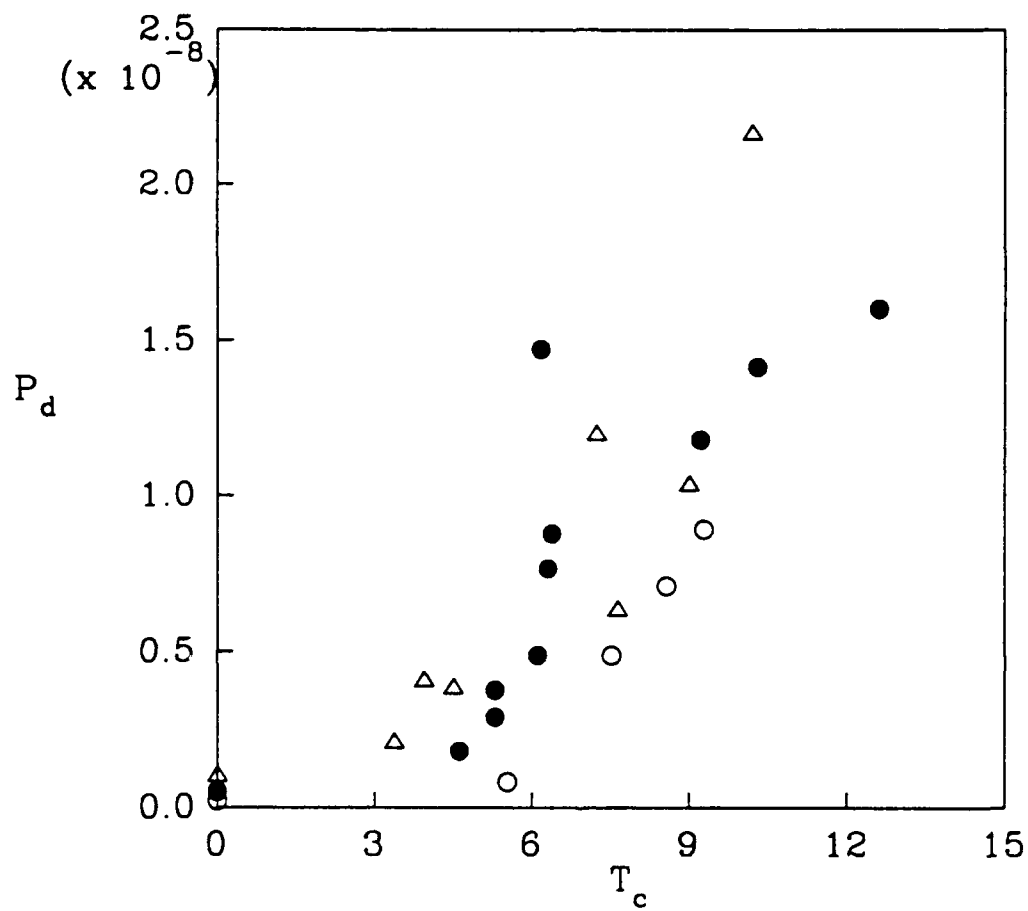


Figure 2.28 Correlation of the dimensionless mean square acoustic pressure P_d with the dimensionless hydrophone signal duration T_c . \circ , P_1 ; \bullet , P_2 ; Δ , P_3 .

and therefore the large cross-sections we measured prior to impact would not be observed in quasi-steady breaking (cf. Banner and Fooks, 1985).

During breaking we observed that the peak frequency of the Doppler spectrum increased and approached a value corresponding to a velocity within 10% of the phase speed of the center component of the wave packet. Field observations have shown that the speed of the scatterers during breaking approaches that of the phase speed of the dominant ocean waves and this is consistent with our results. (Keller, Plant and Valenzuela, 1981; Ewell, Tuley and Horne, 1984). Keller et al (1981) also reported that the bandwidth of the Doppler spectrum was drastically increased by breaking and that it could easily be increased by as much as a factor of two.

The bandwidth of the Doppler spectrum, B , is defined as the square root of the second central moment, and is given by,

$$B = \left[\int_0^{+\infty} (f - \bar{f})^2 G(f) df \right]^{1/2} \quad 2.27$$

where f is the frequency, \bar{f} is the centroid frequency and $G(f)$ is the magnitude of the radar Doppler spectrum. The bandwidth for the event with $S=0.254$, matching the spectra shown in figure 2.11, is plotted in figure 2.29. We see that the bandwidth is 10 Hz at locations where the backscattered power is negligible (7.5m, 8m and 11m) and is increased by a factor of 2.5 to 25 Hz at the locations of large backscattered power. These results are consistent with the field observations of Keller et al (1981).

Our results show that the backscattered microwave power and the radiated acoustic energy both increase as wave slope and wavelength are increased. This is consistent with Phillips' (1988) hypothesis that the radar return from longer waves should be more intense. It is also consistent with Farmer and Vagle's (1988) result, which

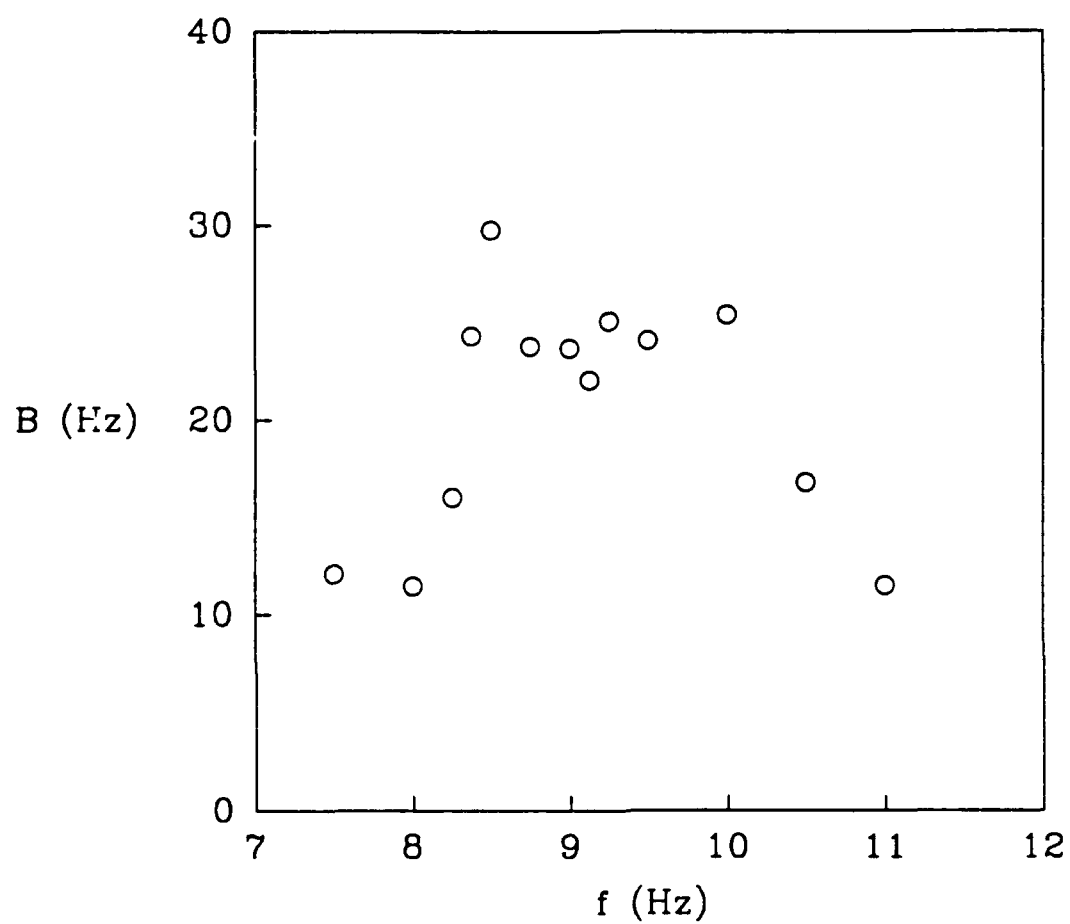


Figure 2.29 Variation of the bandwidth with x , the distance along the channel. \circ , P_1 , $S = 0.254$. Data correspond to the spectra in figure 2.11.

showed that the acoustic strength of individual breakers increased with wind speed. Jessup et al (1990) found that the average radar cross-section of an individual sea spike may be independent of the friction velocity of the wind, u_* . This result is difficult to compare to our laboratory measurements because the relationship between u_* and our wave slope parameter is complicated. The dominant wave slope in the field is a function of both u_* and the wave age defined by u_*/c , where c is the phase speed of the waves.

In Jessup et al (1990) the radar spot was approximately 2m in size and the typical dominant surface wavelength was 50m. It may be that the sea spikes they observe in the field are due to specular reflection as the local wave slope within the illumination area becomes sufficiently steep. If this is the case once the surface waves are sufficiently long and steep to create an area as large as the radar spot, the signal may saturate and further increases in wave slope or wavelength would not increase the power returned in an individual sea spike. In our laboratory experiments the radar spot size was approximately 1m and typical surface wavelengths were 1.5m. Therefore our results are not affected by saturation of the backscattered signal and we observe a strong dependence on both wave slope and wave length.

The experiments were conducted in fresh water and this raises the issue of how applicable our results are to remote sensing of the ocean. The major difference between fresh water and sea water breaking waves is that the bubbles generated in sea water persist longer (Medwin and Daniel, 1990). This has a minimal effect on the microwave signal because we observed that the geometry of the pre-breaking wave dominates and that the duration of the backscattered signal is of the order of the wave period. Medwin and Daniel (1990) have found that the sound radiated by small scale spilling breakers in fresh water and sea water is essentially the same. They state that the issue of bubble persistence is not important because the sound generated by breaking waves is from pulsating bubbles which radiate sound for only a few milliseconds after they are formed at the surface. We conclude that the differences between fresh and salt water breaking

waves are unimportant for these types of measurements and that the results presented here should apply to remote sensing of the ocean surface.

The acoustic energy radiated by a breaking wave can be estimated using the following equation,

$$E_s = \frac{\overline{p^2}}{\rho c} A m T_p \quad 2.28$$

where T_p is the sampling interval and m is a factor used to account for the modal structure in the wave channel. We kept the sampling hydrophone at the center of the channel cross-section for our experiments, so we had a point measurement of the acoustic pressure at each x location. The modal factor m was used to compensate for the fact that the mean square pressure may not be constant across the channel. To obtain m , experiments were carried out in which the hydrophone was moved vertically and transversely, and the variation of $\overline{p^2}$ was measured. The variation of $\overline{p^2}$ in the transverse and vertical directions are shown in figures 2.30a and 2.30b for packet P_1 with $S = 0.263$. The modal factor is given by,

$$m = \frac{\left(\begin{array}{c} \alpha/2 \\ \frac{1}{\alpha} \int \overline{p^2} ds \\ -\alpha/2 \end{array} \right)}{\left(\overline{p^2} (s=0) \right)} \quad 2.29$$

where s equals either y or z and α equals either the depth or the width of the channel depending on whether the vertical or transverse variation is of interest. The average value of m for both the vertical and transverse directions was found to be, $m = 0.84$. This value was then assumed to be constant for other values of the experimental parameters. This is a reasonable assumption because the hydrophone was located 7m

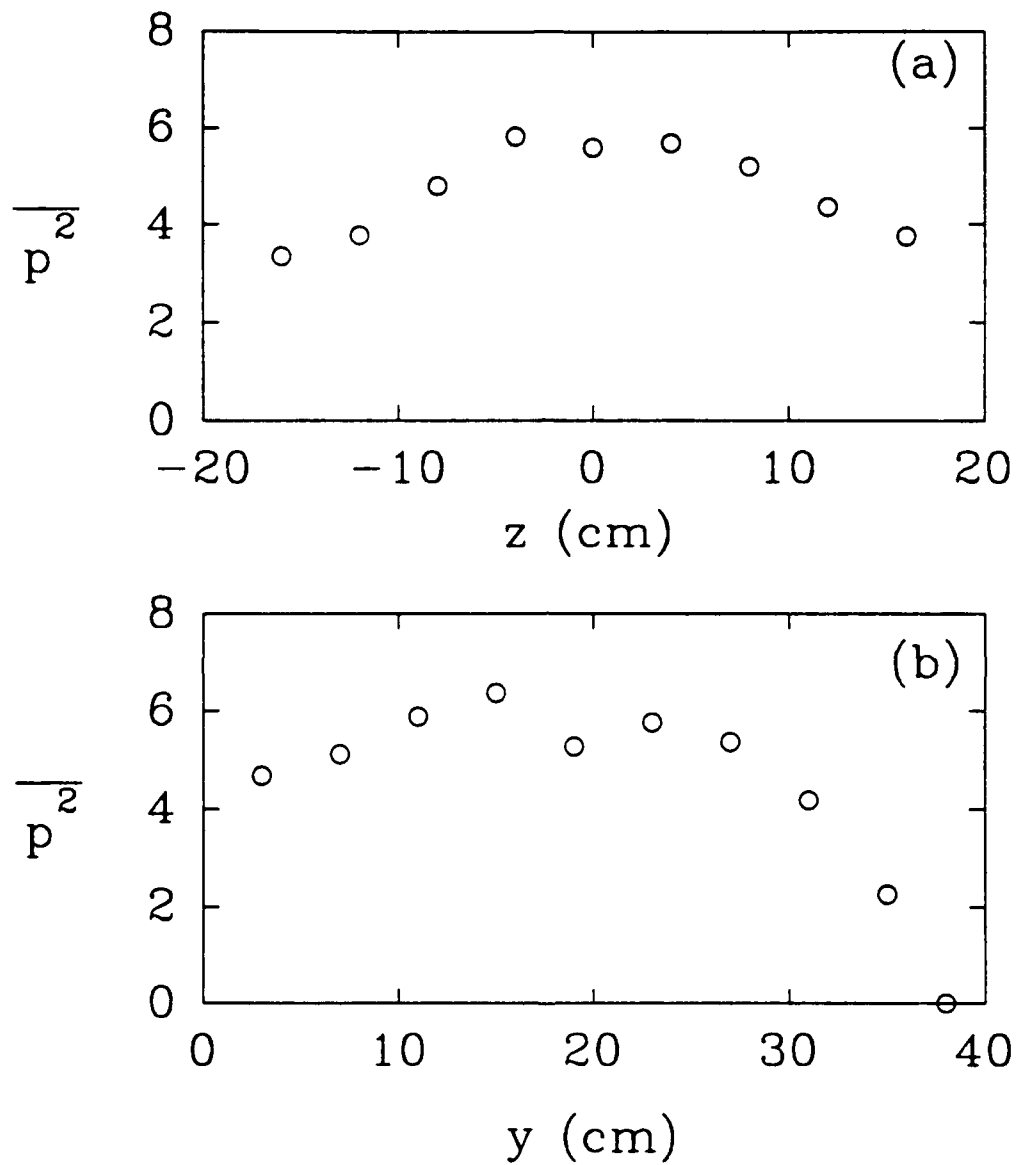


Figure 2.30 (a) Variation of $\overline{p^2}$ in the wave channel with the transverse coordinate, z .
 (b) Variation of $\overline{p^2}$ in the wave channel with the vertical coordinate, y .

downstream of the breaking event, in the acoustic farfield ($kr \gg 1$) where the properties of the waveguide would tend to dominate time averaged quantities such as $\overline{p^2}$. As a result, the functional form of the variation of $\overline{p^2}$ across the channel would not vary as the wave slope was changed, giving a constant value for m .

In order to estimate the total acoustic energy radiated, a measure of the amount of acoustic energy radiated upstream of the event was also required. Figure 2.31 shows the mean square acoustic pressure upstream and downstream of one event for packet P_2 with $S=0.263$. This plot shows that the same amount of energy was radiated upstream as downstream. Therefore the value of E_a calculated from equation 2.28 was multiplied by a factor of two to obtain an estimate of the total acoustic energy radiated away from the breaking region.

The wave energy dissipated is approximated by,

$$E_L = \frac{1}{2} \rho g C_g b T_w \overline{\eta_d^2} \quad 2.30$$

where T_w is the sampling interval, C_g is the group velocity of the center component, b is the channel width and $\overline{\eta_d^2}$ is the surface displacement variance dissipated due to breaking (cf. equation 2.15). Figure 2.32 shows the estimated total acoustic energy radiated scaled by $(k_c h)^{-2}$ versus the energy dissipated by the breaking wave. The correlation produced by this scaling suggests that shorter breaking waves radiate more acoustic energy per unit of mechanical wave energy dissipated. The fraction of dissipated wave energy which is radiated as sound is of order 10^{-8} .

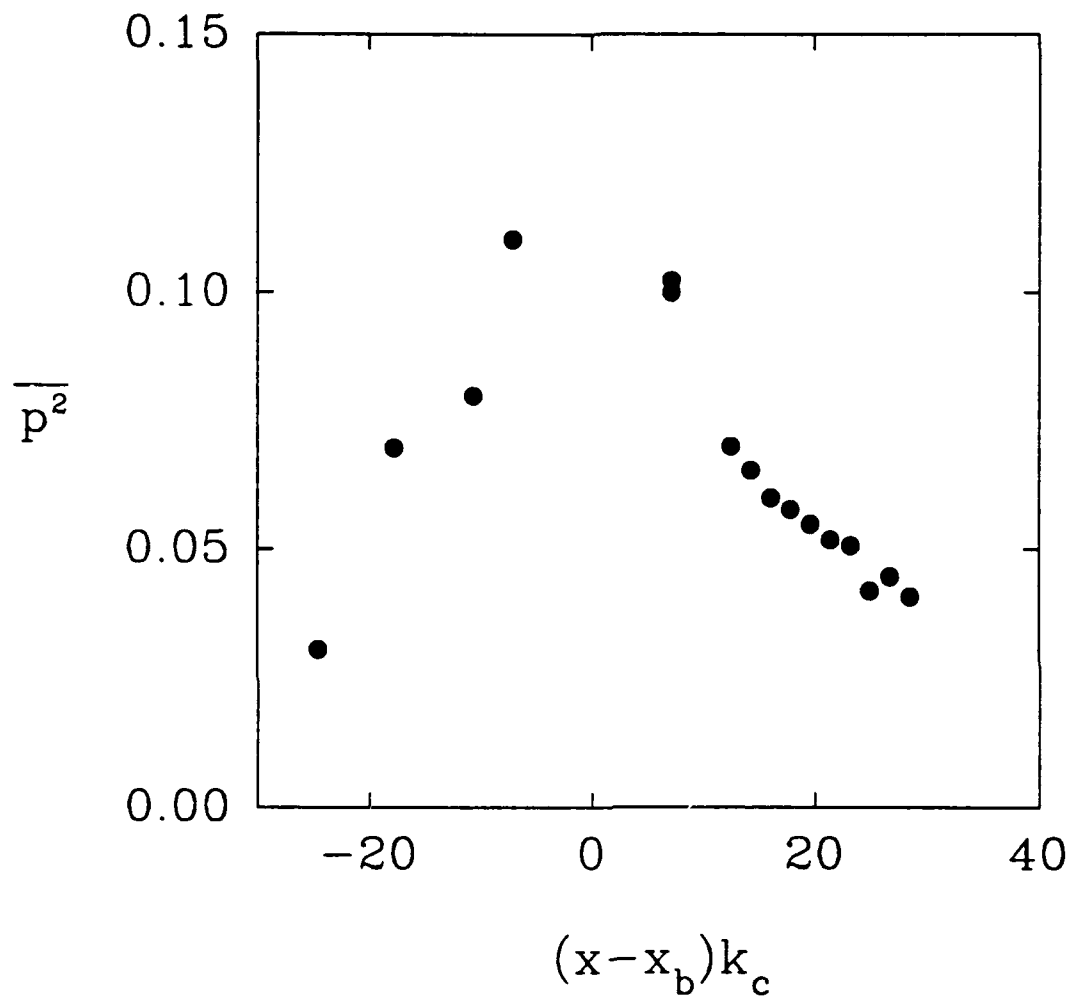


Figure 2.31 The mean square acoustic pressure, $\overline{p^2}$ measured upstream and downstream of the breaking location. Theoretical breaking location is at $(x - x_b)/k_c = 0$.

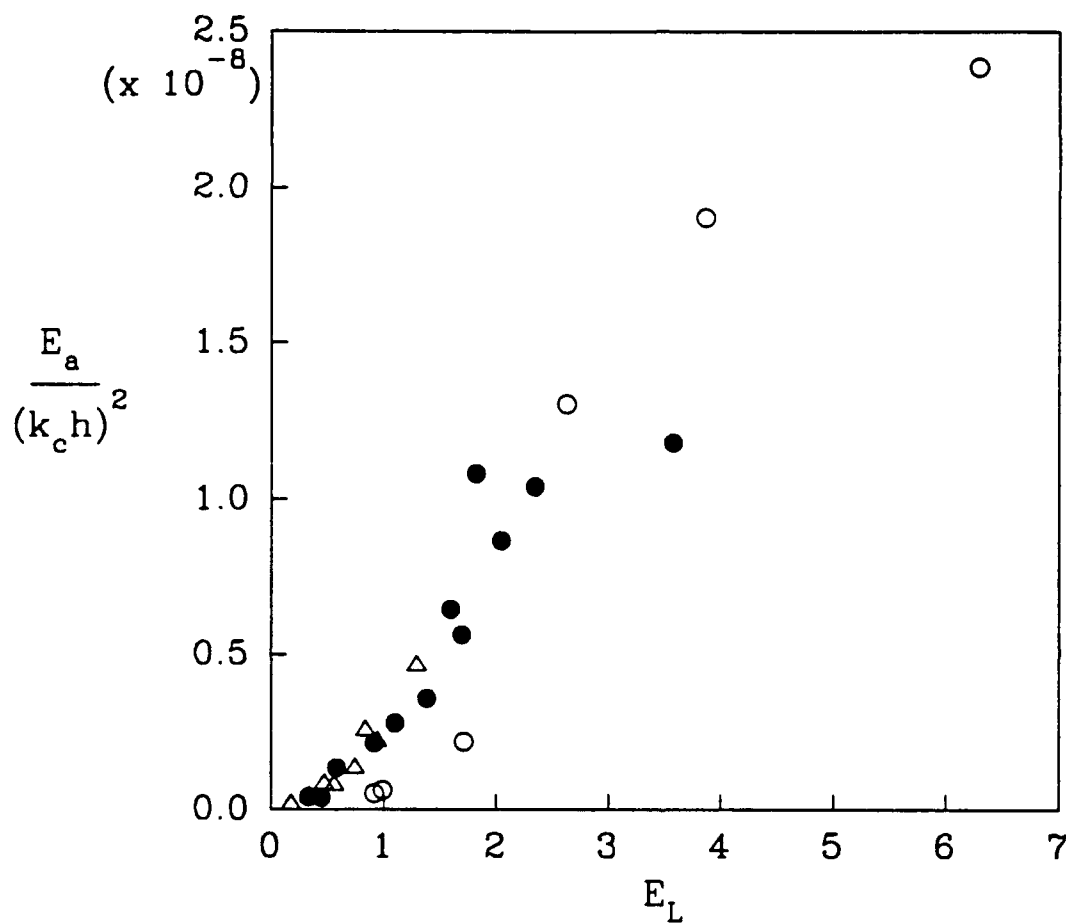


Figure 2.32 Correlation between the estimated radiated acoustic energy E_a scaled by $(k_c h)^{-2}$ and the energy dissipated by the breaking wave E_L . \circ , P_1 ; \bullet , P_2 ; Δ , P_3 .

Chapter 3: Measurements of the Sound Generated by Two and Three-Dimensional Breaking Waves

This chapter reports on two series of laboratory experiments in which the sound generated by breaking waves was measured. The first series of experiments measured the sound generated by two-dimensional breaking waves in a wave channel equipped with a single paddle wavemaker located in the R.M. Parsons Laboratory at the Massachusetts Institute of Technology. The second series of experiments measured the sound generated by three-dimensional breaking waves in the forty eight paddle wave channel at the Offshore Technology Research Center (OTRC) at Texas A&M University.

The two-dimensional breaking experiments were conducted primarily to investigate the low frequency sound generated by breaking waves. In an earlier set of experiments described in chapter 2, it was necessary to high pass filter the hydrophone signal at 500 Hz to remove the noise from the wavemaker hydraulic system. In these experiments the hydrophone was mounted downstream of the breaking locations and therefore sound at frequencies below the cut-off frequency at 2200 Hz were severely attenuated. Therefore the correlations obtained from that data set were for frequencies > 2200 Hz.

In the two-dimensional breaking experiments described in this chapter the problem of noise from the wavemaker hydraulic system was eliminated by shutting off the system prior to sampling the acoustic signals. Several relays were installed on the on/off switch of the hydraulic system which allowed the system to be shutoff under computer control. The wave generation computer was programmed to send a digital pulse which caused the relays to trip, shutting off the hydraulic system 1.5 s prior to the start of data sampling. To avoid cutting off the lower frequency signals the hydrophones were placed directly under the breaking events. Therefore measurements of the low

frequency sound uncontaminated by noise from the wavemaker hydraulic system and unattenuated by propagation through the waveguide were possible.

The three-dimensional breaking experiments at OTRC were conducted for two reasons. First, to investigate if three-dimensional effects are important by comparing the results of the three-dimensional experiments to those of the two-dimensional experiments. Second, to measure the sound generated by breaking waves of considerably large scale. Extrapolating laboratory measurements to make quantitative predictions about the dynamics of large scale ocean surface waves is difficult. At OTRC it is possible to generate breaking waves with wavelengths approximately three times larger than the breaking waves generated at MIT. This is a significant increase in scale and should permit the results to be interpreted with more confidence regarding their applicability to ocean surface wave scales.

3.1 Experimental Procedure: Two-Dimensional breaking

The two-dimensional experiments were conducted in a steel-framed glass-walled wave channel 25 m long, 0.76 m wide filled with 0.6 m of fresh water. A schematic of the experimental equipment and the wave channel is shown in figure 3.1 . The channel is equipped with a single computer-controlled piston wave generator and the breaking waves were generated using the same technique as outlined in section 2.1.1 . An IBM XT computer equipped with a Metrabyte DAS 20 multifunction board was used to control the wavemaker system. The interval between breaking events was 5 to 6 minutes to allow the surface oscillations to decay to negligible amplitudes. The waves were absorbed at the far end of the channel by a wooden beach of slope 1:10 covered by a 50 mm thick layer of "hogs hair" (Wollastic Fibre material supplied by F.P. Woll & Company 5216 E. Comly St., Philadelphia, Pa.) The amplitude and phase of the transfer function, shown in figure 3.2, were measured using a procedure similar to the one

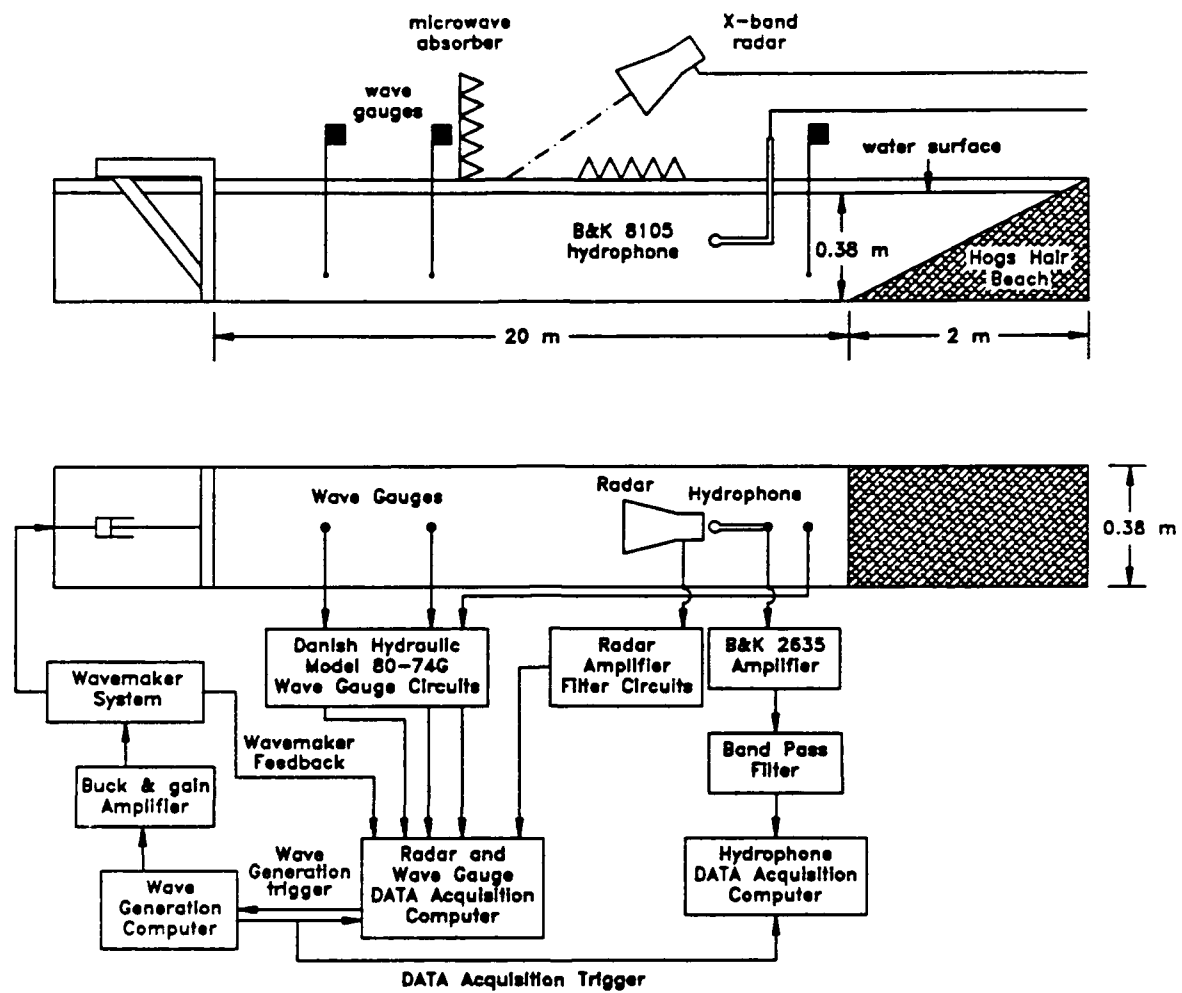


Figure 3.1 Schematic drawing of an elevation view (top) and plan view (bottom) of the 25 m \times 0.76 m \times 0.60 m wave channel at MIT. The configuration of the experimental equipment is also illustrated.

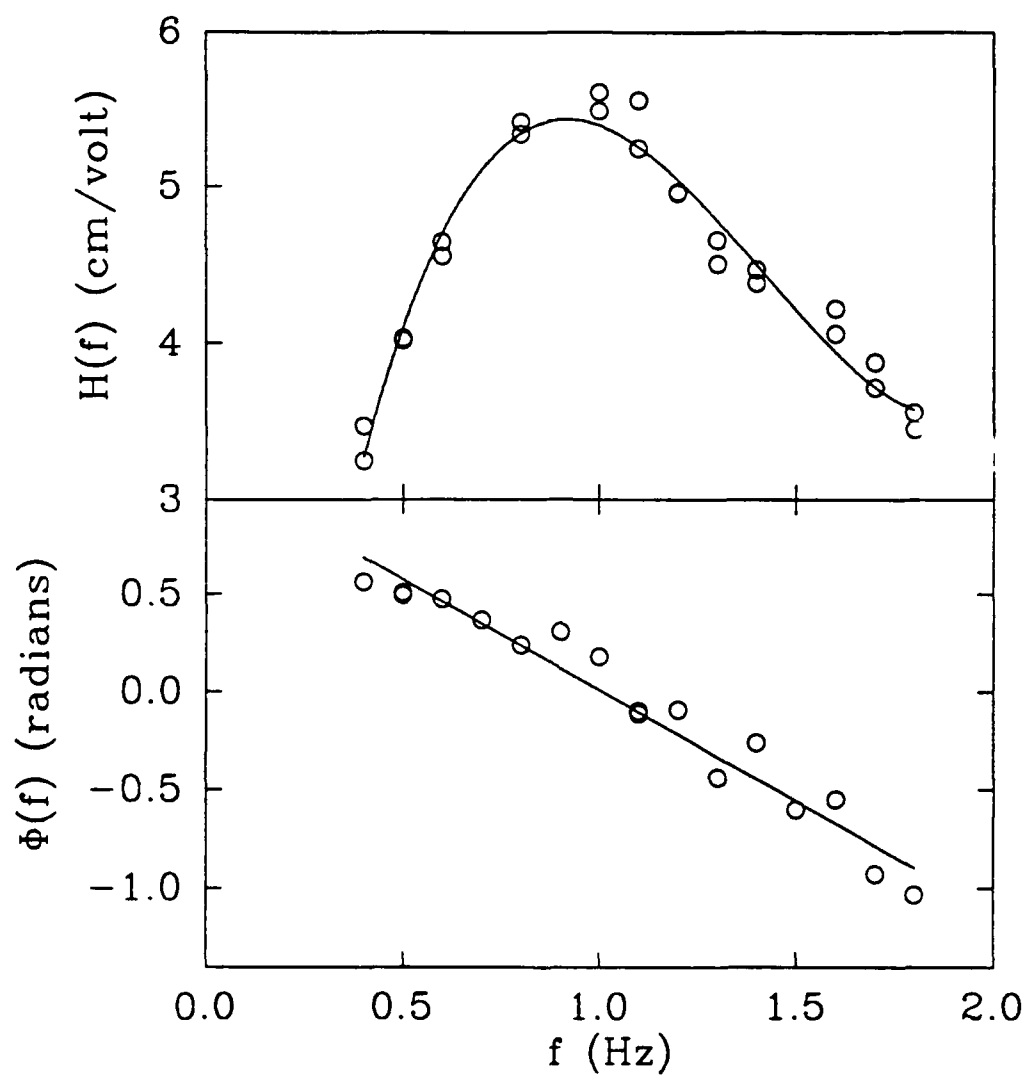


Figure 3.2 The upper plot is the amplitude transfer function $H(f)$ (cm/volt) for the 25 m \times 0.76 m \times 0.60 m wave channel as a function of frequency, f (Hz). The lower plot is the phase transfer function $\Phi(f)$ (radians) as a function of frequency, f (Hz) (E. Lamarre, 1991).

described in section 2.1.1 . The amplitude and phase of the wave packets were adjusted to compensate for the influence of the transfer function. In these experiments , $\Delta f/f_c$ and $x_b k_c$ were held constant at 1.0 and 24.6 respectively and the slope, S (S is defined in equation 2.8) was varied. Table 3.1 lists the characteristics of the three wave packets used in these experiments.

Wave Packet	W_1	W_2	W_3
Center frequency, f_c (Hz)	0.78	0.88	0.98
Theoretical break point, x_b (m)	9.25	7.58	6.25
Center component wavenumber, k_c	2.66	3.25	3.93
Center component phase speed, c_c (m/s)	1.84	1.70	1.57

Table 3.1 Wave packet characteristics; $\Delta f/f_c = 1.0$ and $x_b k_c = 24.6$ for all wave packets.

3.1.1 Surface Displacement Measurements

The surface displacement was measured in an earlier series of experiments in which void fraction measurements were made for the identical wave packets (Lamarre and Melville, 1991). The surface displacement measurements were made with the same resistance wire wave gauges and electronics as those described in 2.1.2 . The calibration procedure and measurement technique were identical to those described in 2.1.2 .

3.1.2 Sound Measurements

The underwater sound measurements were made with a set of omnidirectional International Transducer Corporation model ITC 1089E spherical hydrophones. A typical frequency response calibration plot for the ITC 1089E is shown in figure 3.3 .

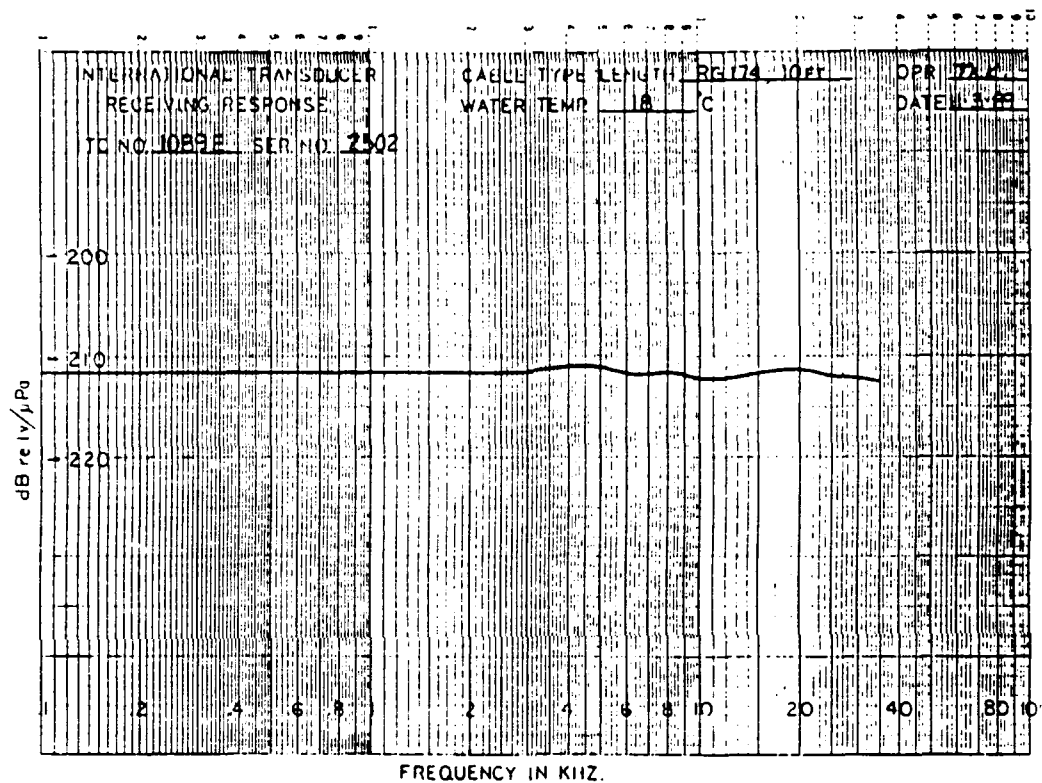


Figure 3.3 A plot of the typical frequency response of an ITC 1089E hydrophone.

Transfer Characteristics

Voltage Gain	
Fixed steps, dB	-10, 0, 10, 20, 30, 40, 50, 60
Continuously variable, dB	0 to -10
Gain Accuracy	
Fixed step, +/-dB	0.2
Frequency Response, -1 dB	
Gain, -10 dB to +30 dB	1 Hz to 80 kHz
Gain, +40, +50 dB	1 Hz to 60 kHz
Gain, +60 dB	1 Hz to 40 kHz
Amplitude Linearity, %FS	< 1.0
Harmonic Distortion, %	< 1.0
Input Impedance, Nominal	
Resistive, megohms	1000
Capacitive, pF	35, max
Input voltage, Max., volts rms	5, divided by gain for all settings
Filtering, Internal	See Section 6.0

Output Characteristics

Output Impedance, Nominal Ohms	50
Load Impedance, Minimum	
Resistive, ohms	10,000
Capacitive, pF	1000 max
Output current, Max., mA rms	3
Output Noise, 1 Hz to 50 kHz	
Referred to input, battery operated at gains of +30 to +60 dB	
200 pF source	5 uV, max.
1000 pF source	3 uV, max.

Table 3.2 The frequency response and output characteristics of the Wilcoxon model AM-5 amplifiers.

The response is flat to within ± 1 dB from 100 Hz to 35 kHz. The manufacturer did not calibrate these particular units at frequencies < 100 Hz but they had done so for other units and found that the response was typically flat down to approximately 10 Hz. The signals were amplified with Wilcoxon model AM-5 amplifiers set at 60 dB gain. The specifications and frequency response of the AM-5 amplifiers are listed in table 3.2. The acoustic signals were sampled digitally at 20 kHz using an HP RS/25C personal computer and an R.C. Electronics ISC-16 digital to analog board with 8 channels of simultaneous sample and hold (SSH) capability. The start of sampling was triggered under software control by switching one of the digital ports of the DAS-20 board installed in the wave maker control computer from low to high and connecting this signal to the trigger port of the ISC-16 board. The signals were bandpass filtered from 20 Hz to 10 kHz with Frequency Devices model 874P8B-3 digitally programmable highpass filters and model 844P8B-5 low pass filters. The specifications for the highpass and low pass filters are listed in table 3.3.

Filter	Specifications
844P8B-5	<p>Low pass filter 4 pole Butterworth Digitally programmable from 200 Hz 51.2 kHz in 200 Hz steps. Frequency response amplitude decreases at 24 dB per octave outside the pass band. Pass band ripple ± 0.05 dB.</p>
874P8B-3	<p>Highpass filter 4 pole Butterworth Digitally programmable from 10 Hz 2560 Hz in 10 Hz steps. Frequency response amplitude decreases at 24 dB per octave outside the pass band. Pass band ripple ± 0.5 dB.</p>

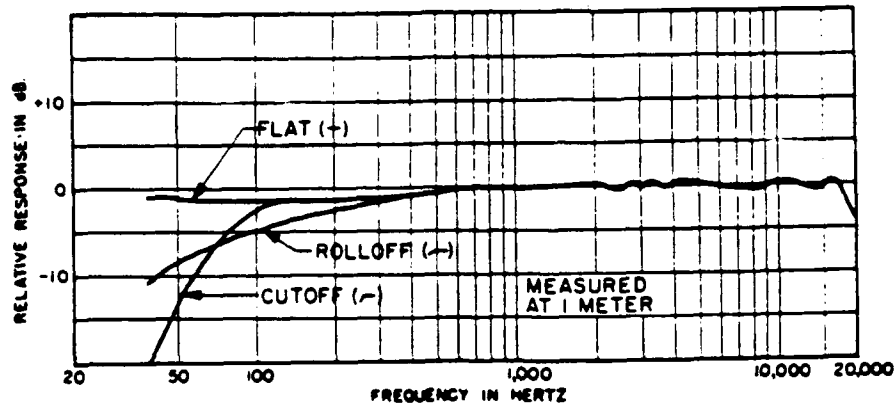
Table 3.3 Specifications of 844P8B-5 low pass and the 874P8B-3 highpass filters

The hydrophones were located in the center of the channel at a depth of 37 cm from the free surface. They were mounted on a submerged frame made of 1/2 inch stainless steel rods which had rubber stoppers installed on the ends of the rods. The frame was then wedged tightly in place against the glass walls of the channel. This allowed the hydrophones to be placed directly beneath the breaking events without introducing large signals due to frame vibrations.

Measurements of the sound in air were made using a Shure SM81 cardioid condenser microphone. The microphone's frequency response is flat (± 1 dB typically) from 20 Hz to 20 kHz. The frequency response and the directional characteristics of the SM81 are shown in figure 3.4. The microphone signal was amplified by 40 dB with a Symetrix SX202 dual microphone preamplifier which also supplied power to the microphone. The frequency response of the SX202 is ± 0.5 dB from 20 Hz to 20 kHz. The complete specifications for the SX202 can be found in table 3.4. The microphone was mounted vertically pointing downwards 50 cm above the still water surface directly above the most energetic part of the breaking event. The signal was bandpass filtered from 20 Hz to 10 kHz using the same Frequency Devices filters as those used to filter the hydrophone signals. The signal was then sampled at 20 kHz using the HP RS/25C and the ISC-16 A/D board.

3.1.3 Video Measurements

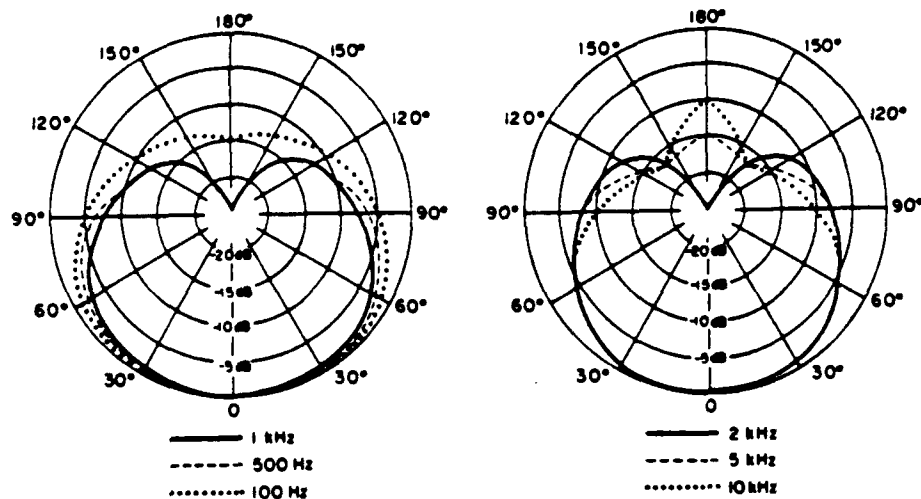
Video recordings were made of all of the experimental runs. The location of the video camera and a schematic of the recording equipment is shown in figure 3.1. The video camera was a black and white NEC model TI-23A 1/2 inch format CCD camera with a 1/1000 second shutter speed. The video recorder was a Panasonic model AG-6300 VHS video cassette recorder. A DATUM model 9300 IRIG-B time code generator/translator was used to insert a time base accurate to within ± 1 milliseconds



TYPICAL FREQUENCY RESPONSE

Polar Pattern

Cardioid (unidirectional) response — uniform with frequency, symmetrical about axis (see Figure 2)



TYPICAL POLAR PATTERNS

Figure 3.4 The upper plot is a typical frequency response of a Shure SM81 microphone. The curve labelled flat corresponds to the setting used in these experiments. The lower plots are typical polar plots of the directional characteristics of a SM81 microphone at various frequencies.

Inputs	
Type	low-Z balanced, transformerless
Input impedance	> 3k ohms
Maximum input level.....	+ 14dBV (with pad)
Connector	XLR-3
<hr/>	
Clip Indicators	red LED's, fire 4dB below clipping
<hr/>	
Frequency Response	20Hz to 20kHz, +0dB, -1dB
<hr/>	
THD007% (1kHz, 0dBm, 600Ω) .01% (1kHz, +24dBm, 600Ω)
<hr/>	
Signal to Noise Ratio	95dB (-50dBV, 150Ω)
<hr/>	
EIN	-128dBm (150Ω)
<hr/>	
Max. Gain	60dB
<hr/>	
Min. Gain	20dB
<hr/>	
Outputs	
Type	low-Z
Output impedance	50Ω balanced 100Ω unbalanced
Max.out (600Ω)	+ 24dBm balanced + 18dBm unbalanced
Connectors	1/4" TRS balanced 1/4" TS unbalanced

Table 3.4 The specifications of the Symetrix model SX202 microphone pre-amplifier.

onto the video image. The wavemaker control computer triggered the time code generator to start when the first digital wave packet data point was sent to the wavemaker control system. The VCR was turned on and off remotely by the wavemaker control computer.

3.2 Two-Dimensional Breaking: Results

3.2.1 Wave Dissipation

The fractional dissipation (eq. 2.15) was obtained by measuring the surface displacement variance (eq. 2.14) upstream and downstream of the breaking event. In figure 3.5 the fractional dissipation is plotted as a function of the wave packet slope, S . The data for the three wave packets do not collapse onto a single curve like the data for the constant slope wave packets used in the experiments of chapter 2 (see figure 2.9). Rapp and Melville (1990) showed that for deep water breaking the dissipation depended primarily on the wave slope, S and was not a function of $k_c h$, if $\Delta f/f_c$ and $x_b k_c$ were held constant. In their experiments using constant amplitude wave packets $\tanh(k_c h) = 0.96, 0.99, 1.00$. For constant slope wave packets the energy is concentrated at the lower frequencies, as is evident in figure 3.6 which shows the frequency spectrum of wave packet W_1 . For the three wave packets W_1, W_2 and W_3 the centroid frequencies are 0.58, 0.65 and 0.71 Hz respectively. If we use the centroid frequency to characterize the constant slope wave packets then the $\tanh(k_{cd} h) = 0.78, 0.84, 0.88$ for the three packets, where k_{cd} is the wavenumber of the centroid frequency component. Clearly, $\tanh(k_{cd} h)$ is not constant and it is not close to 1.0, and therefore the dissipation may depend on the parameter $k_{cd} h$. The dissipation data plotted in figure 3.5 show that at the same slope the longer or lower frequency wave packets dissipate proportionately more energy. This may be because the longer waves are feeling the effects of the finite depth to a greater

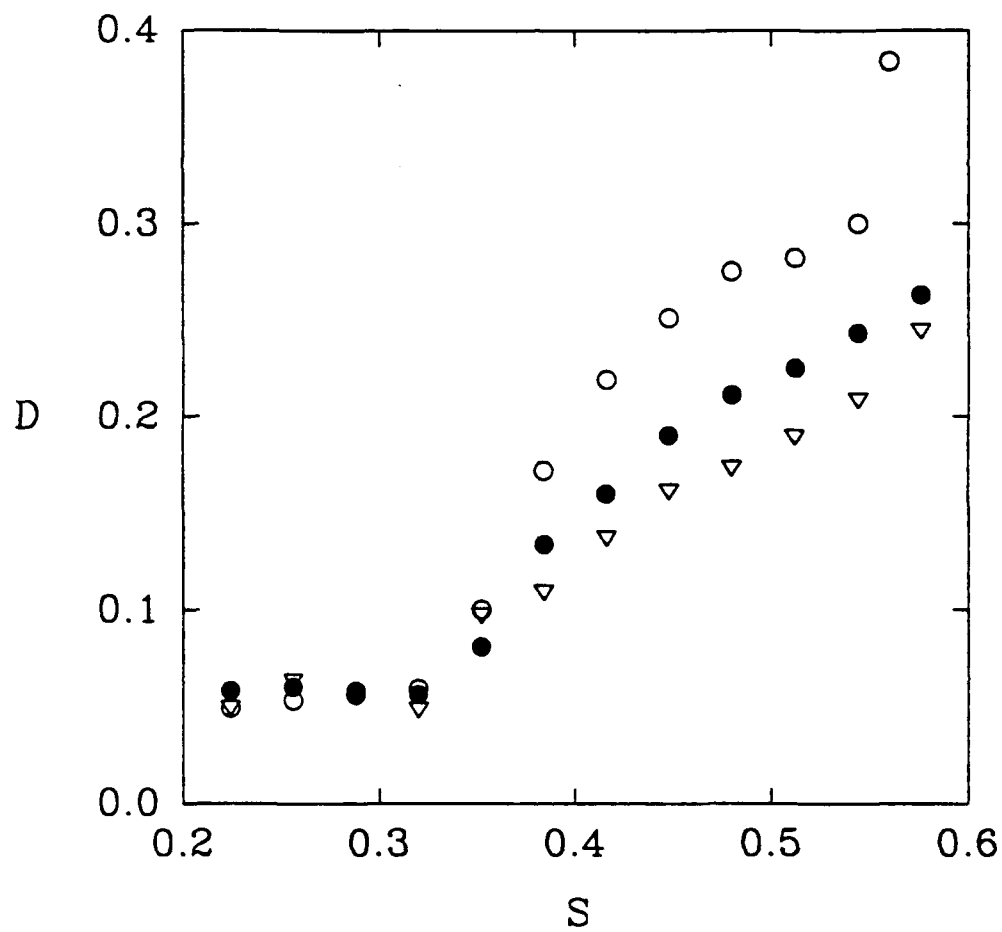


Figure 3.5 The fractional dissipation D as a function of the wave slope parameter, S .
 \circ , W_1 ; \bullet , W_2 ; ∇ , W_3 .

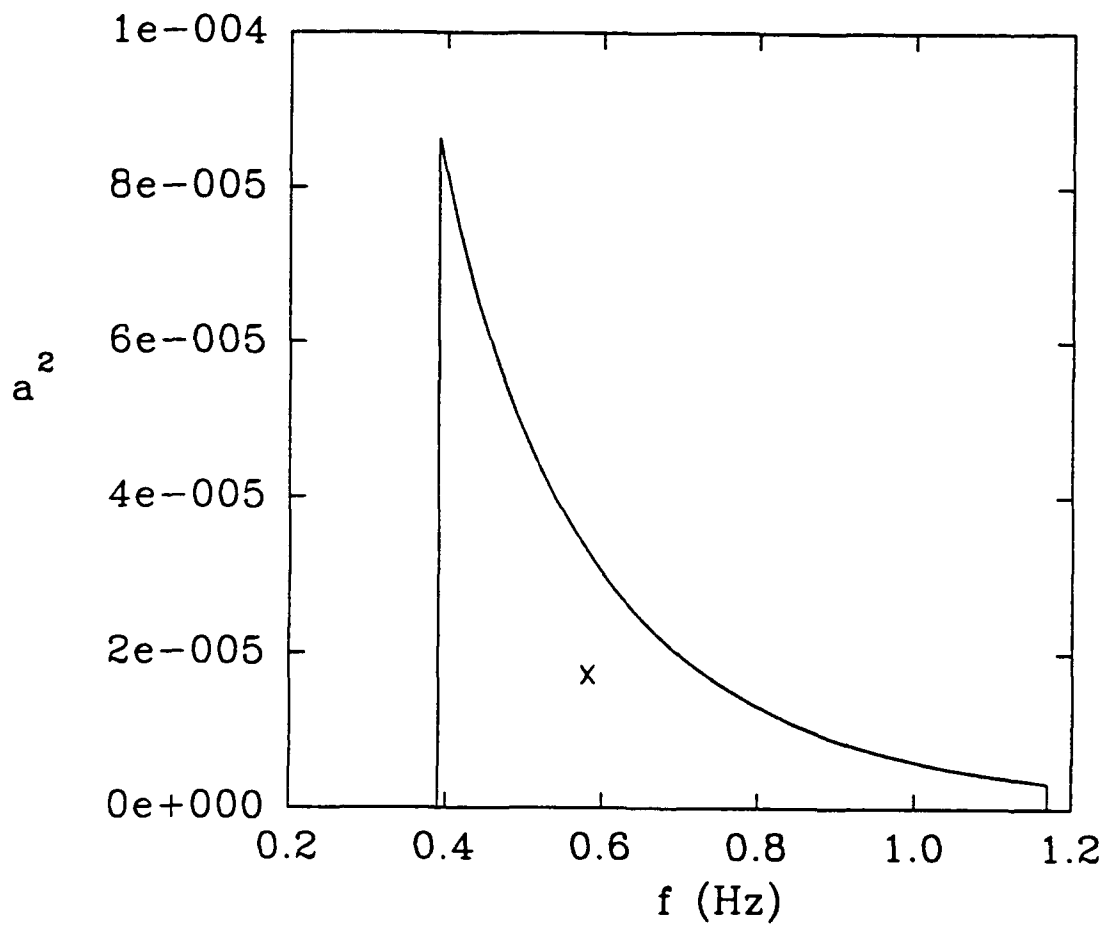


Figure 3.6 The frequency spectrum of wave packet W_1 . The units of the spectral density are arbitrary. \times marks the location of the centroid of the spectrum.

degree and scaling by $k_{cd}h$ should account for this effect. In figure 3.7 the fractional dissipation scaled by $k_{cd}h$ is shown plotted versus the slope and the data collapse reasonably well onto a single curve.

3.2.2 Sound

The glass wave channel acts as a waveguide for underwater sound propagation. If the glass walls and bottom are assumed to be rigid and the water surface a pressure release surface the mode shapes are defined as in equations 2.17 and 2.18. The mode cut-off frequencies are given by equation 2.19 and are tabulated in table 3.5 .

The hydrophones were placed directly beneath the breaking events to avoid cutting off the lower frequency signals. The microphone was placed directly above the breaking events 50 cm above the still water surface to maximize the signal to noise ratio. A typical hydrophone and microphone time series and the matching spectrographs, for packet W_2 with $S = 0.544$, are shown plotted in figures 3.8 and 3.9 . The envelope of the hydrophone time series contains two maxima, one at $t = 0.47$ s and a second at $t = 0.75$ s. Evidence of this structure is seen in the hydrophone spectrograph where spectral levels increase rapidly at $t = 0.47$ s corresponding to the first envelope maximum. The second envelope maximum is seen in the spectrograph where levels rise from a minimum at $t = 0.6$ s to a maximum at $t = 0.75$ s and then decay with time back to the background level. The envelope of the microphone time series has four maxima and the microphone spectrograph contains four bands of higher spectral levels at times matching the envelope maxima.

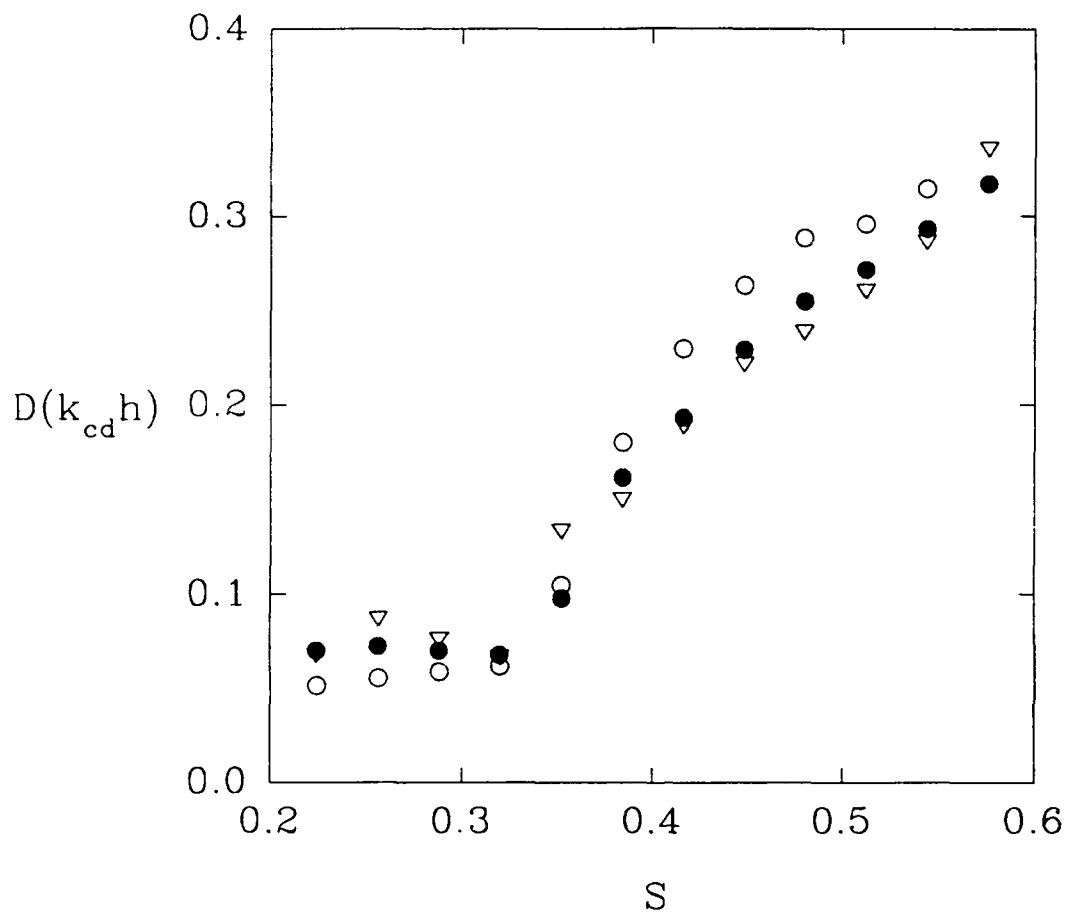


Figure 3.7 The fractional dissipation D scaled by k_{cd} the wavenumber of the centroidal component and the water depth, h as a function of the slope parameter, S .
 \circ , W_1 ; \bullet , W_2 ; ∇ , W_3 .

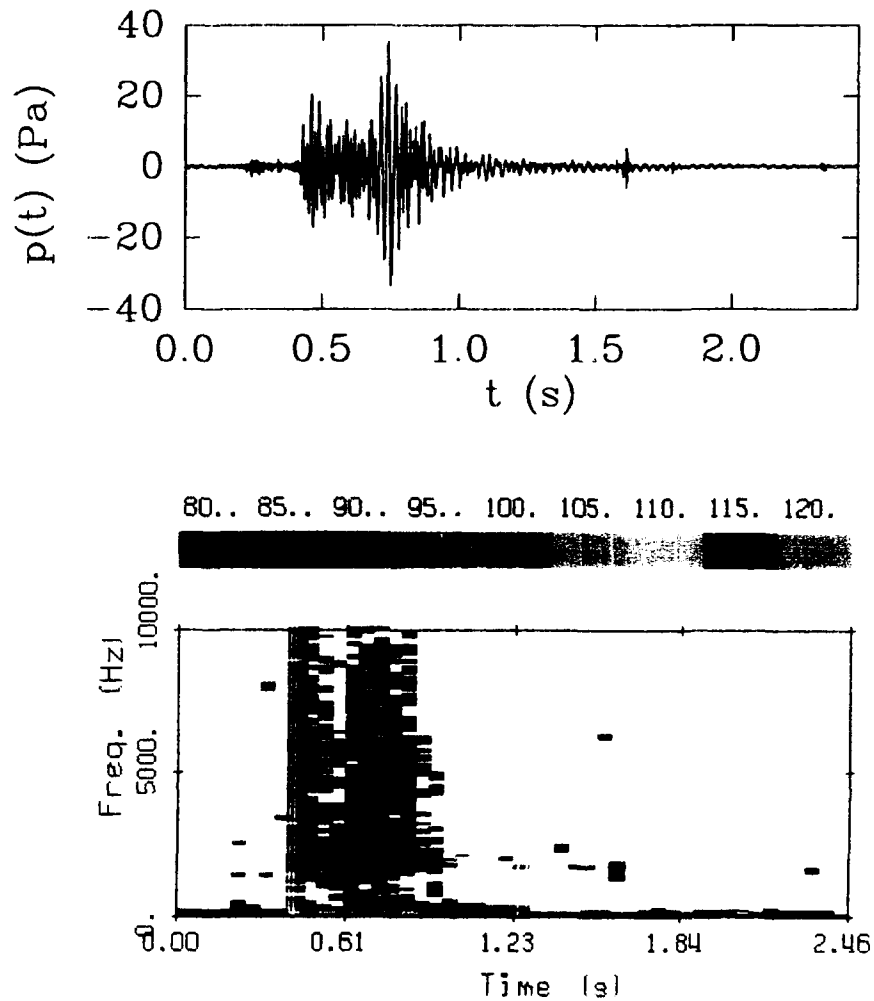


Figure 3.8 The upper plot is a time series of the upstream hydrophone signal band pass filtered from 20 Hz to 10 kHz for packet W_2 with $S = 0.544$. The lower plot is a spectrograph of the time series in the upper plot. 48 spectra with a bandwidth resolution of 39 Hz are shown plotted. They were computed by dividing the time series into 144-512 point segments which overlapped 171 points, windowing with a Blackman-Harris window and computing FFT's which were averaged over every 3 segments. Each color corresponds to a 5 dB re $1 \mu\text{Pa}^2$ increment in spectral level.

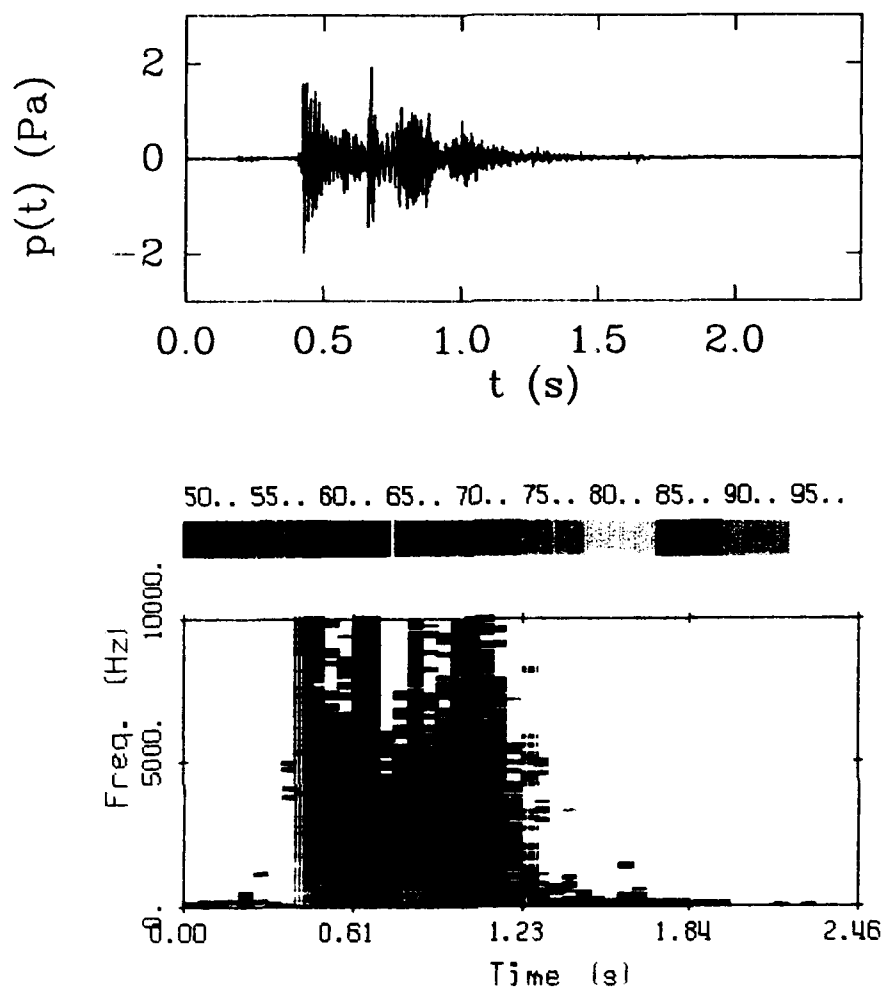


Figure 3.9 The upper plot is a time series of a microphone signal band pass filtered from 20 Hz to 10 kHz for packet W_2 with $S = 0.544$. The lower plot is a spectrograph of the time series in the upper plot. 48 spectra with a bandwidth resolution of 39 Hz are shown plotted. They were computed by dividing the time series into 144-512 point segments which overlapped 171 points, windowing with a Blackman-Harris window and computing FFT's which were averaged over every 3 segments. Each color corresponds to a 5 dB re $1 \mu\text{Pa}^2$ increment in spectral level.

Horizontal mode number n	Vertical mode number m	Theoretical cut-off frequency (Hz)
0	1	625
0	2	1875
0	3	3125
0	4	4370
0	5	5620
1	1	1240
1	2	2160
1	3	3300
1	4	4500
1	5	5730
2	1	2230
2	2	2850
2	3	3790
2	4	4870
2	5	6020
3	1	3270
3	2	3720
3	3	4480
3	4	5430
3	5	6480
4	1	4330
4	2	4680
4	3	5300
4	4	6120
4	5	7070

Table 3.5 Acoustic modes and their theoretical cut-off frequencies for the 0.76 m wide 0.6 m deep wave tank.

The first maximum in the hydrophone envelope corresponds to a time immediately after the initial impact of the wave crest on the free surface as it plunges over. The second maximum corresponds to either the break up of the large volume of air contained in the cylinder formed by the plunging wave crest or to the impact of a secondary jet of water ejected downstream as the crest plunges through the free surface. Both processes are occurring simultaneously and it is difficult to distinguish between the

two. The first maximum in the envelope of the microphone time series occurs at the same time as the first maximum in the hydrophone time series and is also due to the initial impact of the plunging wave crest. The second microphone maximum occurs at the same time as the second hydrophone maximum but its duration is much shorter. The third and fourth maxima in the microphone envelope do not correspond to any similar feature in the hydrophone signal.

The microphone signals are biased to processes which produce sound at or near the water surface. It has been shown by Prosperetti and Lu (1988) that air bubbles which burst at the water surface radiate sound into the air but that very little sound penetrates into the water. Therefore it is possible that the microphone was receiving signals from bursting bubbles and surface agitation which were not detected by the hydrophones. Conversely, it is also possible that the hydrophones received signals produced by processes occurring too deep in the water column to be detected by the microphone. The slightly longer duration of the microphone signal may be due to bubbles which are no longer radiating sound into the water but do radiate sound into the air as they rise back to the water surface and burst.

In figures 3.10, 3.11 and 3.12 averaged frequency spectra, plotted as the pressure spectrum level, of the upstream and downstream hydrophones and microphone signals, respectively for packet W_1 are shown. The spectra were averaged over 5 repeats and a Bartlett smoothing window with a width of 9 was applied to give 80 degrees of freedom. The pressure spectrum level is the average sound pressure level in a frequency band and it is defined as,

$$PSL = 10 \log \left[\frac{G(f)}{1 \mu Pa^2} \right] - 10 \log(BW) \quad 3.1$$

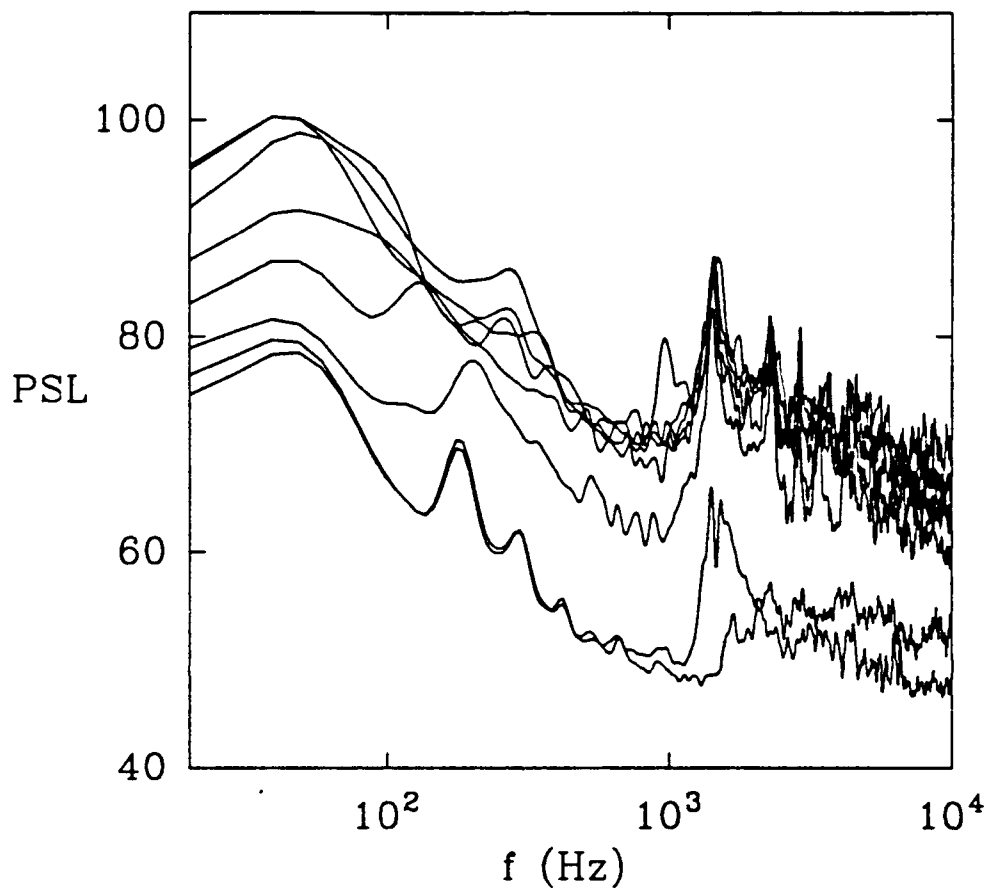


Figure 3.10 Frequency spectra of the signal from the upstream hydrophone for wave packet W_1 with slope, S increasing from 0.288 to 0.512 in 0.032 increments. Pressure spectrum level, PSL in dB re $1 \mu\text{Pa}^2/\text{Hz}$. Each spectrum is the average of 5 repeats and was smoothed in the frequency domain with a 9 point Bartlett window to produce an estimate with 80 degrees of freedom.

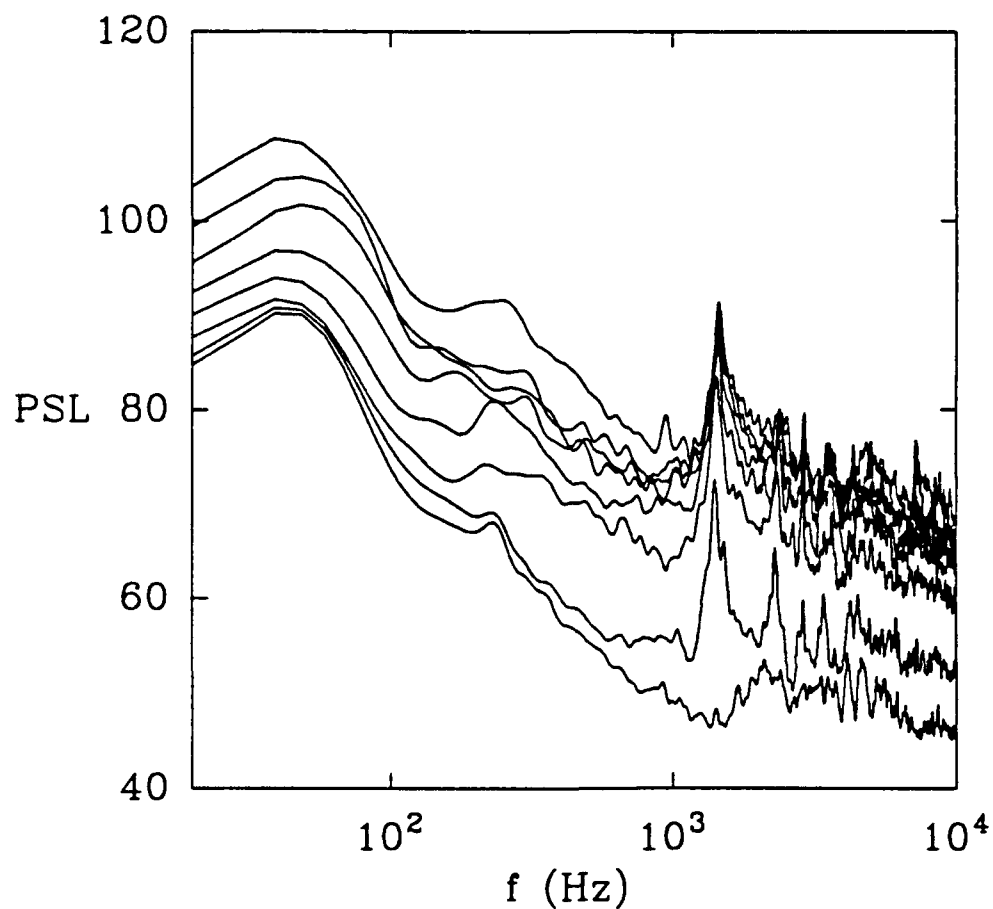


Figure 3.11 Frequency spectra of the signal from the downstream hydrophone for wave packet W_1 with slope, S increasing from 0.288 to 0.512 in 0.032 increments. Pressure spectrum level, PSL in dB re $1 \mu\text{Pa}^2/\text{Hz}$. Each spectrum is the average of 5 repeats and was smoothed in the frequency domain with a 9 point Bartlett window to produce an estimate with 80 degrees of freedom.

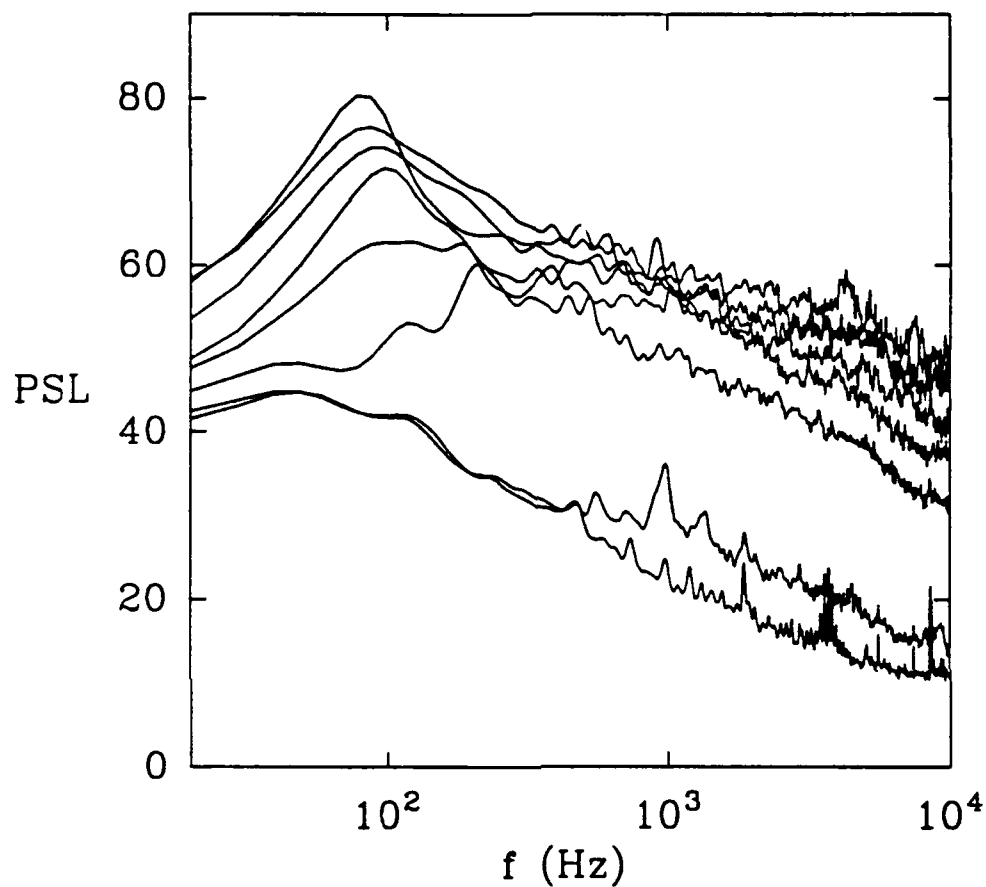


Figure 3.12 Frequency spectra of the signal from the microphone for wave packet W_1 with slope, S increasing from 0.288 to 0.512 in 0.032 increments. Pressure spectrum level, PSL in dB re $1 \mu\text{Pa}^2/\text{Hz}$. Each spectrum is the average of 5 repeats and was smoothed in the frequency domain with a 9 point Bartlett window to produce an estimate with 80 degrees of freedom.

where $G(f)$ (Pa^2) is the autospectral density function and BW (Hz) is the bandwidth resolution of the computed autospectral density function. There are eight spectra plotted in each figure and they correspond to wave slopes from 0.288 to 0.512. The lowest slope of 0.288 is the incipient breaking case for which no breaking occurs. The spectrum for the incipient case is the lowest spectrum in each figure and should be considered the background noise level. Waves of larger slope generally produced spectra with larger amplitudes although some of the spectra do overlap, particularly for the hydrophone data in figure 3.10. The hydrophone spectra in figures 3.10 and 3.11 show clear evidence of the modal properties of the wave channel. As was the case in the experiments presented in chapter 2 there is no evidence of the lowest cutoff frequency at 625 Hz corresponding to the combination of the, $n = 0$, horizontal mode and the, $m = 1$, vertical mode. The first cutoff frequency seen in the spectra is at approximately 1300 Hz and this corresponds to the second lowest mode of, $n = 1$, and, $m = 1$, which has a theoretical cutoff of 1240 Hz. The microphone spectra in figure 3.12 show no evidence of any modal structure and from 500 Hz to 10 kHz the spectral slope varies from -1.4 to -2.0 or -4 to -6 dB per octave.

These spectra demonstrate that there is significant low frequency sound produced by breaking waves. The spectra of the of the incipient event, $S = 0.288$ and the next highest slope event, $S = 0.320$, are almost identical for frequencies less than 500 Hz. When the slope is increased to 0.352 the level of low frequency sound increases dramatically. This increase in slope is where the transition from spilling to plunging breaking occurs. As the wave slope increased further, from 0.352 to 0.512, the levels of low frequency sound continued to increase. Similar results were observed in the sound spectra for the other two wave packets W_2 and W_3 .

The variance of the hydrophone and microphone signals were calculated as a function of time in the frequency bands 0 to 1 kHz and 1 kHz to 10 kHz. Plots of the pressure spectrum level, PSL, as a function of time in these two bands for wave packet

W_1 are shown in figures 3.13, 3.14 and 3.15. At the lowest slope (incipient event) the PSL of the two hydrophones and the microphone do not increase significantly above the background levels. There is some variation of the PSL of the downstream hydrophone signal for the incipient event plotted in figure 3.14h, but this is not due to breaking. In figures 3.13g and 3.14g which correspond to the two hydrophone signals for a wave slope of 0.320, the PSL in the higher band increases above the background levels for approximately 0.5 s but the PSL in the lower frequency band remains at the background level. The lower frequency band PSL does show a very slight increase above the background levels at 1.1 s in figure 3.15g for the microphone signal. The lowest slope event to show significant increases of the PSL in the 0 to 1 kHz band was the breaking event with $S = 0.352$ shown in figures 3.13f, 3.14f and 3.15f. This is consistent with the earlier observation that spectral levels increased dramatically at lower frequencies when the slope was increased from 0.320 to 0.352 because this change in slope caused the transition from spilling to plunging breaking. The PSL in both bands increases simultaneously which is also consistent with the fact that the sound levels were seen to increase simultaneously across the entire spectrum in the spectrographs plotted in figures 3.8 and 3.9.

In order to examine the relationship between the sound and the dynamics of breaking the mean square acoustic pressure was calculated in the two frequency bands from 0 to 1 kHz and from 1kHz to 10 kHz over the entire signal duration. In figures 3.16, 3.17 and 3.18 this mean square acoustic pressure in the two bands, for the two hydrophone signals and the microphone signal, is shown plotted versus the wave slope for all three wave packets. The trend is similar in all three plots. The log of the mean square acoustic pressure of the hydrophone signals in the lower frequency band, plotted in the upper frame, is approximately proportional to the wave slope. The longer wavelength packets produced significantly more low frequency sound energy. This is most evident in the upstream hydrophone data in figure 3.16. The log of the mean square

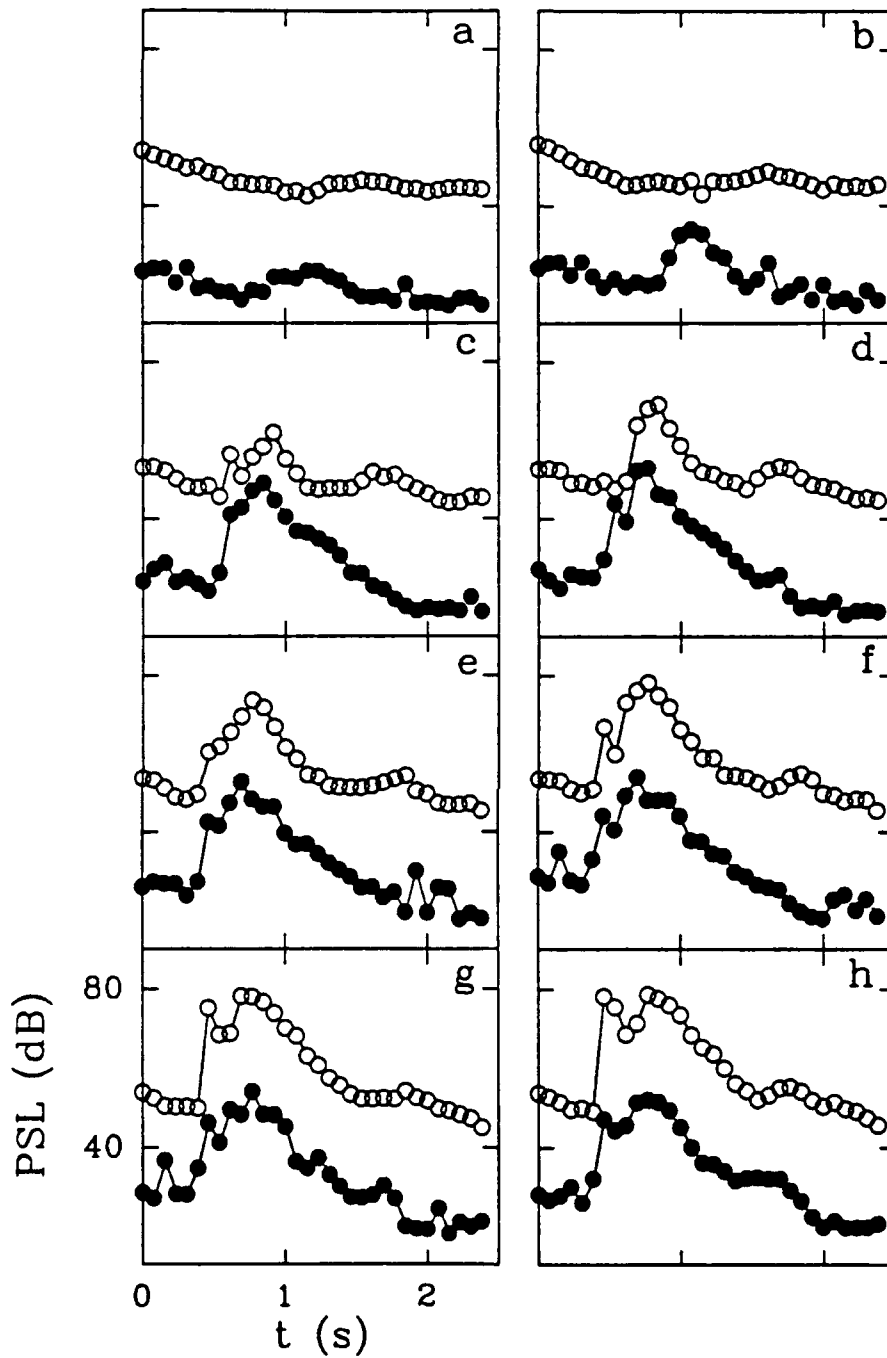


Figure 3.13 The pressure spectrum level PSL (dB re $1\mu\text{Pa}^2/\text{Hz}$) of the signal from the upstream hydrophone in two frequency bands as a function of time for packet W_1 . Each data point is the average of 5 repeats of the event. (a) $S = 0.288$ (b) $S = 0.320$ (c) $S = 0.352$ (d) $S = 0.384$ (e) $S = 0.416$ (f) $S = 0.448$ (g) $S = 0.480$ (h) $S = 0.512$. \circ , 20Hz-1 kHz; \bullet , 1-10 kHz.

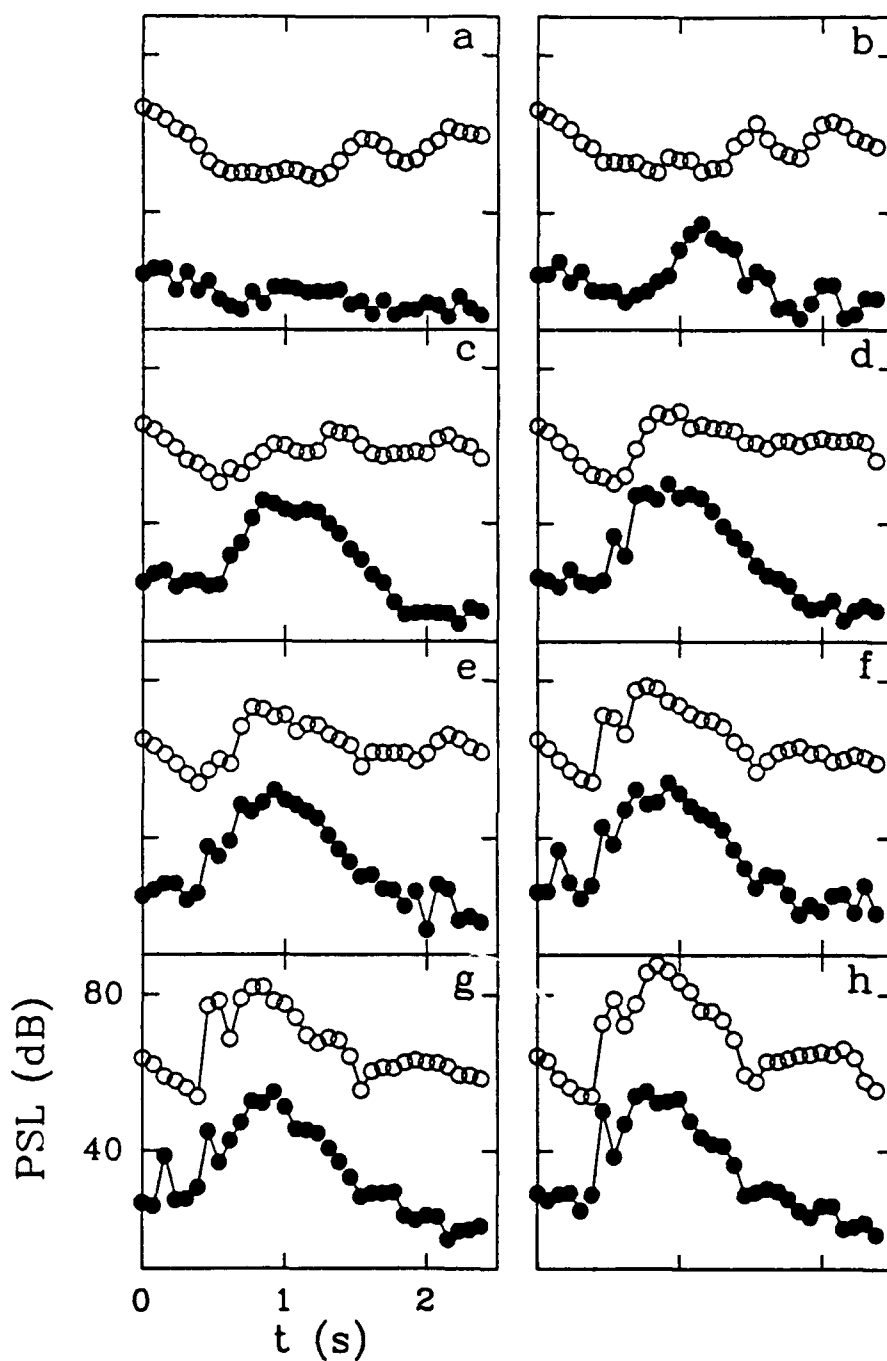


Figure 3.14 The pressure spectrum level PSL (dB re $1\mu\text{Pa}^2/\text{Hz}$) of the signal from the downstream hydrophone in two frequency bands as a function of time for packet W_2 . Each data point is the average of 5 repeats of the event. (a) $S = 0.288$ (b) $S = 0.320$ (c) $S = 0.352$ (d) $S = 0.384$ (e) $S = 0.416$ (f) $S = 0.448$ (g) $S = 0.480$ (h) $S = 0.512$. \circ , 20Hz-1 kHz; \bullet , 1-10 kHz.

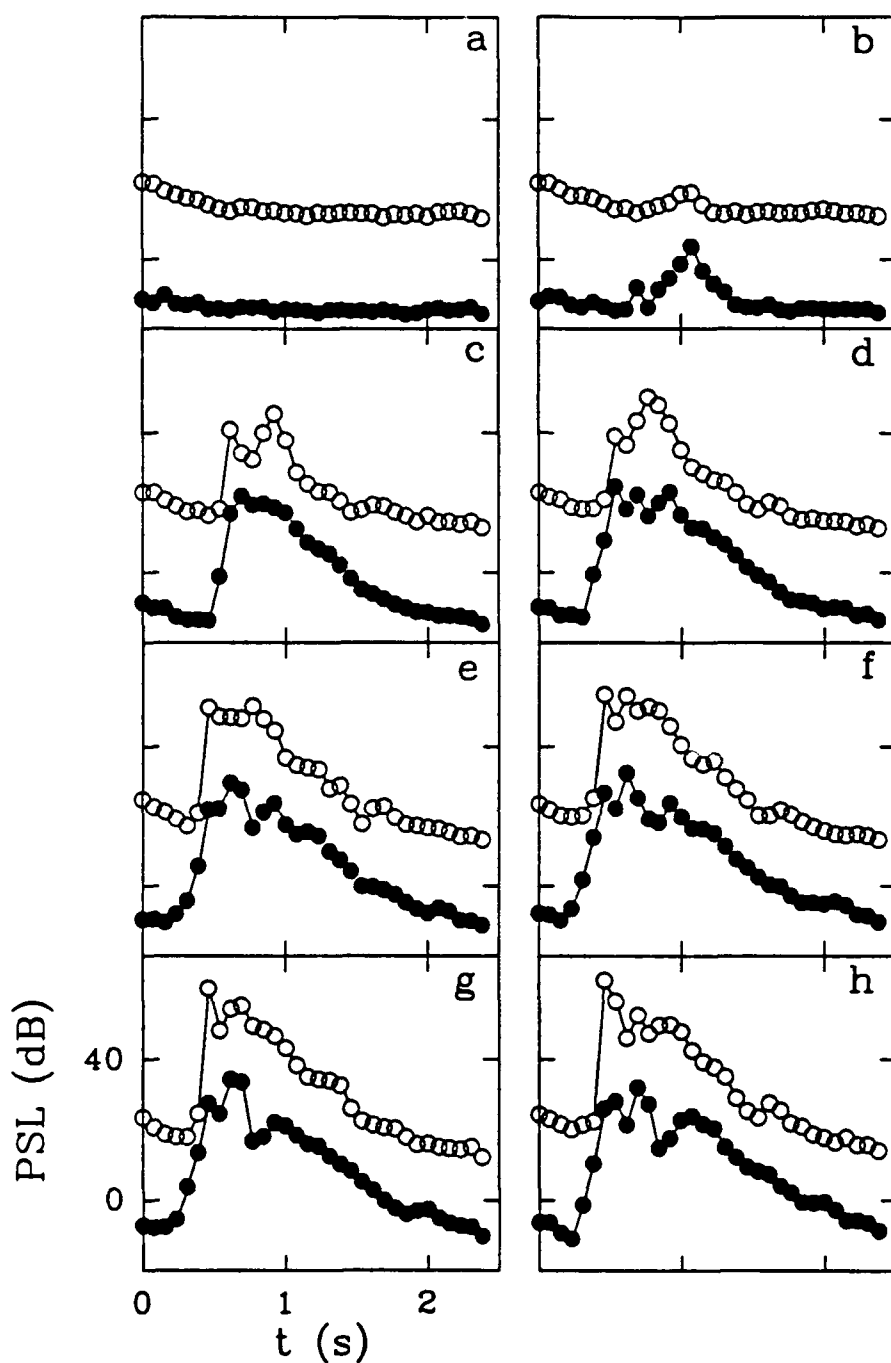


Figure 3.15 The pressure spectrum level PSL (dB re $1\mu\text{Pa}^2/\text{Hz}$) of the signal from the microphone in two frequency bands as a function of time for packet W_3 . Each data point is the average of 5 repeats of the event. (a) $S = 0.288$ (b) $S = 0.320$ (c) $S = 0.352$ (d) $S = 0.384$ (e) $S = 0.416$ (f) $S = 0.448$ (g) $S = 0.480$ (h) $S = 0.512$. \circ , 20Hz-1 kHz; \bullet , 1-10 kHz.

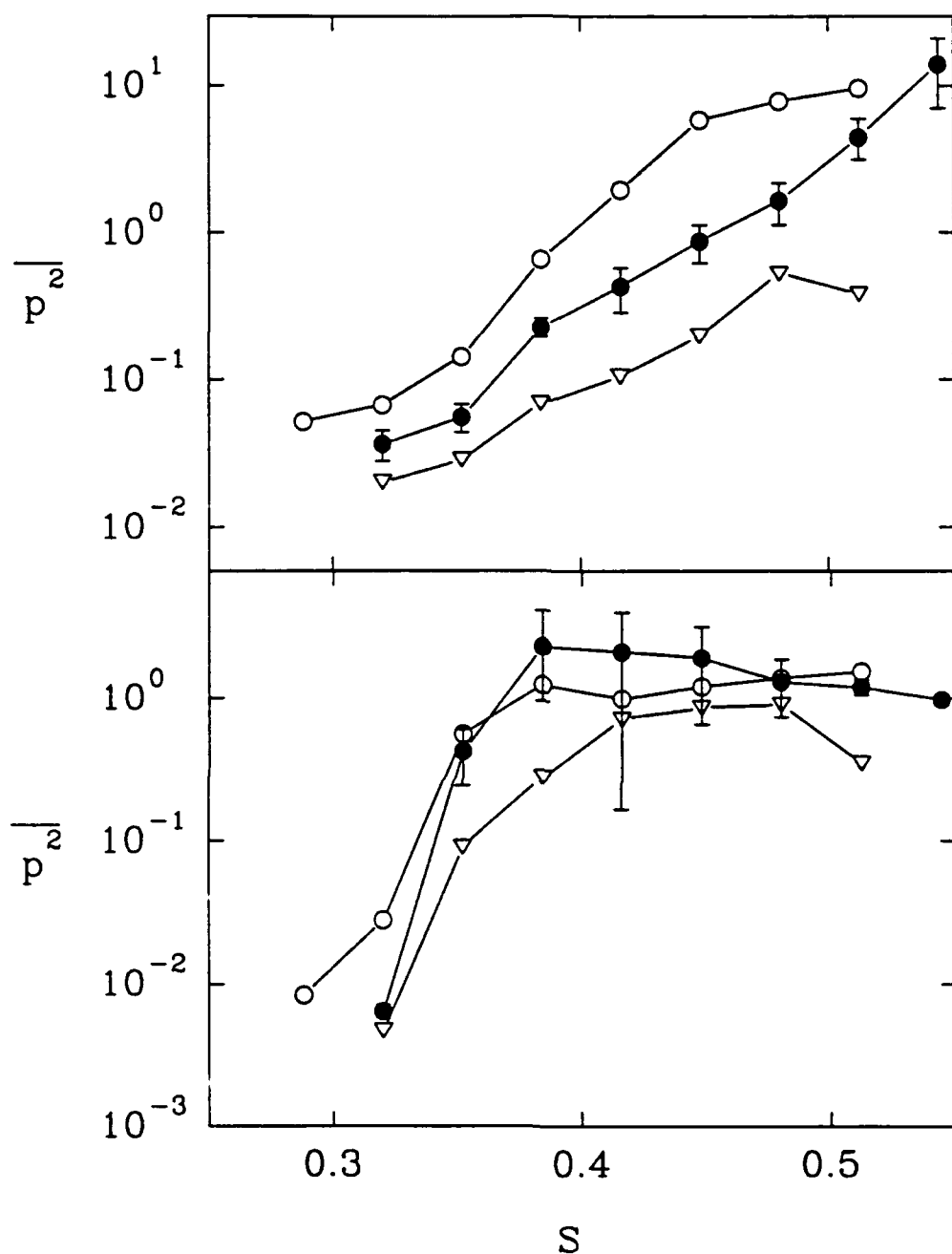


Figure 3.16 The mean square acoustic pressure $\overline{p^2}$ (Pa²) of the signal from the upstream hydrophone calculated over the entire signal duration in two frequency bands as a function of the slope parameter S . The upper plot is for the frequency band 0-1 kHz and the lower plot for the band 1-10 kHz. Each data point is the average of 5 repeats of the measurement and the error bars indicate the 95% confidence limits. \circ , W_1 ; \bullet , W_2 ; ∇ , W_3 .

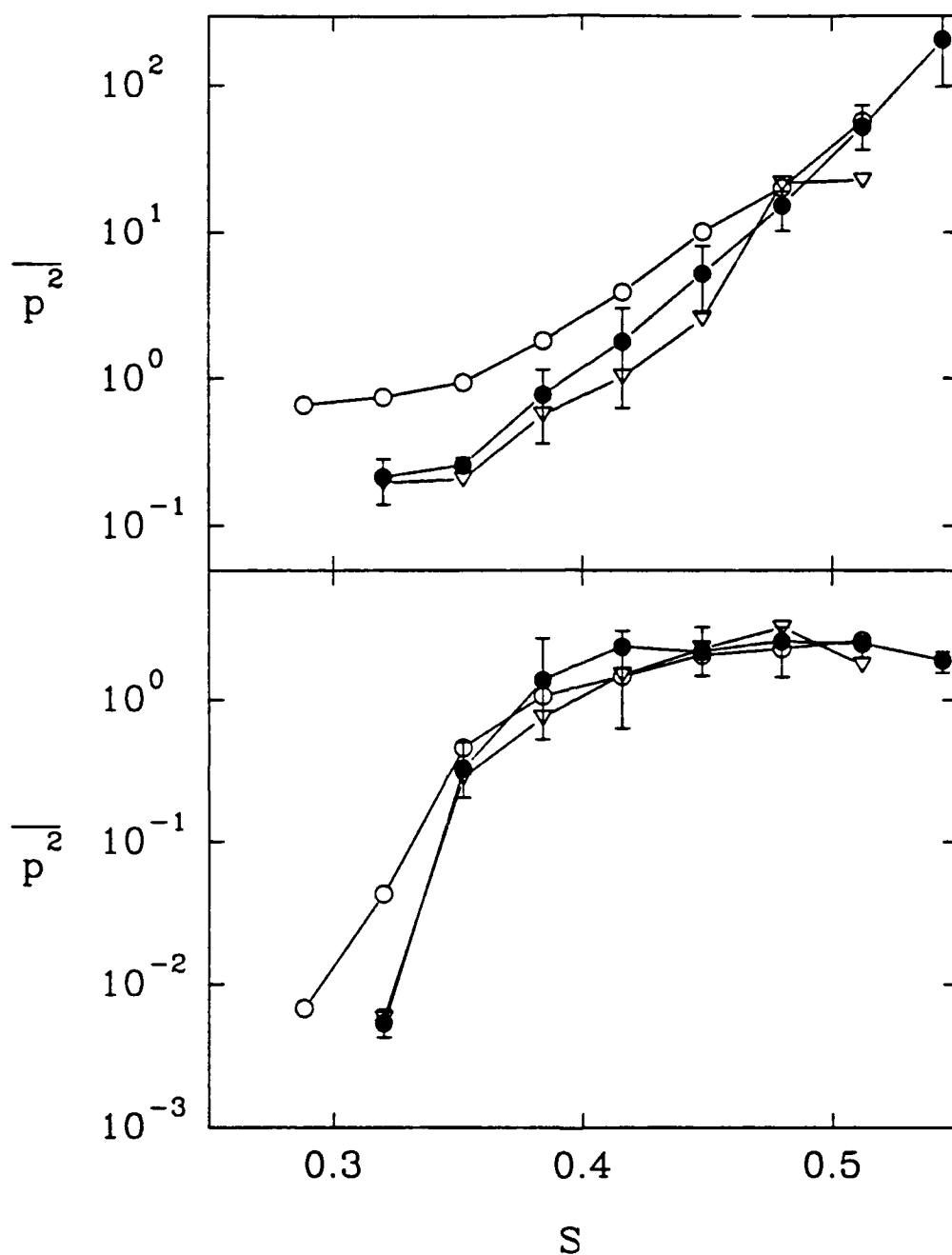


Figure 3.17 The mean square acoustic pressure $\overline{p^2}$ (Pa^2) of the signal from the downstream hydrophone calculated over the entire signal duration in two frequency bands as a function of the slope parameter S . The upper plot is for the frequency band 0-1 kHz and the lower plot for the band 1-10 kHz. Each data point is the average of 5 repeats of the measurement and the error bars indicate the 95% confidence limits. \circ , W_1 ; \bullet , W_2 ; ∇ , W_3 .

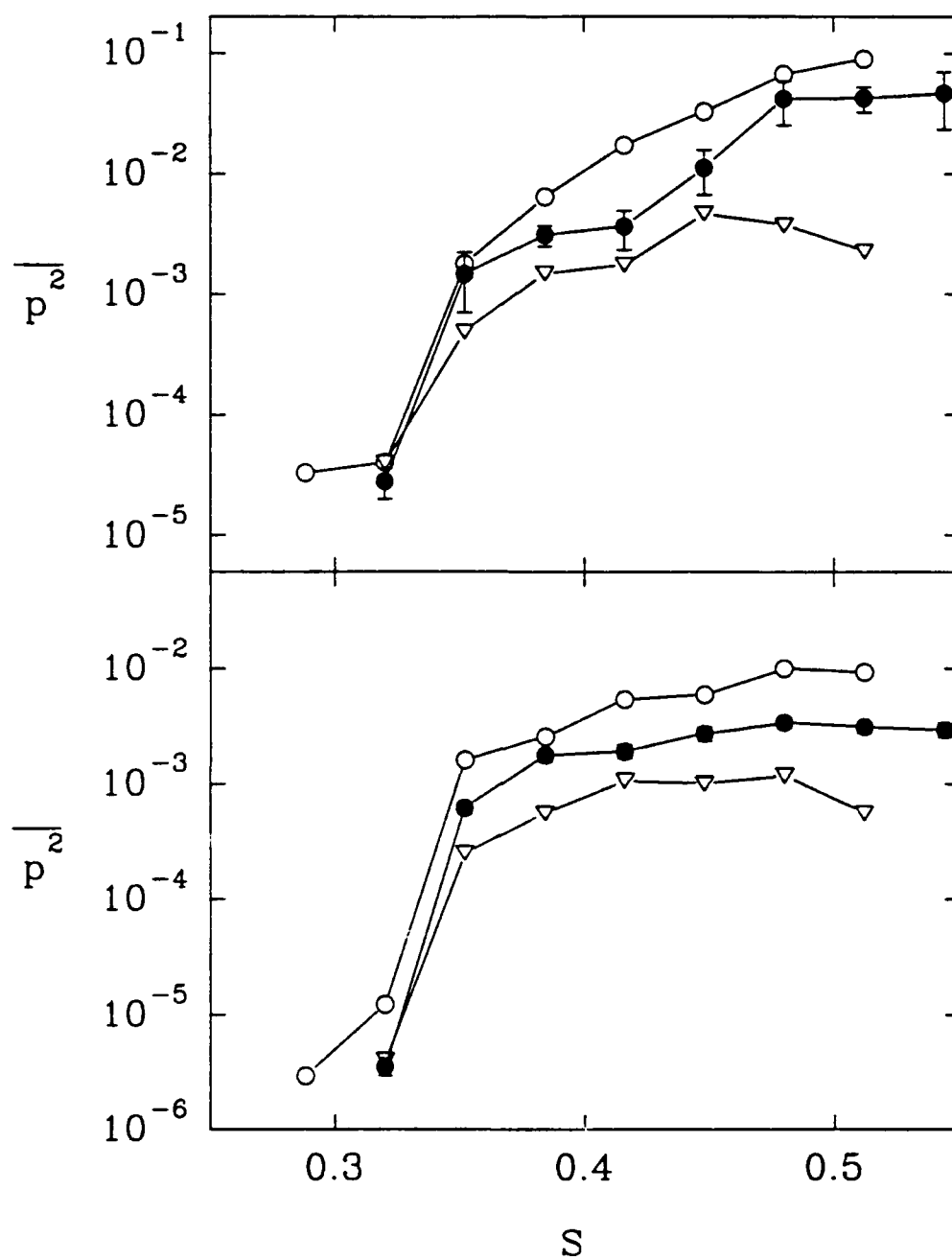


Figure 3.18 The mean square acoustic pressure $\overline{p^2}$ (Pa²) of the signal from the microphone calculated over the entire signal duration in two frequency bands as a function of the slope parameter S . The upper plot is for the frequency band 0-1 kHz and the lower plot for the band 1-10 kHz. Each data point is the average of 5 repeats of the measurement and the error bars indicate the 95% confidence limits. \circ , W_1 ; \bullet , W_2 ; ∇ , W_3 .

acoustic pressure of the microphone signal in the lower frequency band increased rapidly as the slope increased in the range $S = 0.3$ to 0.4 . For larger values of S the mean square acoustic pressure tended toward a maximum value. The longer wavelength packets produced significantly higher levels in the lower frequency band of the microphone signal as well.

The log of the mean square acoustic pressure in the higher frequency band increased rapidly with slope for all three instruments in the range $S = 0.3$ to 0.40 . As the slope increased further the mean square acoustic pressure reached a plateau at $S = 0.4$ and remained essentially constant for larger values of S . The microphone signal showed the strongest dependence on the packet wavelength with significantly higher values of the mean square acoustic pressure for the longer packets. The hydrophone data did not show a similar dependence on the packet wavelength at the higher frequencies.

The mean square acoustic pressure in the same two frequency bands is plotted versus the fractional dissipation for the two hydrophone signals and the microphone signal in figures 3.19, 3.20 and 3.21. The log of the mean square acoustic pressure in the lower frequency band correlates almost linearly with the dissipation for the hydrophone data however there is more scatter in the data for the downstream hydrophone plotted in figure 3.20. The log of the mean square acoustic pressure in the lower frequency band of the microphone signal in figure 3.21 increases more rapidly with dissipation for D in the range 0.05 to 0.1 . For $D > 0.1$ the increase is less rapid but the correlation is approximately linear. There is no consistent dependence on the wavelength of the packet for either the hydrophone or the microphone low frequency mean square acoustic pressure data.

The log of the mean square acoustic pressure in the higher frequency band increases rapidly with dissipation in the range $D = 0.05$ to 0.1 for all three instruments. For larger values of D the rate of increase is slower and for the hydrophone data the mean square acoustic pressure reaches a maximum at $D = 0.15$ and remains

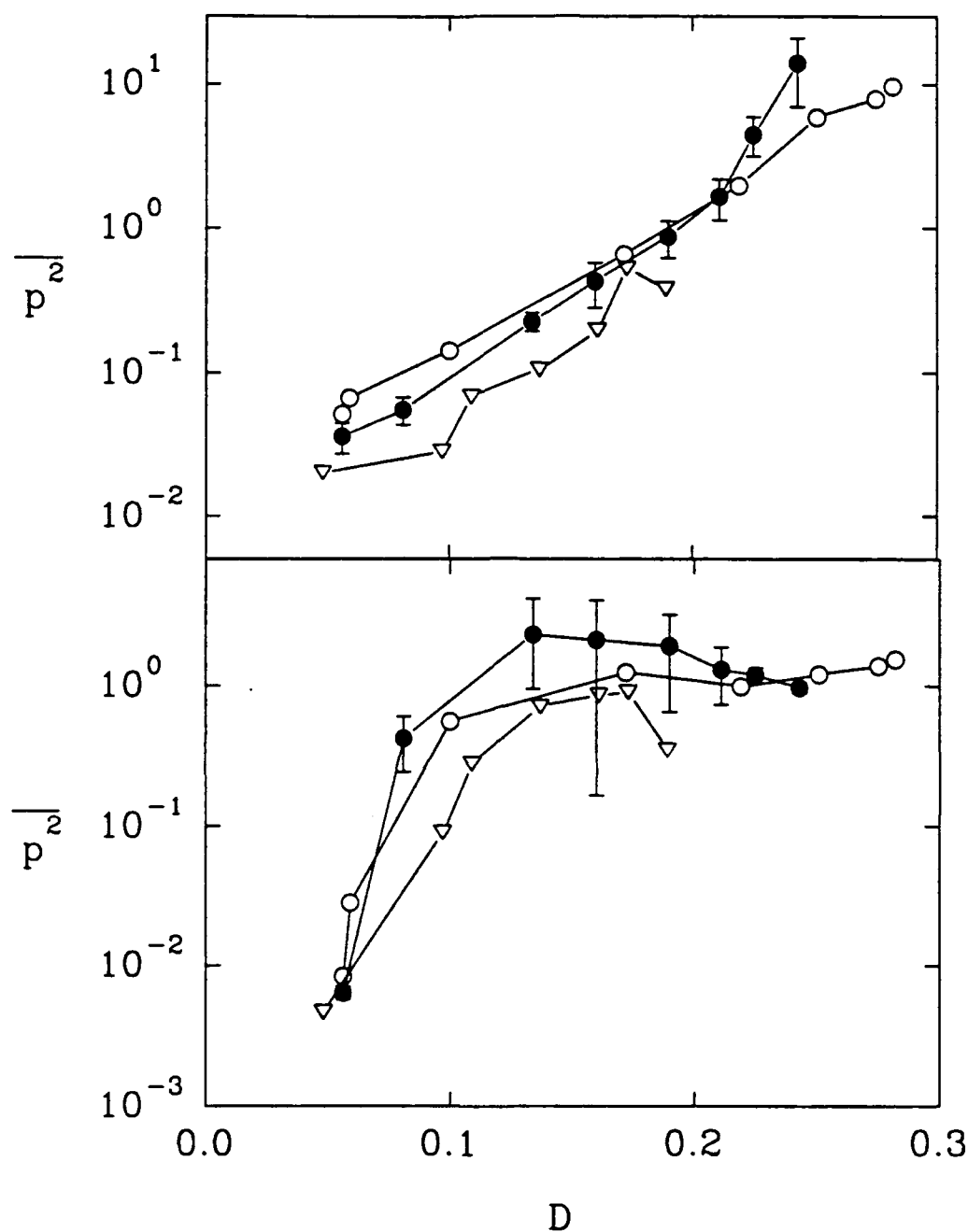


Figure 3.19 The mean square acoustic pressure $\overline{p^2}$ (Pa²) of the signal from the upstream hydrophone calculated over the entire signal duration in two frequency bands as a function of the fractional dissipation D . The upper plot is for the frequency band 0-1 kHz and the lower plot for the band 1-10 kHz. Each data point is the average of 5 repeats of the measurement and the error bars indicate the 95% confidence limits. ○, W_1 ; ●, W_2 ; ▽, W_3 .

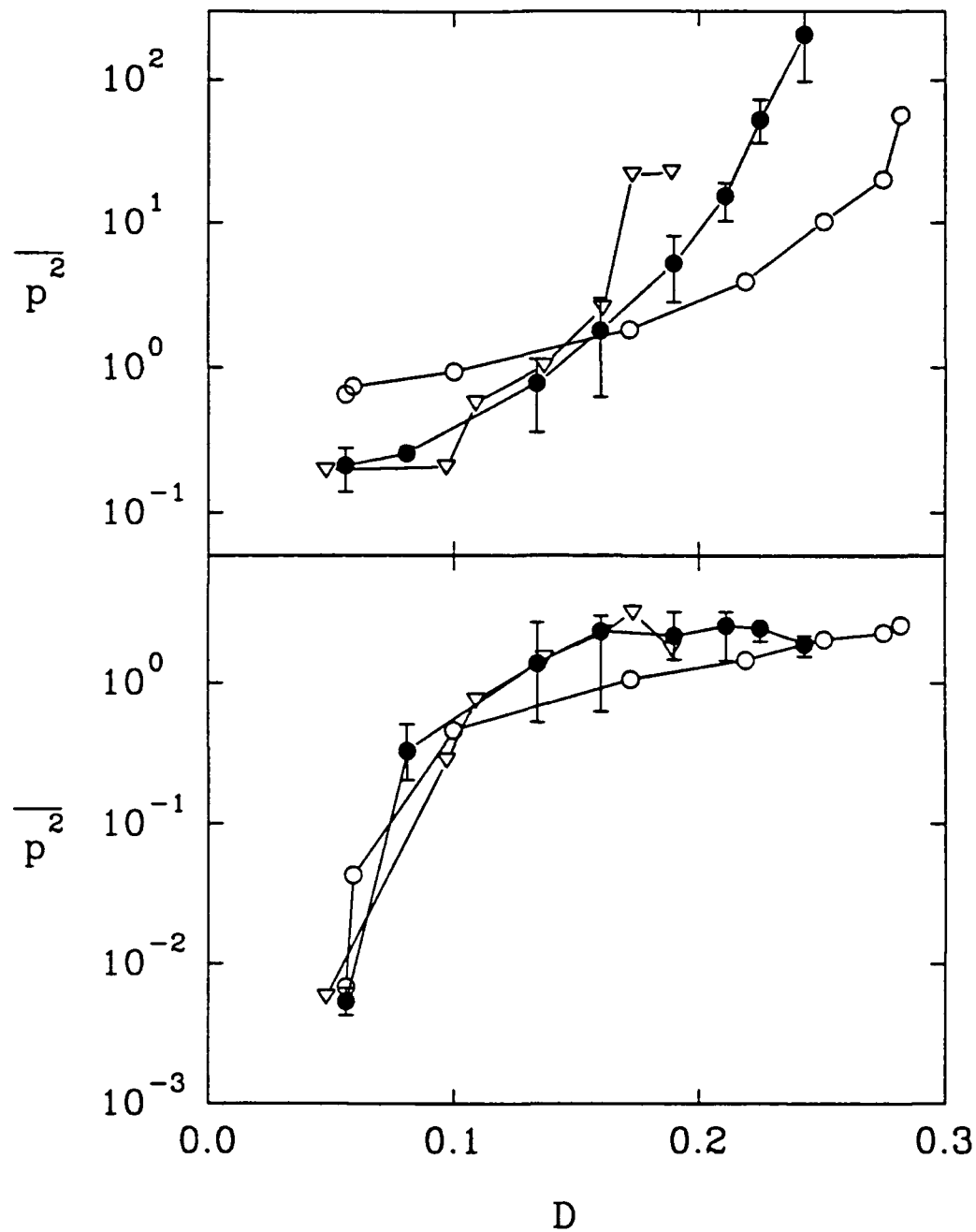


Figure 3.20 The mean square acoustic pressure $\overline{p^2}$ (Pa²) of the signal from the downstream hydrophone calculated over the entire signal duration in two frequency bands as a function of the fractional dissipation D . The upper plot is for the frequency band 0-1 kHz and the lower plot for the band 1-10 kHz. Each data point is the average of 5 repeats of the measurement and the error bars indicate the 95% confidence limits. \circ , W_1 ; \bullet , W_2 ; ∇ , W_3 .

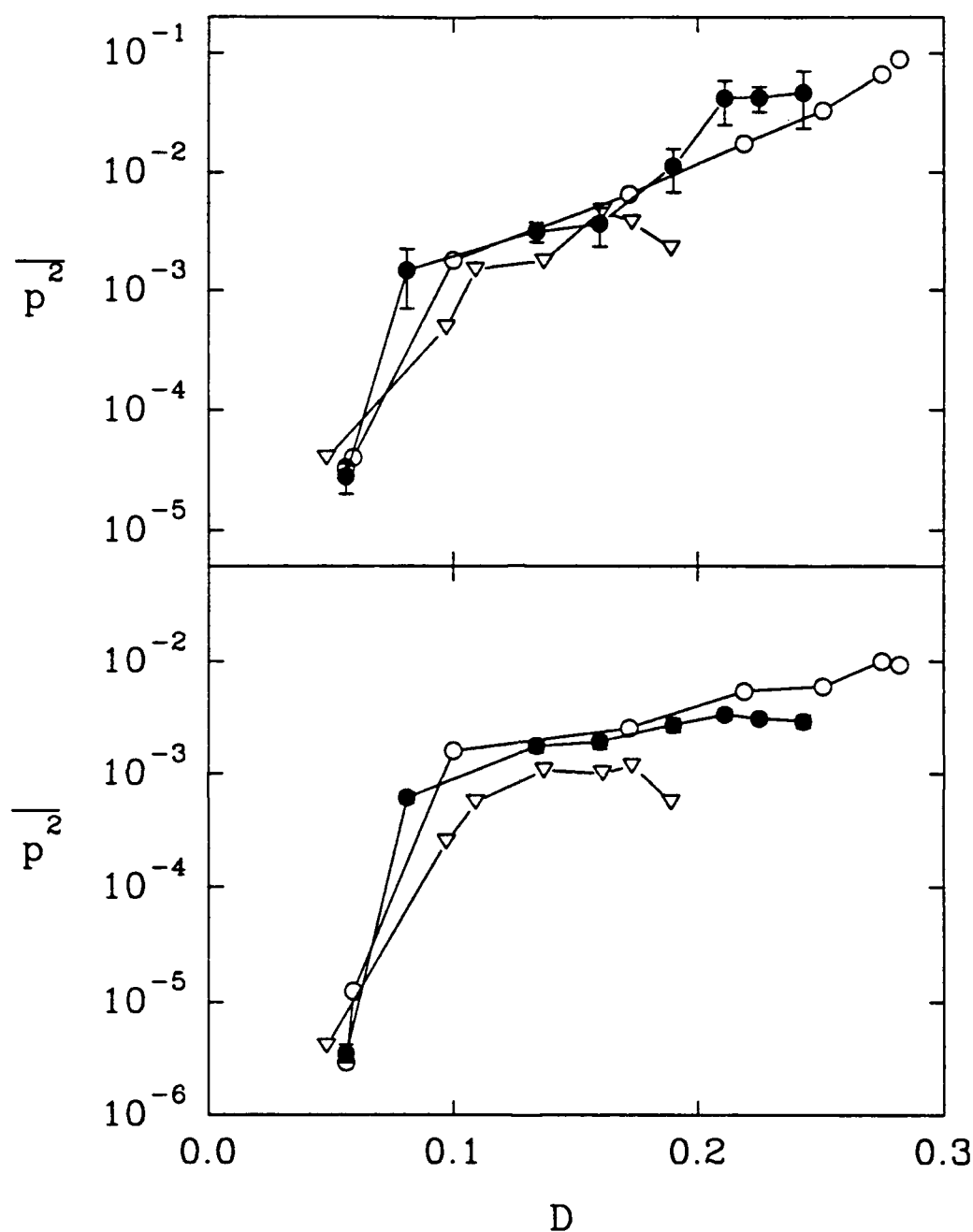


Figure 3.21 The mean square acoustic pressure $\overline{p^2}$ (Pa^2) of the signal from the microphone calculated over the entire signal duration in two frequency bands as a function of the fractional dissipation D . The upper plot is for the frequency band 0-1 kHz and the lower plot for the band 1-10 kHz. Each data point is the average of 5 repeats of the measurement and the error bars indicate the 95% confidence limits. \circ , W_1 ; \bullet , W_2 ; ∇ , W_3 .

approximately constant for $D > 0.15$. The mean square acoustic pressure for the microphone data continues to increase slowly for $D > 0.15$. Again, there appears to be no consistent dependence on the wavelength of the packets except perhaps in the microphone data.

3.3 Experimental Procedure: Three-Dimensional breaking

The three-dimensional breaking experiments were conducted in a wave basin 45.7 m long by 30.5 m wide filled with 5.8 m of fresh water at the Offshore Technology Research Center at Texas A&M University. Measurements were made of the sound produced by breaking waves and the surface wave displacement. Plan and elevation views of this facility are shown in figure 3.22 and a schematic of the wave maker control system and experimental equipment is drawn in figure 3.23. The channel was equipped with forty eight independently controlled hinged wave paddles along the 30.5 m wide endwall. The paddles were hinged at a point 3 m below the still water level. The waves were absorbed by a series of metal screens installed vertically extending from the tank bottom to several meters above the still water level. The tank was equipped with a motorized instrument platform which spanned the width of the tank and could be accurately positioned to within ± 0.25 cm.

The wave paddles were controlled by a Digital Equipment Corp. workstation which fed data to three 80386 PC computers each of which controlled 16 paddles. The software used to generate the breaking waves is proprietary and was supplied by the National Research Council of Canada to OTRC. As a result the details of the software and the exact methodology used to generate the waves is not available. For these experiments the interval between breaking events was 2 minutes. Within this time interval the surface oscillations had decayed enough so that the repeatability of successive events was not affected. Three-dimensional breaking waves were produced

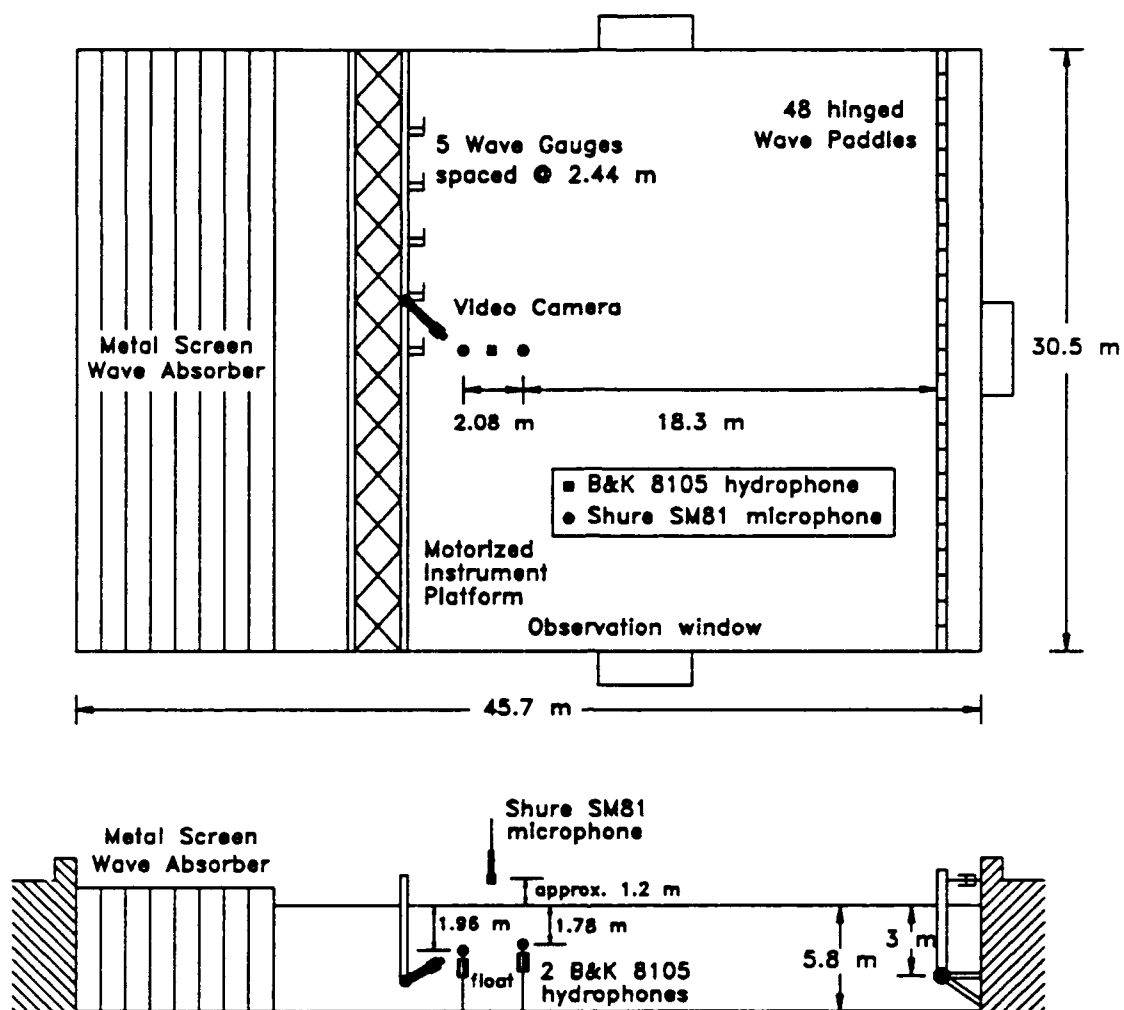


Figure 3.22 A drawing of a plan (top plot) and elevation view (bottom plot) of the three-dimensional wave channel at the Offshore Technology Research Center at Texas A&M University. The layout of some of the experimental equipment is also shown.

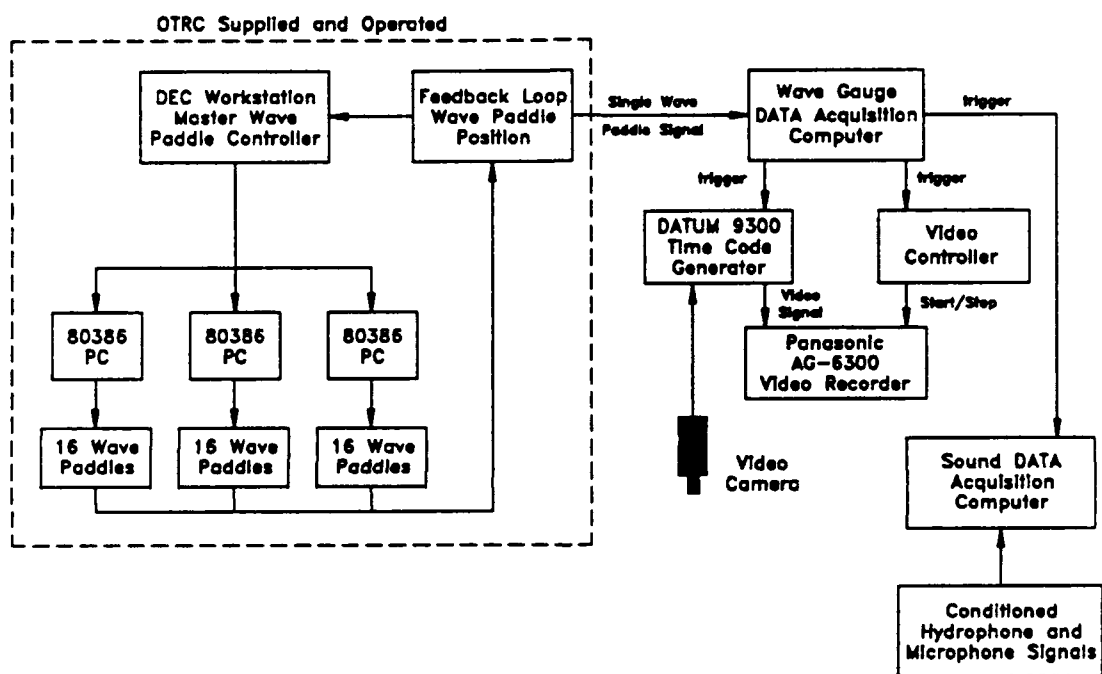


Figure 3.23 A schematic of the experimental equipment set-up and the wavemaker control system.

with the "bulls eye" pattern by focusing wave components spread over a given frequency band similar to the scheme described for two-dimensional breaking in section 2.1.1 . The amplitude of the waves was varied by varying the gain in the wave generation program. The gain simply scaled the wave packet proportionally without altering the form of the signal sent to the wave paddles. The wave amplitude is a maximum at the center of the tank and decreases closer to the sidewalls. The phase of the paddle motion is adjusted so that all forty eight paddles generate waves which are focused towards a prescribed location on the centerline of the tank. This produces circular wave crests which curve concavely toward an observer stationed downstream of the wave paddles and the wave field is symmetric about the centerline.

3.3.1 Surface Displacement Measurements

The surface displacement was measured with a series of capacitance wire wave gauges. The wave gauges and the signal conditioning electronics were built and operated by the staff at OTRC. The surface displacement data was sampled at a rate of 200 Hz per gauge using an 80386 PC computer equipped with a Metrabyte DAS-16 board. Five wave gauges spaced at 2.4 m intervals were mounted from the instrument platform, the position of each gauge is shown in figure 3.22. Measurements of the surface displacement were made at 10 ft. (3 m) intervals along the length of the basin. The gauges consisted of Teflon coated wire mounted on 1/4 inch stainless steel frames. The gauges were calibrated by sampling the still water level in 7.5 inch (19 cm) increments over a 30 inch (76 cm) range. The relationship between the wave amplitude and the output voltage was linear and the gauges were calibrated once a day. The linear term in the calibration equation varied by approximately $\pm 2\%$ from one day to the next.

3.3.2 Video Measurements

Underwater video recordings were made of some of the experimental runs. The video camera was mounted on an L-shaped bracket made of 2 inch aluminum pipe. The bracket was clamped to the railing of the instrument platform so that the camera was submerged approximately 2 m below the still water surface. The angle between the vertical and horizontal tubes was adjusted so that the camera was looking upward at an angle of approximately 30° . Figure 3.22 shows the approximate location and orientation of the video camera. The video camera was a black and white NEC model TI-23A 1/2 inch format CCD camera with a 1/1000 second shutter speed. The video recorder was a Panasonic model AG-6300 VHS video cassette recorder. A DATUM model 9300 IRIG-B time code generator/translator was used to insert a time base accurate to within ± 1 millisecond onto the video image. The wave gauge data acquisition computer monitored the wave paddle position signal of a single paddle and triggered the start of the time code generator and video recorder when the signal reached a prescribed level. After one minute the wave gauge data acquisition computer turned off the video recorder and time code generator and then waited for the next wave to be generated.

3.3.3 Sound Measurements

The underwater sound measurements were made with two omnidirectional B&K model 8105 hydrophones and two B&K model 2635 charge amplifiers. The sound in air was measured with a Shure model SM81 microphone and Symetrix model SX202 microphone preamplifier. This equipment is described in detail in sections 2.1.3 and 3.1.2. The three channels of data were sampled digitally at 40 kHz per channel using an ALR 33 MHz 80386 PC and the ISC-16 analog to digital board described in section

3.1.2. The wave gauge data acquisition computer provided a trigger through the digital port of the DAS-16 board which triggered the ISC-16 board to begin sampling.

Three different signal conditioning configurations were used. A schematic drawing of the three configurations labelled set-up I, II and III is shown in figure 3.24. The signal conditioning of the microphone signal remained the same throughout the entire experiment. The microphone signal was amplified by 40 dB using a Symetrix SX202 preamplifier and then low pass filtered at 10 kHz, see set-up I in figure 3.24. In set-up I the hydrophone signals were notch filtered from 200 to 340 Hz, high pass filtered at 10 Hz and then low pass filtered at 20 kHz. In set-up II the hydrophone signals were bandpass filtered in the frequency range 1 kHz to 20 kHz. For set-up III the hydrophone signals were bandpass filtered from 10 Hz to 200 Hz.

3.4 Three-Dimensional Breaking: Results

3.4.1 Surface Displacement

The time series of the surface displacement for the largest wave with gain = 0.70 measured on the centerline of the tank at six locations are plotted in figure 3.25. These time series are typical of dispersive wave packets which are focused to break at a prescribed location downstream. In figure 3.25a, which is a plot of the surface displacement at a location close to the wave paddles the wave packet is composed of shorter waves followed by longer waves. As the packet propagates away from the paddles it becomes shorter as the longer waves catch up to the slower shorter waves. At the focal point the packet length and period are at a minimum. The focal point or location of breaking is very close to 18.6 m and this time series is plotted in figure 3.25c. Linear theory predicts that the wave packet period will be $T = 2/\Delta f$, and that the number of waves in the packet will be $N = 2f_c/\Delta f$ at the focal point (Rapp and Melville, 1990). In

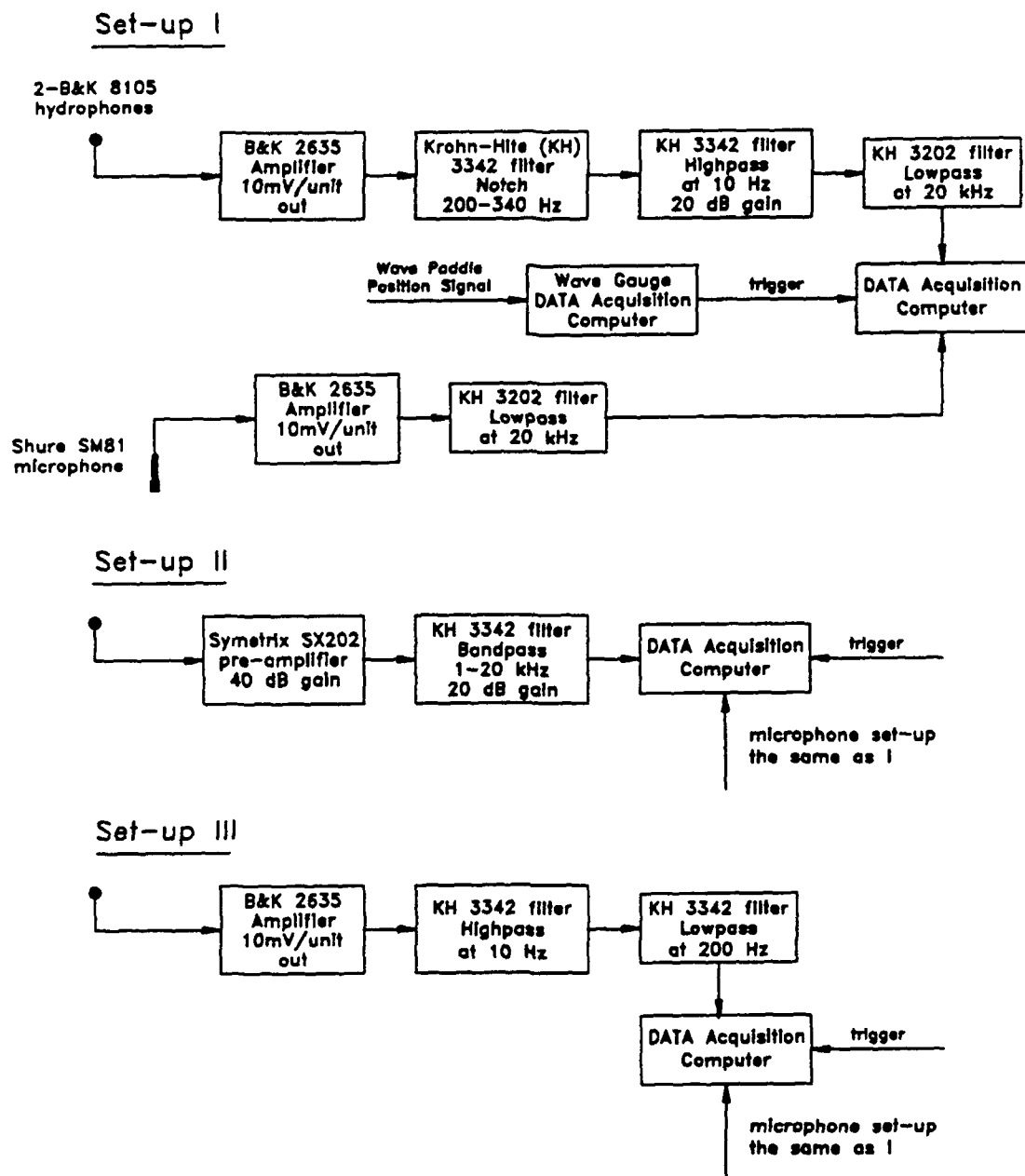


Figure 3.24 A schematic of the three signal conditioning configurations used in the three-dimensional breaking experiments.

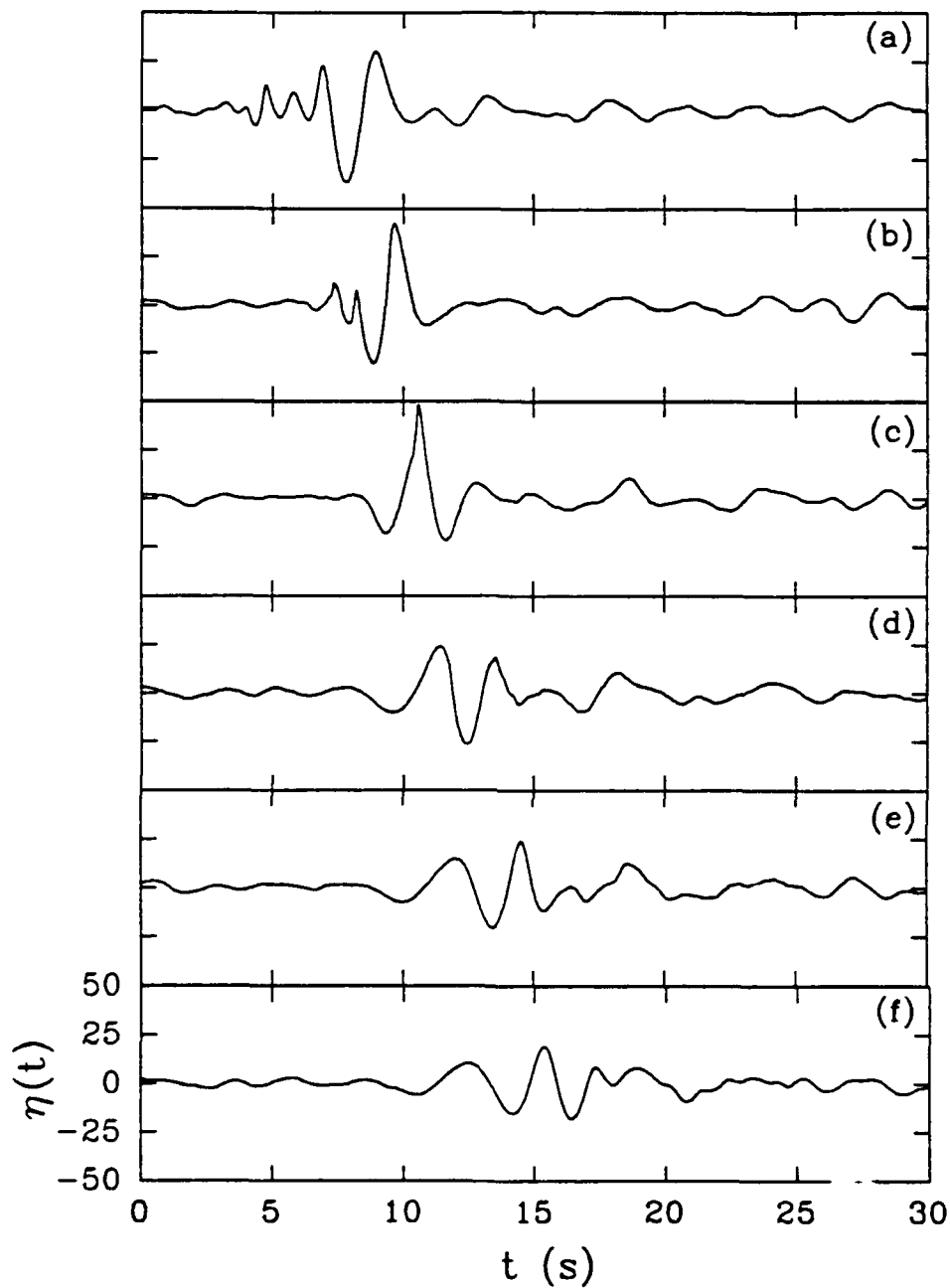


Figure 3.25 Time series of the surface displacement $\eta(t)$ (cm) for a three-dimensional breaking wave with a gain, $A = 0.70$, along the centerline of the channel at six locations. The wave paddles are located at $x = 0$ m and breaking occurs at 18.6 m: (a) 12.5 m (b) 15.5 m (c) 18.6 m (d) 21.6 m (e) 24.7 m (f) 27.7 m.

figure 3.25c the wave packet period is approximately 2 s and there is only one wave in the packet. Using this information the frequency bandwidth Δf predicted by linear theory is, $\Delta f = 1$ Hz and the center frequency, $f_c = 0.5$ Hz.

The frequency spectra of the six time series in figure 3.25 are plotted in figure 3.26. The spectrum for the time series closest to the paddle is shown in figure 3.26a and the peak spectrum level occurs at 0.53 Hz and the bandwidth is approximately 1 Hz in agreement with linear theory. Energy is lost from the wave height spectrum due to breaking and also because downstream of the focal point the waves propagate away from the centerline towards the sides of the channel. This can be seen in figure 3.27 which is a contour plot of the surface displacement variance, defined in equation 2.14, for the wave with gain, $A = 0.70$. Upstream of the breaking location, for $x < 18.6$ m., the variance shows that the wave energy tended to be focused toward the centerline. Then downstream of breaking, for $x > 18.6$ m the wave energy propagates more rapidly away from the centerline.

It was not possible to measure the energy dissipation for the three-dimensional breaking waves studied at OTRC. One of the reasons for this was that the fractional amount of energy dissipated by three-dimensional breaking events is likely much smaller and therefore harder to detect than for two-dimensional breaking. This is because typically when a three-dimensional wave breaks only a section of the wave crest actually breaks. The three-dimensional breaker is steeper near the center and breaking first begins at this location and then spreads laterally across the wave parallel to the crest. Therefore the three-dimensional wave may only break along a small fraction of its crest unlike the two-dimensional breakers which always break across the entire crest. If breaking occurs across only a fraction of the crest then the fractional energy dissipation would be expected to be much lower than the case when breaking occurs across the entire crest.

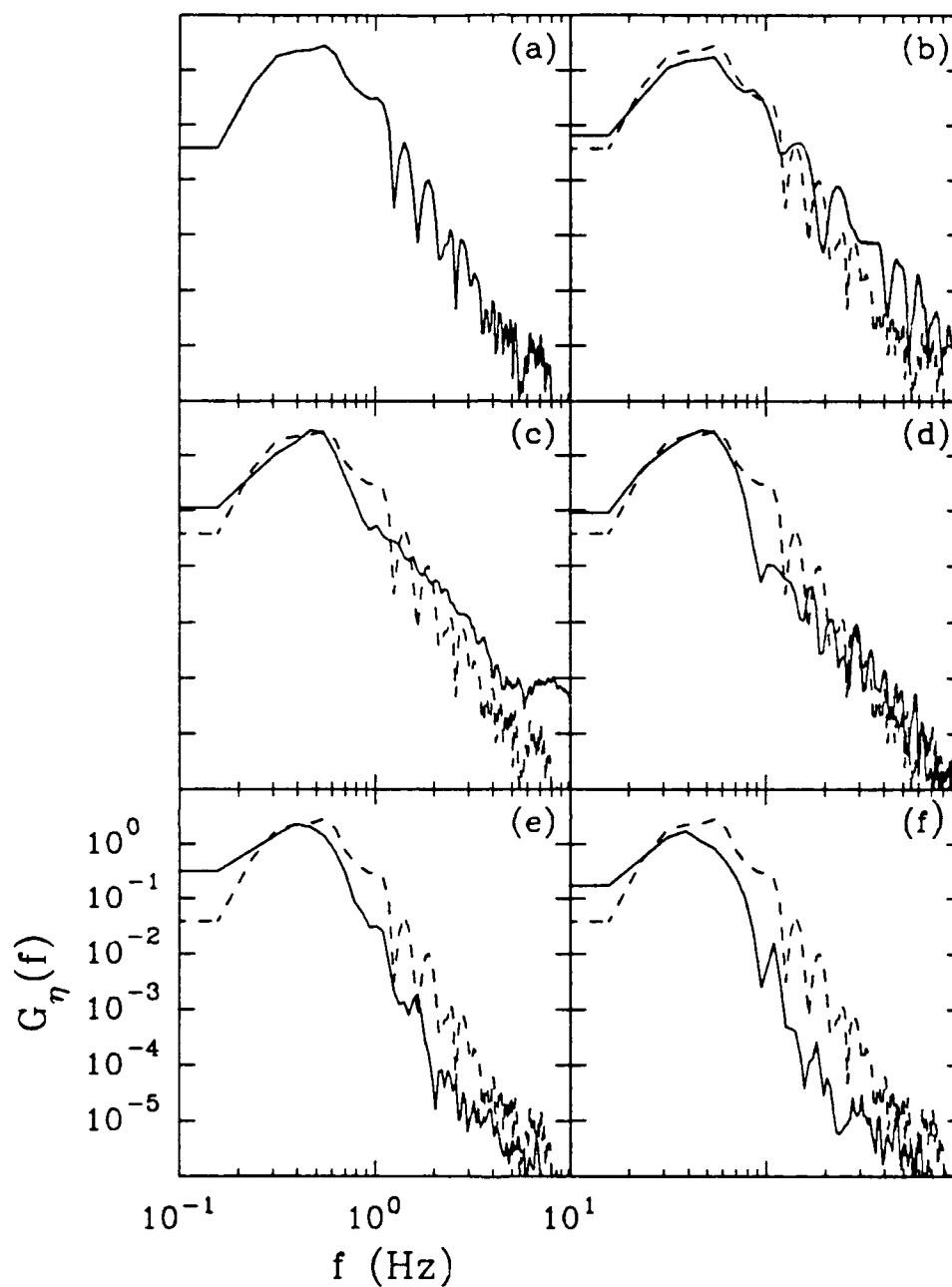


Figure 3.26 Frequency spectra of the surface displacement data plotted in figure 3.25. The dotted line in figure (b) to (f) is the reference upstream spectrum at 18.6 m: (a) 12.5 m (b) 15.5 m (c) 18.6 m (d) 21.6 m (e) 24.7 m (f) 27.7 m.

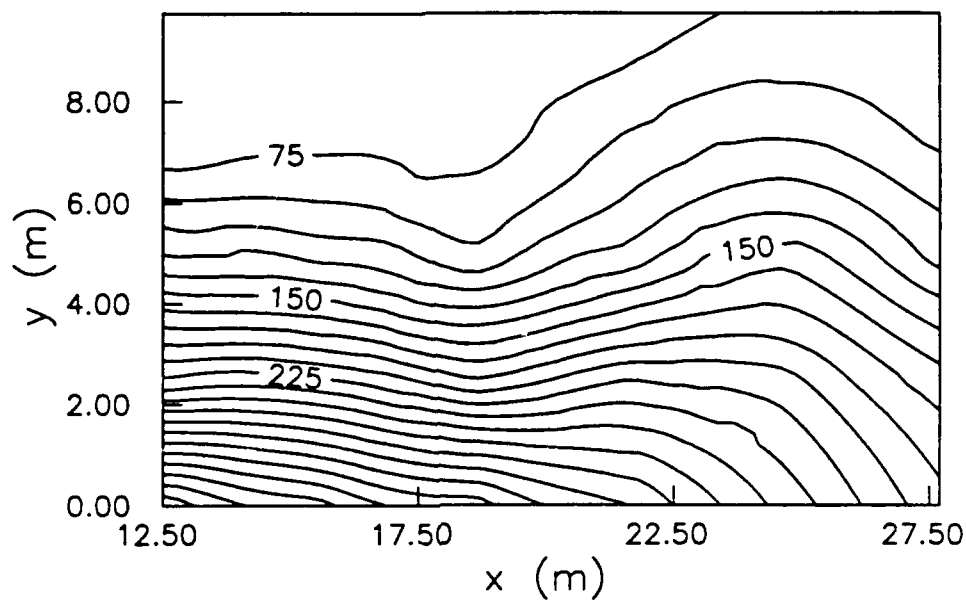


Figure 3.27 Contour plot of the surface displacement variance (cm^2) averaged over the entire signal duration. The x axis is the distance along the channel from the wave paddles and the y axis is the distance across the channel. $y = 0$ is the centerline of the channel and the wave paddles are located at $x = 0 \text{ m}$. Waves propagated from left to right in this coordinate system.

Another reason the energy dissipation could not be measured was that the metal screen wave absorbing beach did not absorb the incident wave energy very effectively and the resulting surface oscillations persisted in the tank for up to 20 minutes. The time between successive breaking events was 2 minutes and while this did not appear to significantly affect the repeatability of the breaking events it did impair our attempts to measure the energy dissipation. The measurement of energy dissipation by three-dimensional breaking waves is clearly a difficult task requiring extensive resources and planning. The primary motivation for the experiments at OTRC was to study the sound radiated by three-dimensional breaking waves and compare this to the measurements from the two-dimensional breaking experiments at MIT. Comparisons between the two data sets were still possible because the three-dimensional waves could be characterized by the gain which is proportional to the wave amplitude and slope.

3.4.2 Sound

The effect of acoustic reflections from the bottom and the sidewalls of the wave tank at OTRC were found to be negligible. The hydrophones were mounted approximately 1.9 meters below the water surface 3.9 m above the tank bottom. For this configuration a sound pulse originating at the surface and then reflected off the tank bottom would be reduced in power by 18 dB due to spherical spreading alone. Measurements were made of the sound reflected from the tank bottom and sidewalls. The two hydrophones were configured as illustrated in figure 3.22, with one acting as a transmitter and the other as a receiver. Pulses at 10 kHz were transmitted and the received time series was analyzed to determine the amplitude of the bottom and sidewall reflections. The direct path signal and the signal reflected from the water surface were clearly visible in the time series. At later times there were several reflected pulses just visible above the background noise. The ratio of the sound power contained in the direct

and surface reflected pulses to that in the later bottom and sidewall reflected pulses was 19 dB. From these results it was concluded that the effects of reverberation in this wave tank were negligible.

The hydrophones were placed directly beneath the breaking events to avoid the effects of any modal cut-off frequencies. The cut-off frequencies F_c are given by ,

$$F_c = \frac{c}{2\pi} (k_z^2 + k_y^2)^{1/2} \quad 3.2$$

where k_z is the vertical wavenumber and k_y is the horizontal wavenumber (see also equation 2.19). The OTRC wave channel is 45.7 m long, 30.5 m wide and 5.8 m deep and therefore $k_z \gg k_y$ whether k_y is calculated using 45.7 m or 30.5 m. Therefore k_y can be neglected and the lowest three cut-off frequencies for this tank are 65 Hz, 194 Hz and 324 Hz for sound propagating across or along the channel.

In figures 3.28, 3.29 and 3.30 typical time series and spectrographs of signals received by the two hydrophones and the microphone are plotted. This data is for the largest amplitude wave with gain, $A = 0.70$. The signals were conditioned using set-up I described in figure 3.23. The underwater sound due to breaking is almost hidden in the background noise in the two time series in figures 3.28 and 3.29. However, it is easily detected in the spectrographs where the spectral levels over the entire frequency range from 0 to 20 kHz increase 10 to 20 dB above the background noise levels at $t = 1.4$ s when the wave plunges over and impacts the free surface.

The microphone time series has a much better signal to noise ratio and the onset of breaking and sound production is clearly observed in the time series in figure 3.30 at $t = 1.4$ s. The large amplitude low frequency signal which begins at $t = 1.8$ s was caused by the reverberation of the signal inside the laboratory. The frequency of this signal is approximately 9 Hz and it remains constant as the wave amplitude is decreased. A 9 Hz

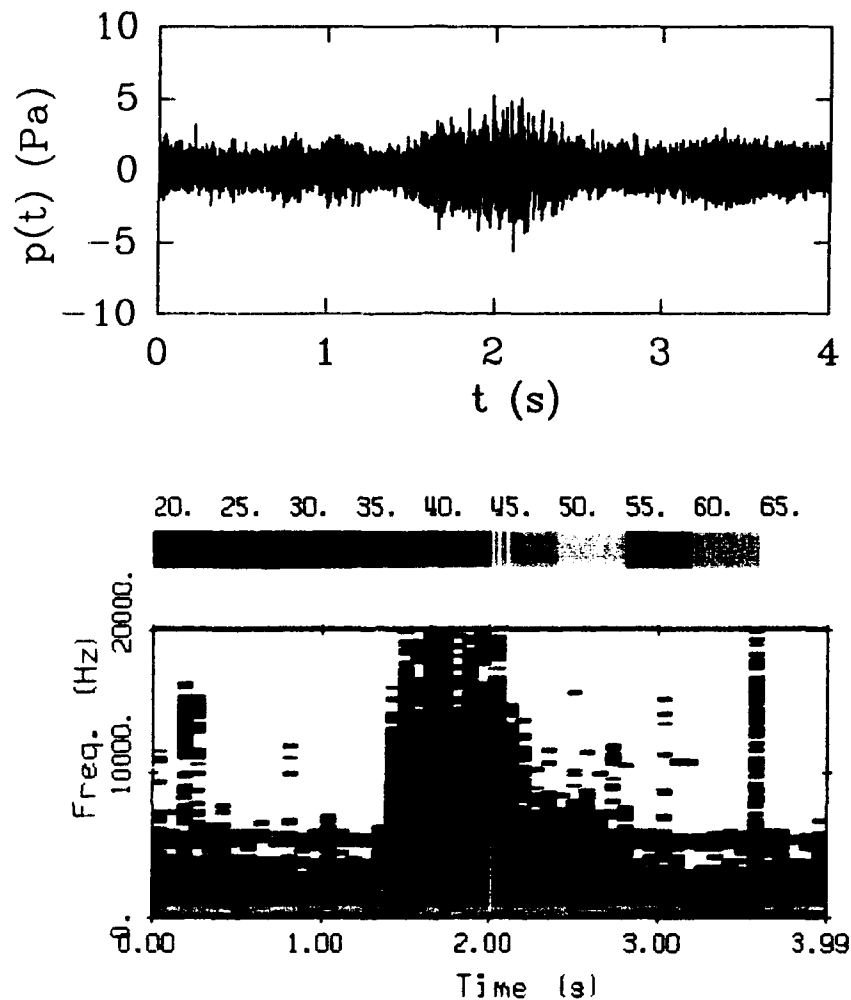


Figure 3.28 The upper plot is a time series of the acoustic pressure from the downstream hydrophone for a three-dimensional breaking wave with gain, $A = 0.70$. The signal was conditioned with set-up I shown in figure 3.24. The lower plot is a spectrograph of the time series in the upper plot. 52 spectra with a bandwidth resolution of 78 Hz are plotted. They were computed by dividing the time series into 416-512 point segments which overlapped 128 points, windowing with a Blackman-Harris window and computing FFT's which were averaged over every 8 segments. Each color corresponds to a 5 dB re $1 \mu\text{Pa}^2$ increment in spectral level.

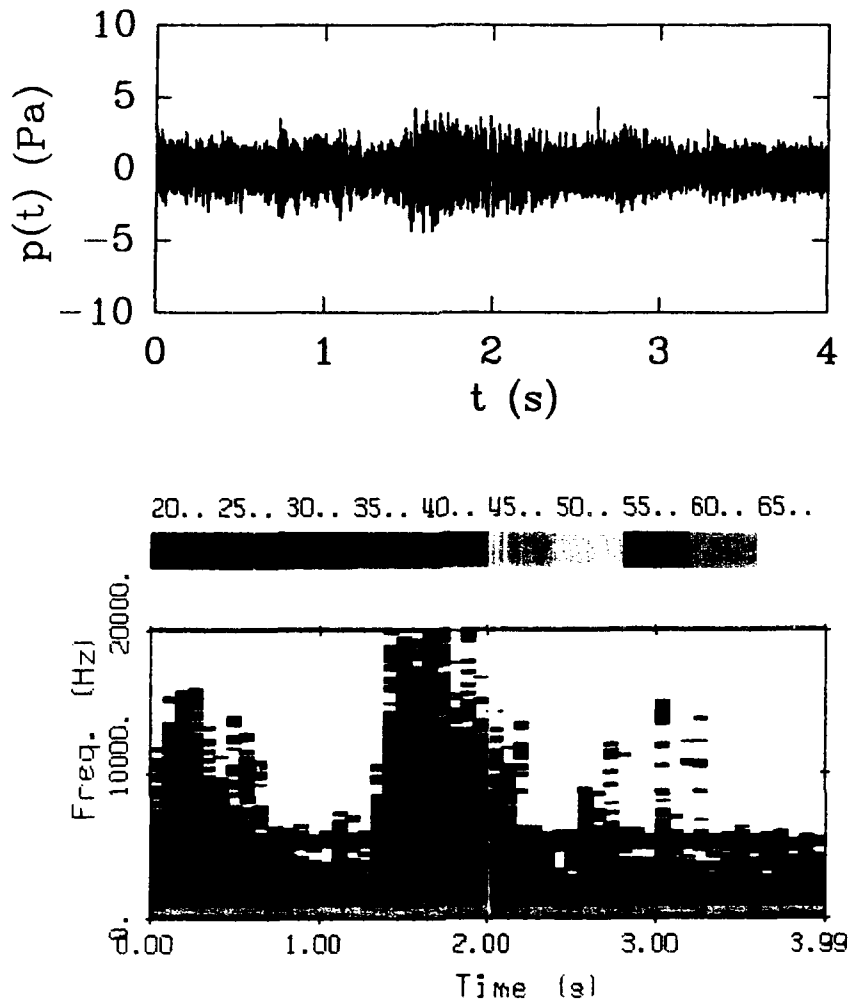


Figure 3.29 The upper plot is a time series of the acoustic pressure from the upstream hydrophone for a three-dimensional breaking wave with gain, $A = 0.70$. The signal was conditioned with set-up I shown in figure 3.24. The lower plot is a spectrograph of the time series in the upper plot. 52 spectra with a bandwidth resolution of 78 Hz are plotted. They were computed by dividing the time series into 416-512 point segments which overlapped 128 points, windowing with a Blackman-Harris window and computing FFT's which were averaged over every 8 segments. Each color corresponds to a 5 dB re $1 \mu\text{Pa}^2$ increment in spectral level.

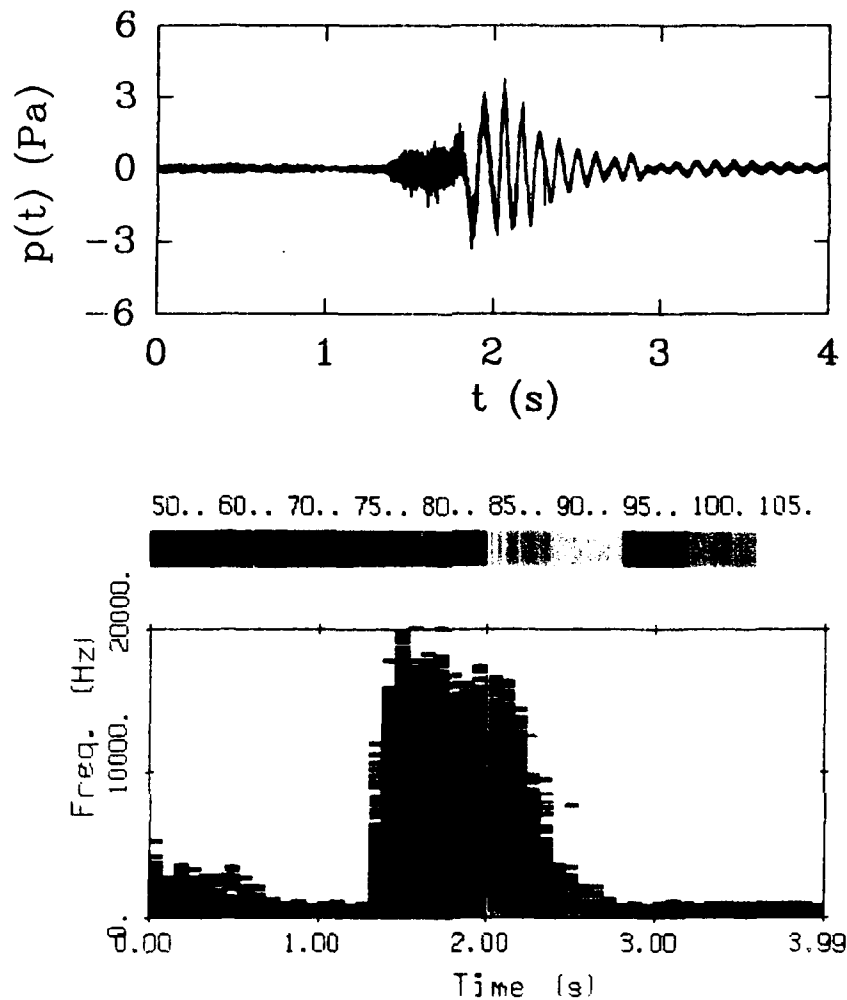


Figure 3.30 The upper plot is a time series of the acoustic pressure from the microphone for a three-dimensional breaking wave with gain, $A = 0.70$. The signal was conditioned with set-up I shown in figure 3.24. The lower plot is a spectrograph of the time series in the upper plot. 52 spectra with a bandwidth resolution of 78 Hz are plotted. They were computed by dividing the time series into 416-512 point segments which overlapped 128 points, windowing with a Blackman-Harris window and computing FFT's which were averaged over every 8 segments. Each color corresponds to a 5 dB re $1 \mu\text{Pa}^2$ increment in spectral level.

sound wave in air has a wavelength of 38 m and the width of the lab was approximately 38 m. The walls were made of concrete blocks and can be assumed to be rigid therefore $1/2, 1, 3/2 \dots$ of a wavelength would satisfy the boundary conditions at each wall. The lowest frequency which would form a standing wave between the two walls is 4.5 Hz corresponding to a wave length of 76 m. The response of the microphone is flat down to 20 Hz and then rolls off as the frequency is decreased. As a result even if the lower frequency, 4.5 Hz, mode were excited it is not likely that it would appear in the microphone signal unless its amplitude was extremely large. The 9 Hz mode is also below the pass band of the microphone but evidently it was a very large amplitude signal and the response has not decreased sufficiently to filter it out. Similar to the underwater sound spectrographs the spectral levels of the microphone signal increase rapidly at $t = 1.4$ s and the spectral levels decrease with increasing frequency.

Frequency spectra averaged over 5 repeats of the same wave amplitude and smoothed with a 9 point Bartlett window to give 80 degrees of freedom are shown plotted in figures 3.31, 3.32 and 3.33 for the two channels of hydrophone data and the single channel of microphone data. The hydrophone signals were band pass filtered from 10 Hz to 20 kHz and notch filtered from 200 to 340 Hz and the microphone signal was low pass filtered at 20 kHz. The six spectra in each figure correspond to a range in gain of, $A = 0.24$ to 0.70. The lowest gain, $A = 0.24$, is the incipient case for which no breaking occurs and in each figure it is the lowest amplitude spectra. The frequency band from 200 Hz to 800 Hz in the underwater sound data is dominated by background machinery generated noise. The two hydrophone spectra show almost no variation in spectral levels with increasing wave amplitude in this frequency range, indicative of a very poor signal to noise ratio. The spectra of the microphone signal also have large spectral peaks within the same frequency range but the signal to noise ratio is much larger.

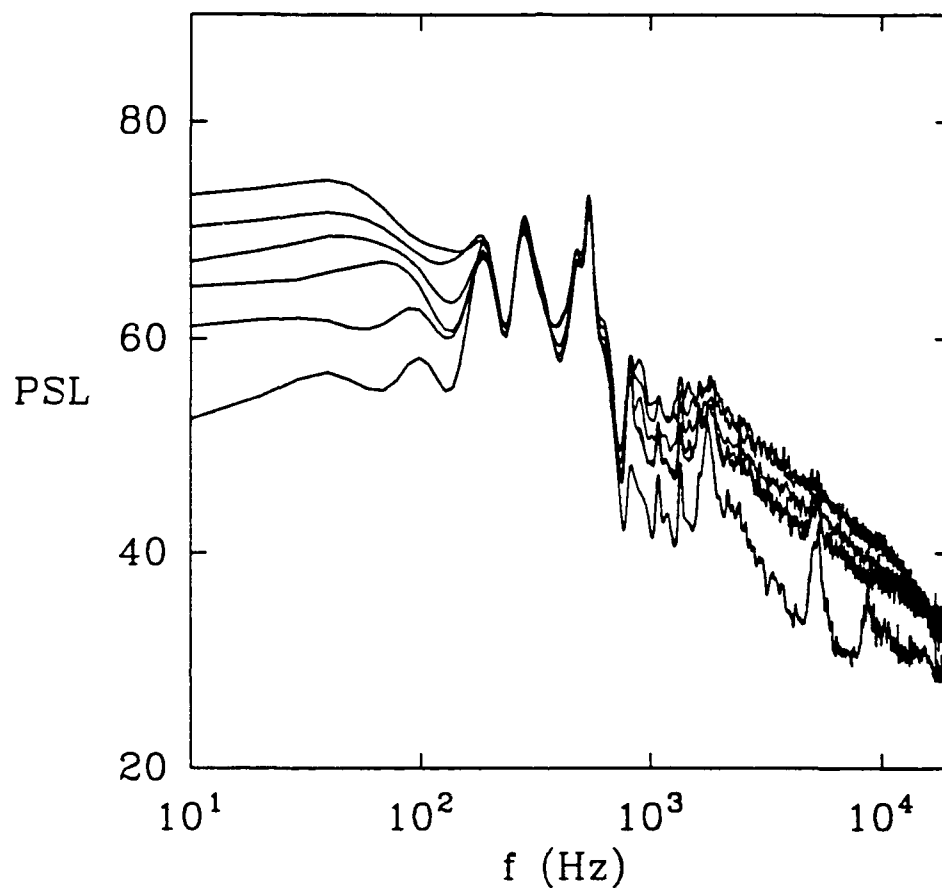


Figure 3.31 Frequency spectra of the signal from the downstream hydrophone conditioned using set-up I (see figure 3.24) for the three-dimensional breaking events with gains, $A = 0.24, 0.40, 0.475, 0.55, 0.675$ and 0.70 . Pressure spectrum level PSL in dB re $1 \mu\text{Pa}^2/\text{Hz}$. Each spectrum was averaged over 5 repeats of the same event and was then smoothed with a 9 point Bartlett window to produce an estimate with 80 degrees of freedom.

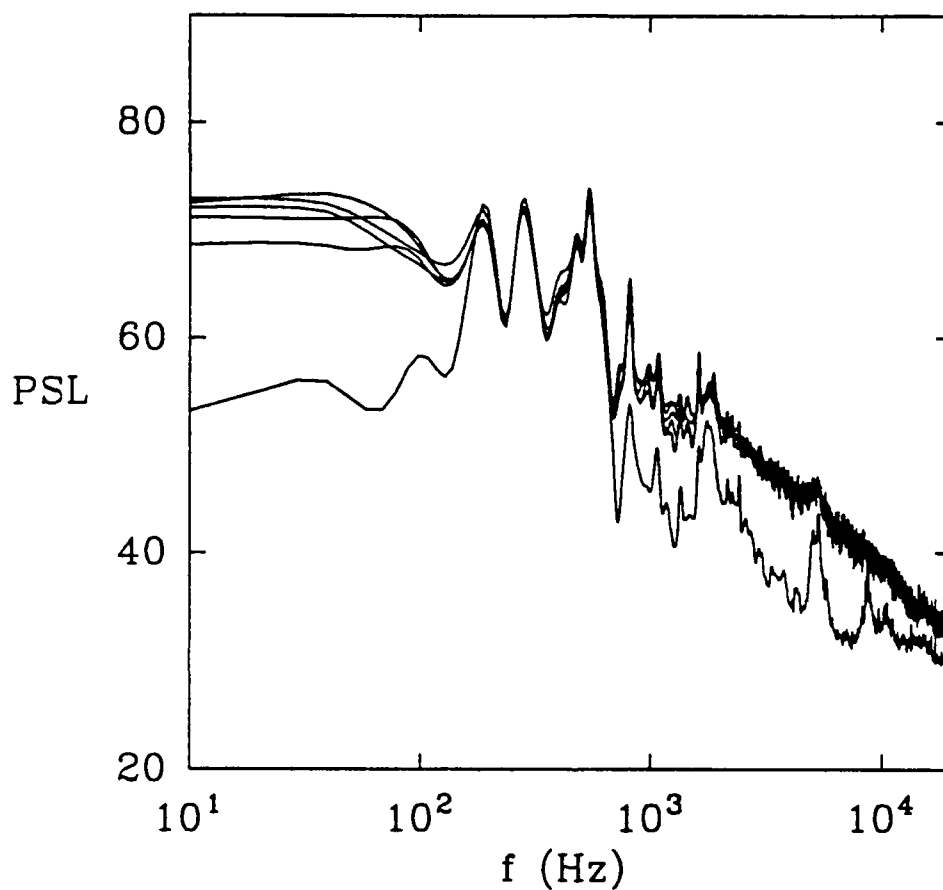


Figure 3.32 Frequency spectra of the signal from the upstream hydrophone conditioned using set-up I (see figure 3.24) for the three-dimensional breaking events with gains, $A = 0.24, 0.40, 0.475, 0.55, 0.675$ and 0.70 . Pressure spectrum level PSL in dB re $1 \mu\text{Pa}^2/\text{Hz}$. Each spectrum was averaged over 5 repeats of the same event and was then smoothed with a 9 point Bartlett window to produce an estimate with 80 degrees of freedom.

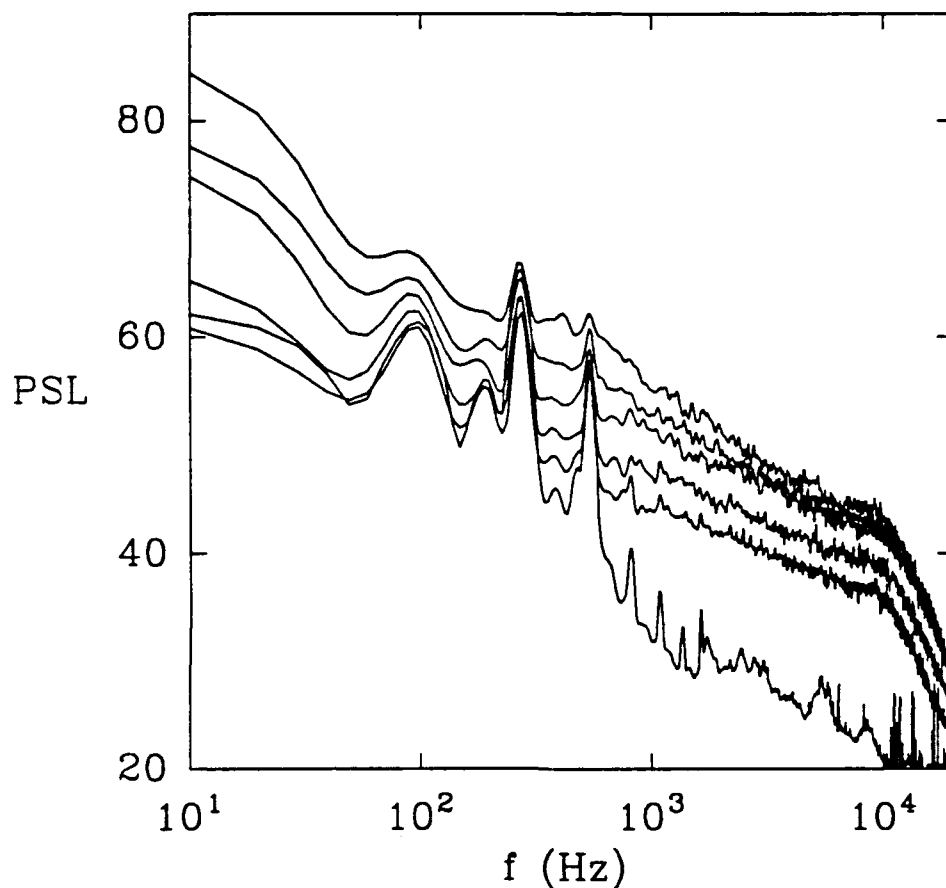


Figure 3.33 Frequency spectra of the signal from the microphone conditioned using set-up I (see figure 3.24) for the three-dimensional breaking events with gains, $A = 0.24, 0.40, 0.475, 0.55, 0.675$ and 0.70 . Pressure spectrum level PSL in dB re $1 \mu\text{Pa}^2/\text{Hz}$. Each spectrum was averaged over 5 repeats of the same event and was then smoothed with a 9 point Bartlett window to produce an estimate with 80 degrees of freedom.

The underwater sound spectra have several notable features. There is no evidence of the modal structure in the form of cut-off frequencies in the spectra. The lowest amplitude event for which breaking occurred had a gain, $A = 0.40$, and the spectral levels for this event are 5 to 10 dB higher than those for the incipient event. There is significant low frequency sound energy in the spectra at frequencies < 200 Hz and this energy increased as the amplitude of the breaking event was increased. For frequencies > 1 kHz the two underwater sound spectra have an almost constant slope of -5 to -6 dB per octave. This is the same slope as Knudsen (1948) and Wenz (1962) observed in frequency spectra of oceanic ambient noise.

The spectra from both hydrophones have a similar shape and are approximately the same level above the incipient event spectrum. However, the spectra of the data from the hydrophone mounted closer to the wave paddles, plotted in figure 3.32, show a much smaller variation in level as the wave amplitude increases. This is caused by the fact that the different amplitude waves break at different locations and spectral levels would be expected to vary as $1/r^2$ (r = range) because of spherical spreading. As the wave amplitude was increased the waves broke progressively further downstream. Knowing the locations of the two receivers and assuming the sound generated by breaking originates at the still water surface the mean square signal levels for $f > 1$ kHz can be used to calculate the location of the sound source. This was done for the five breaking events and the results showed that the location of the sound source for all of the breaking events was located between the two hydrophones. The lowest amplitude event was closer to the upstream hydrophone and as the wave amplitude increased the events moved closer to the downstream hydrophone. These calculations were confirmed by viewing a video taken from directly above the events which confirmed that as the amplitude was increased the waves broke further downstream.

The spectra of the sound data from the microphone, plotted in figure 3.33, are similar in character to the underwater sound spectra. The spectral peaks due to

background noise do not dominate the spectra from 200 Hz to 800 Hz to as great an extent as in the case of the underwater sound spectra. There is significant acoustic energy produced by breaking across the entire spectra from 10 Hz to 10 kHz. As in the spectra of the hydrophone signal there is significant energy at $f < 200$ Hz and the spectral levels increased consistently as the wave amplitude was increased. The spectra slope at approximately -4 dB per octave in from 500 Hz to 10 kHz slightly flatter than the Knudsen (1948) and Wenz (1962) spectra. The sharp roll-off of the spectra at 10 kHz is due to the low pass filter ¹.

The variation of the mean square acoustic pressure with time, for the two channels of hydrophone data and the single channel of microphone data are shown in figures 3.34, 3.35 and 3.36. The lower curves are for the frequency band 1 kHz to 20 kHz and the upper curves are for the band from 0 Hz to 1 kHz. The mean square acoustic pressure remains essentially constant for all channels in both frequency bands for the incipient breaking event. At a gain, $A = 0.40$, the energy in the higher band increases significantly above the background levels for all three channels of data. The first evidence of low frequency sound is seen in figure 3.35e which corresponds to the upstream hydrophone and the event with a gain of, $A = 0.40$. As the amplitude of the waves was increased the levels in both bands continued to increase.

The mean square acoustic pressure in the two bands, $f = 0$ to 150 Hz and $f = 150$ to 500 Hz for the three instruments was calculated and are plotted in figures 3.37, 3.38 and 3.39. These figures show that the majority of the low frequency sound produced by breaking is at frequencies < 150 Hz. There was almost no variation in the PSL of the hydrophone signals in the band from 150 Hz to 500 Hz as the amplitude of the wave was varied. The duration of the low frequency microphone signal is longer than the

¹ It was originally planned that the microphone signal would be low pass filtered at 20 kHz. However, at the start of the experiment either the filter was set incorrectly to low pass at 10 kHz or the filter frequency indicator dial was misaligned and showed 20 kHz when it was actually set at 10 kHz.

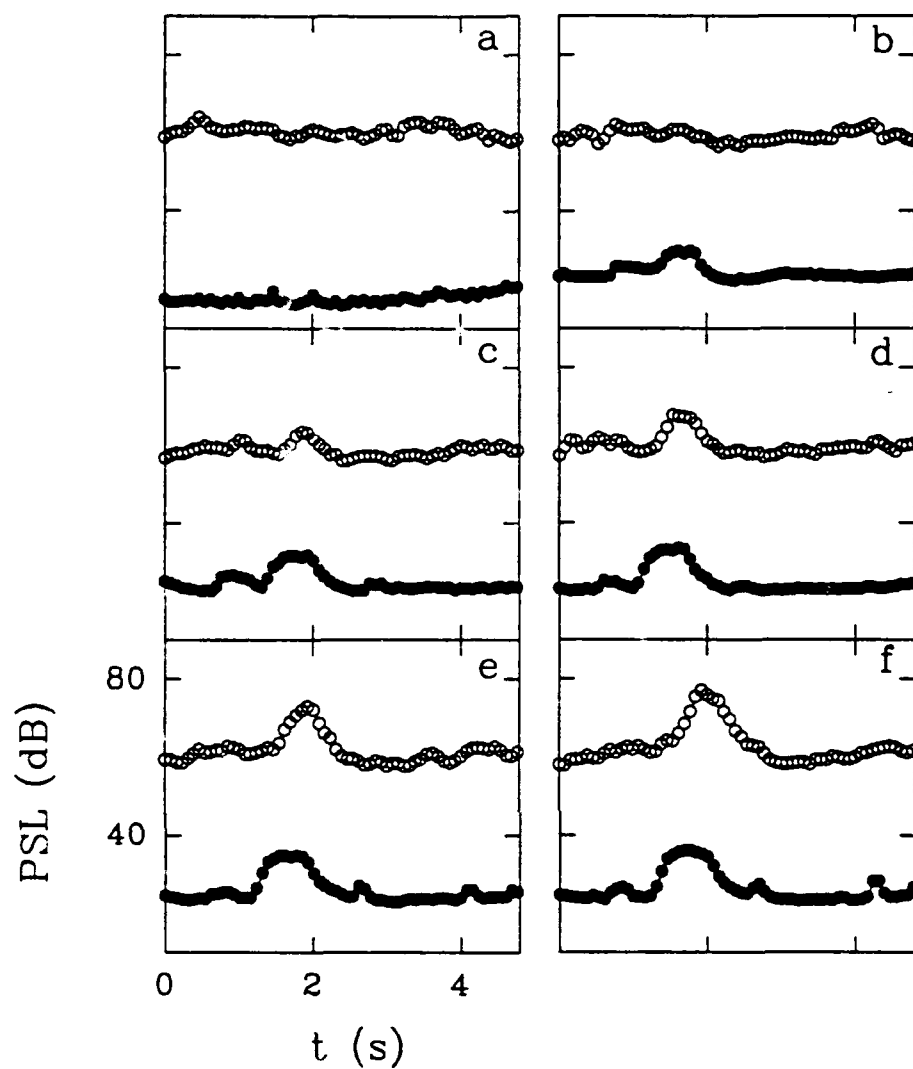


Figure 3.34 The pressure spectrum level PSL (dB re $1\mu\text{Pa}^2/\text{Hz}$) of the signal from the downstream hydrophone as a function of time in two frequency bands for the three-dimensional breaking events. Each data point is the average of at least 3 repeats of the event. (a) $A = 0.24$ (b) $A = 0.40$ (c) $A = 0.475$ (d) $A = 0.55$ (e) $A = 0.625$ (f) $A = 0.70$. \circ , 10Hz-1 kHz; \bullet , 1-20 kHz.

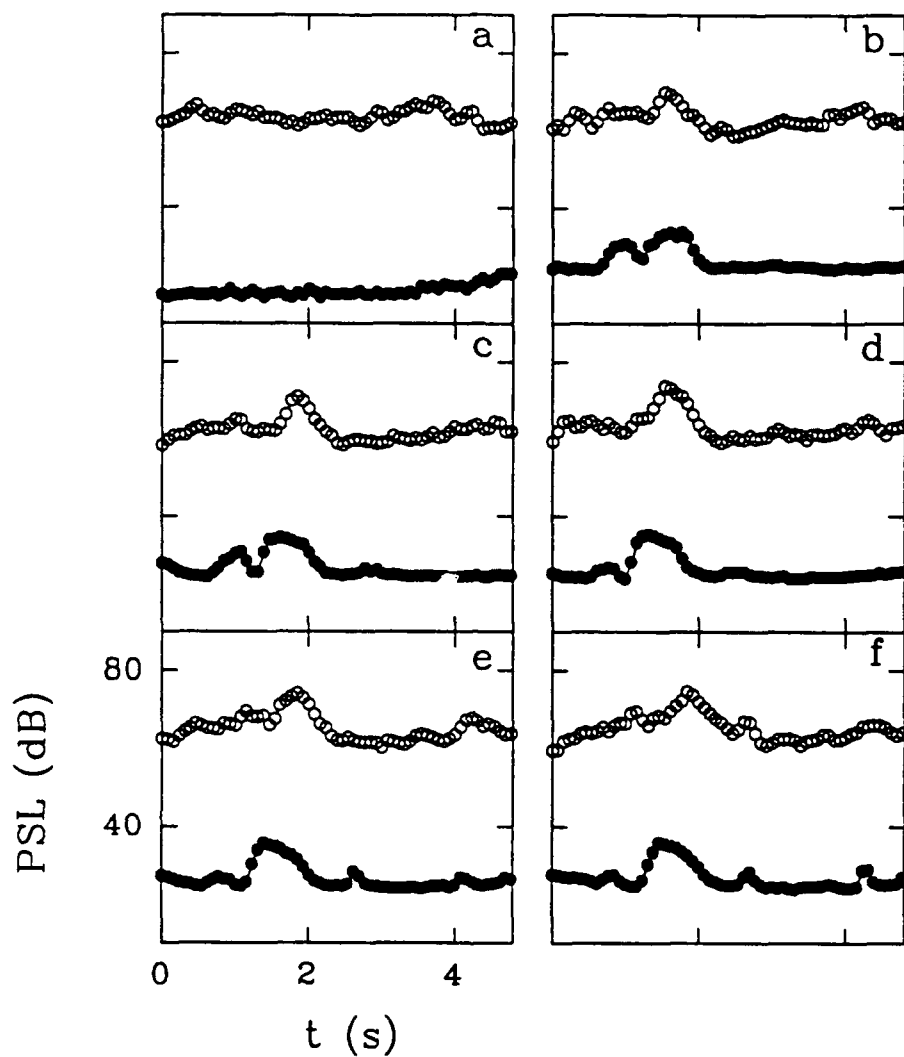


Figure 3.35 The pressure spectrum level PSL (dB re $1\mu\text{Pa}^2/\text{Hz}$) of the signal from the upstream hydrophone as a function of time in two frequency bands for the three-dimensional breaking events. Each data point is the average of at least 3 repeats of the event. (a) $A = 0.24$ (b) $A = 0.40$ (c) $A = 0.475$ (d) $A = 0.55$ (e) $A = 0.625$ (f) $A = 0.70$. \circ , 10Hz-1 kHz; \bullet , 1-20 kHz.

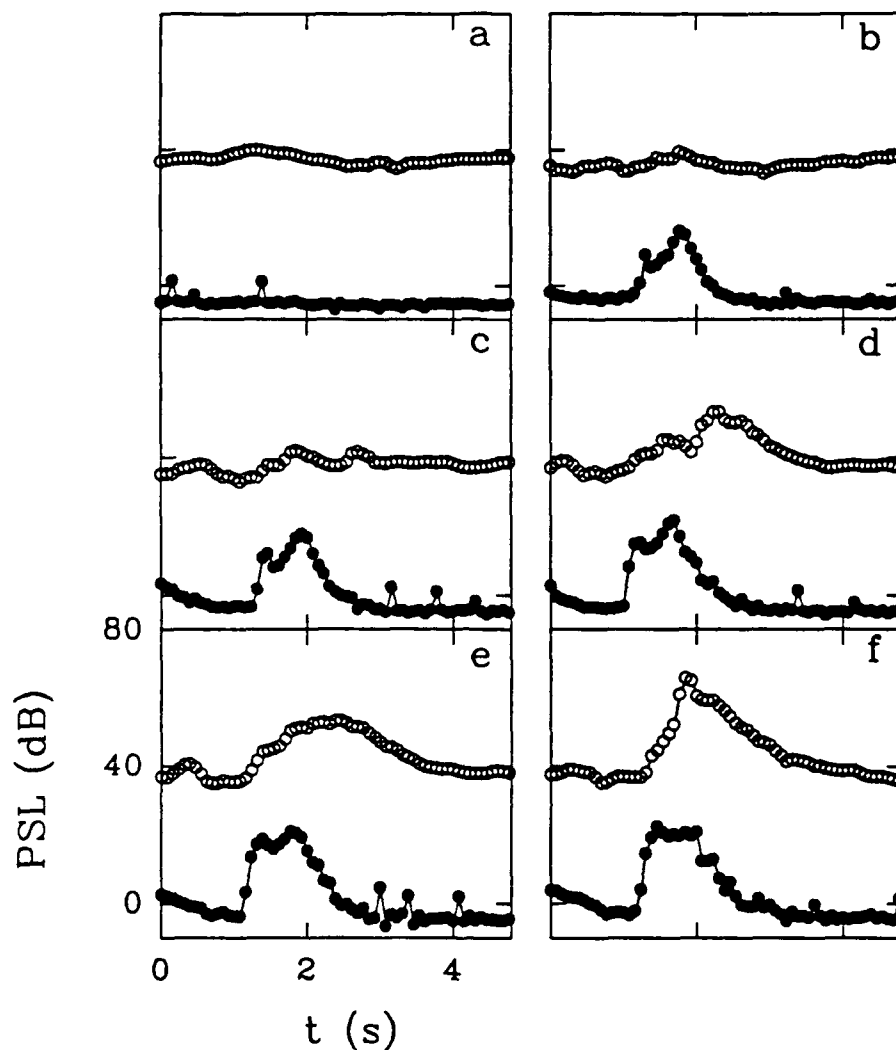


Figure 3.36 The pressure spectrum level PSL (dB re $1\mu\text{Pa}^2/\text{Hz}$) of the signal from the microphone as a function of time in two frequency bands for the three-dimensional breaking events. Each data point is the average of at least 3 repeats of the event. (a) $A = 0.24$ (b) $A = 0.40$ (c) $A = 0.475$ (d) $A = 0.55$ (e) $A = 0.625$ (f) $A = 0.70$. ○, 10Hz-1 kHz; ●, 1-20 kHz.

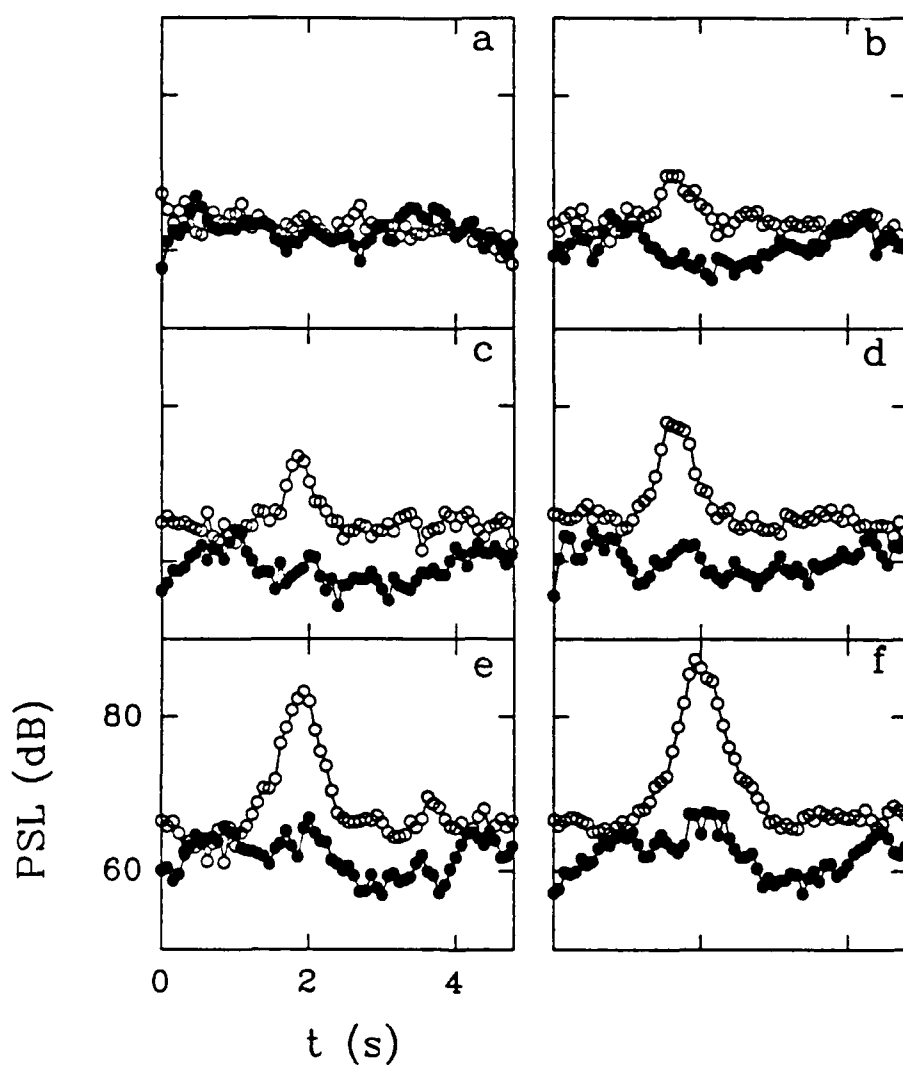


Figure 3.37 The pressure spectrum level PSL (dB re $1\mu\text{Pa}^2/\text{Hz}$) of the signal from the downstream hydrophone as a function of time in two lower frequency bands for the three-dimensional breaking events. Each data point is the average of at least 3 repeats of the event. (a) $A = 0.24$ (b) $A = 0.40$ (c) $A = 0.475$ (d) $A = 0.55$ (e) $A = 0.625$ (f) $A = 0.70$. \circ , 10-150 Hz; \bullet , 150-500 Hz.

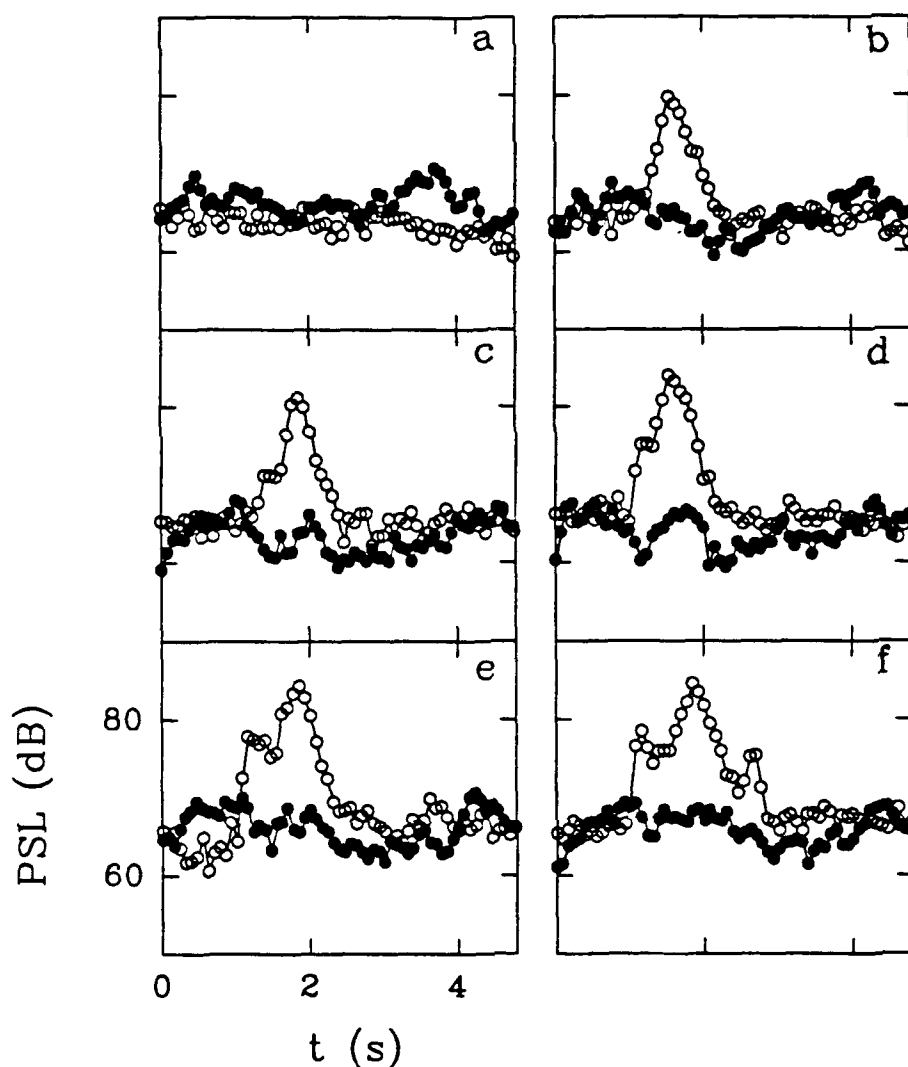


Figure 3.38 The pressure spectrum level PSL (dB re $1\mu\text{Pa}^2/\text{Hz}$) of the signal from the upstream hydrophone as a function of time in two lower frequency bands for the three-dimensional breaking events. Each data point is the average of at least 3 repeats of the event. (a) $A = 0.24$ (b) $A = 0.40$ (c) $A = 0.475$ (d) $A = 0.55$ (e) $A = 0.625$ (f) $A = 0.70$. \circ , 10-150 Hz; \bullet , 150-500 Hz.

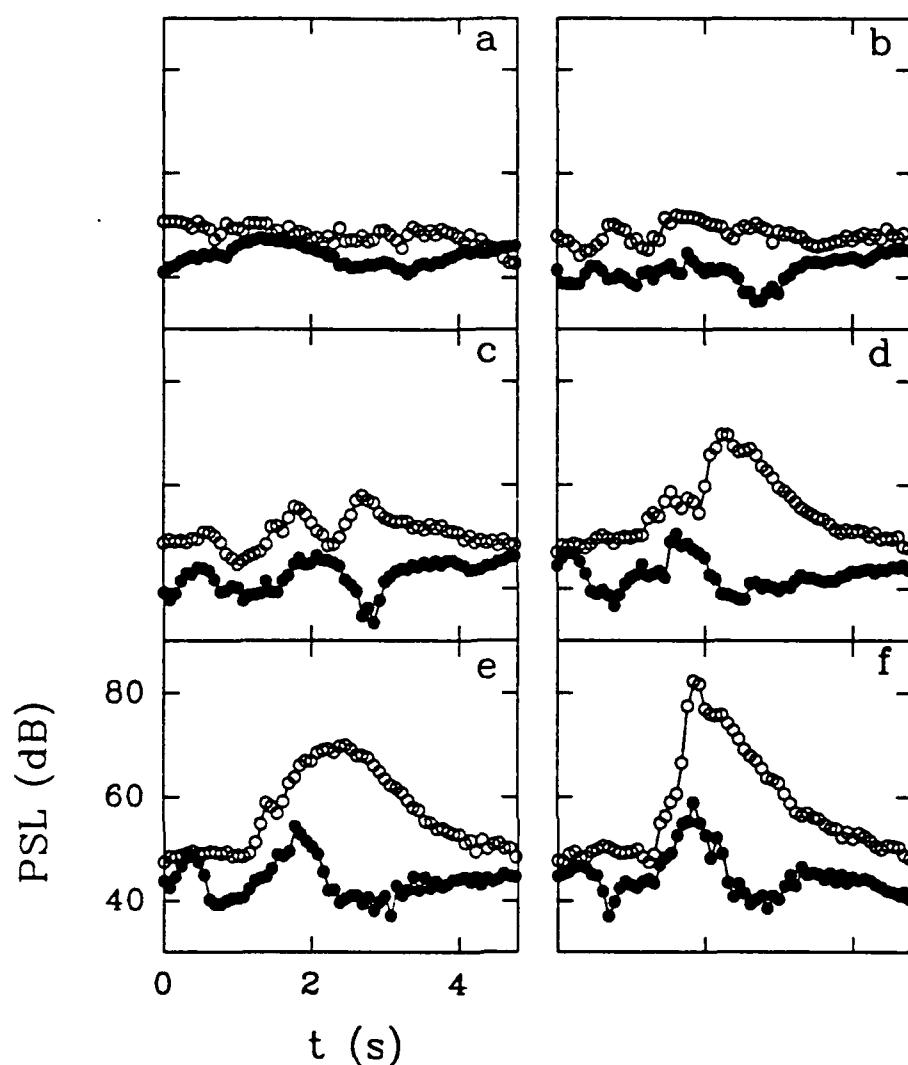


Figure 3.39 The pressure spectrum level PSL (dB re $1\mu\text{Pa}^2/\text{Hz}$) of the signal from the microphone as a function of time in two lower frequency bands for the three-dimensional breaking events. Each data point is the average of at least 3 repeats of the event. (a) $A = 0.24$ (b) $A = 0.40$ (c) $A = 0.475$ (d) $A = 0.55$ (e) $A = 0.625$ (f) $A = 0.70$. \circ , 10-150 Hz; \bullet , 150-500 Hz.

hydrophone signal because of the reverberation of the signal within the laboratory building as discussed earlier.

The mean square acoustic pressure, $\overline{p^2}$, in the two frequency bands, 0 to 1 kHz and 1 kHz to 20 kHz, was calculated over the entire signal duration for the two channels of hydrophone data and is shown plotted as a function of the gain in figure 3.40. The upper plot is for the frequency band 0 to 1 kHz and the lower plot for 1 kHz to 20 kHz. The log of the mean square acoustic pressure in the lower band is constant for the lowest three gains and then increases proportionally with the gain. In the higher band the log of the mean square acoustic pressure increases rapidly when the gain increases from 0.24 to 0.40 and then increases slowly for $A > 0.40$. The error bars indicate the 95% confidence limits of the data. The mean square acoustic pressure of the higher band had very little scatter with the 95% confidence limits plotting within the symbol size. The 95% confidence limits of the mean square acoustic pressure of the lower band is much larger, indicating that the lower frequency signals were much less repeatable than the higher frequency signals. If the mean square acoustic pressure is calculated for the band, $f = 0$ to 150 Hz, the correlation with the gain is better. This is seen in figure 3.41 where the mean square acoustic pressure in the band from 0 to 150 Hz is plotted as a function of the gain. The log of the mean square acoustic pressure is a minimum at $A = 0.24$ and then increases at a constant rate as the gain increases to $A = 0.70$. The mean square acoustic pressure in the band from 150 to 500 Hz is shown in the lower plot in figure 3.41. The mean square acoustic pressure at the lowest and highest gains are equal and there is a minimum when $A = 0.475$. The signals in this frequency range are dominated by the background machinery noise and the observed variation of the mean square acoustic pressure with gain is not related to the dynamics of breaking.

The mean square acoustic pressure of the microphone signal in the two bands, 0 to 1 kHz and 1 kHz to 20 kHz, as a function of the gain is plotted in figure 3.42. The log of the mean square acoustic pressure in the lower band is constant for the lowest three

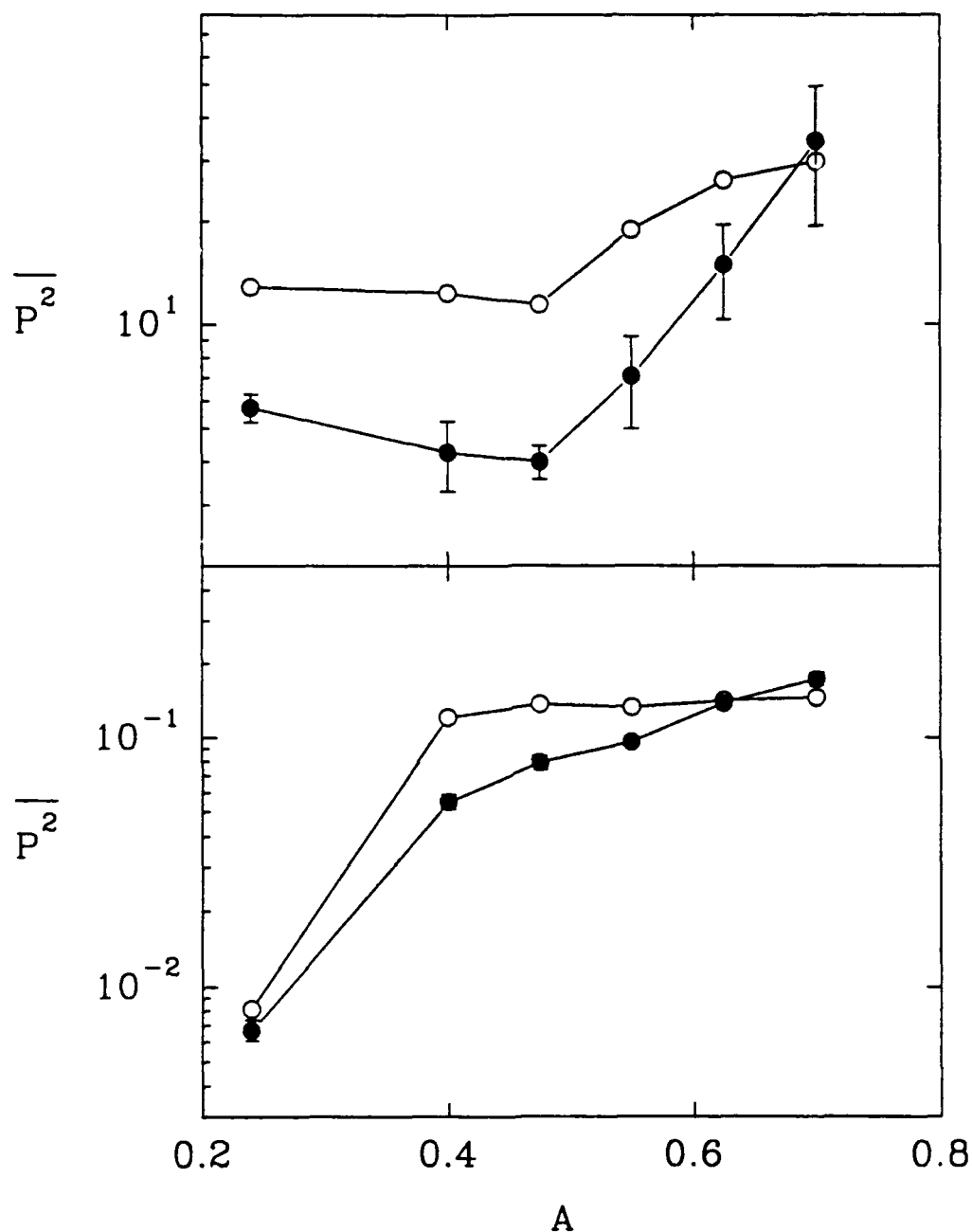


Figure 3.40 Mean square acoustic pressure $\overline{p^2}$ (Pa^2) of the two hydrophone signals calculated over the entire signal duration in two frequency bands plotted as a function of the gain A. The data in the upper plot is for the frequency band 0-1 kHz and the lower plot for 1-20 kHz. Each data point is the average of at least 3 repeats of the same event and the error bars indicate the 95% confidence limits of the data. ●, downstream hydrophone; ○, upstream hydrophone.

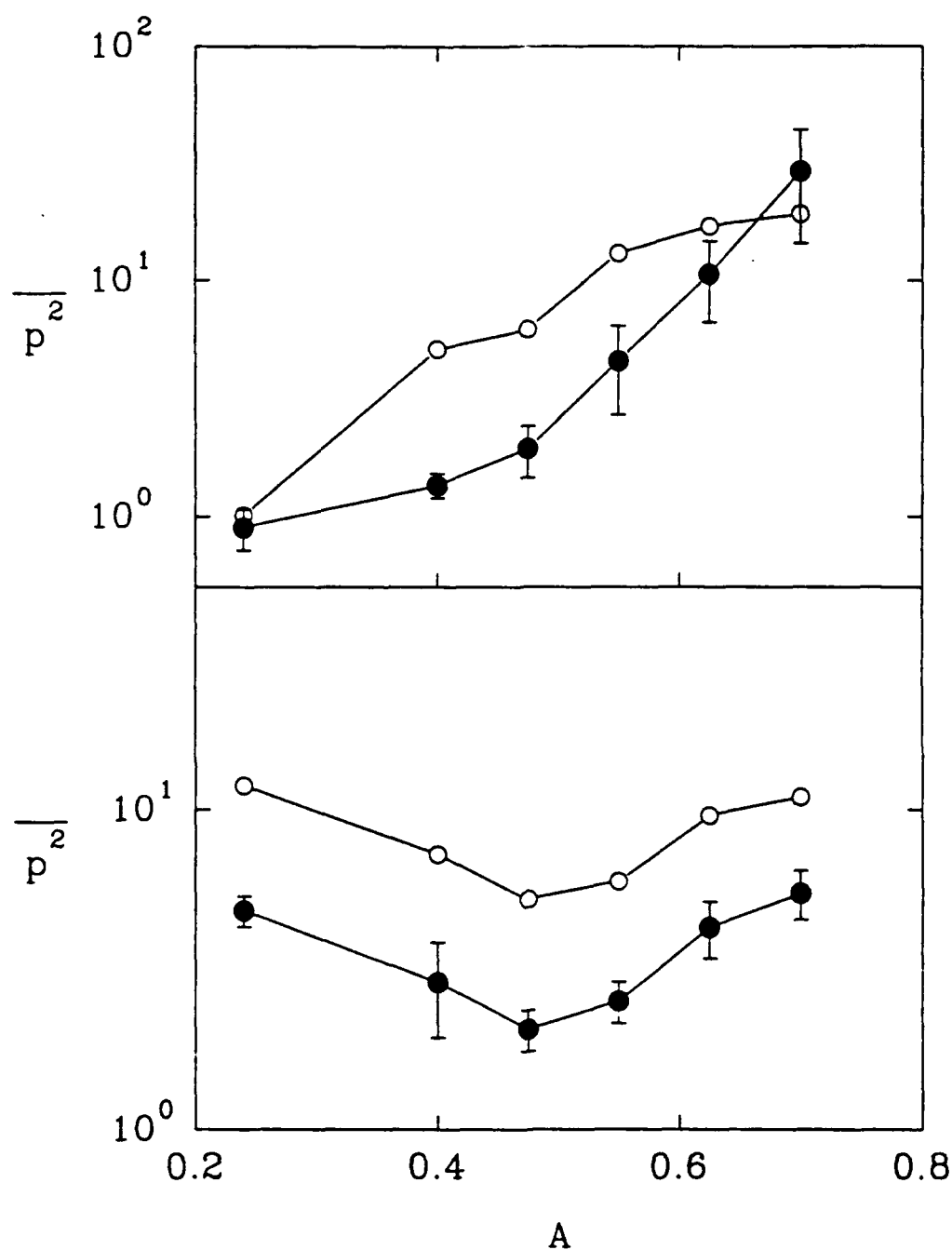


Figure 3.41 Mean square acoustic pressure $\overline{p^2}$ (Pa^2) of the two hydrophone signals calculated over the entire signal duration in two lower frequency bands plotted as a function of the gain A. The data in the upper plot is for the frequency band 0-150 Hz and the lower plot for 150-500 Hz. Each data point is the average of at least 4 repeats of the same event and the error bars indicate the 95% confidence limits of the data. ●, downstream hydrophone; ○, upstream hydrophone.

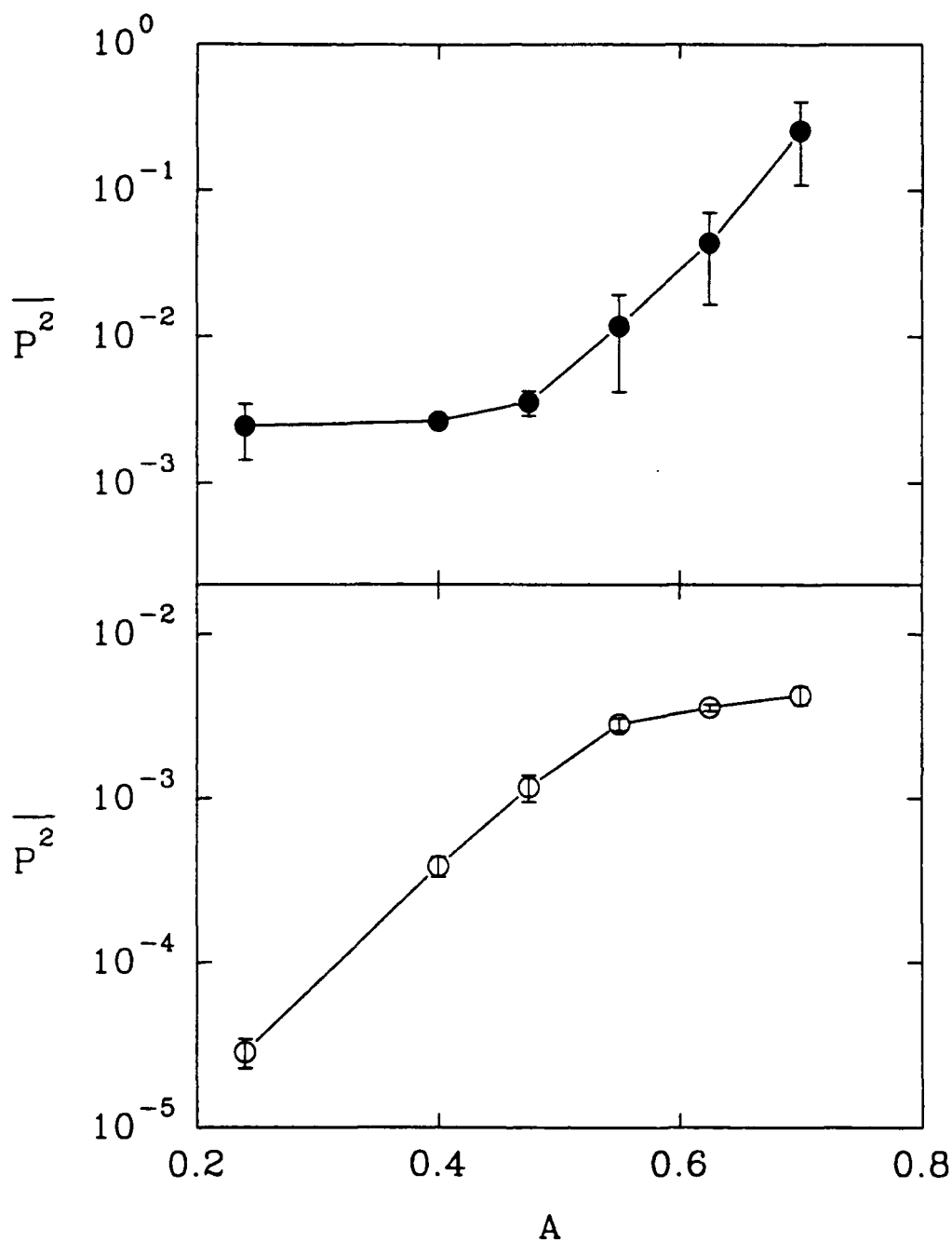


Figure 3.42 Mean square acoustic pressure $\overline{p^2}$ (Pa^2) of the microphone signal calculated over the entire signal duration in two frequency bands plotted as a function of the gain A. The data in the upper plot is for the frequency band 0-1 kHz and the lower plot for 1-20 kHz. Each data point is the average of at least 5 repeats of the same event and the error bars indicate the 95% confidence limits of the data.

gains and then increases proportionally with the gain similar to the hydrophone data. The log of the mean square acoustic pressure in the higher band increases rapidly with gain in the interval, $A = 0.24$ to 0.55 , and then less rapidly for $A > 0.55$. The scatter in the lower frequency band is much larger than that in the higher frequency band as was the case for the hydrophone data.

A video recording of the breaking events was taken from directly overhead. Traces were made of the whitecaps at various stages of breaking for the five wave amplitudes. The traces were digitized and are shown plotted in figures 3.43 to 3.47. The shapes of the whitecaps are similar for all five wave amplitudes. Initially as the wave begins to break there is a single whitecap which is formed at the very leading edge of the plunging wave crest. As the wave continues to plunge forward, the crest near the centerline accelerates faster than the crest near the edges. This produces a whitecap shape like that seen in figure 3.44b and 3.47b where the dimension parallel to the direction of wave propagation is greater at the center of the wave than at the edges. This is because as discussed earlier three-dimensional breakers begin to break near the center of the wave first and breaking spreads laterally across the crest as time progresses. As the plunging crest impacts the free surface a secondary jet of water is ejected out in front of the initial whitecap and this forms a second whitecap. This second whitecap can be seen clearly in frame (c) or (d) in all five figures. The integrated area and the maximum area of each whitecap was calculated and are plotted as a function of the wave gain in figure 3.48. The integrated area and the maximum area both increase almost linearly with the gain.

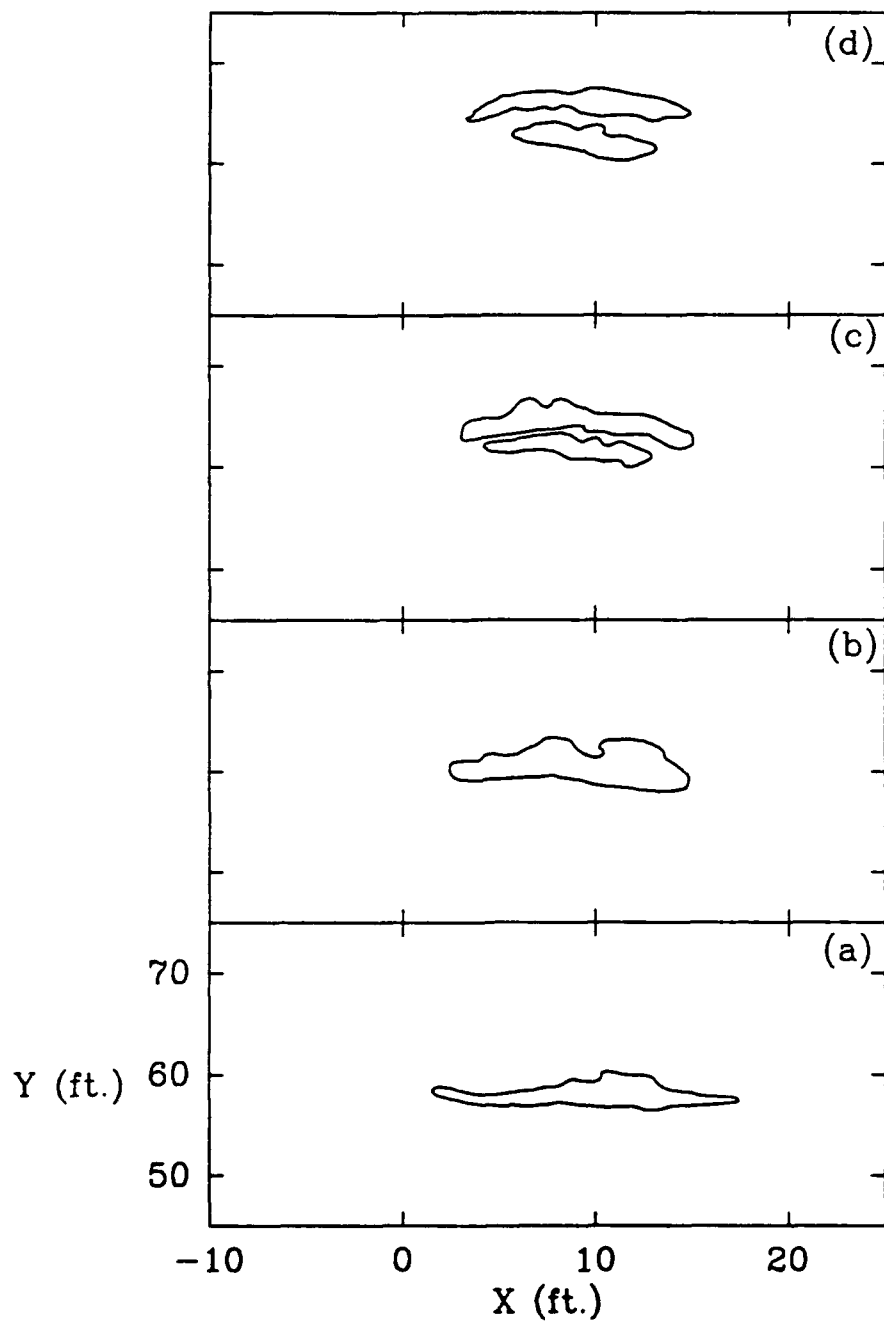


Figure 3.43 Plan view of the whitecap generated by the three-dimensional breaking event with $A = 0.40$. The time is referenced to plot (a) for which $t = 0$ s (b) $t = 0.2$ s (c) $t = 0.47$ s (d) $t = 0.67$ s.

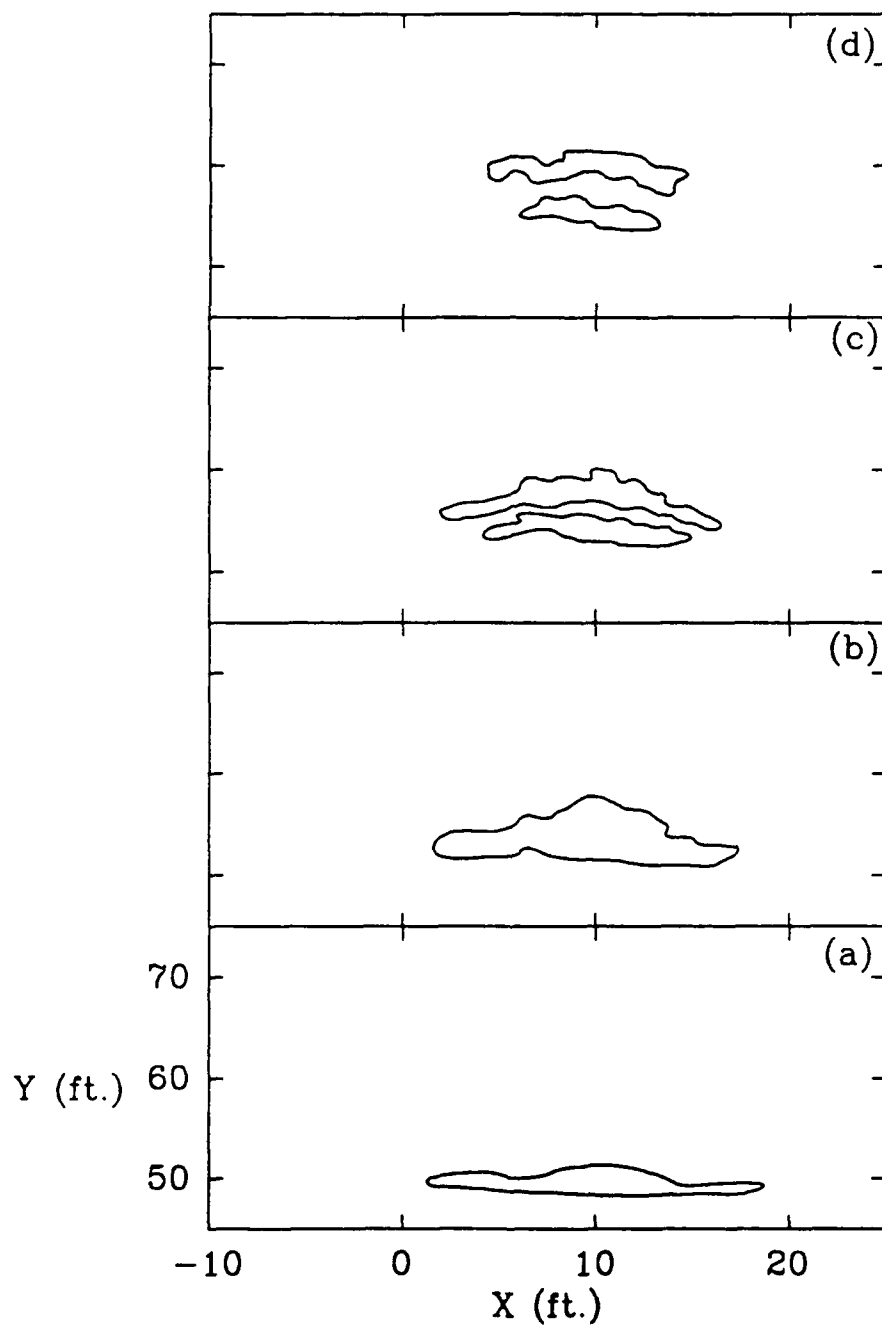


Figure 3.44 Plan view of the whitecap generated by the three-dimensional breaking event with $A = 0.475$. The time is referenced to plot (a) for which $t = 0$ s
 (b) $t = 0.27$ s (c) $t = 0.53$ s (d) $t = 0.8$ s.

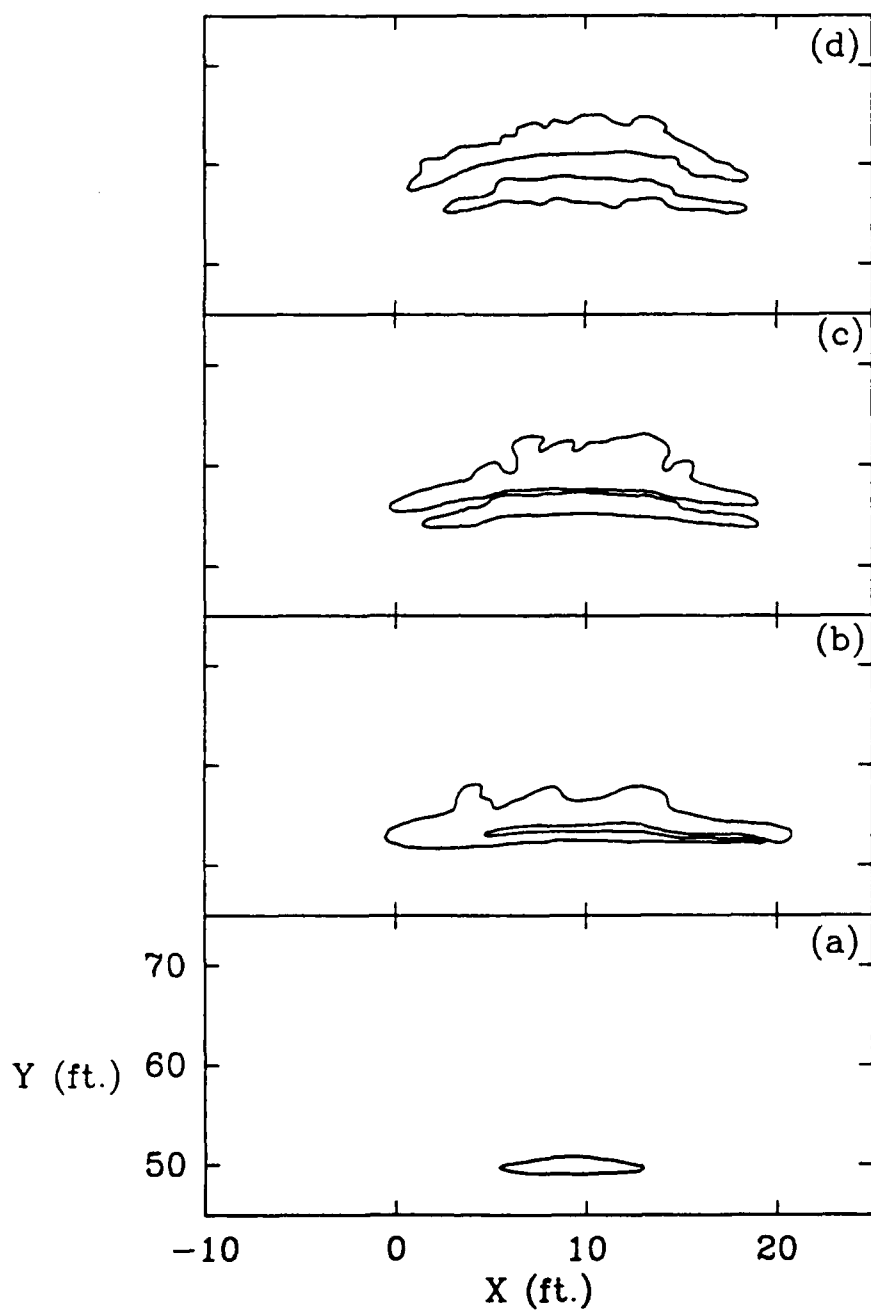


Figure 3.45 Plan view of the whitecap generated by the three-dimensional breaking event with $A = 0.55$. The time is referenced to plot (a) for which $t = 0$ s (b) $t = 0.27$ s (c) $t = 0.53$ s (d) $t = 0.8$ s.

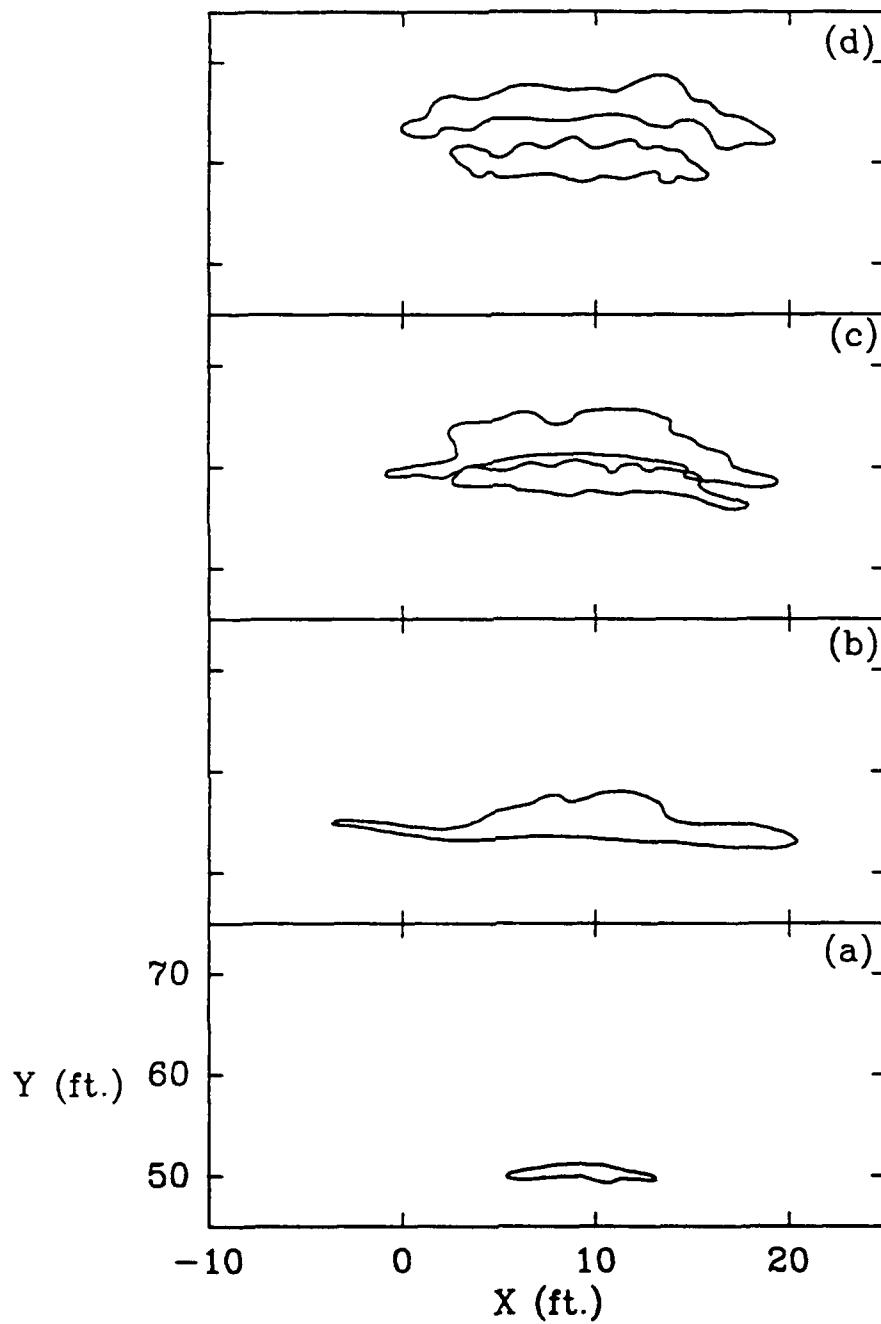


Figure 3.46 Plan view of the whitecap generated by the three-dimensional breaking event with $A = 0.625$. The time is referenced to plot (a) for which $t = 0$ s (b) $t = 0.27$ s (c) $t = 0.7$ s (d) $t = 1.0$ s.

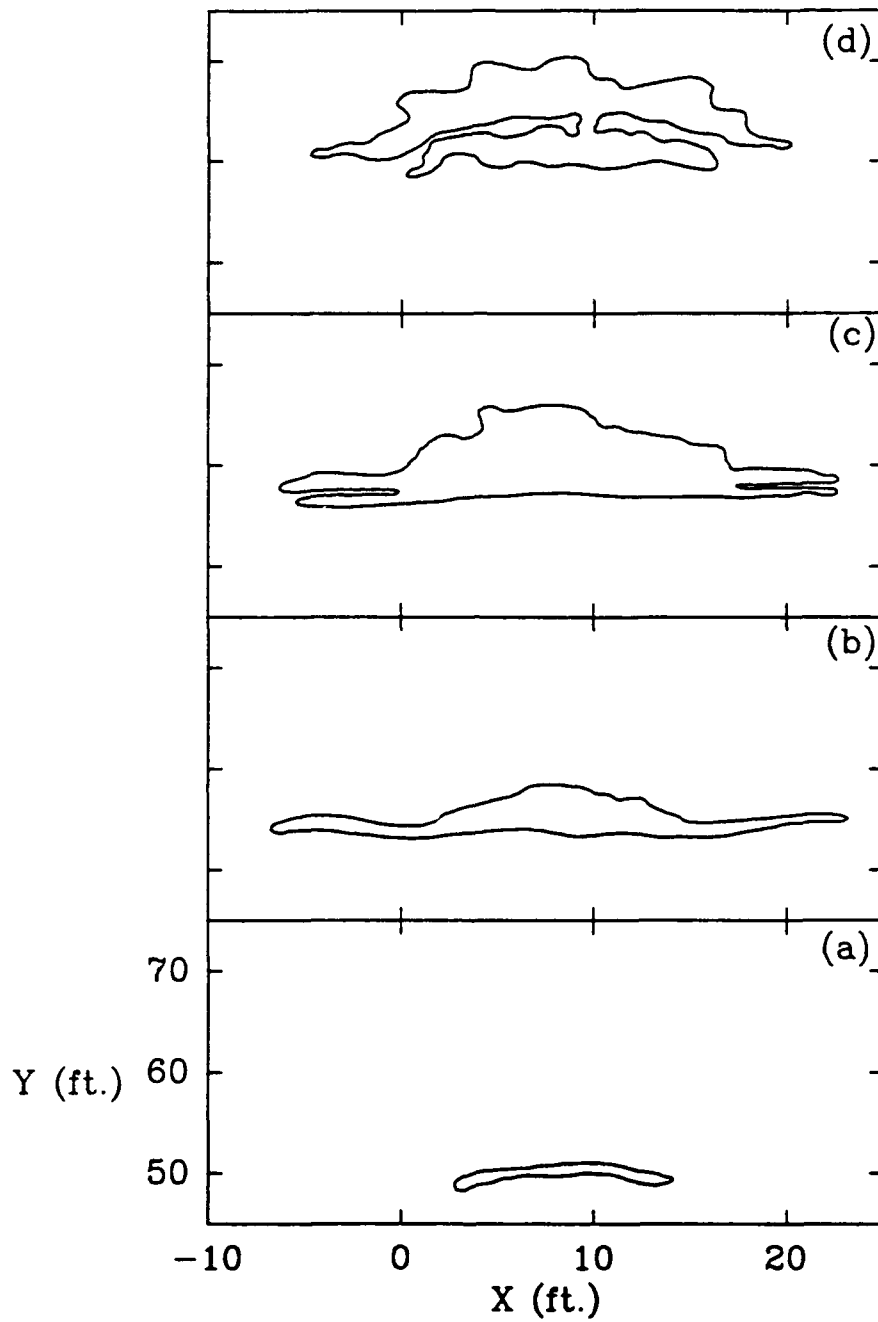


Figure 3.47 Plan view of the whitecap generated by the three-dimensional breaking event with $A = 0.70$. The time is referenced to plot (a) for which $t = 0$ s (b) $t = 0.27$ s (c) $t = 0.53$ s (d) $t = 0.8$ s.

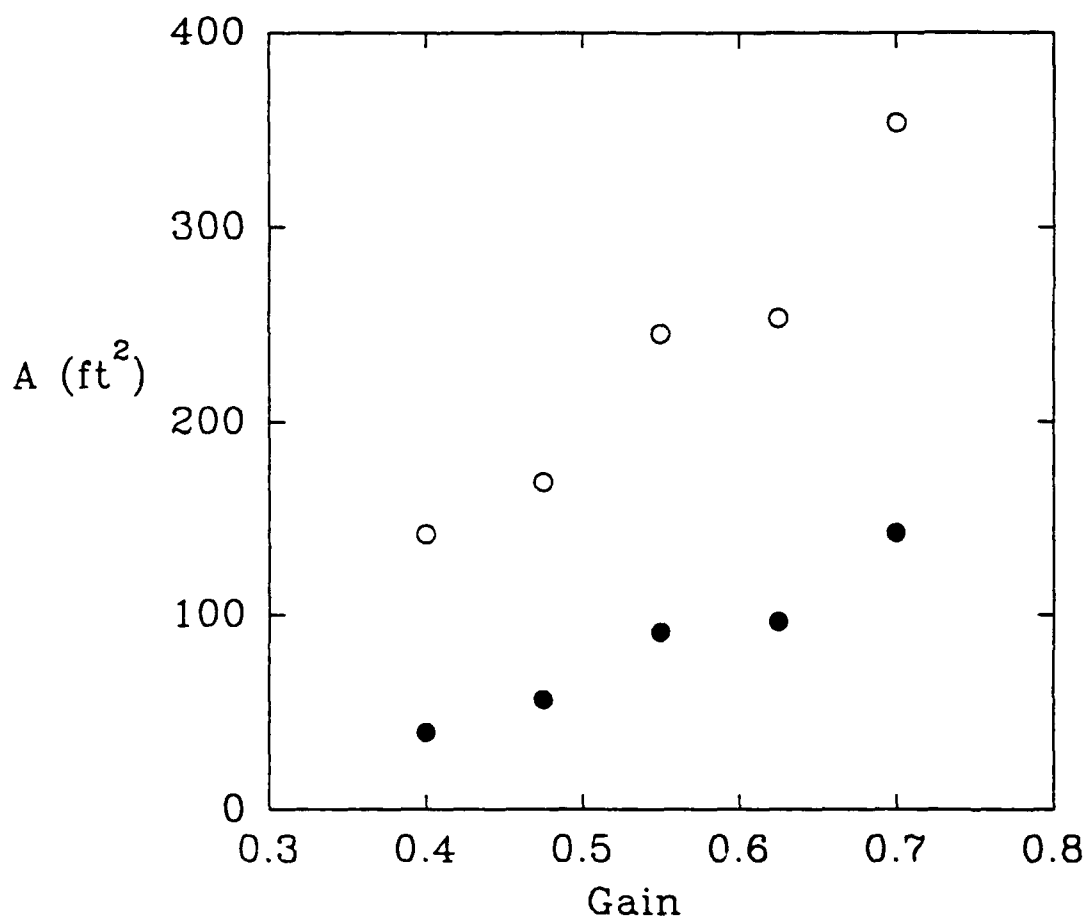


Figure 3.48 The integrated area (ft^2), defined as sum of the area of the whitecap at the four times corresponding to the four frames plotted in figures 3.43 to 3.47, for each breaking event and the maximum area (ft^2), defined as the maximum whitecap area observed for each breaking event, as a function of gain. \circ , integrated area; \bullet , maximum area.

3.5 Discussion

3.5.1 Volume of Entrained Air

Lamarre and Melville (1991) have shown that the process of air entrainment by plunging breakers scales with the prebreaking wave variables and that the bulk properties of the bubble cloud evolve according to simple functions of time. They found that the volume of entrained air decreases exponentially with time from a maximum value corresponding to the volume initially enclosed by the plunging wave crest. Video recordings of the two-dimensional breaking events were made for all the experimental runs. From these recordings it was possible to measure the size of the cylinder of air initially enclosed by the plunging breakers. This was possible for all but the lowest one or two amplitude breakers for each of the three wave packets W_1 , W_2 and W_3 . From the cylinder size the volume of air initially enclosed can be calculated. The volume of air enclosed in the cylinder is plotted in figure 3.49 as a function of the wave slope, S for all three packets. The volume correlates closely with slope and increases as the slope becomes larger and as the wave packet length increases.

The close correlation between the cylinder volume and the slope suggests that the cylinder volume should also correlate with the fractional dissipation. In figure 3.50 the fractional dissipation is plotted versus the cylinder volume. There is a strong correlation and the cylinder volume increases linearly as the dissipation increases. This relationship indicates that the amount of energy dissipated by breaking and the volume of air entrained are closely linked. This coupling was first observed by Lamarre and Melville (1991) who found that up to 50% of the energy dissipated by breaking was expended entraining air against the buoyancy force. They measured the void fraction beneath wave packet W_2 for 3 events with slopes, $S = 0.544, 0.448$ and 0.384 . They observed that the ratio of the energy dissipated by breaking to the volume of air entrained remained

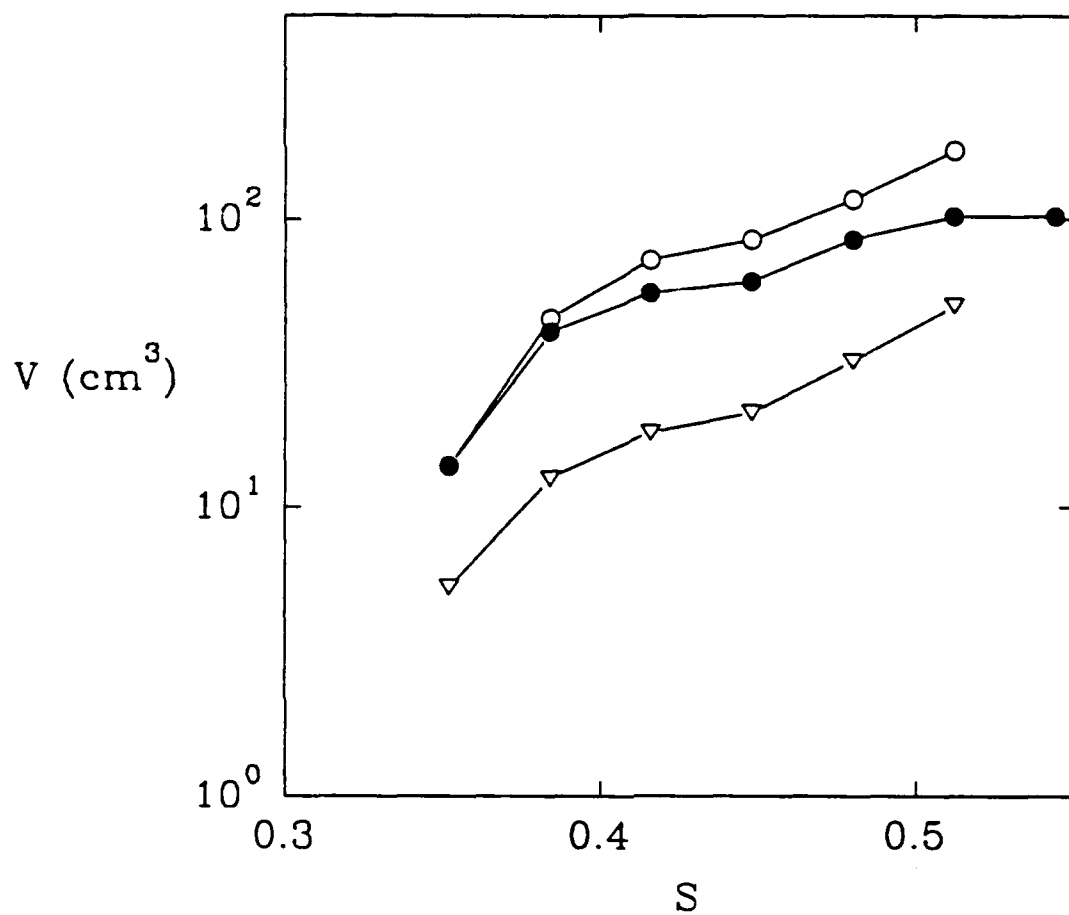


Figure 3.49 The volume of air in the cylinder V (cm^3) formed by the plunging wave crest versus the slope parameter for the 3 wave packets in the two-dimensional breaking experiments. \circ , W_1 ; \bullet , W_2 ; ∇ , W_3 .

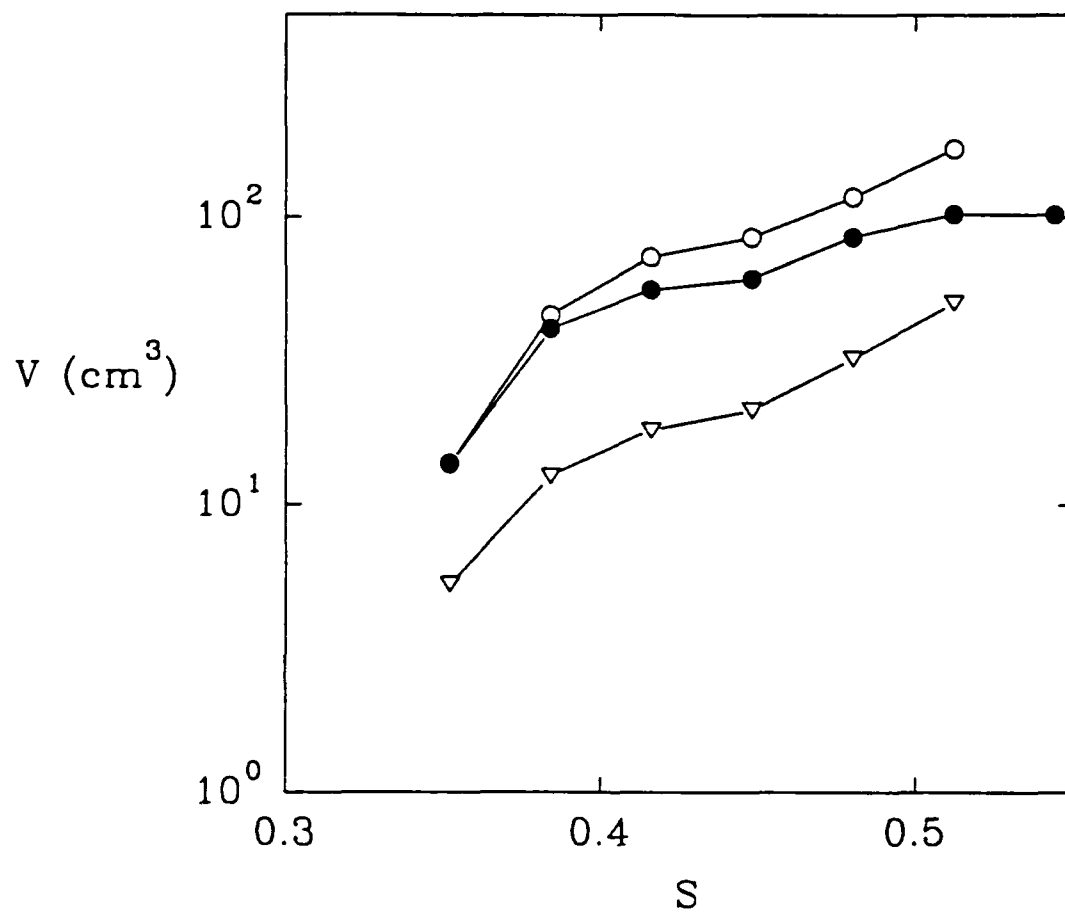


Figure 3.50 The fractional dissipation D as a function of the cylinder volume V (cm³).
 ○, W_1 ; ●, W_2 ; ▽, W_3 .

constant at approximately 0.1 . From this they concluded that the initial volume of air entrained would correlate with the energy dissipation. This hypothesis is confirmed by the data in figure 3.50.

The mean square acoustic pressure in the two frequency bands, 0 to 1 kHz and 1 kHz to 20 kHz, for the two-dimensional breaking events is plotted as a function of the volume of air in figures 3.51, 3.52 and 3.53 for the two hydrophone signals and the microphone signal respectively. The upper plots in each figure correspond to the lower band. There is considerable scatter in the data but the trends are consistent in all three figures. The error bars denote the 95% confidence limits of the data which has been ensemble averaged over 5 repeated runs of the same event. The 95% confidence limits in the upper and lower bands of the microphone signal in figure 3.53 are of similar magnitude. In the hydrophone data plotted in figures 3.51 and 3.52 the scatter is much larger in the higher frequency band. The log of the mean square acoustic pressure in the lower band increases as the entrained air volume increases. This is an indication of the strong coupling between the sound radiated by breaking and the dynamics of breaking and air entrainment. The log of the mean square acoustic pressure in the upper band increases as the entrained air volume increases for smaller values of V , but as the volume increases further it reaches a maximum value and then decreases in some cases. However the large scatter in the higher frequency data from the hydrophones indicates that these trends may not be statistically significant.

3.5.2 Low Frequency Spectral Peaks

It was observed during the course of the two-dimensional breaking experiments that as the wave broke a characteristic low frequency sound was emitted. The signature of this low frequency sound is very clearly visible in the spectra of the microphone signal. This can be seen in figure 3.54 (top plot) where a spectrograph, averaged over 5

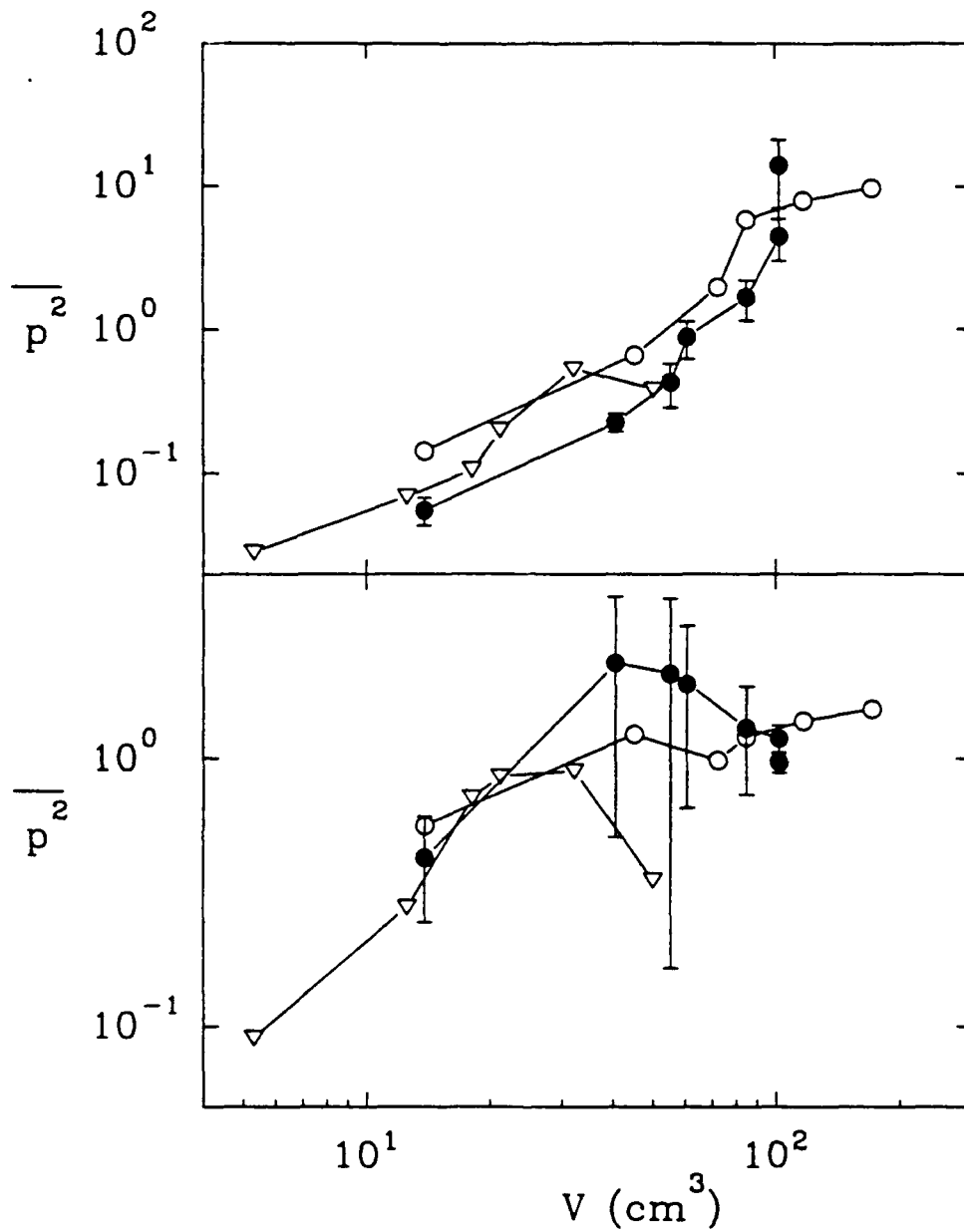


Figure 3.51 The mean square acoustic pressure $\overline{p^2}$ (Pa²) of the signal from the upstream hydrophone calculated over the entire signal duration in two frequency bands as a function of the volume of the cylinder V (cm³). The upper plot is for the frequency band 20 Hz-1 kHz and the lower plot for the band 1-10 kHz. Each data point is the average of 5 repeats of the measurement and the error bars indicate the 95% confidence limits. \circ , W_1 ; \bullet , W_2 ; ∇ , W_3 .

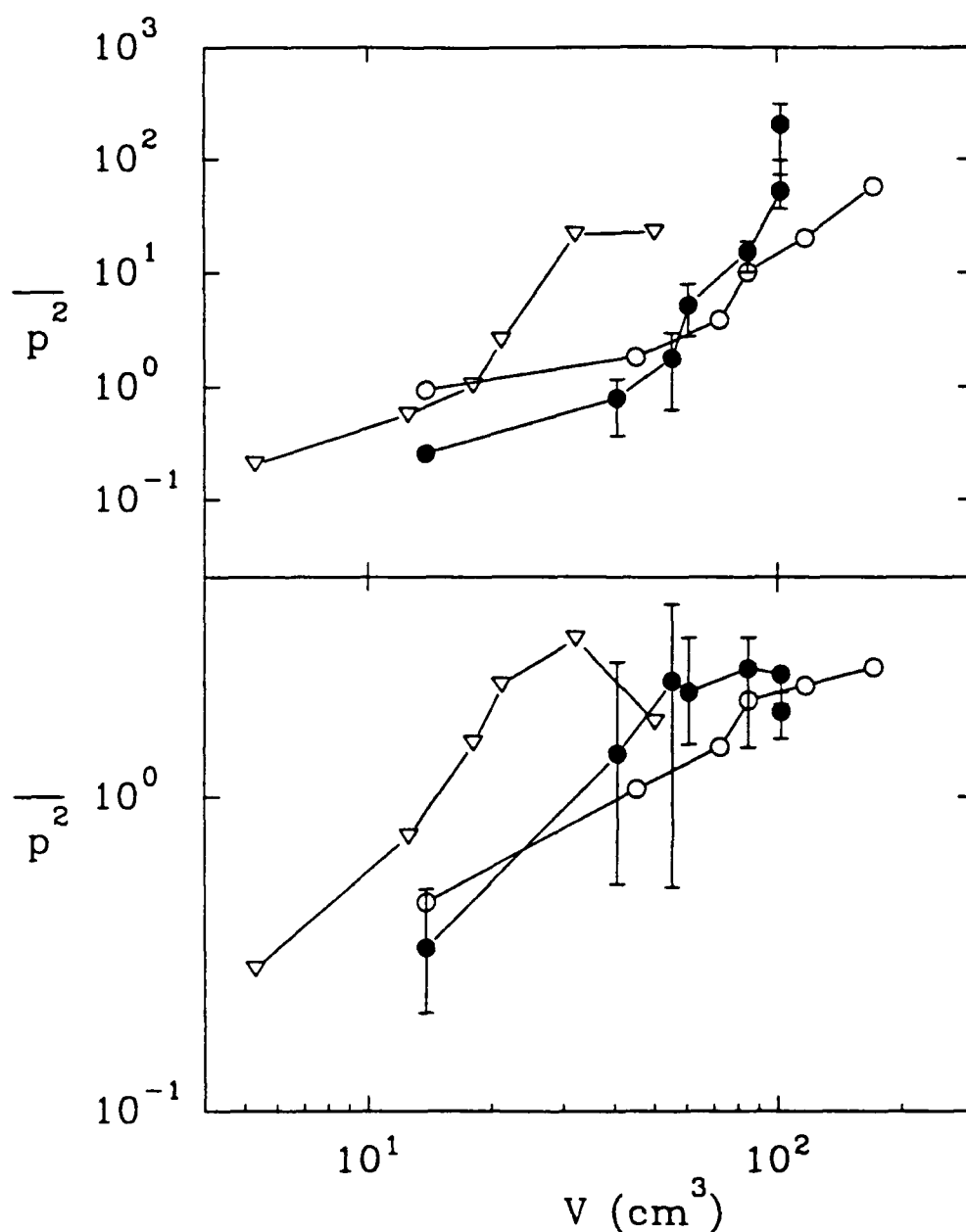


Figure 3.52 The mean square acoustic pressure $\overline{p^2}$ (Pa^2) of the signal from the downstream hydrophone calculated over the entire signal duration in two frequency bands as a function of the volume of the cylinder V (cm^3). The upper plot is for the frequency band 20 Hz-1 kHz and the lower plot for the band 1-10 kHz. Each data point is the average of 5 repeats of the measurement and the error bars indicate the 95% confidence limits. \circ , W_1 ; \bullet , W_2 ; ∇ , W_3 .

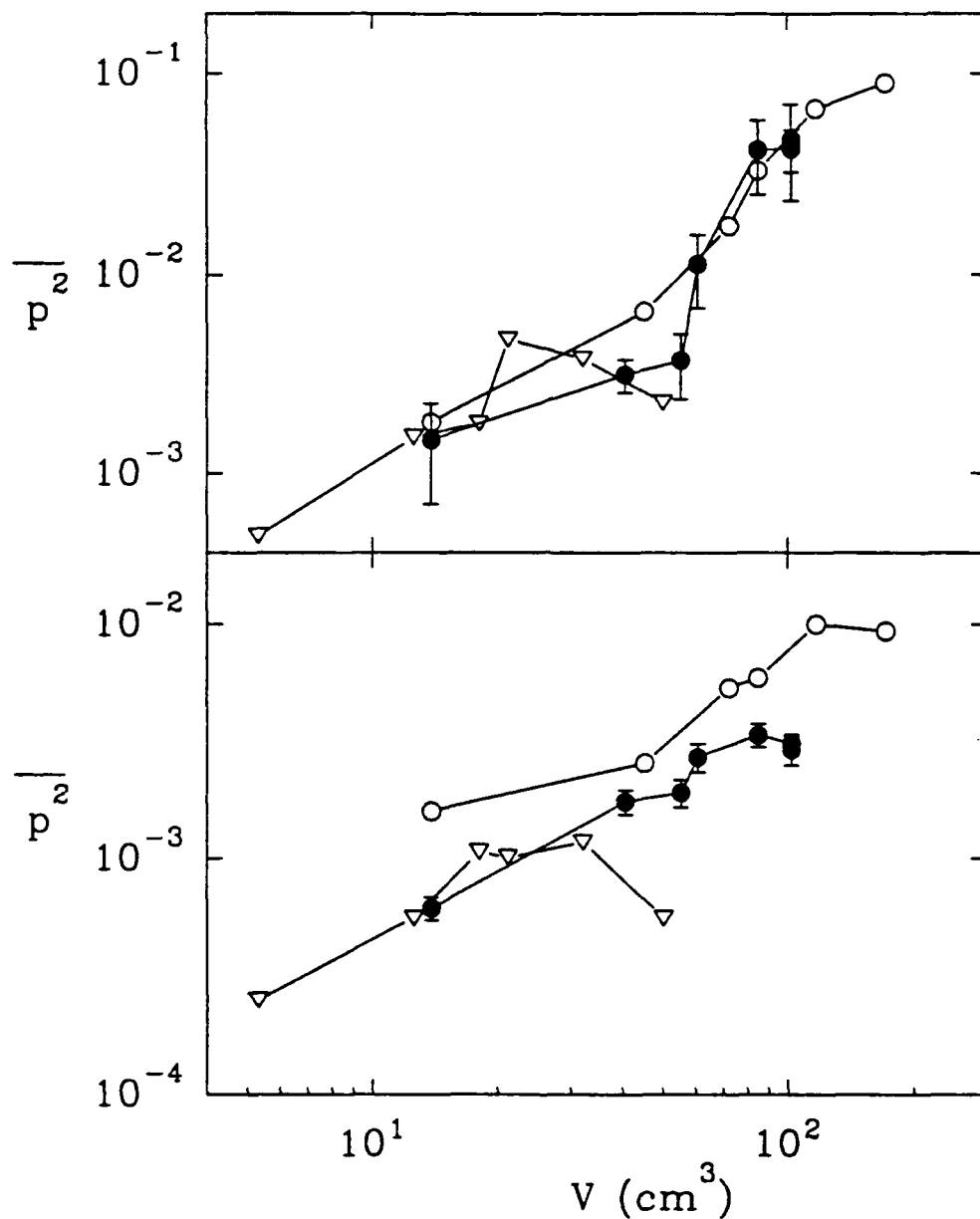


Figure 3.53 The mean square acoustic pressure $\overline{p^2}$ (Pa²) of the signal from the microphone calculated over the entire signal duration in two frequency bands as a function of the volume of the cylinder V (cm³). The upper plot is for the frequency band 20 Hz-1 kHz and the lower plot for the band 1-10 kHz. Each data point is the average of 5 repeats of the measurement and the error bars indicate the 95% confidence limits. \circ , W_1 ; \bullet , W_2 ; ∇ , W_3 .

repeats, of the microphone signal for packet W_3 , the shortest wavelength packet, with a slope, $S = 0.48$, is shown. At $t = 0.4$ s there is a large spectral peak, 85 dB in amplitude, in the spectrum at approximately 130 Hz. This peak occurs immediately after the initial impact of the plunging crest onto the free surface. In figure 3.54 (bottom plot) a spectrograph of the upstream hydrophone for the same wave packet and slope averaged over the same 5 repeated events is plotted. At $t = 0.4$ s there is a spectral peak, 100 dB in amplitude, at approximately 130 Hz matching exactly the peak in the microphone spectrum. In figure 3.55 another set of spectrographs for the microphone and hydrophone signals are plotted. These are for packet W_1 , the largest wave length packet, with a slope, $S = 0.416$. The spectral peak occurs in both spectrographs at $t = 0.5$ s and at a frequency of approximately 120 Hz. These spectral peaks can be seen in the one dimensional acoustic spectra of the microphone signal plotted in figure 3.12 where the spectral peaks can be seen shifting from approximately 75 Hz to 200 Hz as the wave slope decreases.

Spectrographs of the microphone signal and the upstream hydrophone were analyzed and the characteristic frequency which occurred immediately following the impact of the plunging crest was measured. At very low slopes, close to the incipient slope, there was no characteristic frequency that was detectable. This is because these low slope events were spilling breakers for which no cylinder of air is formed. The spectral peaks were easier to detect in the microphone spectrographs. In locating the peaks in the hydrophone spectrographs the time at which they appeared in the microphone signal was used as a guide. With this a priori information the spectral peaks were almost always detectable in the hydrophone signal. One reason the peaks are less clearly visible in the hydrophone spectra is because there were several bands of low frequency noise, one at 60 Hz and another at 200 Hz which obscured other spectral peaks. Reverberation of the signal within the wave channel may also have made detection of the peaks more difficult.

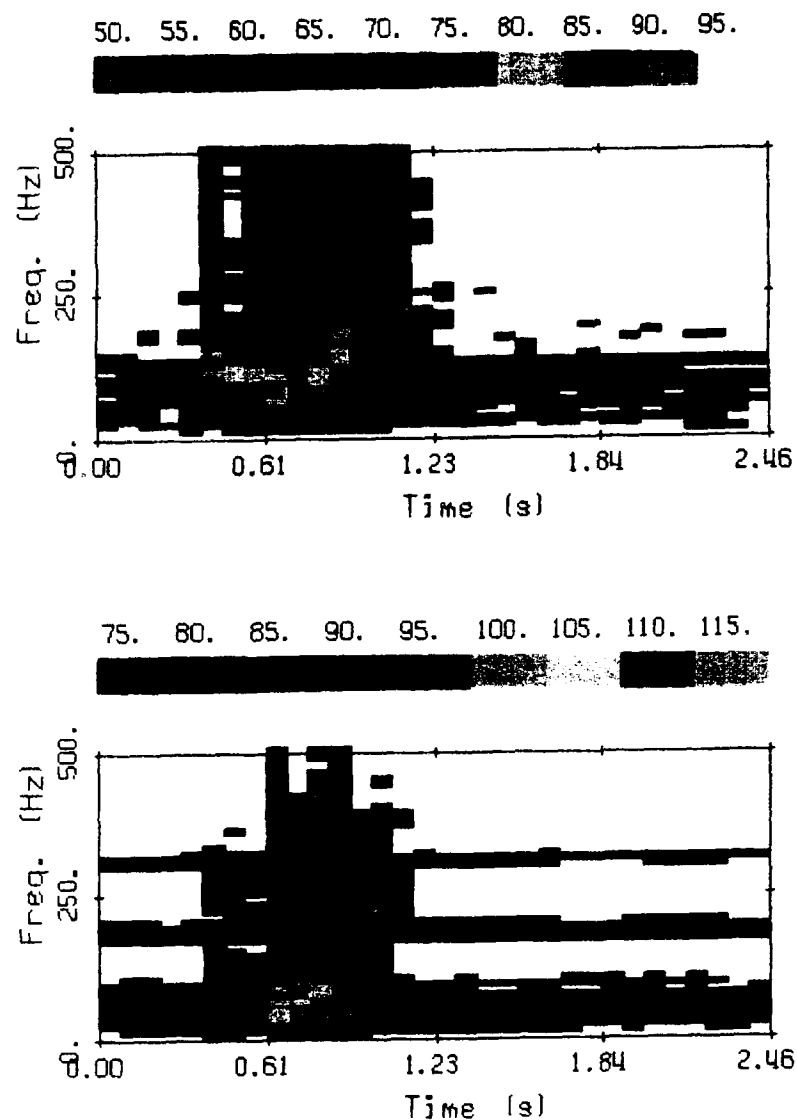


Figure 3.54 Spectrographs of signals from the microphone (top plot) and the upstream hydrophone (bottom plot) for the two-dimensional breaking event packet W_3 with $S = 0.48$. The spectra were averaged over 5 repeats of the event and were calculated for 32-2048 point segments overlapped by 512 points and windowed with a Blackman-Harris window. The bandwidth resolution is 9.8 Hz. Each color corresponds to a 5 dB re $1 \mu\text{Pa}^2$ increment in spectral level.

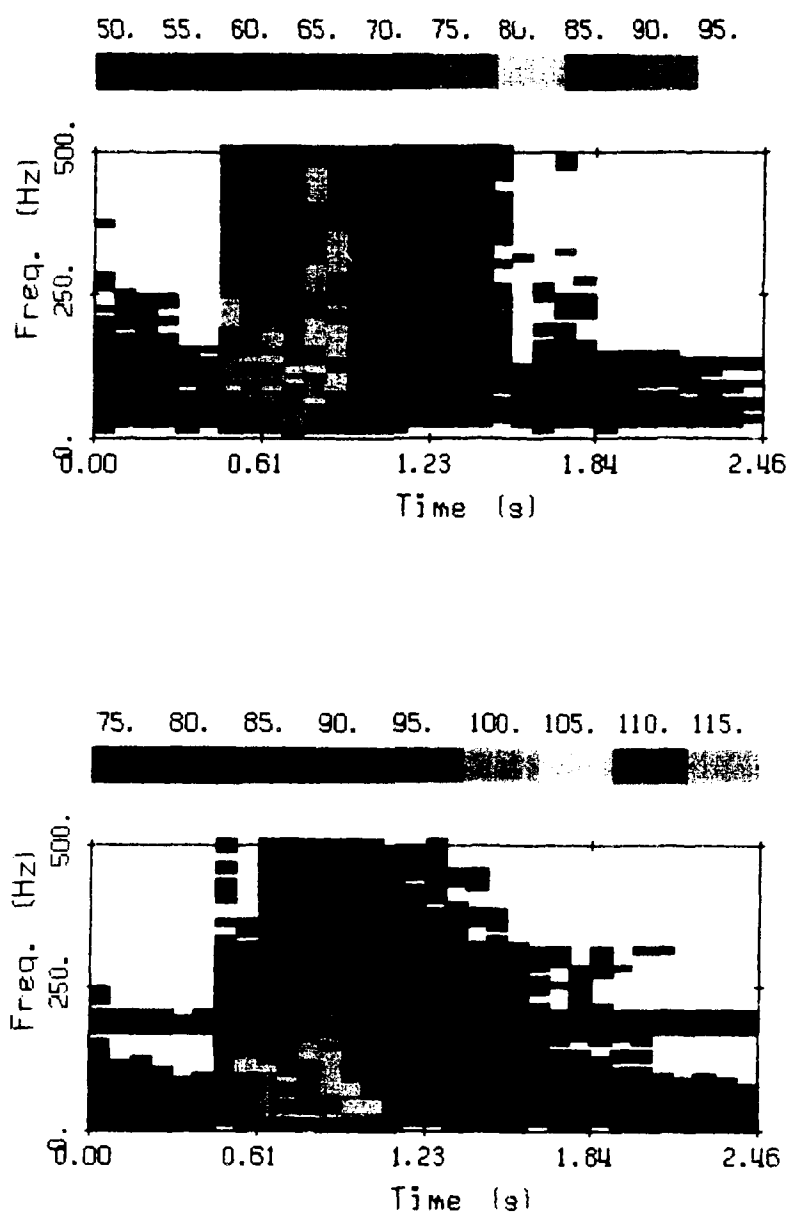


Figure 3.55 Spectrographs of signals from the microphone (top plot) and the upstream hydrophone (bottom plot) for the two-dimensional breaking event packet W_1 with $S = 0.416$. The spectra were averaged over 5 repeats of the event and were calculated for 32-2048 point segments overlapped by 512 points and windowed with a Blackman-Harris window. The bandwidth resolution is 9.8 Hz. Each color corresponds to a 5 dB re 1 μPa^2 increment in spectral level.

The frequency appeared to vary as a function of the wave slope and this is confirmed in figures 3.56a and 3.56b where the characteristic frequency measured from the hydrophone and microphone signals are plotted versus the wave slope for all 3 wave packets. The frequency decreases as the wave slope increases and at the same slope the longer wave length packets produced a lower frequency sound. The frequency of the microphone and hydrophone signals are plotted as a function of the fractional dissipation in figures 3.57a and figure 3.57b. In both plots the data for all 3 wave packets collapse onto a single curve and the frequency decreases monotonically as the dissipation increases. The frequency increases from 75 Hz to 275 Hz as the fractional dissipation decreases from 0.27 to 0.07 . The correlation between the characteristic frequency and the dissipation is additional evidence of the strong coupling between the dynamics of wave breaking and the radiation of sound by breaking waves.

A characteristic low frequency signal which varied with the wave amplitude was not as clearly evident in the data from the three-dimensional breaking events. There appeared to be no consistent variation in the location of the low frequency spectral peaks in the spectrographs of either the hydrophone or microphone signals. However in the spectra of the data from the downstream hydrophone which was low pass filtered at 200 Hz a spectral peak which shifted to higher frequencies as the wave amplitude decreased was observed. The spectra are shown in figure 3.58 and the location of the shifting spectral peaks is marked by the inverted triangular symbols. The spectra are for the 6 wave amplitudes, $A = 0.24$ to 0.70 . The spectral peak is located at 57 Hz for the largest amplitude wave, $A = 0.70$, and shifts to 76 Hz for the wave with, $A = 0.475$. At a gain, $A = 0.40$, no spectral peak appears because either the mechanism which generates it is absent at this low wave amplitude or because it is hidden in the large background noise spectral peak centered at 100 Hz.

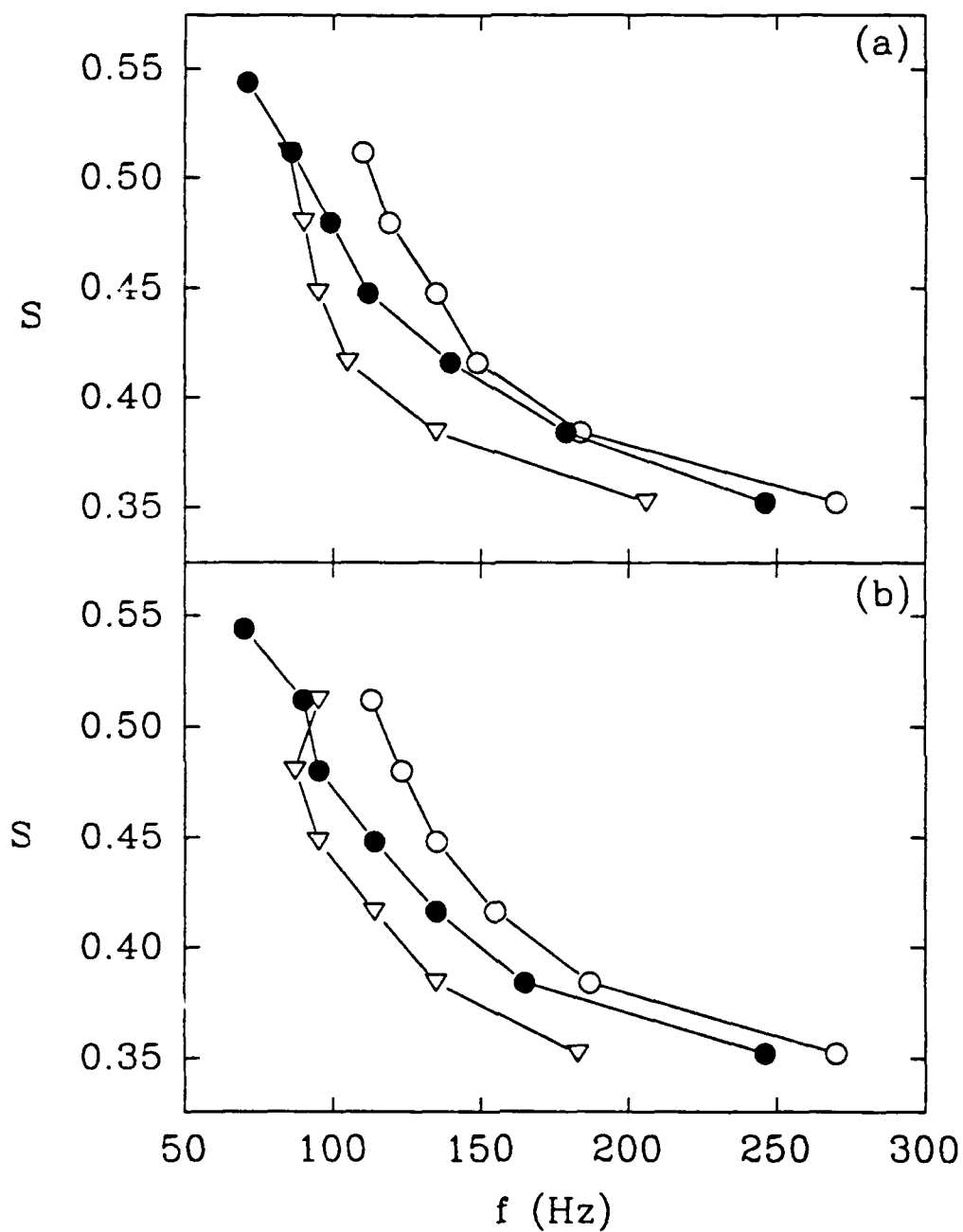


Figure 3.56 The characteristic frequency f (Hz) of (a) the microphone signal and (b) the hydrophone signal for the two-dimensional breaking events plotted versus the slope parameter S . \circ , W_1 ; \bullet , W_2 ; ∇ , W_3 .

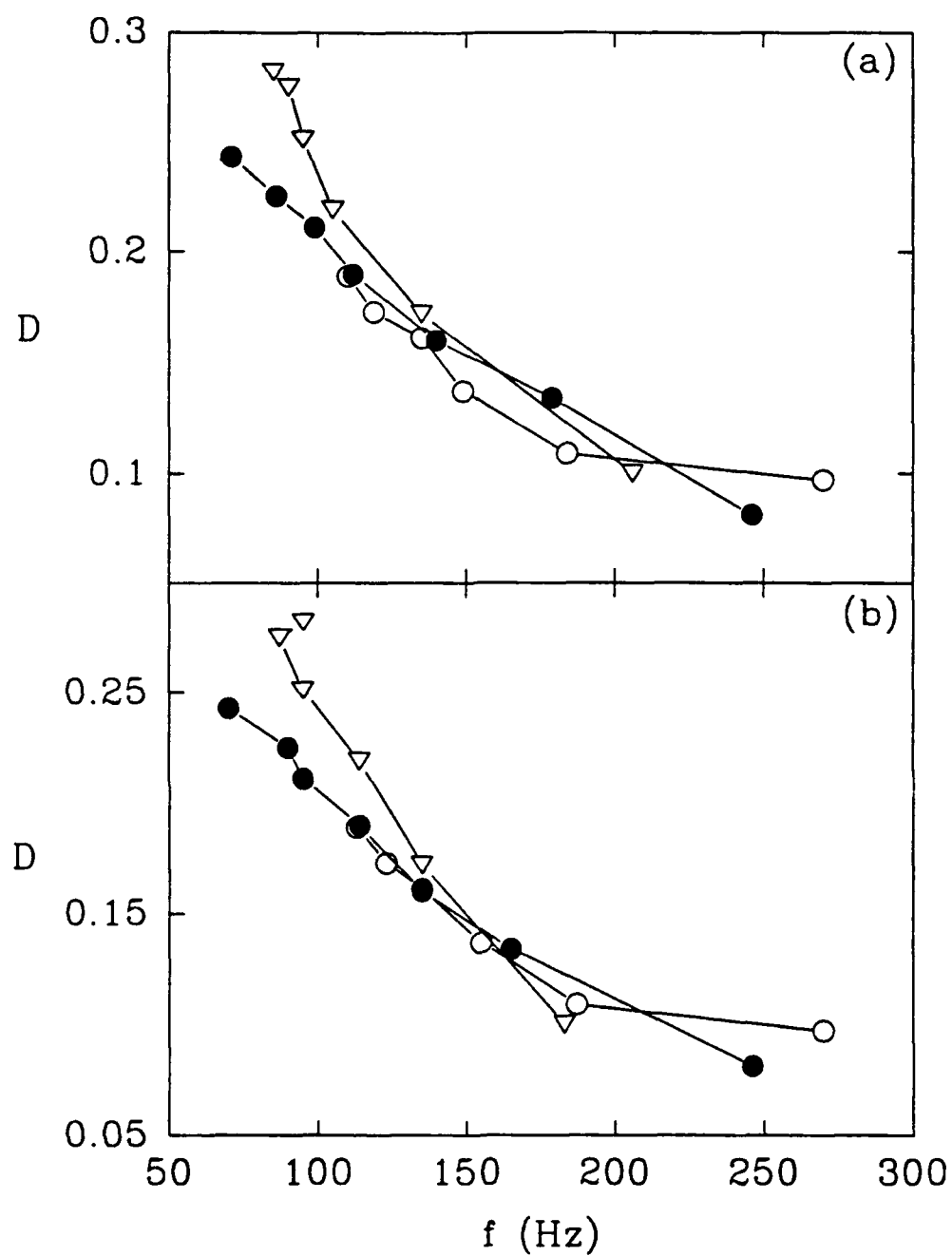


Figure 3.57 The characteristic frequency f (Hz) of (a) the microphone signal and (b) the hydrophone signal for the two-dimensional breaking events plotted versus the fractional dissipation, D . \circ , W_1 ; \bullet , W_2 ; ∇ , W_3 .

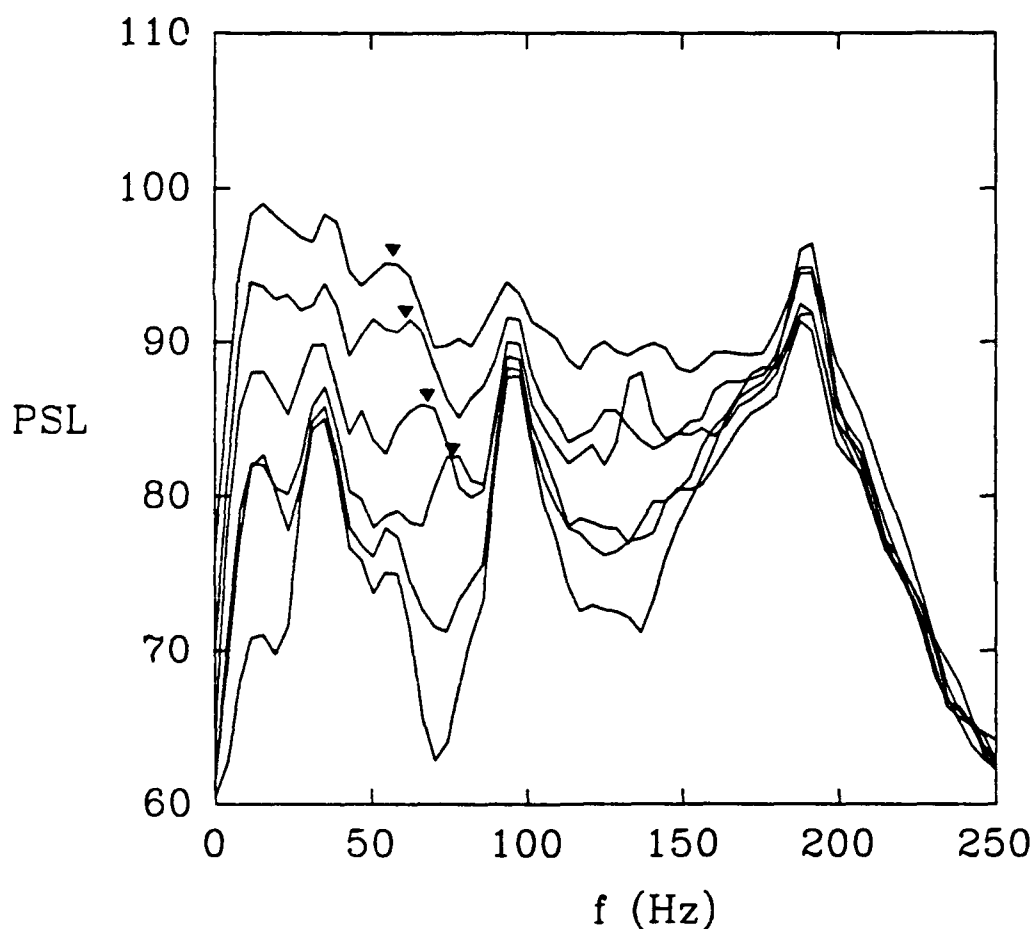


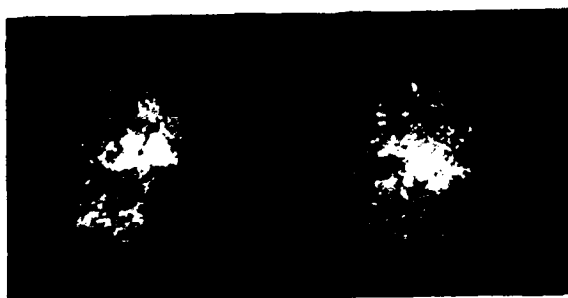
Figure 3.58 Frequency spectra (pressure spectrum level PSL in dB re $1 \mu\text{Pa}^2/\text{Hz}$) of the signal from the downstream hydrophone for the three-dimensional breaking events. The gain $A = 0.24, 0.40, 0.475, 0.55, 0.625$ and 0.70 . The spectra were computed from data conditioned using set-up III and decimated to a sampling rate of 1 kHz. The data was divided into 17-256 point segments, windowed using a Blackman-Harris window, overlapped by 64 points and averaged over 5 repeats of the events. The estimated spectra have 10 degrees of freedom and a bandwidth resolution of 3.9 Hz. ▼ mark the shifting low frequency spectral peaks.

3.5.3 Pulsating Cylinder

The origin of these characteristic low frequency signals in the two-dimensional breaking events was investigated. An underwater video was taken in the wave channel at MIT with the camera submerged at approximately mid-depth located several meters downstream of the breaking location pointing upstream towards the wave paddle. The video showed that a perfectly smooth walled elliptic cylinder of air was formed as the wave crest curls over. The cylinder of air was forced down into the water column by the weight of the water overhead in the curling crest. A series of photographs of packet W_2 with $S = 0.544$ showing frames of the underwater video at various times throughout the breaking events are shown in figure 3.59. The photographs were produced by taking photographs of a video monitor with the video recording stopped using the freeze frame feature of the VCR at the various times throughout the breaking process. The photographs were taken in a darkened room with no light source other than the monitor screen using a Minolta 7000i camera equipped with a 50 mm AF lens. The aperture was set a F6.7, the shutter speed was 1/15 s and Kodak TMAX 100 film was used.

In frame (1) the video camera is half way out of the water and the free surface is seen as a horizontal line across the middle of the frame. The plunging wave crest is visible above the free surface although it is out of focus. In frame (2) the time is 14.465 s and the plunging wave crest has just impacted the free surface. Frames (3) and (4) show the smooth walled cylinder of air being forced down into the water column as the wave continues to break. In frame (5) waves appear on the cylinder as it becomes unstable and in frame (6) the cylinder begins to break-up into smaller air bubbles. In frames (7) and (8) the cylinder continues to break-up and the periodic instabilities seen in frame (5) grow and form the periodic bubble cloud substructures which are visible at the

Figure 3.59 A series of photographs showing the formation and subsequent break-up of the cylinder of air formed by a plunging breaker for wave packet W_2 with $S = 0.544$. Frame (23) $t = 0.322$ s, prior to the impact of the plunging crest, the free surface is visible as a horizontal line across the middle of the photograph and the plunging wave crest is visible above the free surface. Frame (24) $t = 0.465$ s, the crest has just impacted the free surface. Frame (25) $t = 0.532$ s, the smooth-walled cylinder of air is partially visible, the lower edge of the cylinder is the horizontal line slightly above the centerline of the frame. Frame (26) $t = 0.599$ s, the smooth-walled cylinder fills the upper half of the frame. Frame (27) $t = 0.665$ s, the cylinder is becoming unstable, waves can be seen forming along the lower portion of the cylinder. Frame (28) $t = 0.699$ s (29) $t = 0.732$ s (30) $t = 0.766$ s, the break-up of the cylinder into a cloud of small bubbles continues, the waves visible in frame (27) develop into periodic bubble cloud substructures most clearly visible in frame (29). Frame (31) $t = 0.799$ s (32) $t = 0.866$ s, the structure of the bubble cloud becomes finer as the bubbles break-up into progressively smaller sizes.



bottom of the cylinder. In frames (9) and (10) the structure of the cloud becomes finer as the cloud breaks up into progressively smaller sized bubbles.

In figure 3.60 a series of three photographs showing the evolution of the cylinder from the side produced using the same method as the photographs in figure 3.59 are shown. Frame (1) shows the wave crest as it begins to plunge forward. Frame (2) shows the crest plunging downwards and curling over and forming a cylinder. Frame (2) matches the time for frame (1) in figure 3.59. In frame (3) the wave crest has just impacted the free surface and this photograph matches frame (2) from figure 3.59. The photographs from the side show the elliptic shape of the cylinder which typically had a major to minor axis ratio of 3.

It was hypothesized that the origin of the low frequency signals was that the cylinders of air were pulsating volumetrically, in the breathing mode. Similar to the case of an oscillating spherical bubble the frequency of oscillation would be expected to vary as a function of the bubble size or volume of air. In order to assess the validity of this hypothesis the theoretical problem of an infinitely long (the two-dimensional problem) pulsating circular cylinder of air located immediately beneath a free surface was studied.

The pressure radiated by a single pulsating cylinder of infinite length in an infinite fluid is given by,

$$P(r,t) = \frac{\pi \rho \omega a_0 U_0}{2} H_0(kr) e^{-j\omega t} \quad 3.3$$

where ρ is the density of the fluid, ω is the radian frequency, a_0 is the equilibrium cylinder radius, U_0 is the magnitude of the cylinder wall velocity, k is the acoustic wavenumber in the fluid, r is the radial distance from the cylinder center to the receiver location and H_0 is the zeroth order Hankel function of the first kind (Morse and Ingaard, 1968, p. 357). The linearized momentum equation is,



Figure 3.60 A series of photographs showing a view from the side of the cylinder formation for packet W_2 with $S = 0.544$. Frame (34) $t = 0.266$ s, the wave crest has just begun to plunge forward. Frame (35) $t = 0.333$ s, the crest has curled over and the cylinder is partially formed, this frame matches the time of frame (23) in figure 3.59. Frame (36) $t = 0.466$ s, the wave crest has just impacted the free surface and the cylinder is fully formed, this frame matches the time of frame (24) in figure 3.59.

$$\frac{\partial \Phi(r,t)}{\partial t} = - \frac{1}{\rho} \frac{\partial P(r,t)}{\partial r} \quad 3.4$$

where $\Phi(r,t)$ is the velocity potential, $P(r,t)$ is the pressure, ρ is the density of the fluid and r is the radial coordinate. If the dependence on time is assumed to be harmonic then eq 3.4 becomes,

$$\Phi(r) = \frac{1}{j\omega\rho} P(r) \quad 3.5$$

where ω is the radian frequency and $j = \sqrt{-1}$. Substituting for $P(r)$ in equation 3.5 produces the following expression for the velocity potential,

$$\Phi(r,t) = \left[\frac{\pi}{2j} \right] a_0 U_0 H_0(kr) e^{-j\omega t} \quad 3.6$$

If it is assumed that $kr \ll 1$ then equation 3.6 reduces to,

$$\Phi(r,t) = a_0 U_0 \ln(kr) e^{-j\omega t} \quad 3.7$$

If the cylinder is located close to a free surface then the method of images can be used to obtain a solution. The location of the image cylinder and the geometry of the problem are illustrated in figure 3.61. If the pulsating cylinder is located a distance $L/2$ below the free surface then the image cylinder is located $L/2$ above the free surface such that a line joining their two center points is perpendicular to the free surface. The image cylinder must radiate a pressure field which is 180° out of phase with the pressure radiated by the real cylinder in an infinite fluid in order to satisfy the boundary condition of $p = 0$ on the free surface.

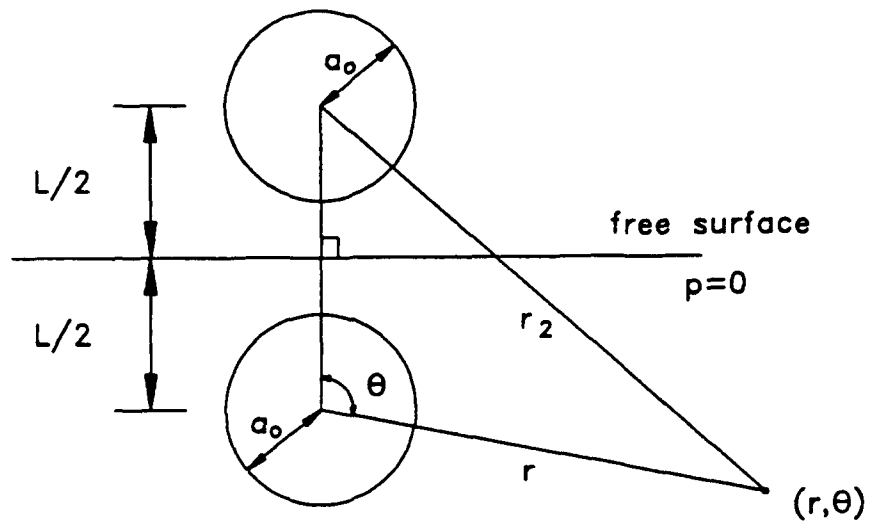


Figure 3.61 Geometry of the problem of an oscillating air cylinder located close to a pressure release surface.

If $ka_0 \ll 1$ and $kL \ll 1$ then the velocity potential for the cylinder plus its image can be written as,

$$\Phi(t) = a_0 U_0 (\ln(kr) - \ln(kr_2)) \quad 3.8$$

where r_2 is the radial distance from the center of the image cylinder to the receiver.

Using the law of cosines equation 3.8 can be rewritten as,

$$\Phi(t) = a_0 U_0 \ln \left(\frac{r}{\sqrt{(r^2 + L^2 - 2Lr \cos \theta)}} \right) \quad 3.9$$

where θ is the angle between a line which joins the two cylinder centers and the line joining the cylinder center and the receiver, see figure 3.61. The kinetic energy of the fluid motion can be calculated using a surface integral evaluated over the surface of the cylinder,

$$T = -\frac{1}{2} \rho \int_A \Phi \mathbf{u} \cdot \mathbf{n} dA \quad 3.10$$

where A is the area of a unit length of cylinder, \mathbf{u} is the velocity vector and \mathbf{n} is the unit vector normal to the cylinder's surface (Batchelor, 1967, p. 383). On the cylinder surface $\mathbf{u} \cdot \mathbf{n} = \dot{a}$, where \dot{a} is the velocity of the cylinder wall. Using equation 3.9 the surface integral in 3.10 can be reduced to the following form,

$$T = -\frac{1}{2} \int_0^{2\pi} a_0^2 (\dot{a})^2 \ln \left(\frac{a_0}{\sqrt{a_0^2 + L^2 - 2a_0^2 L \cos(\theta)}} \right) d\theta \quad 3.11$$

Integrating equation 3.11 is straightforward (CRC Standard Mathematical Tables, 1987, p. 295) and the result is,

$$T = \frac{1}{2} \left[-2\pi\rho a_o^2 \ln \left(\frac{a_o}{L} \right) \right] (\dot{a})^2 \quad 3.12$$

where the quantity $(-2\pi\rho a_o^2 \ln(a_o/L))$ is a "generalized inertia" for the cylinder motion (Lighthill, 1978).

If the amplitude of the cylinder wall oscillations are assumed to be small compared to the undisturbed value of the cylinder radius then,

$$\frac{V(t) - V_o}{V_o} = \frac{\Delta V(t)}{V_o} = 2 \left[\left(\frac{a(t)}{a_o} \right) - 1 \right] \quad 3.13$$

where $V(t)$ is the volume of the cylinder per unit length, V_o is the undisturbed volume of the cylinder per unit length, $a(t)$ is the radius of the cylinder and a_o is the undisturbed cylinder radius. The relative change in the gas density ρ_g is then given by,

$$\frac{\rho_g - \rho_{go}}{\rho_{go}} = -2 \left[\frac{a}{a_o} - 1 \right] \quad 3.14$$

where ρ_{go} is the undisturbed gas density (Lighthill, 1952, p. 33).

The potential energy can be calculated by assuming that the cylinder pulsates slowly enough that the gas density ρ_g remains uniform throughout the cylinder while making small oscillations about the undisturbed value ρ_{go} (Lighthill, 1952, p. 33). The work done per unit volume to compress a gas to density ρ_g from the undisturbed density ρ_{go} is given by,

$$W = \rho_g P (-d\rho_g^{-1}) = \frac{P d\rho_g}{\rho_g} \quad 3.15$$

where P is the perturbation pressure about the atmospheric pressure (Lighthill, 1952, p. 13). Substituting with $P = (\rho_g - \rho_{g0})c_g^2$ in equation 3.15 and integrate from ρ_{g0} to ρ_g produces an expression for the potential energy per unit volume for gas compressed from ρ_{g0} to ρ_g ,

$$h = \frac{1}{2} (\rho_g - \rho_{g0})^2 \left[\frac{c_g^2}{\rho_{g0}} \right] \quad 3.16$$

where c_g is the speed of sound in the gas. Using equation 3.16 and taking the volume to be a unit length of cylinder, $V = \pi a_0^2 (1 \text{ m})$, the total potential energy of the compressed gas in the cylinder can be written as,

$$H = \frac{1}{2} (4\pi\rho_{g0} c_g^2) (a - a_0)^2 . \quad 3.17$$

The quantity $(4\pi\rho_{g0} c_g^2)$ is a "generalized stiffness" of the cylinder motion.

The radian frequency ω_c of the cylinder pulsations is then given by,

$$\omega_c = 2\pi f_c = \sqrt{\frac{\text{stiffness}}{\text{inertia}}} = \frac{c_g}{a_0} \sqrt{\frac{2 \rho_{g0}}{\rho \ln(L/a_0)}} \quad 3.18$$

where for air cylinders in water $c_g = 340 \text{ m/s}$, $\rho_{g0} = 1.23 \text{ kg/m}^3$ and $\rho = 1000 \text{ kg/m}^3$ and the expression for f_c reduces to,

$$f_c = \left(\frac{2.68}{a_o} \right) \frac{1}{\sqrt{\ln(L/a_o)}} \quad 3.19$$

If $a_o = 0.05$ m and $L = 0.2$ m equation 3.19 gives $f_c = 46$ Hz. For these typical values of a_o , L and f_c , $ka_o = 0.01$ and the assumption that $ka_o \ll 1$ is seen to be satisfied. Equation 3.18 shows that the radian frequency ω_c is smaller than the characteristic frequency c_g / a_o for density propagation across the cylinder by a factor $\sqrt{2\rho_{go} / \rho \ln(L/a_o)}$ (Lighthill, 1978). The smallest physically realistic value of the ratio L/a_o corresponds to the case where the cylinder is just touching the free surface and then $L/a_o = 2$. For this value of L/a_o the factor $\sqrt{2\rho_{go} / \rho \ln(L/a_o)}$ has a maximum value of 0.06 which indicates that $\omega_c \ll c_g / a_o$ and the assumption that the gas density in the cylinder is uniform is shown to be plausible.

In figure 3.62 equation 3.19 is shown plotted for several values of L/a_o . The frequency varies as the inverse of the cylinder radius and as the cylinder moves closer to the free surface, that is L/a_o becomes smaller, the pulsation frequency increases. As the cylinder moves closer to the free surface the inertia or mass is reduced while the stiffness remains constant therefore the frequency increases. Strasberg (1953) observed a similar effect for spherical air bubbles oscillating near a free surface. The cylinder radius measured from the video recordings and the pulsation frequencies figure 3.57a are compared to the theoretically predicted values in figure 3.63. The observed cylinders were elliptic and therefore to compare to the theoretical equation for circular cylinders an equivalent radius was calculated for a circular cylinder of the same cross sectional area as the elliptic cylinders. The observed frequencies are all higher than the theoretically predicted values. The highest theoretically predicted frequencies occur when $L/a_o = 2$ and the observed frequencies are up to 50% higher than these predictions.

Strasberg (1953) calculated the effect of nonspherical shape on the pulsation frequency of air bubbles in water. He calculated the pulsation frequencies of air bubbles

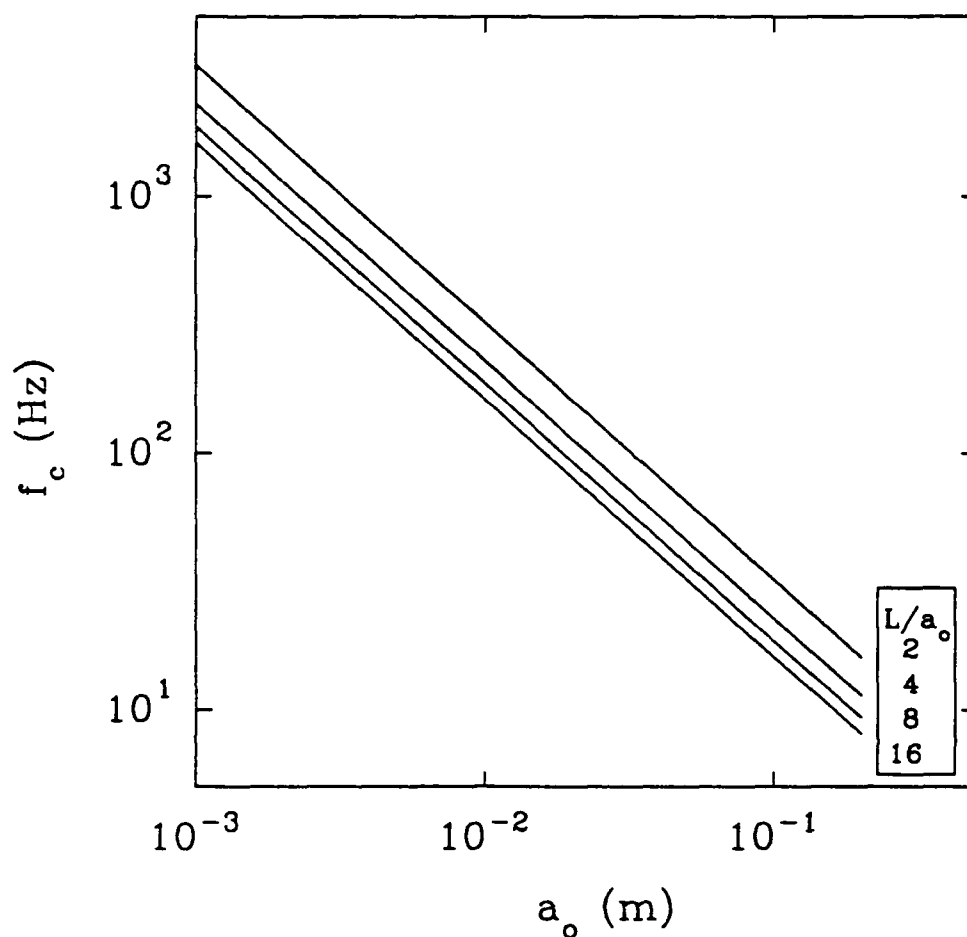


Figure 3.62 The resonant frequency f_c (Hz) of a cylinder of air oscillating near a pressure release surface as given by equation 3.19, evaluated for various values of L/a_o , the ratio of twice the distance between the cylinder center and the free surface to the cylinder radius, plotted as a function of the cylinder radius a_o (m).

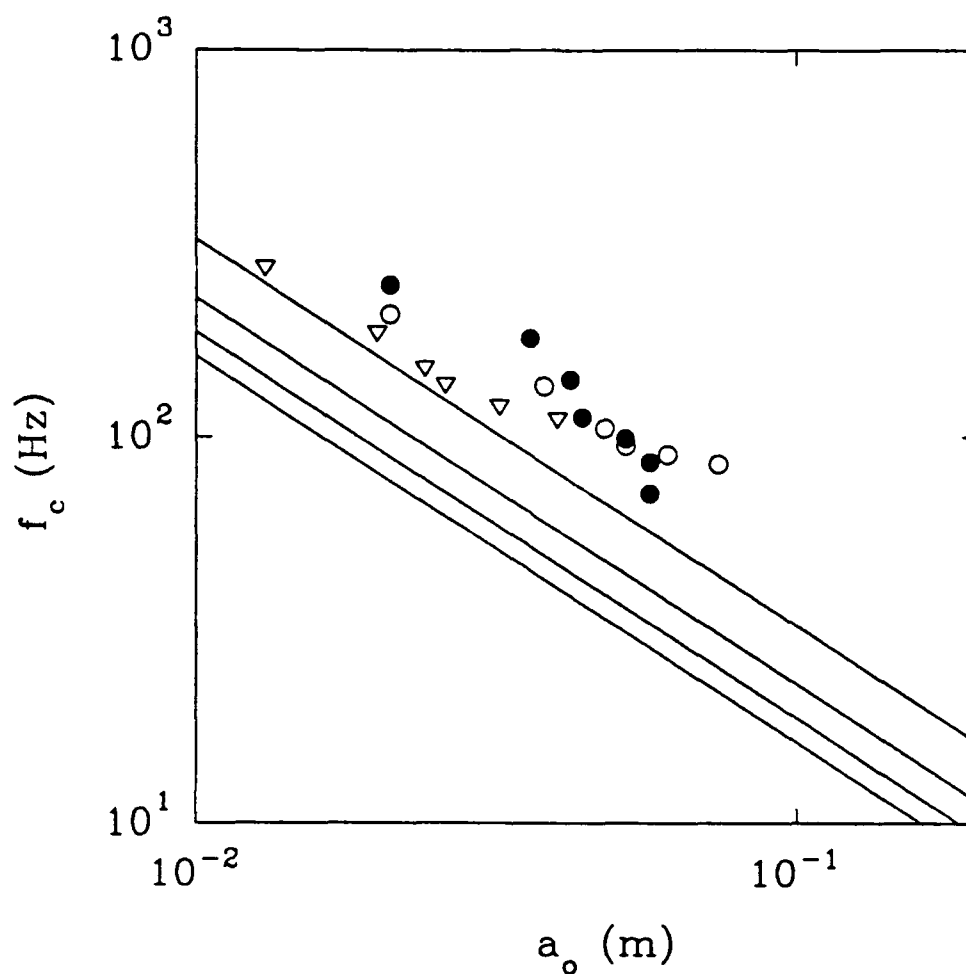


Figure 3.63 The resonant frequency f_c (Hz) a cylinder of air oscillating near a pressure release surface as given by equation 3.19 plotted as a function of the cylinder radius a_o (m) compared to the observed oscillation frequencies and radii of the cylinders of air produced by the two-dimensional breaking waves. \circ , W_1 ; \bullet , W_2 ; ∇ , W_3 .

shaped as oblate spheroids and then compared these frequencies to the pulsation frequencies of spherical bubbles of equal volumes. He found that the pulsation frequency increased as the bubbles became more nonspherical, however the effect was relatively small. For an oblate spheroid with a major to minor axis ratio of 3 the pulsation frequency was predicted to increase by 5%. In order to determine whether the effect of noncircular shape on the pulsation frequency of air cylinders was small an approach similar to Strasberg's was used. This analysis is described in detail in appendix C. The analysis showed that for an elliptic cylinder with a major to minor axis ratio of 3, which was typical of the observed cylinders, the pulsation frequency would be approximately 3% higher than that of a circular cylinder of equal volume. Therefore the effect of noncircular shape is very small and can be neglected.

The reason for the large discrepancies between the observed frequencies and those predicted by the theory was investigated further. The pulsation frequency is inversely proportional to the square root of the inertia. Therefore if the inertia of the fluid was overestimated by the theory the predicted pulsation frequencies would be too low. Equation 3.19 was derived for a plane free surface which is a great simplification compared to the real geometry of the free surface during breaking, as seen in figure 3.59. Examination of the free surface geometry indicates that the inertia or mass of the system may be considerably less than for the case of a plane free surface. One hypothesis is that it is only the mass of the water between the cylinder and the free surface which contributes to the inertia of the system (Dyer, 1991). The reasoning behind this argument is that the cylinder wall will pulsate in the direction of least resistance, towards the free surface where, for the static problem, the only resisting force is due to the weight of the thin layer of water which separates the cylinder from the atmosphere.

The mass contained in the thin layer of water above the cylinders was measured for three breaking events. Traces of the free surface geometry and cylinder were made from video recordings. One of these traces is shown in figure 3.64 for the wave packet

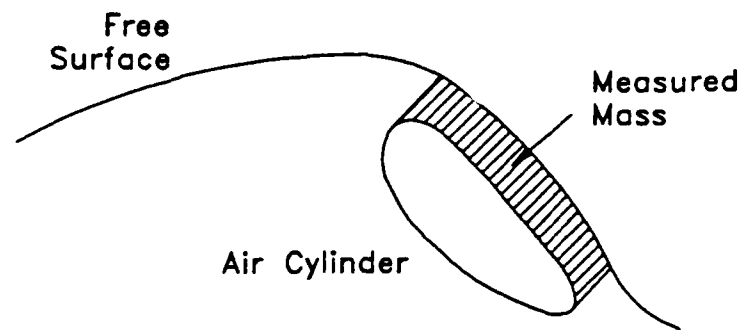


Figure 3.64 Trace of the geometry of the free surface and the air cylinder for packet W_2 with $S = 0.544$. The cross hatched region is the measured mass.

W_2 with a slope, $S = 0.544$. The cross hatched area in the figure was measured and converted to a mass per unit length of cylinder. This was done for three breaking events and the mass measured from the traces was compared to the theoretical inertia or mass predicted by equation 3.12. The correction to the pulsation frequency will be proportional to the square root of the ratio of the theoretically predicted mass to the measured mass. The results from this analysis are tabulated in table 3.6.

Wave Packet	Wave Slope	Measured Mass (kg)	Theoretical Mass (kg)	Correction Factor
W_1	0.512	7.42	23.85	1.79
W_2	0.544	6.45	14.15	1.48
W_2	0.448	3.5	8.43	1.55

Table 3.6 Results from analysis of traces of the free surface geometry and cylinder. The measured mass was obtained from the traces, the theoretical mass from equation 3.12, with $L/a_0 = 2$, and the correction factor equals $\sqrt{(\text{theoretical mass} / \text{measured mass})}$.

The mean of the correction factor is approximately 1.6. If this factor is used to correct equation 3.19 the result is,

$$f_c = \left(\frac{4.29}{a_0} \right) \frac{1}{\sqrt{\ln(L/a_0)}} . \quad 3.20$$

Equation 3.20 is compared to the observed pulsation frequency data in figure 3.65. The theory and observations are seen to agree reasonably well except for the data from the shortest wave packet, W_3 . Equation 3.20 overestimates the pulsation frequency consistently for this packet whereas for the other two longer packets the data scatter

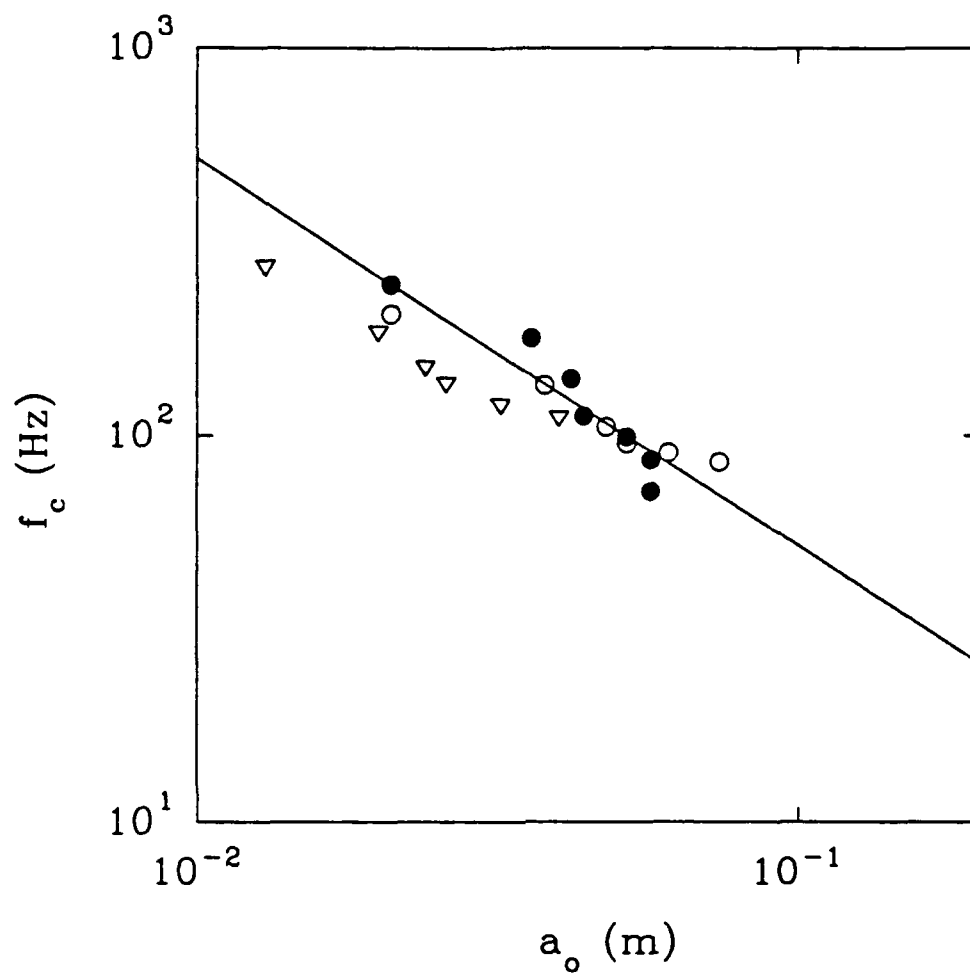


Figure 3.65 Observations of the oscillation frequencies and radii of the cylinders of air produced by the two-dimensional breaking waves compared to equation 3.20. \circ , W_1 ; \bullet , W_2 ; ∇ , W_3 .

above and below predicted values. One explanation for this may be that the mean correction factor does not apply universally to all wave scales.

3.5.4 Bubble Cloud Resonance

In the two-dimensional experiments low frequency sound was observed after the cylinder of air had broken up into a cloud of bubbles. This can be seen in the spectrographs in figures 3.54a and 3.54b. At $t = 0.4$ s the low frequency signal due to the impact of the crest occurs and at $t = 0.61$ s another signal, slightly lower in frequency begins. This second signal is visible in both the microphone and hydrophone measurements. In the microphone signal, figure 3.54a, the frequency can be seen to shift to higher frequencies as time progresses. It was postulated that these low frequency signals were caused by the collective oscillation of bubble clouds.

Felizardo (1990) studied the problem of sound scattering from bubble clouds and derived a simple formula for the resonant frequencies of a cylindrical bubble cloud. The bubble clouds were modeled as infinitely long cylindrical regions where the presence of the air bubbles increased the compressibility of the fluid and reduced the sound speed. The sound speed inside the cloud was equal to a constant value, c_2 and outside the cloud it was equal to a constant value, c_1 . The cloud boundary was assumed to be rigid and the boundary conditions applied at the cloud boundary were that the pressure and the normal component of the velocity were continuous. The radiation boundary condition was applied in the far field. The pressure fields inside and outside of the cloud must satisfy the Helmholtz equation and in the scattering problem an incident sound wave at an angle θ_0 insonifies the bubble cloud. The above formulation leads to a solution for the pressure inside the bubble cloud as follows,

$$p_2 = \sum_{n=0}^{\infty} \epsilon_n j^n \cos(n(\theta - \theta_0)) (A_n J_n(k_2 r)) \quad 3.21$$

where $\epsilon_n = 1$ when $n = 0$ and $\epsilon_n = 2$ when $n > 0$, n is the mode number, θ is the polar angle, J_n is a Bessel function of the first kind, k_2 is the acoustic wavenumber inside the bubble cloud and A_n is the resonant amplification. The resonant amplification A_n is given by,

$$A_n = \frac{2j}{\pi v (s J_n(v) H'_n(s) - H_n(sv) J'_n(v))} \quad 3.22$$

where $s = k_1/k_2$, $v = k_2 a$, a is the cloud radius, H_n is a Hankel function of the first kind and the primes denote differentiation with respect to the argument (Longuet-Higgins, 1967). A typical plot of the magnitude A_n is shown in figure 3.66 as a function of the frequency for the first three modes $n = 0, 1$ and 2 . The peaks are located at frequencies where the corresponding mode would be at resonance. The locations of these resonant peaks are the resonant frequencies of a cylindrical bubble cloud immersed in an infinite fluid.

The sound speed inside and outside of the bubble cloud and the radius of the cloud are required to calculate A_n . Void fraction measurements were made of three breaking events for the two-dimensional wave packet W_2 and for two wave amplitudes of the three-dimensional events at OTRC (Lamarre and Melville, 1991). The void fraction measurements provide the mean void fraction and the cross sectional area of the bubble cloud as a function of time. The mean void fraction was used to calculate the sound speed and the cross sectional area was converted to the radius of the circular cylinder of equal cross sectional area. The sound speed inside the cloud was calculated from the formula,

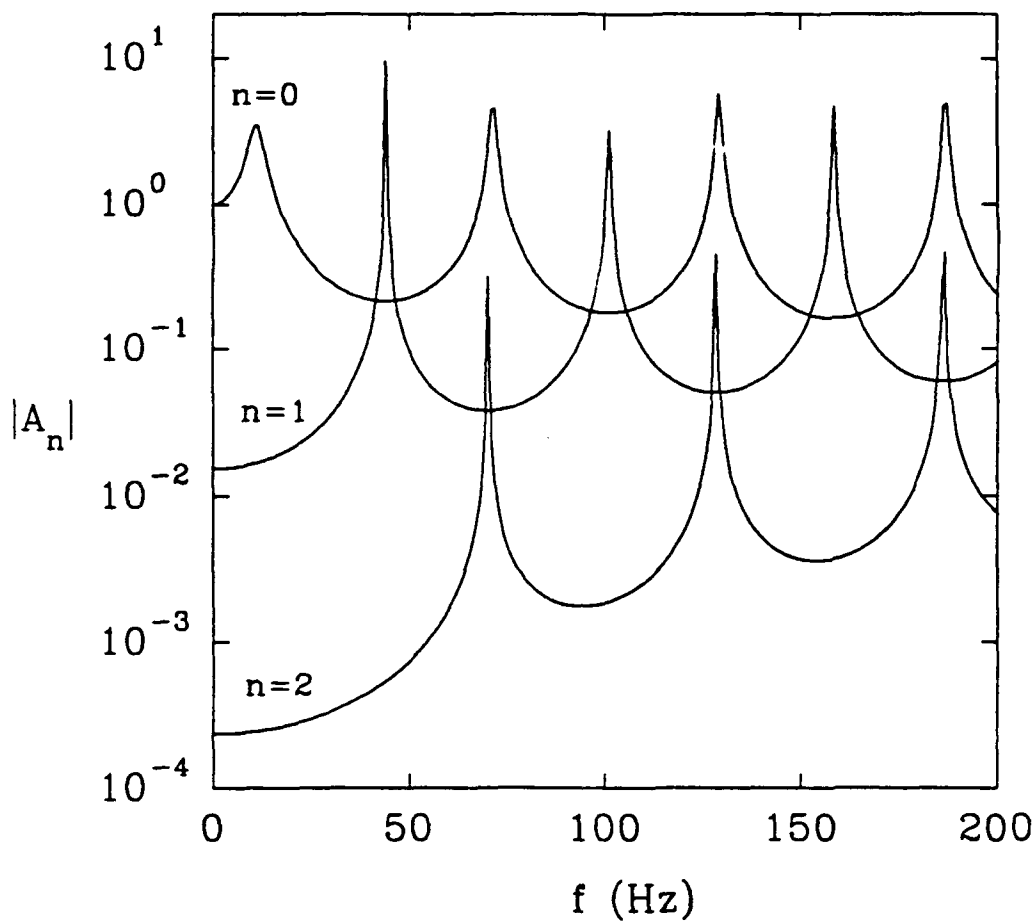


Figure 3.66 Typical plot of the magnitude of the resonant amplification factor A_n as a function of frequency f (Hz) for the first three modes for which $n = 0, 1$ and 2 .

$$c = \sqrt{\frac{P_o}{\rho\alpha(1-\alpha)}} \quad 3.23$$

where P_o is the atmospheric pressure, ρ is the density of water and α is the mean void fraction. Equation 3.23 is valid for void fraction values, $0.002 < \alpha < 0.94$ (Carey and Browning, 1988). The void fraction measurements were only accurate down to a threshold of $\alpha = 0.003$ because of system noise and therefore the cross sectional area of the bubble cloud that was measured is the area which had a void fraction > 0.003 . The error incurred by this non-zero threshold is not considered to be significant. The sound speed outside of the cloud was assumed to be 1500 m/s.

It was not possible to measure the void fraction throughout the entire breaking event because the void fraction probes were not able to resolve the cylinder of air formed immediately after the impact of the wave crest. Therefore the void fraction data begins several tenths of a second after the initial impact of the wave crest and the onset of sound production. The maximum cloud radius and the maximum mean void fraction are tabulated in table 3.7 for the 3 two-dimensional and 2 three-dimensional breaking events for which void fraction measurements were available. The ratio of the maximum cloud diameter to the widths of the bubble clouds, as obtained from the traces of the whitecaps, for the two three-dimensional events was approximately 0.06. A simple analysis can be carried out to determine the effect of the bubble cloud shape on the resonant frequency.

Wave Packet	Wave Slope or Gain	Maximum Mean Void Fraction	Maximum Cloud Radius (cm)
OTRC	0.70	0.226	29.5
OTRC	0.40	0.252	19.1
W ₂	0.544	0.307	17.6
W ₂	0.448	0.138	12.7
W ₂	0.384	0.167	9.4

Table 3.7 The maximum mean void fraction and maximum bubble cloud radius for the five breaking events for which void fraction measurements are available.

Carey et al (1990) derived an equation for the resonant frequency of the lowest mode of a spherical bubble cloud using a formulation very similar to one described previously for the two-dimensional clouds. They found that the resonant frequency of the lowest mode of a spherical bubble cloud of radius, r_o and void fraction, α was given by,

$$f_{o1} = \frac{1}{2\pi r_o} \sqrt{\frac{3\gamma P_o}{\rho\alpha}} \quad 3.24$$

where P_o is the gas pressure in the bubbles which is equal to the atmospheric pressure, γ is the ratio of the specific heats set equal to 1 corresponding to isothermal conditions and ρ is the density of pure water 1000 kg/m³. For the two three-dimensional breaking events for which void fraction data are available the width of the bubble cloud can be estimated by measuring the width of the whitecap in frame (b) of figures 3.43 and 3.47. The measurements of the void fraction provide the cross-sectional area of the cloud and

therefore the volume of the cloud can be estimated. Then, the radius of a spherical bubble cloud of equal volume, r_o can be calculated and this can be used in equation 3.24 to calculate the resonant frequency of the lowest mode. This value can be compared to the resonant frequency of the lowest mode of a two-dimensional bubble cloud predicted by locating the peaks in the magnitude of A_n , given by equation 3.22. The results of such a comparison for the two three-dimensional breaking events is shown tabulated in table 3.8

gain	t (s)	a_o (cm)	r_o (cm)	α	f_o	f_{os}
0.40	1.6	15.6	39.2	0.252	14	14
0.40	2.1	17.1	41.7	0.039	31	34
0.40	2.6	11.5	31.2	0.017	71	68
0.70	1.6	19.7	61.5	0.226	12	9
0.70	2.1	28.3	78.0	0.057	15	15
0.70	2.6	27.0	76.0	0.018	30	27

Table 3.8 A comparison of the predicted resonant frequency of the lowest mode of a two-dimensional bubble cloud, f_o (calculated from the magnitude of A_n given by equation 3.22) and the predicted resonant frequency of the lowest mode of a spherical bubble cloud of equal volume, f_{os} (calculated from equation 3.24). a_o is the radius of the observed bubble cloud, r_o is the radius of a spherical bubble cloud of equal volume and α is the mean void fraction of the observed bubble cloud.

The results in table 3.8 show that the resonant frequencies predicted by either method differ by a maximum of 25%. This indicates that the shape of the bubble cloud has very little effect on predictions of the resonant frequency of the lowest mode.

Therefore, it is believed that reasonable predictions of the resonant frequencies of the three-dimensional bubble clouds can be obtained by assuming they are two-dimensional.

The locations of the resonant peaks were evaluated for the first four modes, $n = 0, 1, 2$ and 3 , and are shown plotted in figures 3.67 to 3.71. The predicted resonant frequencies for each event and mode show a similar trend. As time elapses the resonant frequencies increase. This is to be expected as the mean void fraction decreased monotonically from its maximum value and this translates into a sound speed which increases monotonically for the range of void fractions observed. Although the size of the bubble cloud initially increases, and this would tend to decrease the resonant frequencies, the increase in the sound speed due to the decrease in the mean void fraction appears to dominate and therefore the predicted trend is for the resonant frequencies to increase with time. Another feature of the theoretical results is that the clouds of larger radius have many more resonant peaks than the smaller clouds. The largest bubble cloud was produced by the three-dimensional breaking event with a gain of 0.70 and it had a maximum radius of 29.5 cm and 7 resonant peaks below 500 Hz for mode 1 . The smallest bubble cloud was produced by the two-dimensional breaking event, packet W_2 with a slope of 0.384 and it had a maximum radius of 9.4 cm and 2 resonant peaks below 500 Hz.

The resonant frequencies were plotted directly on the spectrographs of the hydrophone and microphone signals to determine if any of the spectral peaks in the data matched the predicted resonant frequencies. In figures 3.72 and 3.73 spectrographs from the two-dimensional experiments are plotted for packet W_2 with a slope of, $S = 0.384$. The resonant frequencies for the first two modes, mode 0 in the upper plot and mode 1 in the lower plot, are also plotted. It was found that the resonant frequencies of the higher modes were too large to correspond to the low frequency spectral peaks in the data and therefore they are not shown plotted with the spectrographs here. Both the hydrophone spectrograph plotted in figure 3.72 and the microphone spectrograph in figure 3.73 have

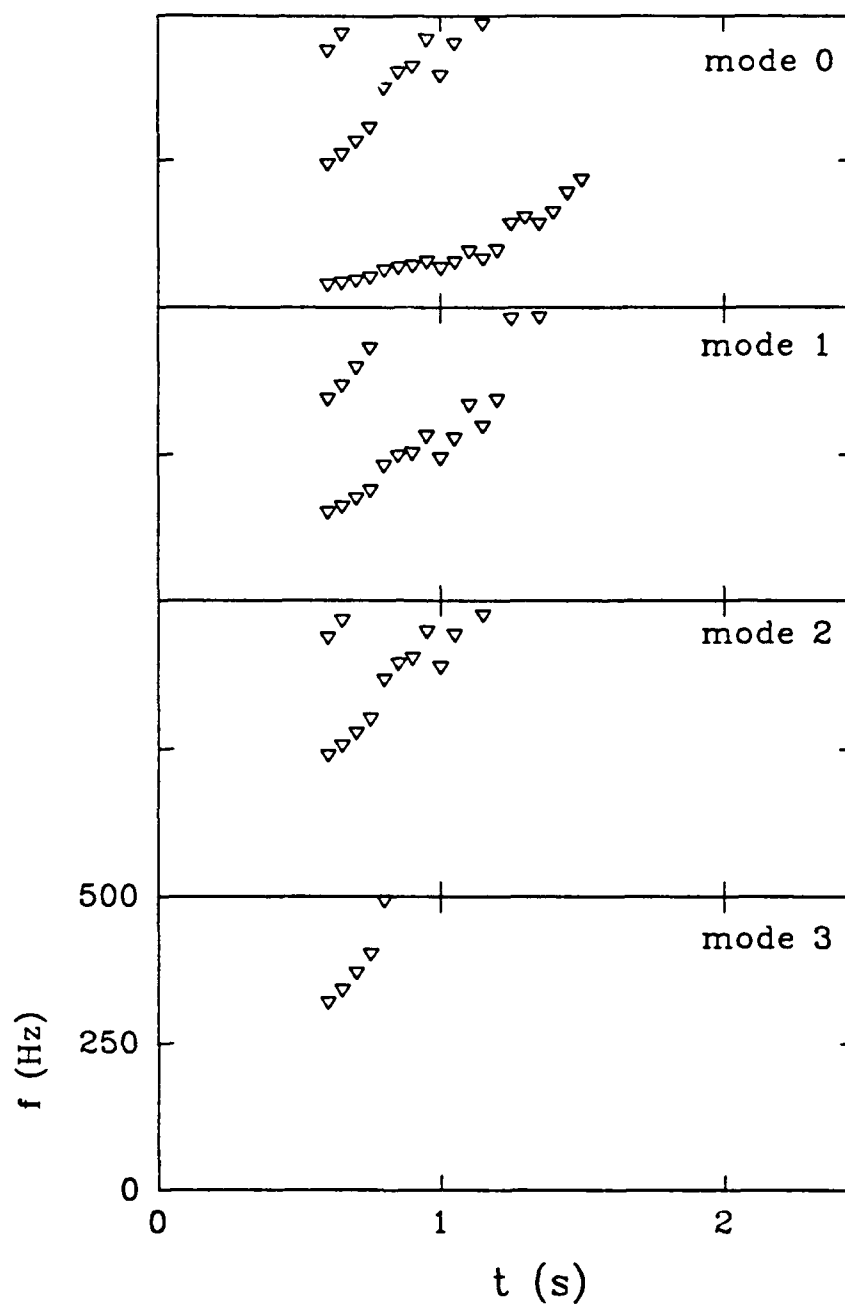


Figure 3.67 Theoretical predictions of the resonant frequencies f (Hz) of the first 4 modes ($n = 0, 1, 2$ and 3) of a cylindrical bubble cloud as a function of time for the two-dimensional packet W_2 with $S = 0.384$.

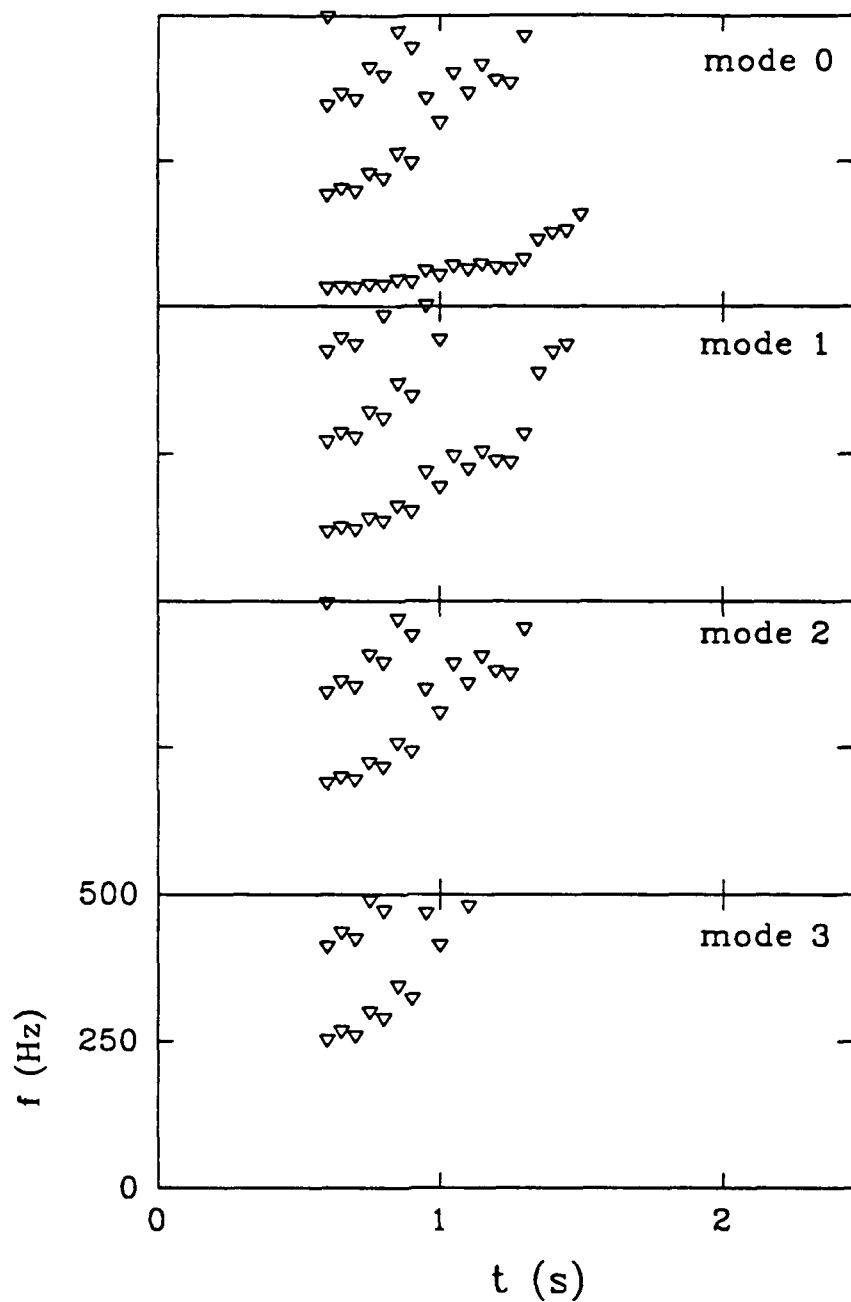


Figure 3.68 Theoretical predictions of the resonant frequencies f (Hz) of the first 4 modes ($n = 0, 1, 2$ and 3) of a cylindrical bubble cloud as a function of time for the two-dimensional packet W_2 with $S = 0.448$.

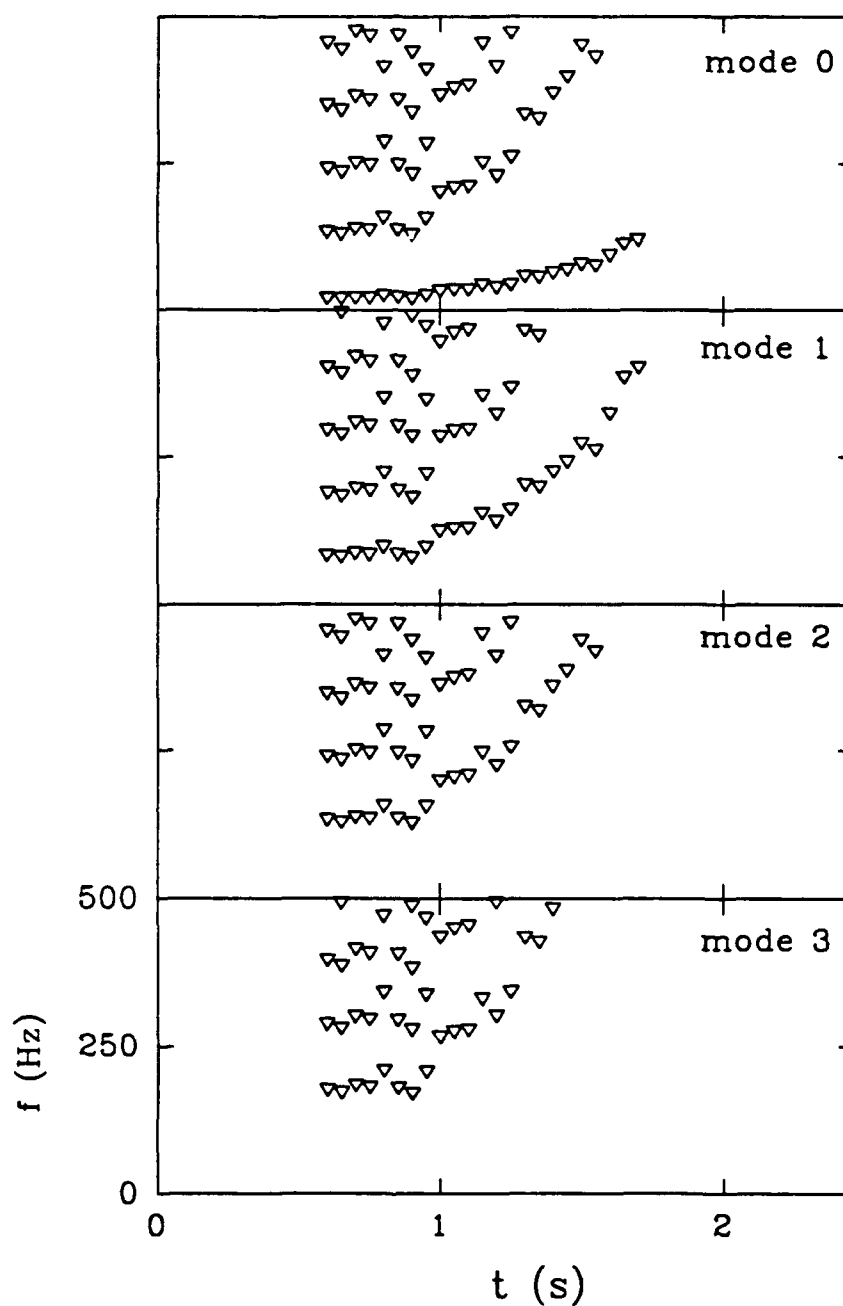


Figure 3.69 Theoretical predictions of the resonant frequencies f (Hz) of the first 4 modes ($n = 0, 1, 2$ and 3) of a cylindrical bubble cloud as a function of time for the two-dimensional packet W_2 with $S = 0.544$.

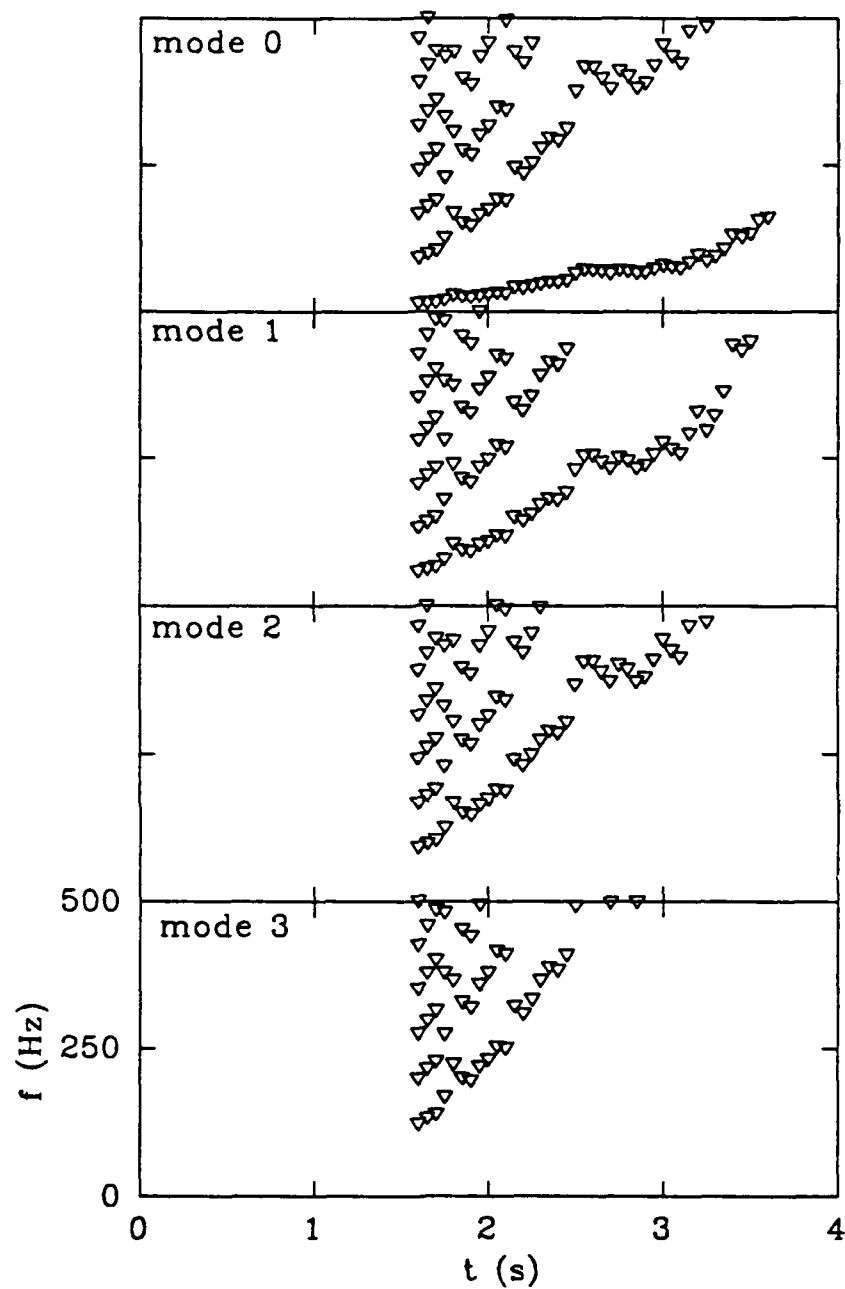


Figure 3.70 Theoretical predictions of the resonant frequencies f (Hz) of the first 4 modes ($n = 0, 1, 2$ and 3) of a cylindrical bubble cloud as a function of time for the three-dimensional packet with gain $A = 0.40$.

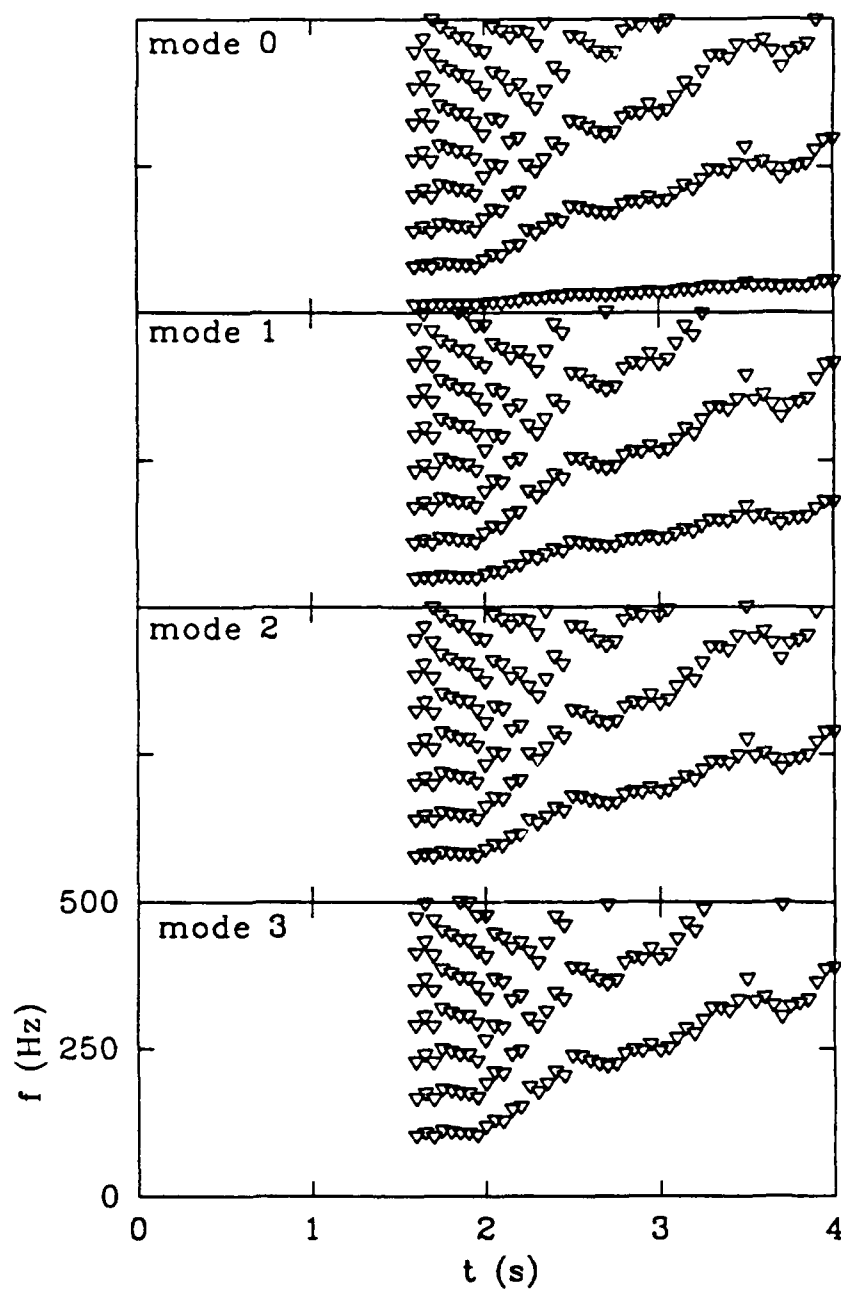


Figure 3.71 Theoretical predictions of the resonant frequencies f (Hz) of the first 4 modes ($n = 0, 1, 2$ and 3) of a cylindrical bubble cloud as a function of time for the three-dimensional packet with gain $A = 0.70$.

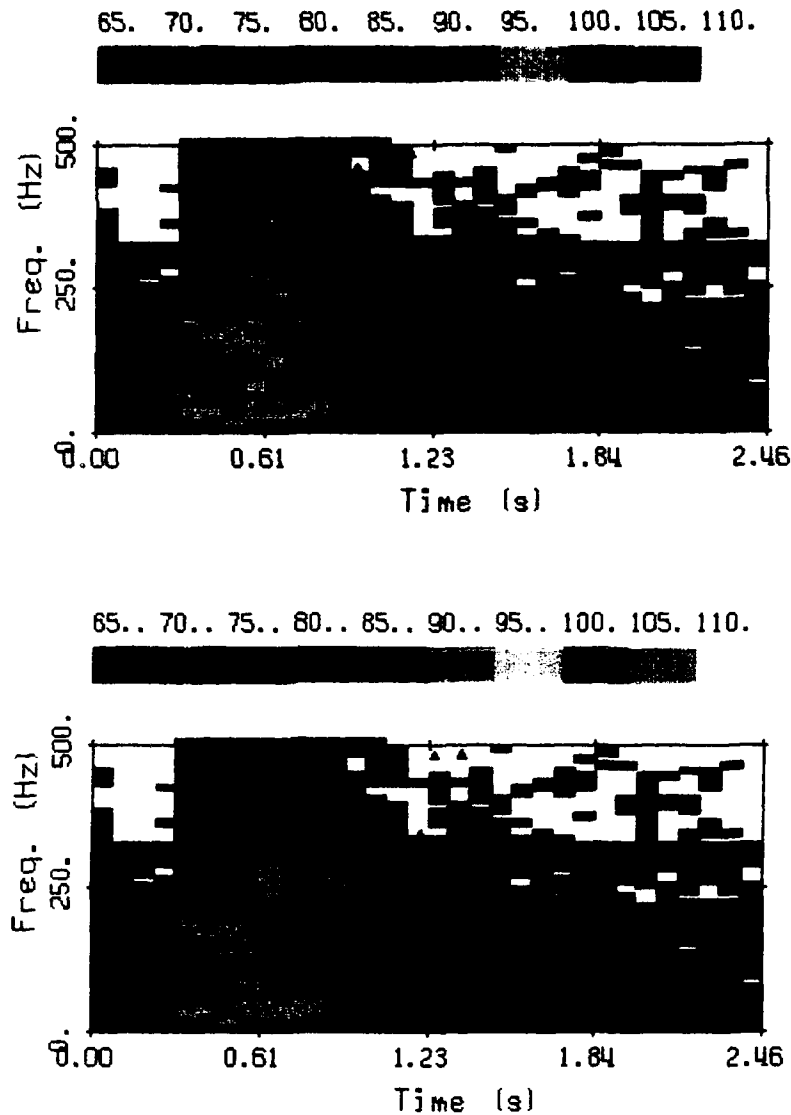


Figure 3.72 Spectrograph of the signal from the upstream hydrophone for the two-dimensional breaking event packet W_2 with $S = 0.384$. The theoretical resonant frequencies of a cylindrical bubble cloud computed using the void fraction data are marked with Δ for mode 0 in the upper plot and for mode 1 in the lower plot. The spectra were averaged over 5 repeats of the event and were calculated for 32-2048 point segments overlapped by 512 points and windowed with a Blackman-Harris window. The bandwidth resolution is 9.8 Hz. Each color corresponds to a 5 dB re $1 \mu\text{Pa}^2$ increment in spectral level.

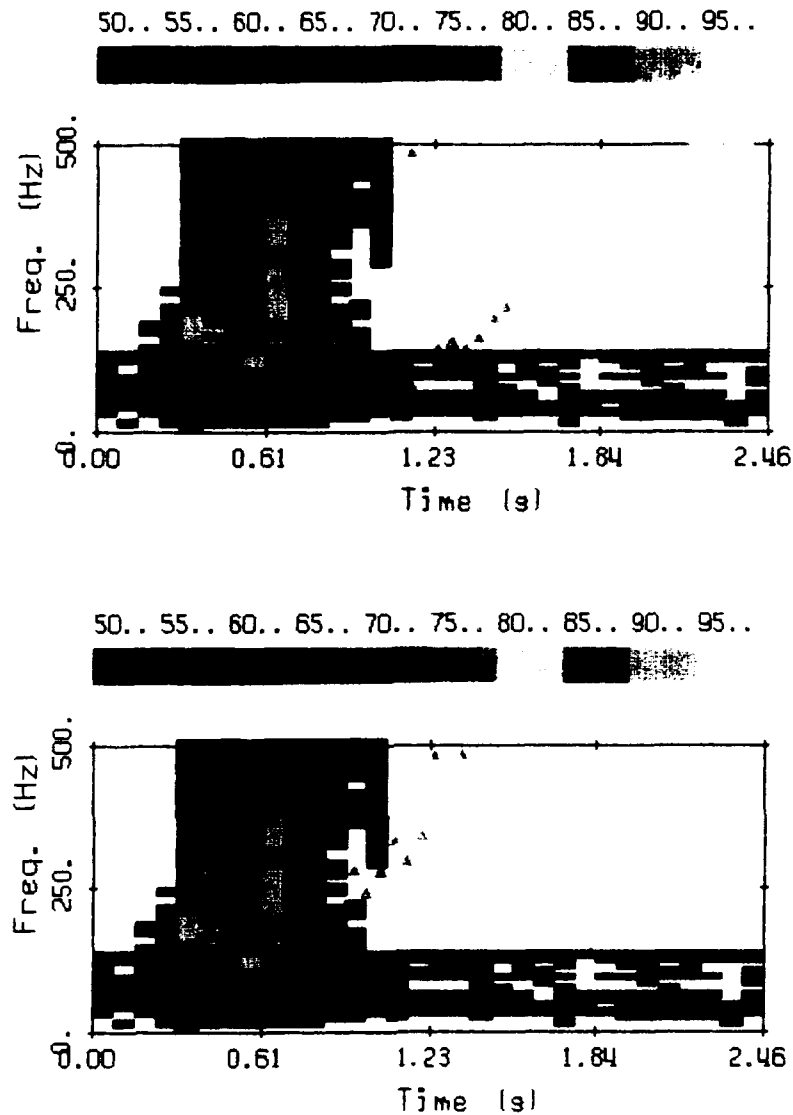


Figure 3.73 Spectrograph of the signal from the microphone for the two-dimensional breaking event packet W_2 with $S = 0.384$. The theoretical resonant frequencies of a cylindrical bubble cloud computed using the void fraction data are marked with Δ for mode 0 in the upper plot and for mode 1 in the lower plot. The spectra were averaged over 5 repeats of the event and were calculated for 32-2048 point segments overlapped by 512 points and windowed with a Blackman-Harris window. The bandwidth resolution is 9.8 Hz. Each color corresponds to a 5 dB re 1 μPa^2 increment in spectral level.

spectral peaks which agree with the predicted resonant frequencies of the second mode, for which $n = 1$. The predicted resonant frequencies for the lowest mode, $n = 0$, do not match the spectral peaks in this data. The spectral peaks in both the hydrophone and microphone spectrographs shift to higher frequencies as time increases and this feature is predicted by the theoretical results. Void fraction measurements were not possible before $t = 0.6$ s and therefore predictions of the resonant frequencies for times earlier than this are not possible. However, if the predicted resonant frequency in both spectrographs are extrapolated linearly to earlier times they agree very closely with the observed spectral peaks. It is evident from these plots that the acoustic signals cease long before the bubble clouds have disappeared. This can be seen in figures 3.72 and 3.73 where the void fraction data and therefore the predicted resonant frequencies extend out to $t = 1.5$ s whereas the acoustic signals end at approximately $t = 1$ s.

The low frequency sound is produced during the early stages of the bubble cloud's lifetime. The most energetic period of breaking is immediately following the impact of the crest when large volumes of air are forced down into the water column. The process of bubble cloud formation as these large volumes of air break-up is also very violent and energetic. As energy is dissipated, the fluid motions become less violent and there is less energy available to excite individual bubbles or clouds of bubbles and the acoustic signals become weaker and eventually stop. At the point when the acoustic signals have stopped, a bubble cloud of significant void fraction is still present in the water column. Lamarre and Melville (1991) observed that the mean void fraction remained above 0.01 within the first wave period following breaking. The duration of the low frequency signals observed in the two-dimensional experiments was approximately $1/2$ a wave period.

Prosperetti (1988) states that the damping constant of the individual bubbles in the cloud will be approximately equal to the value for a single isolated bubble oscillating at the resonant frequency of the cloud. The damping of individual bubbles is greatly

increased at frequencies much smaller than the resonant frequency of the individual bubbles (see figure 1.7). He concluded that bubble clouds oscillating at their resonant frequencies would not produce significant sound unless the clouds were comprised of bubbles with radii > 1 mm. This may be another reason why the low frequency signals are much shorter in duration than the period over which the mean void fraction inside the cloud is significant. It may be that the low frequency oscillations are increasingly damped out as the bubble sizes become smaller and the larger bubbles rise rapidly back up to the free surface. Lamarre and Melville (1991) found that while the mean void fraction remained above 0.01 for one wave period that only 5% of the initially entrained air remained in the water column after one wave period.

The spectral data from the three-dimensional breaking experiments was also compared to the theoretically predicted resonant frequencies. In figures 3.74 and 3.75 two hydrophone spectrographs are compared to the resonant frequencies of the first and second modes. The resonant frequencies of the first mode, $n = 0$, are plotted in the upper plot and those of the second mode, $n = 1$, in the lower plot. In these figures the first 15 spectra were averaged to give an estimate of the background noise spectrum which was then subtracted from each spectra plotted in the spectrograph. This procedure removed the large spectral peaks due to machinery noise and made it much easier to detect the spectral peaks produced by breaking. The spectrograph in figure 3.74 is for the largest amplitude event, $A = 0.70$ and is an ensemble average of 5 repeats using the data from the downstream hydrophone. The resonant frequencies of the second mode, $n = 1$, appear to match the spectral peaks in the data more closely than those of the first mode, $n = 0$. In figure 3.75 a spectrograph ensemble-averaged over 3 repeats of the event with $A = 0.40$ with measurements from the upstream hydrophone is plotted. There are two spectral peaks of 101 dB, one at approximately 15 Hz and a second at approximately 90 Hz. The predicted resonant frequencies of the lowest mode, $n = 0$, match the peak at 15 Hz and the resonant frequencies of the second mode, $n = 1$, match the peak at 90 Hz. It

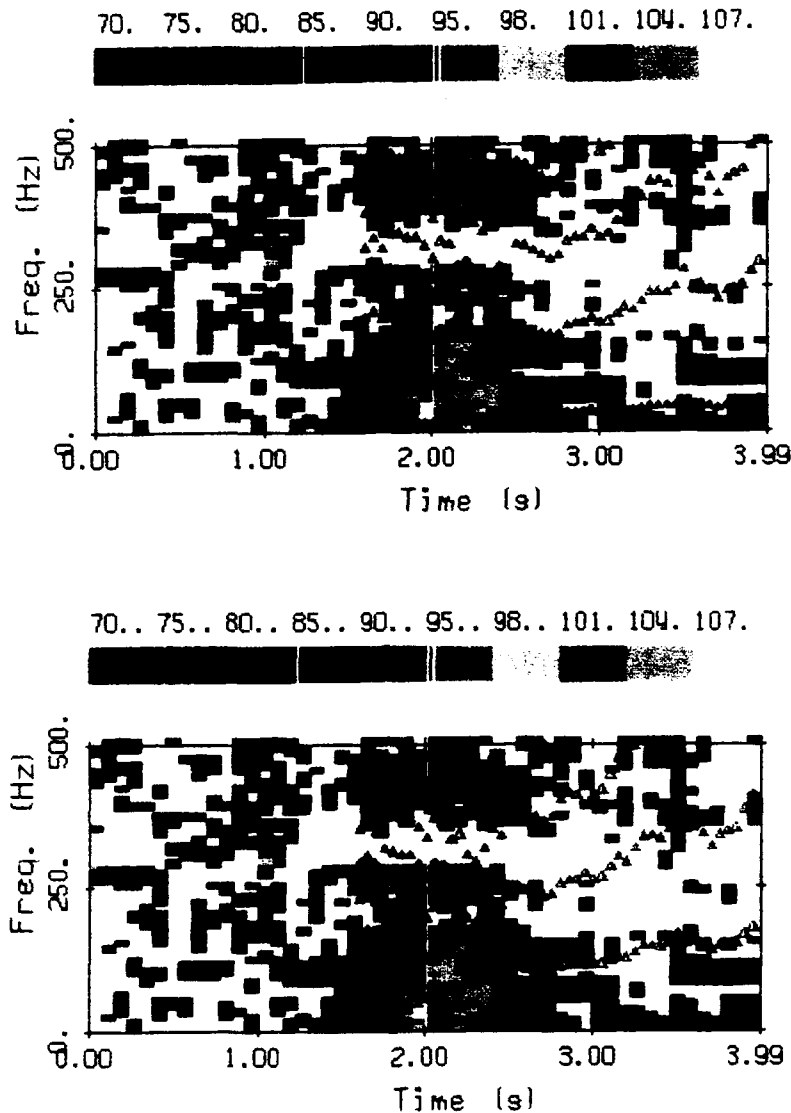


Figure 3.74 Spectrograph of the signal from the downstream hydrophone for the three-dimensional breaking event with $A = 0.70$. The theoretical resonant frequencies of a cylindrical bubble cloud computed using the void fraction data are marked with Δ for mode 0 in the upper plot and for mode 1 in the lower plot. The spectra were averaged over 5 repeats of the event and were calculated for 52-4096 point segments overlapped by 1024 points and windowed with a Blackman-Harris window. The bandwidth resolution is 9.8 Hz. Each color corresponds to a 5 or 3 dB re $1 \mu\text{Pa}^2$ increment in spectral level.

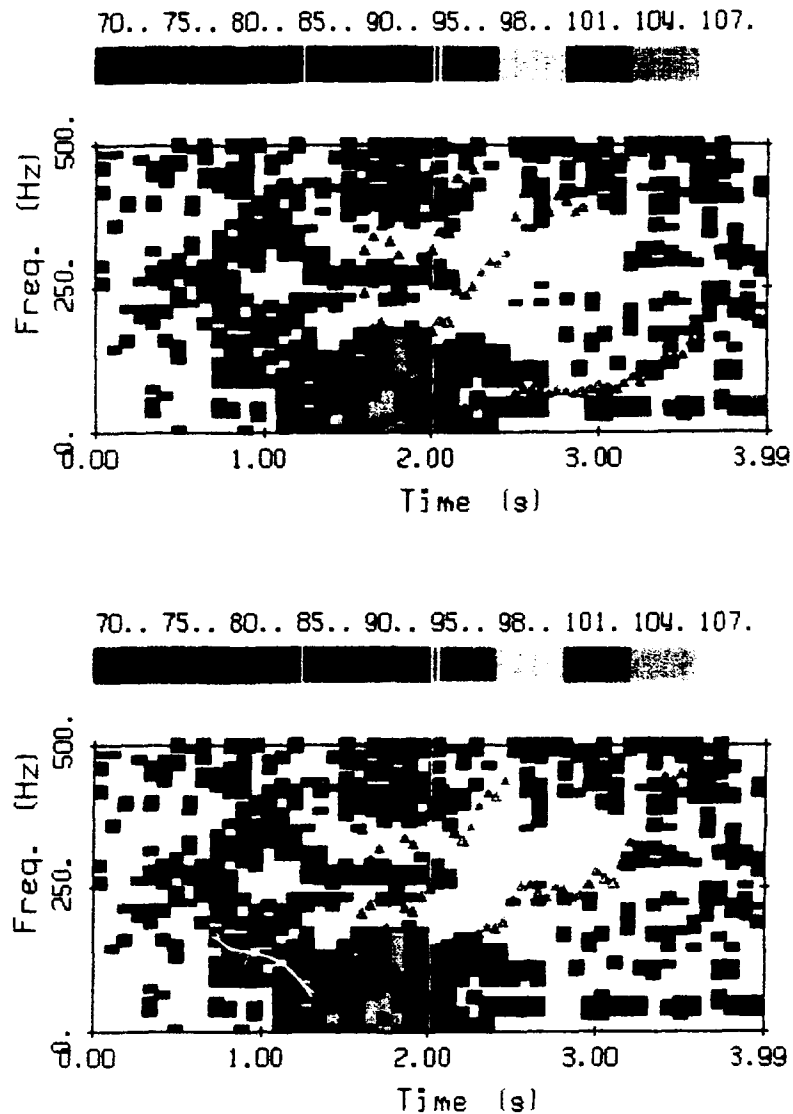


Figure 3.75 Spectrograph of the signal from the upstream hydrophone for the three-dimensional breaking event with $A = 0.40$. The theoretical resonant frequencies of a cylindrical bubble cloud computed using the void fraction data are marked with Δ for mode 0 in the upper plot and for mode 1 in the lower plot. The spectra were averaged over 5 repeats of the event and were calculated for 52-4096 point segments overlapped by 1024 points and windowed with a Blackman-Harris window. The bandwidth resolution is 9.8 Hz. Each color corresponds to a 5 or 3 dB re $1 \mu\text{Pa}^2$ increment in spectral level.

was more difficult to determine for the three-dimensional breaking events which mode matched the data more closely. After analyzing all the data it was concluded that the resonant frequencies of the second mode did agree more closely with the observations.

The two-dimensional breaking waves produce low frequency sound through two mechanisms. The pulsation of the cylinder of air and the resonant oscillation of the bubble clouds. The air cylinder begins to pulsate immediately upon its formation and continues to radiate sound up until the time it breaks up and forms a cloud of smaller air bubbles. The frequency of the radiated sound remains constant throughout the lifetime of the cylinder. The second mechanism begins to produce low frequency sound when the bubble cloud is formed following the break-up of the cylinder. The sound radiated by the resonant oscillation of the bubble cloud is generally lower in frequency than that radiated by the pulsating cylinder. This is because the sound speed inside the air cylinder prior to its break-up is 340 m/s the sound speed in air. After the cylinder breaks up the void fraction abruptly decreases from a value of 1.0 to approximately 0.3 and the sound speed decreases to 22 m/s. This dramatic decrease in the sound speed produces a resonant frequency of the bubble cloud which is generally lower than that of the air cylinder from which it was spawned. As the air cylinder breaks up the radius of the bubble cloud must grow because the volume of air is conserved for up to a quarter of the wave period after breaking (Lamarre and Melville, 1991). The larger bubble cloud radius will also tend to decrease the resonant frequencies.

An estimate of the decrease in the frequency can be made by calculating the inertia and stiffness for the case of the bubble cloud compared to the air cylinder. For the case of an air cylinder near a free surface, the inertia of the fluid is $(-2\pi\rho a_0^2 \ln(a_0/L))$ and the stiffness is $(4\pi\rho_g c_g^2)$. It is assumed that these equations also apply to the bubbly mixture in the cloud. The volume of air is initially conserved as the cylinder of air breaks up and forms a bubble cloud with a mean void fraction of α . If V_0 is the volume of air in the cylinder then V_1 the total volume in the bubble cloud is given by, $V_1 = V_0/\alpha$.

The volume is proportional to the radius squared and therefore the inertia of the fluid around the oscillating bubble cloud is $1/\alpha$ times larger than the inertia of the fluid around the oscillating cylinder of air. The density of the air-water mixture with void fraction of α is $\rho_m = \rho (1 - \alpha)$ where ρ is the density of the pure fluid. The sound speed in the mixture is given by $c_m = \sqrt{P/(\rho\alpha(1-\alpha))}$ and c_g is the sound speed in air. If it is assumed that a_0/L is constant then the ratio of the pulsation frequency of the bubble cloud to that of the air cylinder is given by,

$$\frac{f}{f_0} = \sqrt{\frac{\rho_m c_m^2}{\rho_g c_g^2} \frac{1}{\alpha}} = \sqrt{\frac{\rho(1-\alpha)P_0\alpha}{\rho_g c_g^2 \rho\alpha(1-\alpha)}} = \sqrt{\frac{P_0}{\rho_g c_g^2}} \quad 3.25$$

With $P_0 = 101$ kPa, $\rho_g = 1.23$ kg/m³ and $c_g^2 = 340$ m/s equation 3.25 reduces to a constant value, $f/f_0 = 0.84$. It is interesting to note that the percentage decrease is constant and does not depend on the void fraction α . A 16% decrease in the frequency is approximately equal to 1/2 the magnitude of the typical decrease in frequency observed in the data. This can be seen in figure 3.54 where the initial impact frequency is 130 Hz and the spectral peak shifts down to approximately 85 Hz, a decrease of 35% which was equal to the average decrease observed for all the events. One reason the predicted decrease in the frequency underestimates the observed decrease may be because the ratio a_0/L is not constant. A second reason may be that the equations for the stiffness and mass of a cylinder of pure air do not apply exactly to the case of a bubble cloud comprised of a mixture of air and water. This example shows that both the inertia and the stiffness increase when the cylinder of air breaks apart and forms the bubble cloud but the inertia increases more than the stiffness and therefore the resonant frequency decreases.

3.5.5 Comparison of Two and Three-Dimensional Results

The observed sound spectra from the two-dimensional experiments are quite different in character from those observed in the three-dimensional experiments. This is as discussed earlier due to the fact that the underwater acoustic signals in the two-dimensional experiments were altered because of their propagation in the waveguide formed by the wave channel. The spectra observed in the three-dimensional experiments were not affected significantly by the modal properties of the OTRC wave channel. Comparisons of the sound spectra of the two data sets are not very meaningful. However, comparisons of some of the averaged acoustic measures can be made.

If the plots of the pressure spectrum level as a function of time are compared, there appears to be a significant difference. In figures 3.13 and 3.14 the pressure spectrum level as a function of time for the two hydrophone signals from the two-dimensional experiments are plotted and it is apparent that for the steeper, large amplitude events that the sound levels increase abruptly at all frequencies when the wave impacts the free surface. In figures 3.34, 3.35, 3.37 and 3.38 the pressure spectrum level as a function of time for the two hydrophone signals from the three-dimensional experiments are plotted and it is evident that the sound levels do not rise as abruptly as for the case of the two-dimensional breakers in figures 3.13 and 3.14. This is probably due to the fact that the mechanics of the breaking process are quite different in the two sets of experiments. When the two-dimensional waves break, the crest curls over and impacts the free surface uniformly across the entire channel width. In the case of the three-dimensional breakers, breaking begins near the center of the wave and the crest curls over and impacts the free surface first at the center and then progressively later in time the greater the transverse distance from the wave center. Therefore, two-dimensional breaking switches on the sound abruptly because the entire crest impacts the

free surface simultaneously whereas in three-dimensional breaking the sound levels build up more gradually because the entire crest does not impact the free surface simultaneously. Farmer and Vagle (1989) measured the sound generated by breaking ocean waves and a typical time series of the pressure spectrum level observed by them is shown plotted in figure 3.76 (another example is shown plotted in figure 1.3). It is clear from this figure that the results from the three-dimensional experiments agree more closely with field observations. This is to be expected because breaking ocean waves are always three-dimensional and they only occasionally approach the two-dimensional case when they break simultaneously across a large fraction of their width.

The other comparison which can be made between the two and three-dimensional experiments is the correlation of the mean square acoustic pressure, $\overline{p^2}$ with the wave slope, S and gain, A . In the two-dimensional experiments the wave slope, S is proportional to the wave amplitude and in the three-dimensional experiments the gain is proportional to the wave amplitude, A . The correlations of the mean square acoustic pressure, $\overline{p^2}$ with wave slope, S from the hydrophone signals are shown plotted in figures 3.16 and 3.17 for the two-dimensional experiments and with gain, A in figures 3.40 and 3.41 for the three-dimensional experiments. In both the two and three-dimensional experiments the log of the mean square acoustic pressure $\overline{p^2}$ in the lower frequency band is proportional to the wave slope S or the gain A . Similarly, a comparison of the correlation of the mean square acoustic pressure, $\overline{p^2}$ with the wave slope, S or the gain, A in the higher frequency band, $f > 1$ kHz, shows that the results from the two and three-dimensional experiments are very similar. In both cases the mean square acoustic pressure, $\overline{p^2}$ increases rapidly as the slope or gain is increased from the value for the incipient event until a plateau is reached and then the value of $\overline{p^2}$ remains essentially constant for larger values of S and A . This close agreement between the two data sets is confirmation that measurements of the sound generated by two-dimensional

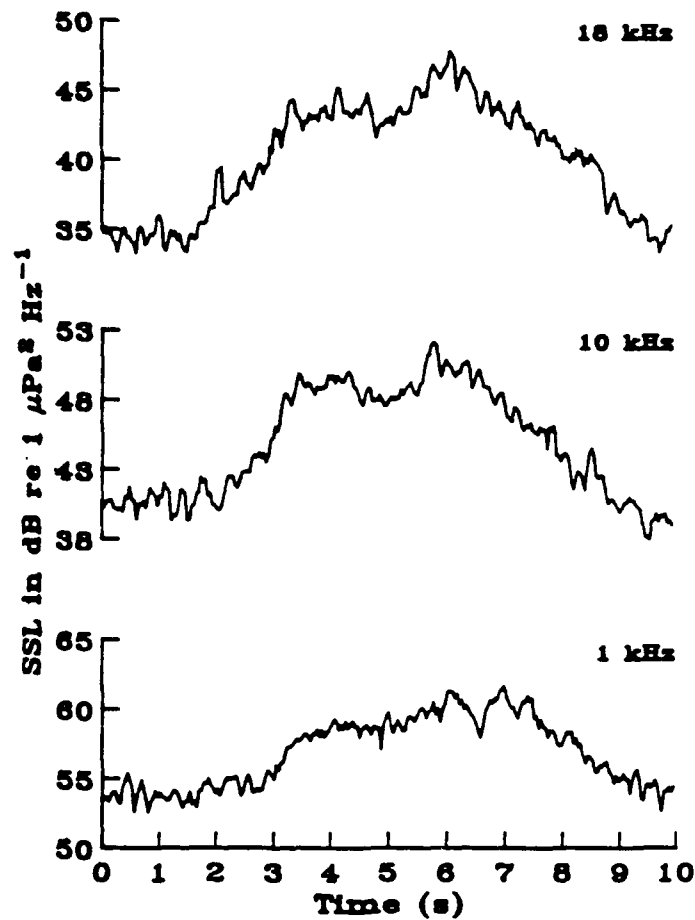


Figure 3.76 Time series of the sound spectrum level, SSL (same as PSL) in dB re 1 $\mu\text{Pa}^2/\text{Hz}$ in three frequency bands centered at 1 kHz, 10 kHz and 18 kHz when an ocean surface wave is breaking overhead of the sampling hydrophone (Farmer and Vagle, 1989).

breaking can be used to study how the dynamics of breaking are related to averaged acoustic measurements such as the mean square acoustic pressure.

The excellent agreement between the correlations of the mean square acoustic pressure with wave slope and gain from the two and three-dimensional experiments also implies that it may be possible to scale the averaged acoustic measurements from experiments conducted in smaller wave channels to larger scales. The variation in the scale of the waves from the wave channel at MIT to OTRC is significant. It can be seen in figure 3.26 from the spectra of the surface displacement that the breaking wave packet at OTRC had significant energy at frequencies from 0.7 Hz down to 0.3 Hz. This corresponds to wavelengths from 3 m to 17 m compared to wavelengths of approximately 2 m in the MIT wave channel.

One of the most obvious differences between the two and three-dimensional experiments was the absence of the pulsating cylinder of air in the three-dimensional experiments. There are two factors which may be responsible for this. First, in the three-dimensional experiments there were no sidewalls to confine the air laterally. Second, as discussed above, breaking occurs first near the center of the wave in the three-dimensional case and as a result the crest does not impact the free surface simultaneously across the entire width of the wave. These two factors in combination prevent a single large cylinder of air from being formed. Under the three-dimensional breakers underwater video recordings showed that no smooth-walled cylinder existed. In the two-dimensional case when the crest impacts the free surface the cylinder closes off and this may cause the pressure of the gas inside the cylinder to increase slightly above the atmospheric pressure because it is confined laterally by the sidewalls of the tank. The cylinder can maintain this pressure for a short period of time because the air is trapped. The increased pressure inside the cylinder may be what permits it to remain stable for as long as it does. In the three-dimensional case, no increase in pressure is possible because the air can escape laterally very easily because the cylinder is not closed off

simultaneously across the entire width of the wave. The underwater video recordings of the three-dimensional breakers showed that a cylindrical bubble cloud tapered at the ends was formed and grew laterally in size as breaking progressed and that from the start of breaking, the cloud was comprised of relatively small air bubbles.

Chapter 4: A Model Of the Sound Generated by Gently Breaking Waves

4.1 Introduction

In this chapter a model of the sound produced by gently spilling breaking waves is presented. A large portion of this chapter is taken from "A model of the sound generated by breaking waves", M.R. Loewen and W.K. Melville, J. Acoust. Soc. Am., 90, p. 2075-2080, 1991. Recent experiments in the laboratory and at sea have proven convincingly that the sound generated by gently spilling breakers is due to newly created bubbles oscillating at their linear resonant frequencies (Medwin and Beaky, 1989, Medwin and Daniel, 1990 and Updegraff and Anderson, 1991a,b). The observed sound spectra in the laboratory and at sea sloped at -5 dB per octave in agreement with field measurements (Knudsen et al, 1948 and Wenz, 1962). From these observation it was concluded that the dominant source of ambient sound in the ocean at frequencies from 1 kHz to 20 kHz is oscillating air bubbles entrained by spilling breakers. Both the field and laboratory measurements were made in the presence of only very small scale breaking waves and therefore their observations and conclusions are only applicable to low windspeeds and relatively mild breaking.

Medwin and Daniel (1990) used an array of four hydrophones to identify the radius, position and the time of creation of several hundred bubbles beneath gently spilling waves. However, they did not report the dipole strength as a function of bubble size and therefore it is not possible to directly confirm that their measured sound spectrum is consistent with their measured bubble population. Updegraff and Anderson (1991b) conducted a very similar experiment at sea and they observed that the peak oscillation pressures radiated by individual bubbles was not a function of the resonant

frequency or bubble radius. This can be seen in figure 4.1 where the peak oscillation pressure for 81 bubbles observed by Updegraff and Anderson (1991b) are shown plotted as a function of frequency. The solid line is a plot of the average peak oscillation pressure in 1 kHz wide bins. The averages in the 1 kHz bins do not show any dependence on the frequency or bubble radius.

Bubbles which are formed at the free surface are not in equilibrium initially and must relax to an equilibrium spherical shape. It is this relaxation process which leads to the linear oscillation of the bubbles at the lowest mode (i.e. breathing mode) which has a frequency given by

$$\omega_b = \frac{1}{a} \left(\frac{3\gamma P_o}{\rho} \right)^{1/2} \quad 4.1$$

where ω_b is the resonant radian frequency of the breathing mode, a is the equilibrium radius of the bubble, γ is the ratio of the specific heats of the bubble gas, P_o is the ambient bubble pressure and ρ is the density of water (Minnaert, 1933). Longuet-Higgins (1989a,b) has presented a non-linear theory which proposes that the asymmetric or "shape" oscillations of the newly created bubbles produce significant sound energy. The search for experimental evidence that this mechanism is important remains an area of active research but to date the results are inconclusive.

Medwin and Daniel (1990) used eq. 4.1 to calculate the bubble size distribution from the sound data¹. In figure 4.2 we have plotted their bubble size distribution data recomputed to show the number of bubbles per wave per radius increment. A plot of

¹Since Medwin and Daniel used an acoustic method to measure the bubble size distribution it may seem that the work described here is tautological. This is not the case. According to this model the relationship between the bubble size distribution and the sound spectrum produced depends on the dipole strength as a function of bubble size. It is our simple hypothesis regarding the dipole strength (or equivalently $\epsilon \times L$) which supplements the measurements and leads to the success of the model.

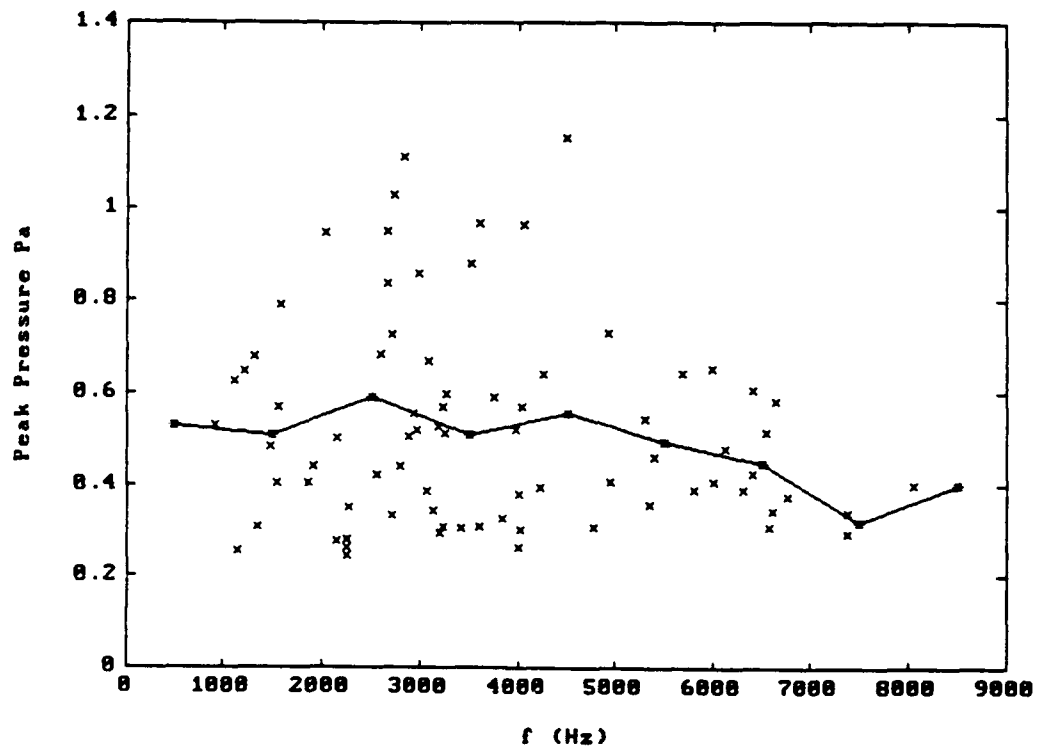


Figure 4.1 Peak pressures (x) (Pa) of the bubble oscillation pulses observed by Updegraff and Anderson (1991) as a function of the oscillation frequency. The * symbols joined by the solid line are the mean of the peak pressures in a frequency bandwidth 1 kHz wide centered at the symbol locations.

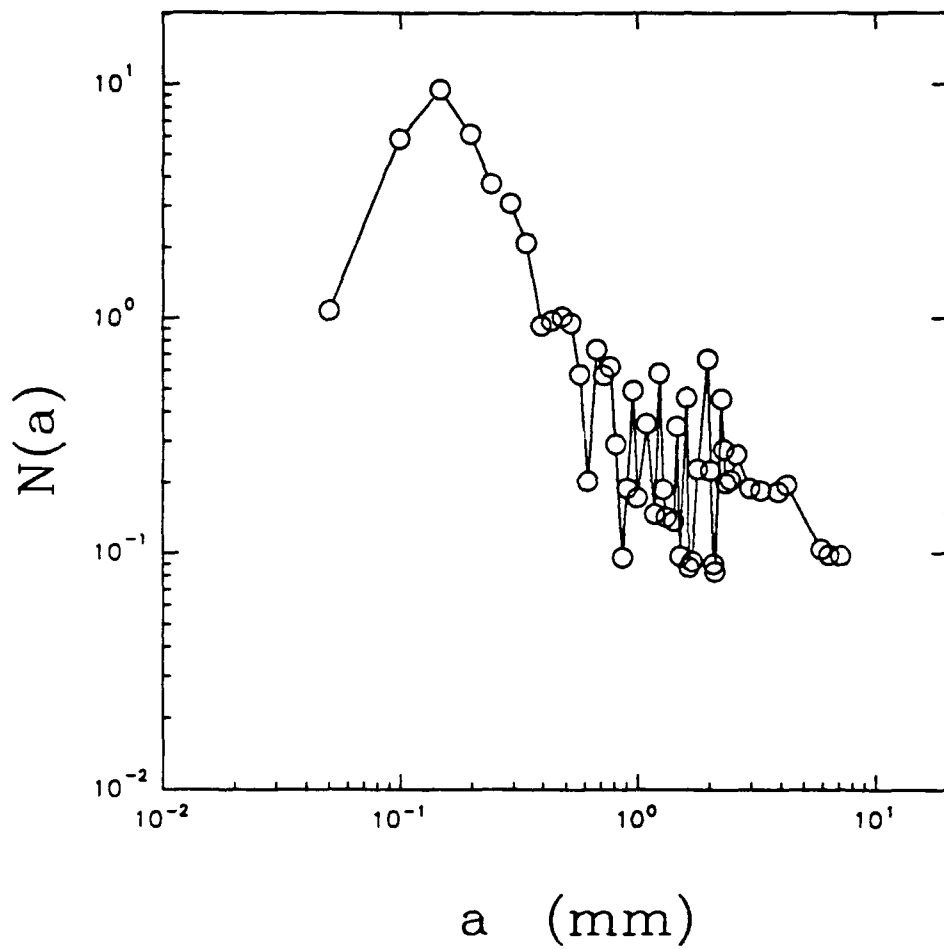


Figure 4.2 $N(a)$ the number of bubbles per wave in the radius interval from $(a_i + a_{i-1})/2$ to $(a_{i+1} + a_i)/2$ centered at a_i , (Medwin and Daniel, 1990).

their measured sound spectrum is shown in figure 4.3. The sound spectrum and bubble size data were obtained from two separate series of experiments. The sound spectrum was averaged over six breaking waves and the bubble size distribution data was measured from a series of ten breakers (Daniel, 1989). By using a simple dipole model of the sound generated by individual bubbles we will demonstrate that the measured sound spectrum may be simply related to the measured bubble-size distribution. It will also be shown that Medwin and Daniel's data and our model both support the hypothesis that low frequency sound may be generated under breaking waves without recourse to collective bubble cloud oscillations: observed single bubbles oscillating at their lowest mode may radiate sound at frequencies below 500 Hz.

4.2 Formulation

In figure 4.4 a sketch of the basic geometry and definitions of some of the parameters is shown. A bubble oscillating close to a free surface will radiate sound as a dipole. If $kL < 1$ and $ka \ll 1$, the pressure field produced by a single bubble radiating can be written as,

$$p(t-t_i) = \left[\frac{3\gamma P_0}{\rho} \right]^{1/2} \frac{\rho \epsilon d L}{R^2 c} e^{-\omega_b \delta(t-t_i)/2} \left[\sin(\omega_b(t-t_i)) - \frac{\cos(\omega_b(t-t_i))}{kR} \right] H(t-t_i) \quad 4.2$$

where k is the acoustic wavenumber, d is the receiver depth, R is the range from the receiver to the bubble, c is the speed of sound in water, L is twice the distance from the bubble center to the free surface, δ is the damping constant, t is the time at which the oscillations begin, ϵ is the amplitude of the bubble surface oscillations divided by the equilibrium bubble radius and $H(t)$ is the Heaviside unit step function (Morse and Ingaard, 1968, p. 312 and Clay and Medwin, 1977, p. 452). For bubbles from 50 μm to

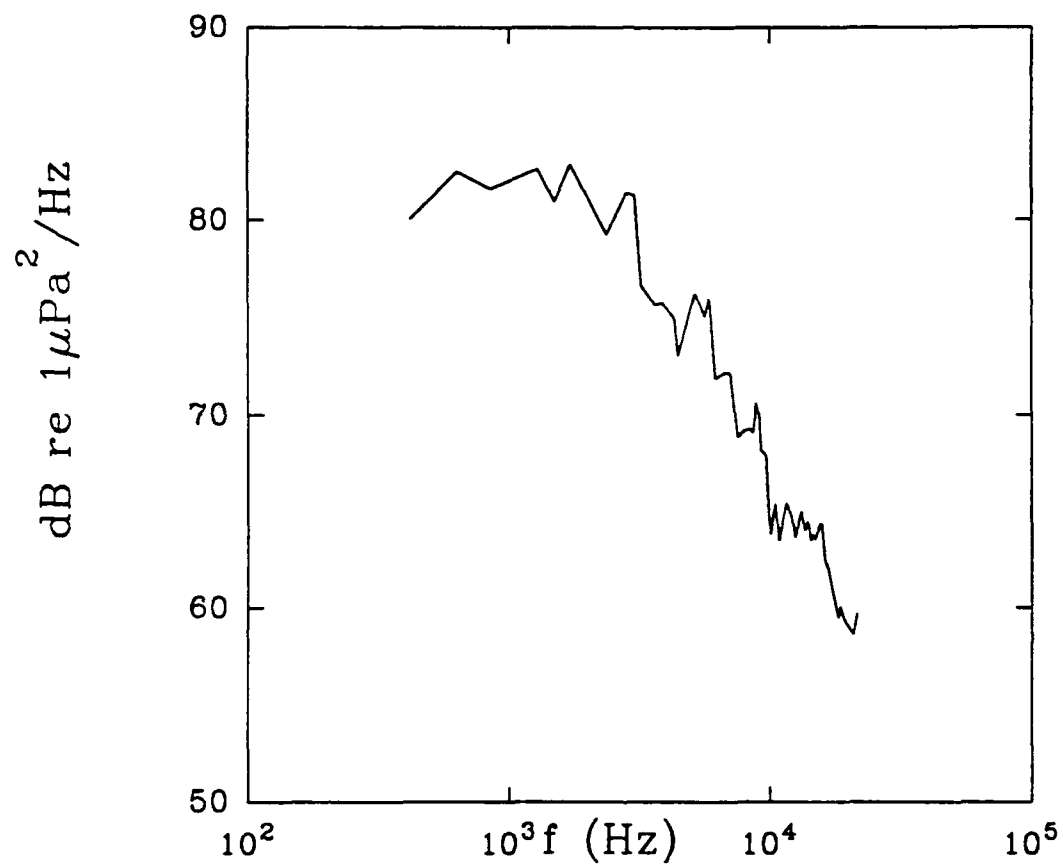


Figure 4.3 Measured sound power spectrum averaged over six gently spilling waves (Medwin and Daniel, 1990).

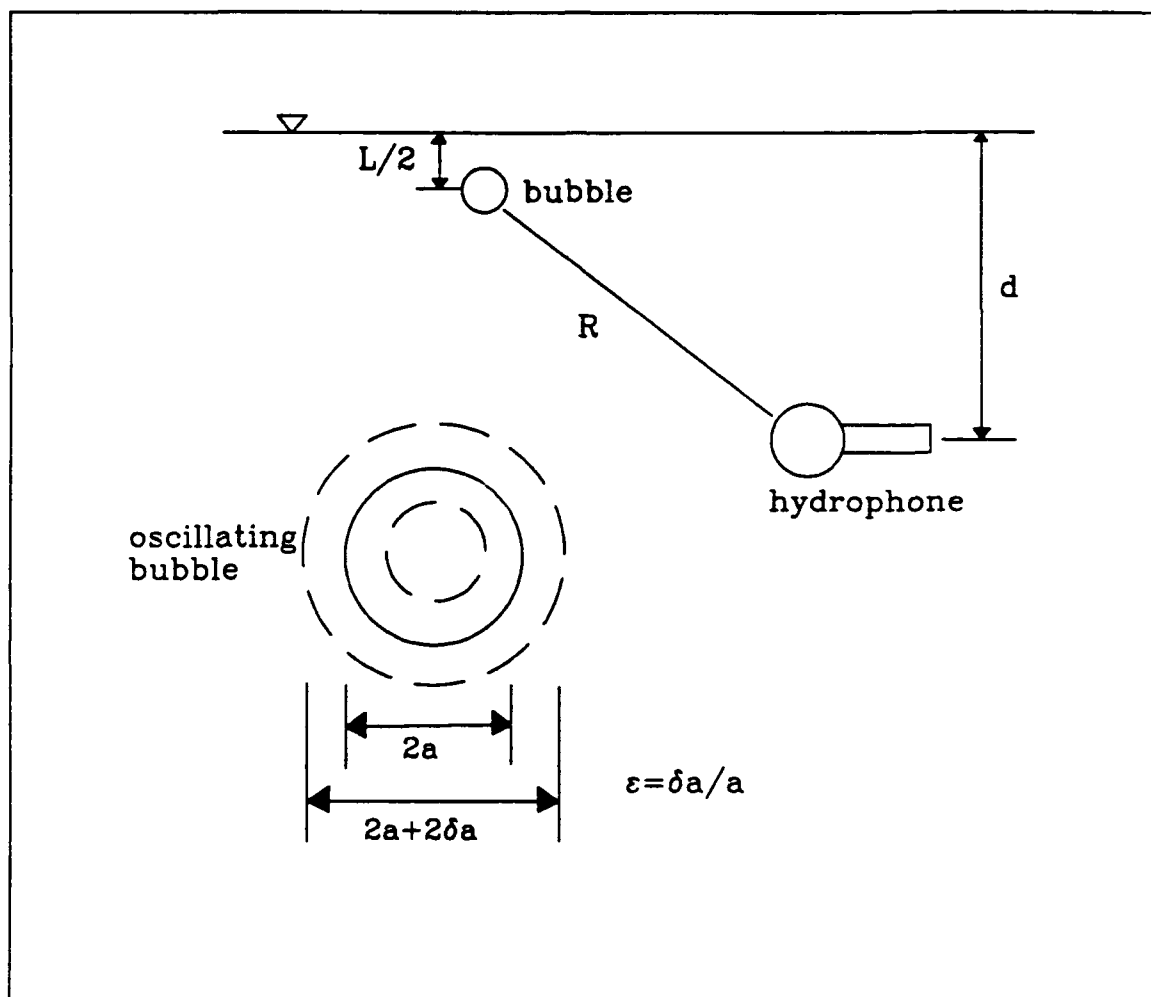


Figure 4.4 Sketch of the geometry of the problem and definitions of some of the parameters.

7 mm radius oscillating near a free surface it has been shown that radiation and viscous damping are negligible compared to thermal damping (Crowther, 1988 and Devin, 1959). Crowther (1988) has shown that Devin's (1959) equation (Devin's eq. 68) for the thermal damping constant could be approximated to within a few percent for frequencies below 60 kHz by,

$$\delta(f) = \frac{4.4 \times 10^{-4} f^{1/2}}{\left[1 + \frac{f}{2.5 \times 10^5}\right]} \quad 4.3$$

where f is the resonant bubble oscillation frequency in Hz^2 .

The power spectrum of an individual bubble pulse as given by eq. 4.2 is,

$$g(\omega:\omega_b) = \left[\frac{3\gamma P_o}{\rho}\right]^3 \left[\frac{\rho \epsilon d L}{R^2 c}\right]^2 \left[\frac{\omega_b^2 (\delta - 2kR)^2 + 4\omega^2}{(kR)^2 ((\delta\omega_b)^2 + 4(\omega_b - \omega)^2)((\delta\omega_b)^2 + 4(\omega_b + \omega)^2)}\right] \quad 4.4$$

Figure 4.5 shows a plot of eq. 4.4 and it is evident that the energy is concentrated in a very small band around ω_b .

The sound spectrum is modeled by reproducing the bubble size distribution of Medwin and Daniel's (1990) for a given number of bubbles, K . The total sound spectrum is the sum of the individual bubble pulse spectra calculated from eq. 4.4. The inputs to the model are,

- 1) K the total number of bubbles
- 2) Medwin and Daniel's bubble size distribution
- 3) ϵ , L , R_{\min} and R_{\max} .

In figure 4.2 is a plot of the measured bubble size distribution $N(a)$ (Medwin and Daniel, 1990). It is a set of discrete points N_i which specify the number of bubbles that

²In this and subsequent equations dependent on δ , SI units are applicable.

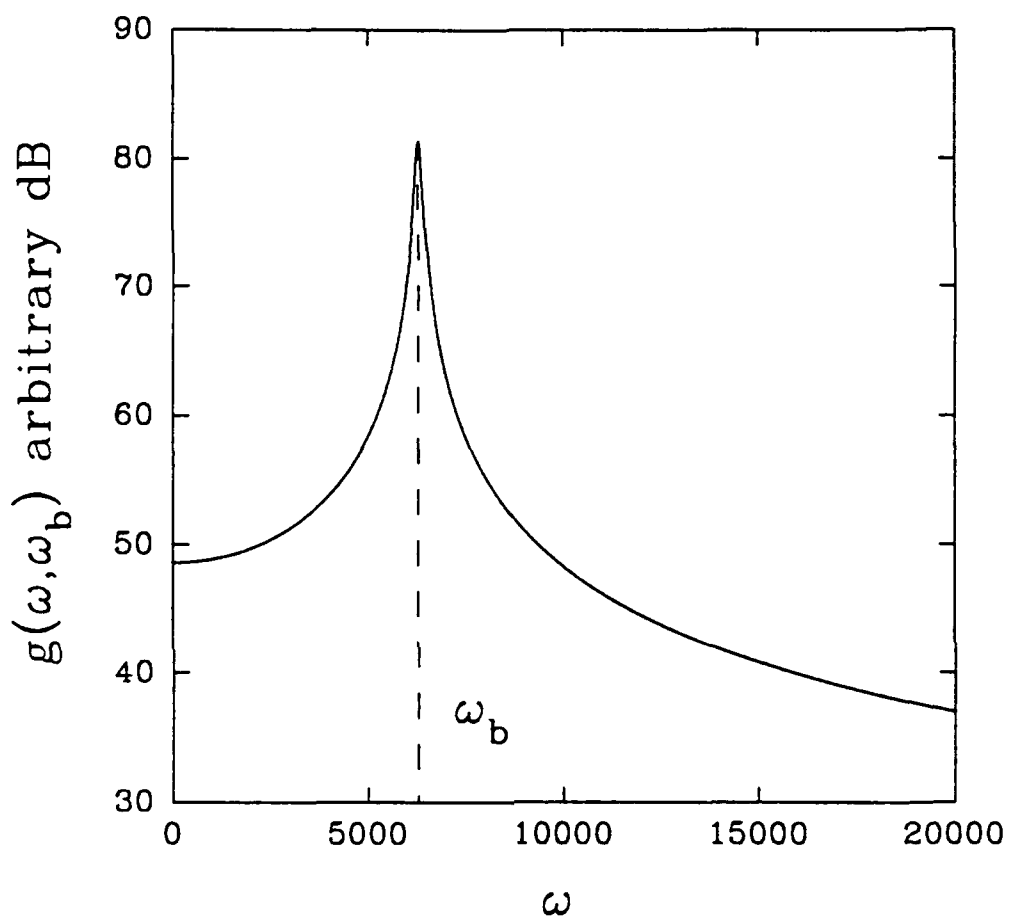


Figure 4.5 The power spectrum of an individual bubble pulse $g(\omega; \omega_b)$ as given by equation 4.4.

are created by one gently spilling wave in the radius interval from $(a_i + a_{i-1})/2$ to $(a_i + a_{i+1})/2$ centered at the radius a_i . The number of bubbles, n_i , in the radius interval centered at a_i is given by,

$$n_i = \frac{K}{\sum_{i=1}^m N_i} N_i \quad 4.5$$

The model randomly distributes the n_i bubbles across the radius interval centered at a_i . The range R was varied randomly between R_{\min} and R_{\max} and, ϵ and L where kept constant for a given run. The final sound power spectrum is given by,

$$G(\omega) = \sum_{i=1}^K g(\omega; \omega_i) \quad 4.6$$

where ω_i corresponds to a_i through eq. 4.1.

In order to check the results obtained by this method, (which we called the analytic spectrum model) a second Monte Carlo method was used. It simulates the sound pressure time series directly. It evaluates eq. 4.2 for each bubble formed and produces a time series from the sum of the individual bubble pulse time series. Inputs to the model are,

- 1) K the number of bubbles
- 2) Medwin and Daniel's bubble size distribution
- 3) R_{\min} , R_{\max} , ϵ_{\min} , ϵ_{\max} , L_{\min} , L_{\max} and t_{\max} .

The number of bubbles in each radius interval is calculated as outlined for the analytic spectrum model. The model starts each bubble pulse at a random time between $t = 0$ and $t = t_{\max}$. For each bubble, R , ϵ and L are varied randomly between the corresponding

minimum and maximum values. The sound pressure time series of the ensemble of oscillating bubbles is given by,

$$P(t) = \sum_{i=1}^K p_i(t-t_i) \quad 4.7$$

where $p(t-t_i)$ is given by eq. 4.2 . The sound spectrum is then calculated using standard signal processing techniques.

Spectra computed by the two methods are shown compared in figure 4.6. They are seen to produce very similar results when the mean values of ϵ and L in the Monte Carlo model are set equal to the constant values of ϵ and L used in the analytic spectrum model. This suggests that the sound spectrum is insensitive to the higher order statistical moments of the parameters.

Both models contain a certain amount of randomness. They both distribute the bubbles randomly across a given bubble radius interval, they both randomly vary the range between a minimum and maximum value and the second Monte Carlo method varies ϵ and L randomly between minimum and maximum values. In figure 4.7 we have plotted a mean spectrum averaged from ten spectra modeled with the analytic spectrum model and the 95% confidence limits. This figure indicates that the randomness of the model results in 3 to 4 dB of variation in the amplitude of the modeled spectrum. As a result we would not expect modeled spectra to match measured spectra closer than these limits.

4.3 Results

The goal of this study was to show that the bubble size distribution beneath a breaking wave could be used to calculate the sound pressure spectrum. The values

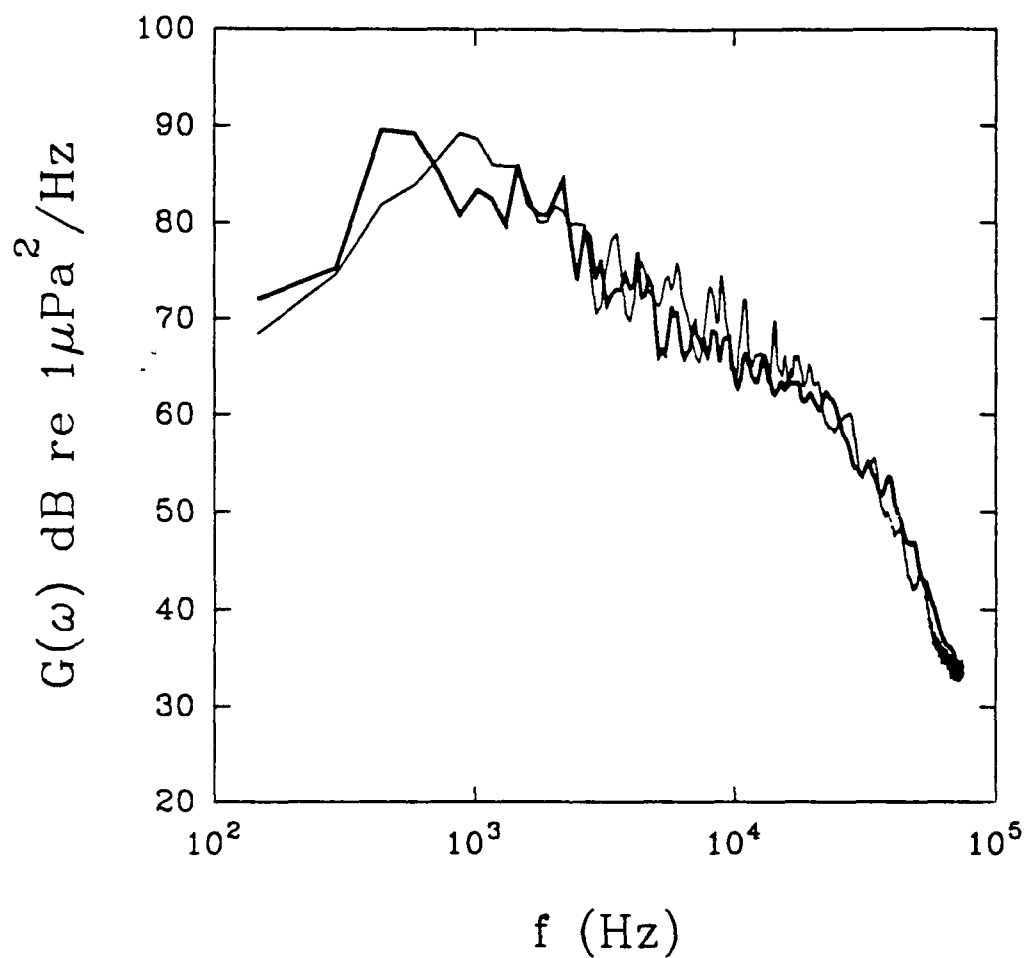


Figure 4.6 A comparison of the sound spectrum calculated using the analytic spectrum model, plotted with the bold line, and the Monte Carlo model, plotted with the thin line.

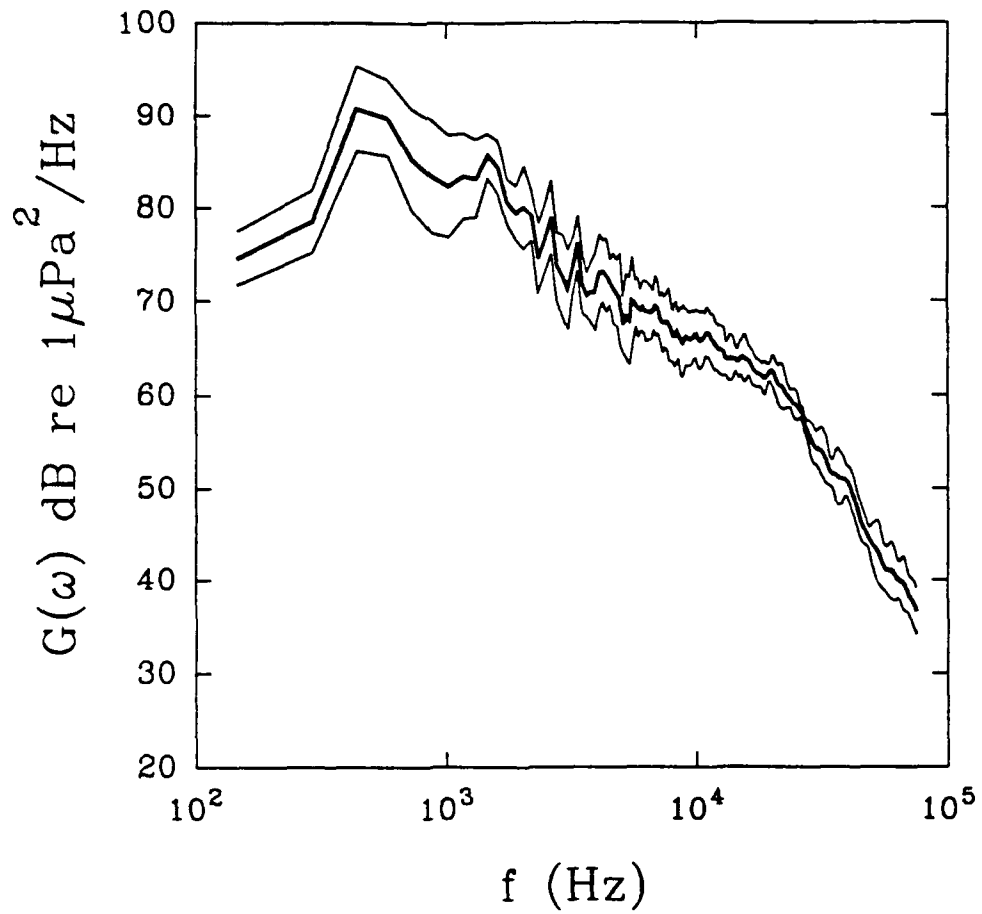


Figure 4.7 The bold line is the mean spectrum averaged from ten spectra generated by the analytic spectrum model. The upper and lower lines are the 95% confidence limits.

chosen for K , ϵ , L and R will obviously determine how well the sound spectrum is predicted. Medwin and Daniel (1990) observed approximately 50 bubbles per wave and their sound pressure spectrum (figure 4.3) was averaged over 6 waves therefore, $K = 300$, for all of the model runs. The depth of the hydrophone, d , in their experiments was 0.24 m. The range from the hydrophone to the bubbles was estimated from figures 12 and 13 of Daniel's thesis (Daniel 1989) which show the horizontal distribution of the bubbles in two breaking waves. These plots show that R varied from 0.24 m to approximately 0.5 m. Therefore we set $R_{\min} = 0.24$ m and $R_{\max} = 0.5$ m for the model runs.

The values for ϵ and L were more difficult to estimate. Medwin and Beaky (1989) estimated the value ϵ of for a single bubble and found $\epsilon = 0.014$ for $a = 0.3$ mm. We assume that the value for L is of the order of the wave amplitude. This follows from the conjecture that in these gently spilling waves the bubbles are entrained at the toe of the spilling region as shown in figure 4.8. Medwin and Daniel (1990) do not provide any wave height data, but Daniel (1989) states in his thesis that the maximum wave amplitude was 0.03 m. Therefore we assume that $L = O(10^{-2} \text{ m})$ for the model runs.

In figure 4.9 the sound spectra produced by the Monte Carlo model with $\epsilon = 0.005$ -0.025 and $L = 0.01$ -0.03 m and Medwin and Daniel's spectrum are plotted. The modeled spectrum matches the amplitude and slope of the measured spectrum closely when ϵ and L are set to these physically realistic values. The bars indicate the 95% confidence limits of the modeled spectrum.

Results from the analytic spectrum model with $\epsilon = 0.015$ and $L = 0.02$ m are shown in figure 4.10, compared to Medwin and Daniel's (1990) spectrum. The amplitude and slope of the modeled spectrum agree well with the observed data when ϵ and L are set equal to these values. The bars again indicate the 95% confidence limits of the modeled spectrum. These values of ϵ and L would give a maximum farfield dipole pressure 1 m on axis of 1.7 Pa.

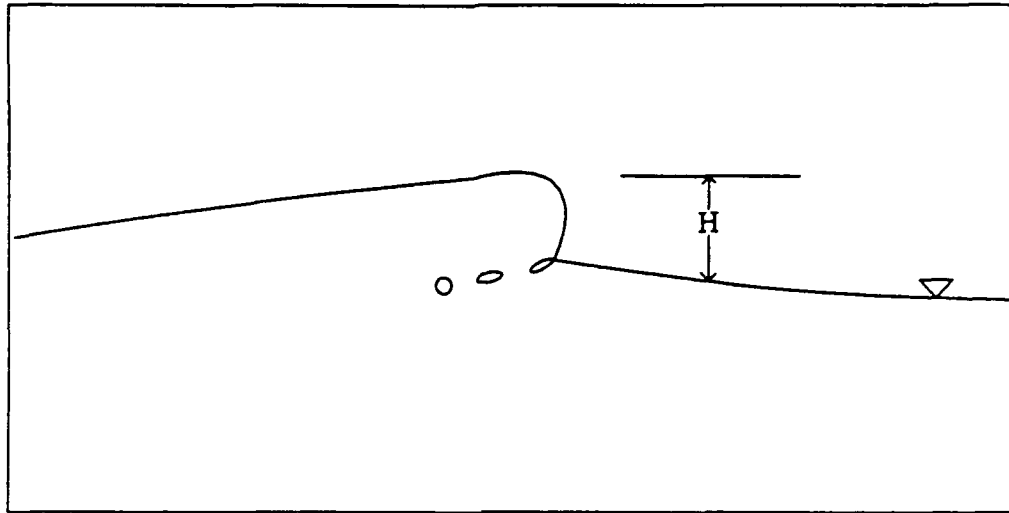


Figure 4.8 Sketch of the formation of bubbles at the toe of the spilling region in a gently spilling wave.

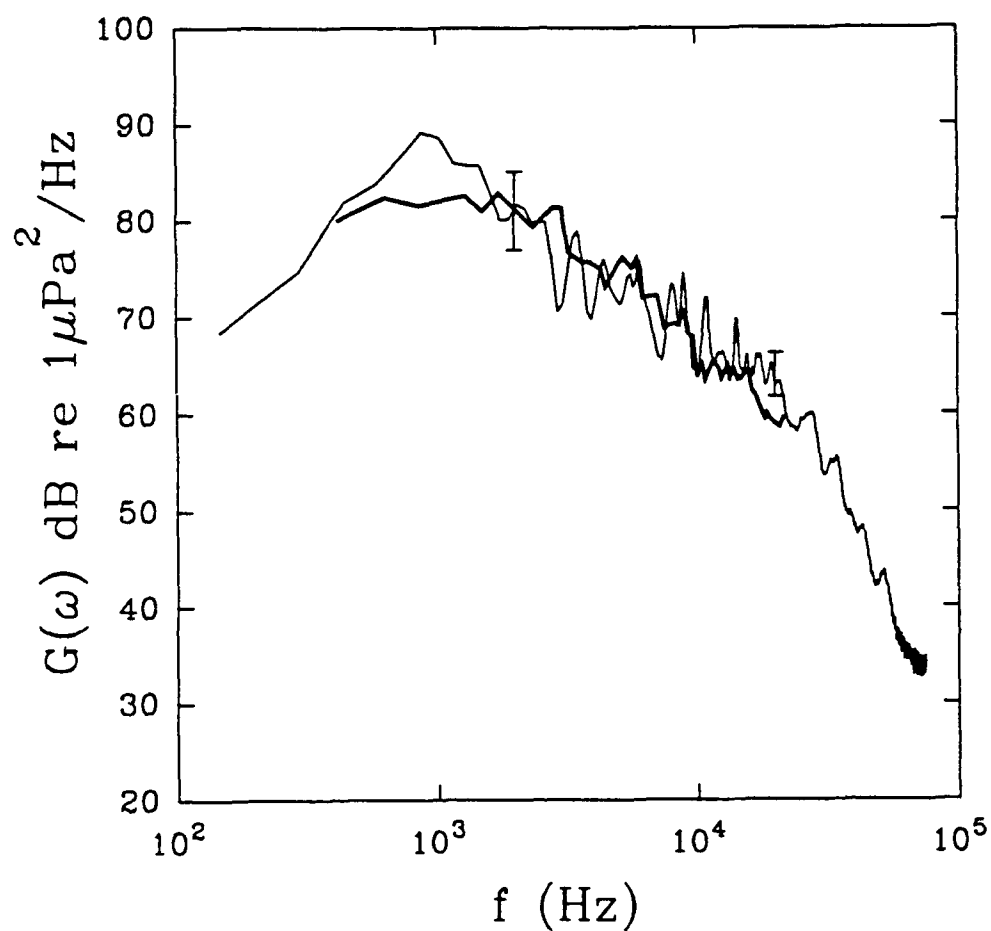


Figure 4.9 Comparison of a sound spectrum from the Monte Carlo model with $\epsilon = 0.005\text{-}0.025$ and $L = 0.01\text{-}0.03$ m and the measured sound spectrum of Medwin and Daniel (1990), plotted with a bold line. The bars indicate the 95% confidence limits of the modeled spectrum.

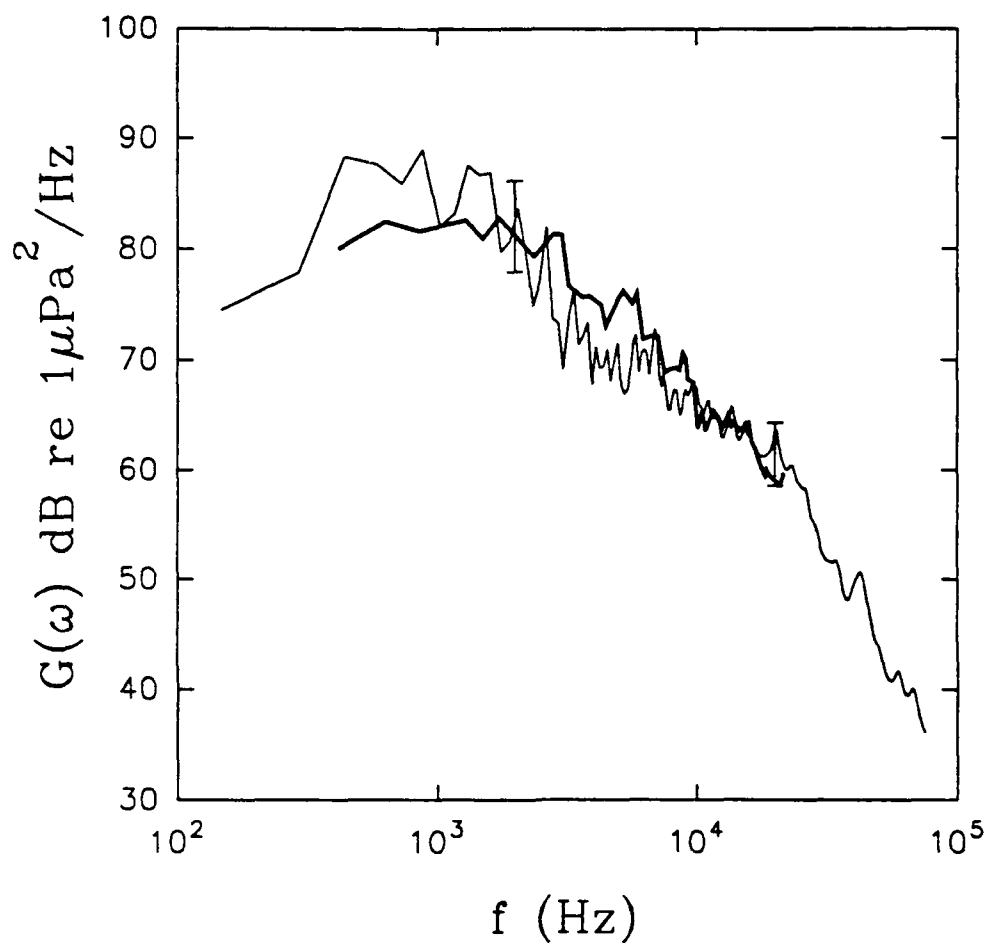


Figure 4.10 Comparison of a sound spectrum from the analytic spectrum model with $\epsilon = 0.015$ and $L = 0.02$ m and the measured sound spectrum of Medwin and Daniel (1990), plotted with a bold line. The bars indicate the 95% confidence limits of the modeled spectrum.

4.4 Discussion

We have shown that a simple model of the sound produced by a single oscillating bubble can be used to obtain the sound spectrum from the bubble size distribution under breaking waves. If the range, R , from the receiver to the breaker is known then the model has only 2 unknown parameters ϵ and L . Our results indicate that the product ϵL is not a function of the bubble radius, a , but is effectively constant across the sound spectrum. This is supported by Updegraff's measurements which showed that the peak oscillation pressures were not a function of frequency (Updegraff, 1989).

It is possible that ϵ and L are functions of the wave geometry or the energy dissipation. For waves of moderate slope Loewen and Melville (1991) found that the acoustic energy radiated by a breaking wave was approximately proportional to the energy dissipated and the wave slope. Longer or steeper waves might be expected to entrain bubbles to larger depths increasing the dipole moment L . Under larger breaking waves L may increase because extremely large pockets of air are injected to greater depths initially, and when they break up to form smaller bubbles the dipole moment arm is of the order of the depth to which the pocket of air was initially injected. It could be the depth to which the large pockets of air are injected which scales with the wave parameters. It may also be that larger waves produce more sound simply because more air is entrained and hence more bubbles are formed.

The largest bubble that Medwin and Daniel (1990) observed had a radius of 7.4 mm which corresponds to a resonant frequency of 440 Hz. We expect that bubbles considerably larger than this will be present under waves larger than the 1.4 Hz and 0.03m amplitude waves generated by Medwin and Daniel (1990). Therefore it should be possible for these larger bubbles to radiate sound at frequencies as low as several hundred Hz.

We believe that these results clearly demonstrate that bubble population data can be used to accurately and simply model the shape and the amplitude of the sound spectrum produced by a breaking wave. The more practical application would be to solve the inverse problem. That is, to calculate the bubble size distribution from the sound spectrum. If ϵ and L , or at least the product ϵL , is a constant as assumed in our model, then the problem is easily inverted.

If we assume that the energy in the sound spectrum at a given radian frequency ω_b is due only to bubbles corresponding to a radius, a , calculated from eq. 4.1, the problem becomes even simpler. We are assuming that the spectrum of a single bubble pulse is a delta function which is a reasonable approximation, (see figure 4.5). The mean square signal level for an individual bubble sound pulse is found by integrating eq. 4.2 in time to give,

$$\overline{p^2}(\omega_b) = \left[\frac{3\gamma P_o}{\rho} \right]^3 \left[\frac{\rho \epsilon d L}{R^2 c} \right]^2$$

$$\left[\left(\frac{2}{\delta \omega_b (\delta^2 + 4)} \right) + \left(\frac{\delta^2 + 2}{(kR)^2 (\delta \omega_b (\delta^2 + 4))} \right) - \left(\frac{2}{kR \omega_b (\delta^2 + 4)} \right) \right] \quad 4.8$$

where $\overline{p^2}(\omega_b)$ is the mean square signal level of a bubble resonating at radian frequency ω_b . The mean square value of the signal within the frequency range $\omega_b - \Delta\omega$ and $\omega_b + \Delta\omega$ is given by ,

$$\varphi^2(\omega_b; \Delta\omega) = \int_{\omega - \frac{\Delta\omega}{2}}^{\omega + \frac{\Delta\omega}{2}} P(\omega) d\omega \quad 4.9$$

(Bendat and Piersol, 1986). For the inverse problem the input is the sound spectrum $P(\omega)$ which has a resolution of $\Delta\omega$. The number of bubbles in each frequency bin from $\omega_b - \Delta\omega/2$ to $\omega_b + \Delta\omega/2$ is then given by,

$$n_i = \frac{\phi^2(\omega_b; \omega_b)}{p^2(\omega_b)} \quad 4.10$$

if we assume the range R is the same for bubbles of a given radius. The complete bubble size distribution can be calculated by evaluating eq. 4.10 in each frequency bin across the entire sound spectrum.

Chapter 5: Summary and Conclusions

This thesis has reported on laboratory measurements of the acoustic radiation and microwave backscatter from breaking waves and a model of the sound generated by breaking waves. The primary motivation of the research was to determine whether measurements of the sound generated by breaking waves could be used to quantitatively study the dynamics of the breaking process. Correlations of the averaged acoustic and microwave measurements with the dynamics of breaking waves were determined and detailed measurements of the sound radiated by two- and three-dimensional breaking waves were reported. Comparisons were made between the sound generated by two and three-dimensional breaking waves and the mechanisms responsible for the generation of low frequency sound beneath breaking waves were studied. It was discovered that a close link exists between the dynamics of breaking and the process of air entrainment and the generation of sound. A model of the sound generated by breaking waves was developed which uses the bubble size distribution to predict the sound spectrum.

From laboratory measurements of the microwave backscatter and acoustic radiation from two-dimensional breaking waves (described in chapter 2) the major findings were that: 1) the mean square acoustic pressure and backscattered microwave power correlate with the wave slope and dissipation for waves of moderate slope, 2) the backscattered microwave power and mean square acoustic pressure correlate strongly with each other, 3) the amount of acoustic energy radiated by an individual breaking event scaled with the amount of mechanical energy dissipated by breaking, and 4) when the mean square acoustic pressure and the backscattered microwave power were scaled with the wave packet center component wavelength or phase speed, the data from the three packets collapsed onto single curves.

The fact that the mean square acoustic pressure and the backscattered microwave power correlate with the wave slope and fractional dissipation is significant because it implies that it may be possible to use acoustic or microwave measurements in the field to remotely study the processes associated with wave breaking, including gas transfer, momentum transfer and energy dissipation at the air-sea interface. The observation that the mean square acoustic pressure and the backscattered microwave power correlate strongly with each other suggests that, because the microwave backscatter is dependent on the geometry of the prebreaking wave, the sound radiated by breaking must also be dependent on the prebreaking wave geometry. The fact that the amount of acoustic energy radiated by an individual breaking event scaled with the amount of mechanical wave energy indicates that it may be possible to use measurements of the sound radiated by breaking waves at sea to quantify dissipation in the field. The correlations of the mean square acoustic pressure and the backscattered microwave power with the wave slope and dissipation collapsed onto single curves when the data was scaled with the appropriate wave packet parameter. This implies that the correlations obtained may be extended to waves of larger scale.

In the combined microwave and acoustic experiments the hydrophone was located several meters downstream of the breaking location and therefore the acoustic signals at frequencies below the cut-off frequency at 2200 Hz were severely attenuated. As a result, the observed correlations with the mean square acoustic pressure are only relevant to sound generated by breaking waves at frequencies > 2200 Hz.

In order to extend these results and to study the sound generated by breaking waves at lower frequencies another series of experiments was conducted in the larger wave channel (0.76 m wide by 0.60 m deep) at MIT. The sound was measured from breaking waves generated using three wave packets with center component wavelengths of 1.60 m, 1.93 m and 2.36 m. Efforts were made to ensure that low frequency sound generated by breaking could be detected if it existed. The hydrophones were placed

directly underneath the breaking events to avoid cutting off the low frequencies and the wavemaker hydraulic system was shut off prior to sampling the acoustic signals to eliminate the low frequency noise produced by the hydraulic pump. These steps produced an acceptable signal to noise ratio at lower frequencies and the sound was sampled in the frequency band from 20 Hz to 10 kHz.

A significant result from these experiments was that sound at frequencies as low as 20 Hz was observed. The spectral levels at frequencies < 1 kHz increased consistently as the slope of the wave packets was increased and the mean square acoustic pressure in the frequency band from 0 Hz to 1000 Hz was found to correlate strongly with the wave slope and dissipation. It was noted that the spectral levels at low frequency did not increase until the slope was increased to a large enough value that the waves began to plunge. The transition from spilling to plunging occurs very quickly as the slope is increased from the incipient breaking value and as a result the majority of the events were plunging events. The spilling events that were observed did not generate any significant sound energy at frequencies < 1 kHz. If this distinction is shown to be true in the field then it may be possible to use acoustic measurements to differentiate between spilling and plunging breakers in the field.

Another major finding was that a characteristic low frequency signal occurred immediately following the impact of the plunging wave crest onto the free surface. The frequency of this signal decreased as the slope and fractional dissipation increased. The frequency was strongly correlated with both the wave slope and the fractional dissipation. An underwater video revealed that as the wave crests plunged over and impacted the free surface along the forward face of the wave a perfectly smooth-walled cylinder of air was forced down into the water column. It was proposed that the characteristic low frequency signals were due to the pulsations of the smooth-walled cylinders of air.

An expression for the pulsation frequency of an infinitely long circular cylinder located near a pressure release surface was derived. The cylinder was modeled as a

linear oscillator and the resonant pulsation frequency was calculated by deriving expressions for the stiffness and mass of the system. The theoretical expression predicted that the pulsation frequency was inversely proportional to the radius of the cylinder and that the pulsation frequency increased as the cylinder moved closer to the free surface. However, when the expression was evaluated using the observed cylinder sizes the resulting pulsation frequencies were approximately 50% lower than the observed values. When the mass term was corrected so that the mass of the system was equal to only the mass of the thin layer of fluid separating the cylinder from the atmosphere the equation predicted pulsation frequencies which matched closely with the observed values.

It was found that the volume of air in the cylinders was correlated with the fractional dissipation. This observation is consistent with the results of Lamarre and Melville (1991) who also found that the volume of air entrained by breaking correlated with the energy dissipated and that up to 50% of the energy dissipated by breaking was expended entraining air against the buoyancy force. Their results were for three breaking events and therefore the correlation observed for nineteen breaking events in the experiments presented here strengthens their conclusion considerably. The volume of air was also found to be well correlated with the mean square acoustic pressure in the frequency band from 0 Hz to 1000 Hz. The correlation of the volume of air with the mean square acoustic pressure in the low frequency band shows that the process of air entrainment is closely linked to the generation of sound. The correlations of; 1) the volume of air to the fractional dissipation, and 2) the fractional dissipation to the mean square acoustic pressure in the low frequency band, establish that the process of air entrainment and the generation of sound are directly related to the dynamics of breaking.

To determine whether three-dimensional effects were important and to measure the sound generated by breaking waves of considerably larger scales, a series of experiments were conducted in the large multi-paddle wave basin (45.7m long by 30.5 m wide and 5.8 m deep) at the Offshore Technology Research Center (OTRC) at Texas

A&M University. Three-dimensional breaking waves were generated and the sound produced by breaking was measured in the frequency range from 10 Hz to 20 kHz. Breaking events were generated using one wave packet with a center frequency of 0.5 Hz and center component wavelength of 6.3 m. It was not possible to measure the fractional dissipation for the three-dimensional breaking events and therefore the gain of the signal sent to the wave paddles which is proportional to the wave amplitude was used to characterize the events. Comparisons with results from the two-dimensional experiments were still possible because the slope parameter S , used to characterize the two-dimensional breaking waves, is also proportional to the wave amplitude.

Two important results were that sound spectra showed significant increases in level across the entire bandwidth from 10 Hz to 20 kHz and the spectra sloped at -5 to -6 dB per octave at frequencies > 1 kHz. The observed -5 to -6 dB spectral slope of the sound measured beneath very energetic, large scale, plunging three-dimensional breaking waves supports the conclusion that the observed dependence of ambient sound levels in the field for frequencies > 1 kHz at high windspeeds (which corresponds to larger more violent breaking events) is due to the sound generated by breaking waves. It has been demonstrated previously that the dependence of ambient sound levels for frequencies > 1 kHz at very low windspeeds, corresponding to small gently spilling waves, is due to the sound generated by breaking waves (Medwin and Beaky, 1989 and Updegraff and Anderson, 1991). However, this is direct evidence that the -5 dB per octave spectral slope is consistent with the high frequency sound generated by large scale, plunging breaking waves. The implication is that the same mechanism, the oscillation of individual air bubbles at their linear resonant frequencies, is responsible for the observed spectral shape of the sound generated by both small and large scale breaking waves. If this is true, then a model of the sound generated by breaking waves based on the sound radiated by a single bubble oscillating at its linear resonant frequency may be used to estimate the high frequency sound generated by breaking waves of all scales.

In chapter 4 a model of the sound produced by breaking waves which uses the sound radiated by a single bubble oscillating at its linear resonant frequency, and the bubble size distribution to estimate the sound spectrum was presented. The data of Medwin and Daniel (1990) was used to evaluate the performance of the model. The model generates a damped sinusoidal pulse for every bubble formed, as calculated from the bubble size distribution. If the range to the receiver is known then the only unknown parameters are ϵ , the initial fractional amplitude of the bubble oscillation and L , the dipole moment arm or twice the depth of the bubble below the free surface. It was found that if the product $\epsilon \times L$ is independent of the bubble radius the model reproduces the shape and magnitude of the observed sound spectrum accurately. The success of the model implies that it may be possible to calculate the bubble size distribution from the sound spectrum. The model was validated using data from experiments conducted by Medwin and Daniel (1990) where the breaking events were small scale gently spilling waves. In addition, the observed sound spectra from the experiments at OTRC imply that a similar model may also be used to estimate the higher frequency sound radiated by much larger scale breaking events.

The mean square acoustic pressure in the frequency bands from 0 Hz to 150 Hz and from 1 kHz to 20 kHz were correlated with the wave amplitude in the three-dimensional breaking experiments. The observed correlations are very similar to the correlations of the mean square acoustic pressure in the frequency bands from 0 Hz to 1000 Hz and from 1 kHz to 10 kHz for the two-dimensional breaking events. The close agreement between the two and three-dimensional measurements demonstrates that averaged measures of the sound radiated by breaking are quite robust. That is, measurements of the mean square acoustic pressure generated by two-dimensional breakers in smaller wave channels are representative of observations of the sound generated by three-dimensional breaking waves in larger scale wave basins.

In the three-dimensional experiments underwater video recordings showed that no smooth-walled cylinders of air were present and that the entrained bubble clouds were comprised of relatively small air bubbles right from the start of breaking. As a result, no characteristic low frequency signals similar to those observed in the two-dimensional experiments were detected. Low frequency sound was observed but it occurred approximately 0.7 s after the initial impact of the plunging wave crest. In the two-dimensional experiments the smooth-walled cylinder of air radiated low frequency sound from the moment the crest impacted the free surface until the time the cylinder broke up into a cloud comprised of smaller air bubbles. At this time a lower frequency signal began and the frequency of this signal increased slowly with time. The origin of this lower frequency signal in the two-dimensional experiments and the origin of the observed low frequency sound in the three-dimensional experiments was investigated.

It was postulated that in both cases these low frequency signals were due to the collective oscillations of the bubble clouds. To test this hypothesis the resonant frequencies of a two-dimensional bubble cloud immersed in an infinite fluid were calculated and compared to the spectral peaks observed in the data. In the case of the two-dimensional breaking waves the observed spectral peaks matched the resonant frequency of the second mode consistently. The spectral peaks in the data from the three-dimensional breaking waves matched the predicted resonant frequencies of the first or second mode. This result supports the conjecture that the observed frequencies were due to the collective oscillations of bubble clouds. Additional analysis was carried out in an attempt to confirm this hypothesis.

In the two-dimensional experiments it was observed that the characteristic low frequency signal associated with the oscillating cylinder of pure air occurred immediately following the impact of the plunging wave crest and continued for approximately 0.25 s. Following this, at a time corresponding to the cylinder of air breaking up into a cloud of smaller bubbles, the frequency of the signal would decrease abruptly by approximately

35% and then as time progressed the frequency would slowly increase. A simple analysis was carried out in which it was shown that, if the volume of air is conserved and the ratio of the cloud radius a_0 to its depth below the free surface L remains constant when a cylinder of pure air breaks up to form a bubble cloud, the resonant frequency of the resulting bubble cloud would be approximately 16% lower than the resonant frequency of the cylinder of pure air. The factor of two difference between the predicted decrease and the observations may be due to the fact that the ratio a_0/L does not remain constant or to the fact that the stiffness and mass of the bubble cloud are not predicted accurately by the equations for a cylinder of pure air. It is believed that the observed low frequency signals generated by the two-dimensional breaking waves can be explained as follows. Immediately following the impact of the plunging wave crest a low frequency signal is observed which lasts approximately 0.25 s and remains at a constant frequency. This signal is believed to be due to the pulsating smooth-walled cylinder and its resonant frequency can be estimated by assuming the mass of the system is equal to the mass of the thin layer of fluid separating the cylinder from the atmosphere. At the time when the cylinder breaks up to form a cloud of smaller bubbles the frequency of the signal decreases by approximately 35%. This decrease in frequency is consistent with the predicted decrease in frequency which would occur when a cylinder of pure air breaks up to form a bubble cloud. The frequency of the observed signals agree closely with the predicted resonant frequencies of a two-dimensional cylindrical bubble cloud. As time progresses, the frequency of the signal increases slowly and this trend is also seen in the predicted resonant frequencies. The frequency increases with time because as the bubble cloud degases the sound speed inside the cloud increases and hence the resonant frequency increases.

The sequence of events for the three-dimensional breaking waves is less well understood. Some low frequency sound is generated almost immediately following the impact of the plunging crest but the largest amplitude spectral peaks occurred

approximately 0.7 s after the initial impact. The underwater videos showed that the occurrence of the largest amplitude spectral peaks coincides approximately with the time when the forward motion and rotation of the three-dimensional bubble cloud has stopped. In the case of the three-dimensional breaking events the crest does not impact the free surface simultaneously across its width. Therefore the bubble cloud is formed first near the center of the wave and then grows in width as the crest continues to plunge down onto the free surface. During this time the bubble cloud is being carried downstream rapidly by the wave and it is also rotating because of the overturning motion of the wave. Then, as the cloud increases in size, the drag force increases, the rotation slows and the cloud's horizontal velocity decreases. At this time there is very little active breaking occurring at the surface and the largest amplitude low frequency sound is radiated.

The evidence presented in this thesis which supports the hypothesis that the low frequency sound observed beneath both the two and three-dimensional breaking waves is due to the collective oscillations of bubble clouds is:

- 1) the fact that the observed spectral peaks in the data match closely with estimates of the resonant frequencies of a two-dimensional cylindrical bubble cloud,
- 2) the fact that the entire evolution of the low frequency signals beneath the two-dimensional breakers can be explained by the theories of the pulsating cylinder of air and of the collective oscillations of a cylindrical bubble cloud,
- 3) the fact that the decrease in frequency observed when the cylinder of pure air breaks up to form a cloud of smaller bubbles can be estimated,
- 4) the observation that the time at which the largest low frequency spectral peaks occur beneath the three-dimensional breakers surface agitation and spray impact are minimal and therefore the observed signals are not originating at the free surface.

In chapter 3 it was found that predictions of the resonant frequencies of the three-dimensional bubble clouds from equations based on the assumption that: 1) the bubble cloud was an infinitely long circular cylinder with a radius equal to the observed value, or 2) the bubble cloud was a spherical cloud with a volume equal to the observed volume; were approximately equal. If the resonant frequency of bubble clouds is really this insensitive to the shape of cloud this could have important implications. For example, if the low frequency sound radiated by a breaking wave at sea is measured and if it is assumed that the observed frequency corresponds to the lowest mode of oscillation and that the void fraction of the cloud is known within a reasonable range of values, then the volume of the cloud can be estimated. Typical void fraction values for the bubble clouds observed in the laboratory at the times when the clouds were radiating low frequency sound were $0.15 < \alpha < 0.25$. Then, because the resonant frequency of a spherical bubble cloud is proportional to $(\alpha)^{-1/2}$ the radius, r_0 , of the spherical bubble cloud of equal volume can be estimated to within approximately 30%. It has not been shown that the resonant frequencies of the higher modes are as insensitive as the lowest mode to the shape of the cloud however, if this were shown to be true then it may be possible to determine both the bubble cloud volume and the void fraction by measuring the low frequency sound radiated by breaking. If two low frequencies are measured corresponding to the first and second modes then, because there are only two unknowns r_0 and α , the volume of the cloud and the void fraction can be estimated. Further study of this issue is certainly warranted because if estimates of the total volume of entrained air were possible in the field this could lead to more accurate estimates of the contribution of breaking waves to the transfer of gas across the air-sea interface.

Another issue which warrants further study is the possibility that low frequency sound may be useful for differentiating between spilling and plunging breaking waves. It may be that the distinction is only observed beneath two-dimensional breaking waves

because of the presence of the oscillating cylinder in the case of plunging events and its absence in the case of spilling events. In the three-dimensional experiments, all of the breaking events were plunging events and therefore it was not possible to verify whether significantly less low frequency sound was radiated by spilling events as compared to plunging events.

The most obvious extension of the research reported here would be to conduct experiments at sea to determine whether significant low frequency sound can be detected consistently beneath breaking waves. If simultaneous void fraction measurements and video recordings were made in addition to the sound measurements then the hypothesis that the cloud volume and void fraction can be estimated from sound measurements alone could also be evaluated. However, it may be that this hypothesis could be verified more easily by conducting more laboratory experiments in large multi-paddle wave basins similar to the one at OTRC.

References

- Alpers, W., Ross, D.B. and Rufenach, C.L., 1981, "On the detectability of ocean surface wave by real and synthetic aperture radar", J. Geophys. Res., 86(C7), 6481-6498.
- Banner, M. L. and Fooks, E. H., 1985 "On the microwave reflectivity of small-scale breaking water waves", Proc. R. Soc. London, Ser. A, 399, 93-109.
- Banner, M.L. and Cato, D.H., 1988, "Physical mechanisms of noise generation by breaking waves - laboratory study", Proc. NATO Adv. Workshop on Sea Surface Sound - Natural Mechanisms of Surface Generated Noise in the Ocean, Lerici, Italy, Kluwer Academic, 429-436.
- Batchelor, G.K., 1967, An Introduction to Fluid Mechanics, Cambridge University Press.
- Bendat, J.S. and Piersol, A.G., 1986, Random Data. Analysis and Measurement Procedures, Second Edition, Wiley-Interscience, New York.
- Beyer, W.H. ed., 1987, CRC Standard Mathematical Tables, CRC Press, Boca Raton, Fl.
- Brekhovskikh, L. and Lysanov, Yu., 1982, Fundamentals of Ocean Acoustics, Springer-Verlag, New York.
- Carey, W.M., Fitzgerald, J.W. and Browning, D.G., 1990, "Low Frequency Noise from Breaking Waves", Natural Physical Sources of Underwater Sound, ed. B.R. Kerman, in press.
- Carey, W.M. and Browning, D., 1988, "Low frequency ocean ambient noise: measurements and theory", Proc. NATO Adv. Workshop on Sea Surface Sound - Natural Mechanisms of Surface Generated Noise in the Ocean ed. B.R. Kerman, Lerici, Italy, Kluwer Academic, 361-376.
- Cato, D.H., 1976, "Ambient sea noise in waters near Australia" J. Acoust. Soc. Am., 60, 320-328.
- Chan, E.S. and Melville, W.K., 1988, "Deep-water plunging wave pressures on a vertical plane wall", Proc. R. Soc. Lond., A417, 95-131.
- Clay, C.S. and Medwin, H., 1977, Acoustical Oceanography, Wiley, New York.
- Crighton, D.G. and Ffowcs Williams, J.E., 1969, "Sound generation by turbulent two-phase flow", J. Fluid Mech., 36, 588-603.
- Crouch, W.W. and Burt, P.J., 1972, "The logarithmic dependence of surface-generated ambient sea-noise spectrum level on wind speed", J. Acoust. Soc. Am., 51, 1066-1072.
- Crowther, P.A., 1988, "Bubble noise creation mechanisms", Proc. NATO Adv. Workshop on Sea Surface Sound - Natural Mechanisms of Surface Generated Noise in the Ocean, Lerici, Italy, Kluwer Academic, 131-150.

- Crowther, P.A., 1989, "Some statistics of sea noise", J. Acoust. Soc. Am., supplement 1, Vol. 85, 117th meeting of ASA, Syracuse N.Y. (abstract).
- Crowther, P.A., 1980, "Acoustical scattering from near-surface bubble layers", Cavitation and inhomogeneities in underwater acoustics, ed. W. Lauterborn, Springer-Verlag, 194-294.
- Daniel, A.C. Jr., 1989, "Bubble Production by Breaking Waves", M.Sc. Thesis, Naval Postgraduate School, Monterey, Ca.
- Devin, C., 1959, "Survey of Thermal, Radiation, and Viscous Damping of Pulsating Air Bubbles in Water", J. Acoust. Soc. Am., 31, 1654-1667.
- Donelan, M., Longuet-Higgins, M.S. and Turner, J.S., 1972, "Periodicity in Whitecaps", Nature, 239, 449-451.
- Dowling, A.P. and Ffowcs Williams, J.E., 1983, Sound and Sources of Sound, Wiley, New York.
- Dyer, Ira, 1991, personal communication.
- Ewell, G. W., M. T. Tuley, and W. F. Horne, 1984, "Temporal and spatial behavior of high resolution sea clutter 'spikes' ", IEEE Radar 84 Conf., 100-104.
- Farmer, D.M. and Vagle, S., 1988, "Observations of high frequency ambient sound generated by the wind", Proc. NATO Adv. Workshop on Sea Surface Sound - Natural Mechanisms of Surface Generated Noise in the Ocean, Lerici, Italy, Kluwer Academic, 403-416.
- Farmer, D.M., and Vagle, S., 1988, "On the determination of breaking wave distributions using ambient sound", J. Geophys. Res. 93, 3591-3600.
- Farmer, D.M. and Lemon D.D., 1984, "The influence of bubbles on ambient noise in the ocean at high wind speeds", J. Phys. Oceanogr. 14, 1762-1778.
- Farmer, D.M. and Vagle S., 1989, "Wave propagation of ambient sound in the ocean-surface bubble layer", J. Acoust. Soc. Am., 86, 1897-1908.
- Felizardo, F.C., 1990, "Acoustic scattering by bubble clouds", M.Sc. thesis Civil Engineering, Massachusetts Institute of Technology.
- Ffowcs Williams, J.E. and Guo, Y.P., 1988, "Mechanisms of sound generation at the ocean surface", Proc. NATO Adv. Workshop on Sea Surface Sound - Natural Mechanisms of Surface Generated Noise in the Ocean ed. B.R. Kerman, Lerici, Italy, Kluwer Academic, 309-324.
- Franz, G.J., 1959, "Splashes as sources of sound in liquids", J. Acoust. Soc. Am., 31, 1080-1096.
- Guo, Y.P., 1987, "Sound generation in the ocean by breaking surface waves", J. Fluid Mech., 181, 329-347.
- Hollet, R., 1989, "Underwater sound from whitecaps at sea", J. Acoust. Soc. Am., 85(S1), S145.

- Hollet, R.D. and Heitmeyer, R.M., 1988, "Noise generation by bubbles formed in breaking waves", Proc. NATO Adv. Workshop on Sea Surface Sound - Natural Mechanisms of Surface Generated Noise in the Ocean ed. B.R. Kerman, Lerici, Italy, Kluwer Academic, 449-462.
- Jessup, A.T., Keller, W.C. and Melville, W.K., 1990, "Measurements of sea spikes in microwave backscatter at moderate incidence angles", J. Geophys. Res., vol. 95, 9679 - 9688.
- Jessup, A.T., Melville, W.K. and Keller, W.C., 1991, "Breaking waves affecting microwave backscatter, 1, Detection and Verification", J. Geophys. Res., 96, 20457-20560.
- Jessup, A.T., Melville, W.K. and Keller, W.C., 1991, "Breaking waves affecting microwave backscatter, 2, Dependence on Wind and Wave Conditions", J. Geophys. Res., 96, 20461-20570.
- Johnson, B.D. and Cooke R.C., 1979, "Bubble population and spectra in coastal waters: a photographic approach", J. Geophys. Res., 84, 3761-3766.
- Keller, W. C, Plant, W.J. and Valenzuela, G.R., 1981, "Observations of breaking ocean waves with coherent microwave radar", in IUCRM Symposium on Wave Dynamics and Radio Probing of the Ocean Surface, Miami Beach, Fl.
- Kerman, B.R., 1984 "Underwater sound generation by breaking wind waves", J. Acoust. Soc. Am., 75(1), 149-165.
- Kerman, B.R. , Evans, D.L., Watts, D.R. and Halpern, D., 1983, "Wind dependence of underwater ambient noise", Boundary-Layer Meteor., 26, 105-113.
- Knudsen, V.O., Alford, R.S. and Emling, J.W. 1948 "Underwater ambient noise", J. Marine Res., 7, 410-429.
- Kolaini, A., Roy, R.A. and Crum, L.A., 1991, "An investigation of the acoustic emissions from a bubble plume", J. Acoust. Soc. Am., 89, 2452-2455.
- Kwoh, D. S. and Lake, B. M., 1981, "Microwave backscatter from short gravity waves: deterministic, coherent, dual-polarized study of the relationship between backscatter and water wave properties", in IUCRM Symposium on Wave Dynamics and Radio Probing of the Ocean Surface, Miami Beach, Fl.
- Lamarre, E. and Melville, W.K., 1991, "Air entrainment and dissipation in breaking waves", Nature, 351, 469-472.
- Lamarre, E., 1991, personal communication.
- Lamb, H., 1932, Hydrodynamics, Cambridge University Press.
- Lewis, B.L. and Olin, I.D., 1980, "Experimental study and theoretical model of high-resolution radar backscatter from the sea", Radio Sci., 15, 815-828.
- Lighthill, J.M., 1978, Waves in Fluids, Cambridge University Press, New York, N.Y.

- Lighthill, J.M., 1952, "On sound generated aerodynamically: 1. general theory", Proc. R. Soc. Lond., A221, 564-587.
- Loewen, M.R. and Melville, W.K., 1991, "Microwave Backscatter and Acoustic Radiation from Breaking Waves", J. Fluid Mech., 224, 601-623.
- Longuet-Higgins, M.S. and Smith, N.D., 1983, "Measurements of breaking waves by a surface jump meter", J. Geophys. Res., 88, 9823-9831.
- Longuet-Higgins, M.S., 1989, "Monopole emission of sound by asymmetric bubbles oscillation, Part 1. Normal modes", J. Fluid Mech., 201, 525-542.
- Longuet-Higgins, M.S., 1989, "Monopole emission of sound by asymmetric bubbles oscillation, Part 2. An initial value problem", J. Fluid Mech., 201, 543-565.
- Longuet-Higgins, M.S. and Turner, J.S., 1974, "An entraining plume model of a spilling breaker", J. Fluid Mech., 63, 1-20.
- Longuet-Higgins, M.S., 1990, "Bubble noise spectra", J. Acoust. Soc. Am., 87, 652-661.
- Longuet-Higgins, M.S., 1969, "On wave breaking and the equilibrium spectrum of wind generated waves", Proc. R. Soc. Lond., A310, 151-159.
- Longuet-Higgins, M.S., 1967, "On the trapping of wave energy round islands", J. Fluid Mech., 29, 781-821.
- Lu, N.Q., Prosperetti, A. and Yoon, S.W., 1990, "Underwater noise emissions from bubble clouds", IEEE J. of Ocean. Eng., 15, 275-281.
- Medwin, H. and Beaky, M.M., 1989, "Bubble sources of the Knudsen sea noise spectra", J. Acoust. Soc. Am., 86, 1124-1130.
- Medwin, H. and Daniel, A.C., 1990, "Acoustical Measurements of Bubble Production by Spilling Breakers", J. Acoust. Soc. Am., 88, 408-412.
- Mei, C.C., 1983, The applied dynamics of ocean surface waves, Wiley, New York, N.Y.
- Melville, W.K. and Rapp, R.J., 1985, "Momentum flux in breaking waves", Nature, 317, 514-516.
- Melville, W.K., Loewen, M.R., Felizardo, F.C., Jessup, A.T. and Buckingham, M.J., 1988, "Acoustic and microwave signatures of breaking waves", Nature, 336, 54-59.
- Minnaert, M., 1933, "On musical air bubbles and the sound of running water", Phil. Mag., 16, 235-248.
- Monahan, E.C. and O'Muirheartaigh, I.G., 1986, "Whitecaps and the passive remote sensing of the ocean surface", Int. J. Remote Sensing, vol. 7, No. 5. 627-642.
- Morse, P.M. and Ingaard, K.U., 1968, Theoretical Acoustics, McGraw-Hill, New York.
- Perrone, A.J., 1969, "Deep-ocean ambient-noise spectra in the northwest Atlantic", J. Acoust. Soc. Am., 46, 762-770.

- Phillips, O. M., 1988, "Radar returns from the sea surface - Bragg scattering and breaking waves", J. Phys. Ocean., 18, 1065-1074.
- Phillips, O.M., 1977, The dynamics of the upper ocean, Cambridge University Press.
- Piggott, C.L., 1964, "Ambient sea noise at low frequencies in shallow waters off the Scotian Shelf", J. Acoust. Soc. Am., 36, 2152-2163.
- Prosperetti, A., 1987, "Bubble dynamics in oceanic ambient noise", Proc. NATO Adv. Workshop on Sea Surface Sound - Natural Mechanisms of Surface Generated Noise in the Ocean, Lerici, Italy, Kluwer Academic, 151-171.
- Prosperetti, A. and Lu, N.Q., 1988, "Cavitation and bubble bursting as sources of oceanic ambient noise", J. Acoust. Soc. Am., 84, 1037-1097.
- Prosperetti, A., 1984, "Bubble phenomena in sound fields: part one", Ultrasonics, 22, 69-77.
- Prosperetti, A. and Lu, N.Q., 1988, "Cavitation and bubble bursting as sources of oceanic ambient noise", J. Acoust. Soc. Am., 84, 1037-1041.
- Pumphrey, H.C. and Ffowcs Williams, J.E., 1990, "Bubbles as Sources of Ambient Noise", IEEE J. of Oceanic Eng., 15, 268-274.
- Pumphrey, H.C. and Crum, L.A., 1988, "Acoustic Emissions Associated with Drop Impacts", Proc. NATO Adv. Workshop on Sea Surface Sound - Natural Mechanisms of Surface Generated Noise in the Ocean, Lerici, Italy, Kluwer Academic, 463-483.
- Pumphrey H.C., Crum, L.A. and Bjørnø, L., 1989, "Underwater sounds produced by individual drop impacts and rainfall", J. Acoust. Soc. Am., 85, 1518-1526.
- Rapp, R.J., 1986, "Laboratory measurements of deep water breaking waves", Ph.D. thesis, Ocean Engineering, Massachusetts Institute of Technology.
- Rapp, R.J. and Melville, W.K., 1990, "Laboratory measurements of deep water breaking waves", Phil. Trans. Royal Society of London, A331, 735-800.
- Ross, D.B. and Cardone, V., 1974, "Observations of oceanic whitecaps and their relation to remote measurements of the surface wind speed", J. Geophys. Res., 79, 444-452.
- Shaw, P.T., Watts, D.R. and Rossby, H.T., 1978, "On the estimation of oceanic wind speed and stress from ambient noise measurements", Deep-Sea Res., 25, 1225-1233.
- Shooter, J.A. and Gentry, M.L., 1981, "Wind generated noise in the Parece Vela Basin", J. Acoust. Soc. Am., 70, 1757-1761.
- Smythe, W.R., 1939, Static and Dynamic Electricity, McGraw-Hill, New York, N.Y.
- Strasberg, M., 1953, "The Pulsation Frequency of Nonspherical Gas Bubbles in Liquids", J. Acoust. Soc. Am., 25, 536-538.

- Strasberg, M., 1956, "Gas Bubbles as Sources of Sound in Liquids", J. Acoust. Soc. Am., 28, 20-26.
- Ulaby, F.T., Moore, R.K. and Fung, A.K., 1982, Microwave Remote Sensing Active and Passive, Volume II, Addison-Wesley, Reading, Ma.
- Updegraff, G.E. and Anderson, V.C., 1991, "An instrument for the in situ measurement of sea surface noise from a depth of 1m under low wind conditions", J. Acoust. Soc. Am., 89, 2253-2263.
- Updegraff, G.E. and Anderson, V.C., 1991, "Bubble noise and wavelet spills recorded 1m below the ocean surface", J. Acoust. Soc. Am., 89, 2264-2279.
- Vagel, S., 1989, "An Acoustical Study of the Upper Ocean Boundary Layer", Ph.D. thesis, University of Victoria and Institute of Ocean Sciences, Victoria, B.C.
- Vagle, S., Large, W.G. and Farmer, D.M., 1990, "An evaluation of the WOTAN technique of inferring oceanic winds from underwater ambient sound", J. Atmos. Ocean. Tech., 7, 576-595.
- Watson, A.J., Upstill-Goddard, R.C. and Liss, P.S., 1991, "Air-sea gas exchange in rough and stormy sea measured by a dual-tracer technique", Nature, 349, 145-147.
- Wenz, G.M., 1962, "Acoustic Ambient Noise in the Ocean: Spectra and Sources", J. Acoust. Soc. Am., 34, 1936-1956.
- Wilson, J.H., 1983, "Wind-generated noise modeling", J. Acoust. Soc. Am., 73, 211-216.
- Wu, J., 1979, "Oceanic whitecaps and sea state", J. Phys. Ocean., 9, 1064-1068.
- Yoon, S.W., Crum, L.A., Prosperetti, A. and Lu, N.Q., 1991, "An Investigation of the Collective Oscillations of a Bubble Cloud", J. Acoust. Soc. Am., 89, 700-706.

Appendix A: Chapter 2 Programs

PROGRAM	PROGRAM FUNCTION
WAVES2.FOR	Used on the XT computer which controlled the wave maker, generated sinusoidal surface waves and triggered data acquisition computer.
MADTS2.FOR	Used on AT data acquisition computer, began data acquisition after receiving trigger, sampled the wave gauge signal and the signal produced by the XT computer.
WAVAMP6.FOR	Used to analyze the amplitude data, removes the D.C. and finds the maxima and minima and calculates the amplitude.
PHOOMP.FOR	Used to calculate the phase data, measures the phase lag between the maxima in the two time series of the surface displacement and the XT output signal.
SPLINE2.FOR	Program which fits a cubic spline to the transfer function amplitude and phase data.
GENPACK2.FOR	Program to generate a raw wave packet signal for viewing on the oscilloscope. The wave maker system transfer function is implemented and the slope of each frequency component is held constant. The program outputs analog data through D/A channel 1 for viewing the raw packet data on the oscilloscope.
SEND4.FOR	Uses the data produced by genpack2.for as input and tapers the packet data with a cosine function at both ends.
WAVREP3.FOR	Program which converts the digital wave packet data to an analog voltage signal which is sent to the buck and gain amplifier and then to the wave maker electronics. It also sends a trigger to the data acquisition computers.

Table A.1 Computer programs used in the experiments described in Chapter 2.


```

195      call atodtk(0.1,ifake)
        call DTOA(1,0)
        continue
        do 200 i=1,100
          call atodtk(0.1,ifake)
          call DTOA(ichan,mindle)
          continue
          ij=0
          do 300 j=1,np
            do 310 i=1,ip
              ij=ij+1
              call atodtk(0.1,ifake)
              call DTOA(ichan,idsa(i))
              if(ij.eq.nval)then
                call digout(15)
              endif
            continue
            i=1
          continue
          do 400 i=1,100
            call atodtk(0.1,ifake)
            call DTOA(ichan,mindle)
          continue
          call digout(0)
        stop
      end

```

MADTESFOR

Function: To receive a trigger and then sample the wave gauge and wave maker feedback signal in order to determine the wave maker transfer function.

The program uses subroutines from the RT.LIB software library.

```

PROGRAM MADTES
INTEGER*2 IVAL,M,N,NSAMP,IERR,IZERO,IG
DIMENSION IVAL(10000)
CHARACTER FNAME1*16
IZERO=0
WRITE(*,*) 'TYPE FREQ, START CH., END CH., NSAMP'
READ(*,*) FREQ,M,N,NSAMP
IG=1
PER=1.0/FREQ
WRITE(*,*) 'INPUT DATA OUT FILE'
READ(*,*) (A) FNAME1
OPEN(20,FILE=FNAME1,STATUS=NEW)
WRITE(*,*) 'LAB INTERFACE IS OPENED NEXT'
CALL FOPEN
WRITE(*,*) 'THE INTERFACE IS OPEN'
CALL SETCLOCK(PER,IZERO)
WRITE(*,*) 'THE CLOCK IS SET'
DO 10 I=1,10000
  CALL ATODTK(0.1,IFAKE)
  CALL DIGIN(ITEST)
  IF(ITEST.EQ.15)GOTO 20
CONTINUE
WRITE(*,*) '*****TRIGGERED*****'
CALL MCBATOD(M,N,IG,NSAMP,IVAL(L))
NSP=NSAMP*(N-M+1)
NCH=N-M+1
NSPP=NSP-1
WRITE(*,*) 'M= ',M, 'N= ',N, 'NSP= ',NSP
WRITE(20,50)NCH,M,NSAMP,PER
FORMAT(3I6,5X,F10.5)
WRITE(20,100)(IVAL(KK),KK=0,NSPP)
FORMAT(2I7)
CLOSE(20)
END

```

10
20

50

100


```

mt(na,imt)=k
write(21,*)a=,a(na,imt), na=,na, k=k
na=na+1
kk=kperiod
endif
continue
na=na-1
num(imt)=na
350
c
c 5. computing the average of the amplitude
c
na2=na/2
neven=na-na2*2
na=na-(1-neven)
na1=na-1
sum=0.0
do 400 kk=1,na1,2
    sum=sum+a(kk,imt)-a(kk+1,imt)
    sum=sum+a(kk+2,imt)-a(kk+1,imt)
400
    qual=floor(na1)
    write(21,*)sum=,sum, 'ds1=',ds1, 'qual=',qual
    aaver(imt)=sum/floor(na1)*ds1/2.0
    write(21,*)na1=,na1, 'aaver(imt)=,aaver(imt)
    write(21,*) 'CH=,mm, ' amplitude(average)=,aaver(imt)
    write(21,502)
    format(/)
    continue
    do 550 k=1,jtc
        t(k)=(k-1)*period
502
800
        format(3e14.6)
        open(3,file='peak.dat',status='old')
        write(3,*)rk,w,period
        write(3,*)aaver(1),aaver(2)
        do 700 k=1,2
            write(3,*)num(k)
            write(3,*)(a(j,k),mt(j,k),j=1,num(k))
700
            continue
            open(22,file='p.crv')
            write(22,701)(data(i,1),data(i,2),i=1,jtc)
701
            format(3e14.6)

```

now the zeroes crossing points are found

do 3000 ib=1,2

ma=1

imt=ib

itest=0

do 220 iq=2,njc

k1=iq-1

if(data(iq,imt).lt.0.0.and.data(k1,imt).gt.0.0)go to 221

go to 220

k5=iq+10

if(k5.ge.nsamp)go to 220

k1=iq

do 230 jj=k1,k5

if(data(jj,imt))222,223,223

continue

test=999.0

go to 224

continue

test=0.0

if(test.ne.-999.0)go to 220

continue

if(iq.lt.itest)go to 220

b(ma,imt)=data(iq,imt)

mb(ma,imt)=iq

write(19,*)b=,b(ma,imt), ma=,ma, k=,iq

ma=ma+1

mnum(ib)=ma-1

itest=iq+30

continue

write(19,2999)

format(/)

continue

open(17,file='phase.out',status='old')

write(17,*)rk,w,period

write(17,*)aaver(1),aaver(2)

do 3100 k=1,2

write(17,*)mnum(k)

write(17,*)(b(j,k),mb(j,k),j=1,mnum(k))

continue

close(3)

close(21)

3100

```

close(20)
close(22)
close(17)
close(19)
stop
end

```

PHCOMP.FOR

Written by Mart Loewen

Function: Uses the zero crossing data outputted by WAVAMP6.FOR to calculate the average phase lag between the wave maker feedback and the wave gauge data.

PROGRAM PHCOMP

```

character fname1*16, fname2*16
character date*32
character fname3*16
dimension c1(100,2), g(100,2)
open(30, file='peak.dat', status='old')
read(30, *) n1, w, period
read(30, *) ave1, ave2
read(30, *) n1
read(30, *) (c1(j,1), g(j,1), j=1, n1)
read(30, *) n2
read(30, *) (c1(k,2), g(k,2), k=1, n2)
write(*, *) 'input the output file name'
read(*, *) fname2
open(21, file=fname2, status='new')
write(*, *) 'input start values for calculations'
write(*, *) 'for the phase lag calculations'
write(*, *) 'is1 and is2'
read(*, *) is1, is2
write(*, *) 'input the date'
read(*, *) date
write(*, *) 'input wave freq. and amplitude'
write(*, *) 'The amplitude which was inputted to conan1w.for'
read(*, *) frequency, amp
write(21, *) date
write(*, *) 'input the distance from w/m to gauge'
read(*, *) dist

```

```

write(21,400)
write(21,*) 'Wave Frequency=', frequency, ' Amplitude=', amp
write(21,400)
write(21,*) 'n Lag'
write(21,*) 'n Lag'
write(21,400)
pi=3.1415927
in1=n1-is1+1
in2=n2-is2+1
in=min0(in1,in2)
iend1=is1+in-1
iend2=is2+in-1
kj=0
do 100 i=is1,iend1
kj=kj+1
c1(kj,1)=c1(i,1)
g(kj,1)=g(i,1)
continue
jk=0
do 200 m=is2,iend2
jk=jk+1
c1(jk,2)=c1(m,2)
g(jk,2)=g(m,2)
continue

```

Now the average time difference between peaks is calculated

```

sum=0.0
do 300 j=1,in
ndiff=abs(g(j,1)-g(j,2))
sum=sum+ndiff
write(21,290), ndiff
continue
sumave=sum/in
lave=sumave*period

```

The phase delay caused by the wave maker is calculated

```

dphase=((rk*dist)-(w*lave))
degrees=(360/(2.*pi))*dphase
vcn=ave22/lave1

```



```

c
c
for wmp,wt spline fit dimension c(9,3)

real*8 c(8,3),x(10),f(10),df(10),wk(84),y(10),sm,u(64),s(64)
character*16 fname1
write(*,*) 'input filename'
read(*,*)fname1
write(*,*) 'enter nx the number of data points to fit'
read(*,*)nx
ic=nx-1
write(*,*) 'input smoothing factor, sm'
read(*,*)sm
write(*,*) 'input the m the number of evaluation pts.'
read(*,*)m
open(20,file=fname1,status='old')
read(20,10)((f(i),x(i),df(i),i=1,nx)
write(*,*)((f(i),x(i),df(i),i=1,nx)
open(21,file='sp.out',status='old')
format(3e14.6)
call icsscu(x,f,df,nx,sm,y,c,ic,wk,ier)
write(*,*) ier=ier
write(21,100)((y(i),i=1,nx)
format(e14.6)
write(21,200)
format(/)
write(21,100)((x(i),i=1,nx)
write(21,200)
do 300 j=1,ic
    write(21,10)(c(j,i),i=1,3)
continue
do 400 j=1,64
    u(j)=(j*0.025)+0.375
continue
call icsevu(x,y,nx,c,ic,u,s,m,ier)
open(22,file='ph.out',status='old')
write(22,500)((s(i),u(i),i=1,m)
format(2e14.6)
end

```

```

400 write(21,400)
format(/)
write(21,*) 'phase lag= ',dphase,' radians'
write(21,400)
write(21,*) 'phase lag= ',degrees,' degrees'
write(21,400)

c
c
c
c
Now the average amplitude is calculated using
only the matched peaks.

asum=0.0
avsum=0.0
do 5000 i=1,in
    asum=abs(c(i,1))+asum
    tv=(c(i,2)*1000.0*5.0)/2048.0
    av=tv/10.0
    avsum=abs(av)+avsum
continue
format(2i10)
ave1=asum/in
ave2=avsum/in
vcm=ave2/ave1
cmg=ave1/amp
write(21,*) 'average wave amplitude= ',ave1,' cm'
write(21,400)
write(21,*) 'average voltage amplitude= ',ave2,' volts'
write(21,400)
write(21,*) 'volts per centimeter= ',vcm
write(21,400)
write(21,*) 'wave amplitude/gain, cm/gain', cmg
stop
end

5000
290

SPLINE2.FOR

c
c
c
c
Function: This program is used to fit a smooth cubic spline
through a set of data points. It uses various IMSL routines.
Note: this program was run on the Micro Vax computer.

c
c
c
c
Note that the c matrix must be exactly dimensioned
for the number of points it is interpolating.
For wmp,ave spline fit dimension c(8,3) and

```



```

2320      GOTO 2310
CONTINUE
write(30,*)'tcc=';tcc
c      The amplitude corrections are computed next
c
c      do 2350 k=1,9
        kp=k+1
        if(x1(k).le.fc.and.fc.lt.x1(kp))then
            d=fc-x1(k)
            d2=d*d
            d3=d2*d
            ac=(cc1(k,3)*d3)+(cc1(k,2)*d2)+(cc1(k,1)*d)+y1(k)
        endif
2350      continue
        write(30,*)'ac=';ac
        write(30,*)'d=';d
        do 2400 i=1,nfc
            do 2400 j=1,9
                jp=j+1
                if(x1(i).le.f(i).and.f(i).lt.x1(jp))then
                    d=f(i)-x1(i)
                    d2=d*d
                    d3=d2*d
                    cc1(j)=(cc1(j,3)*d3)+(cc1(j,2)*d2)+(cc1(j,1)*d)+y1(j)
                    a(i)=ac*((cc1(j,3))/(cc1(j,2)*d2))
                endif
2400      continue
            do 364 i=1,nfc
                ak(i)=(a(i)*5.*cc1(i)*f(i))/100.
            continue
            write(30,2000)(a(i),i=1,nfc)
            write(30,2401)
            write(30,2000)(ak(i),i=1,nfc)
            format(/)
            write(30,2401)
2401      c      The phase corrections are calculated next
c
c      do 77 i=1,nfc
            do 77 j=1,10
                jp=j+1
                if(x2(i).le.f(i).and.f(i).lt.x2(jp))then

```

```

b=f(i)-x2(j)
b2=b*b
b3=b2*b
dph(i)=(c2(j,3)*b3)+(c2(j,2)*b2)+(c2(j,1)*b)+y2(i)
endif
77      continue
        write(30,2000)(dph(i),i=1,nfc)
c      THE PHASES ARE CALCULATED
c
c      DO 25 I=1,NFC
        PHA(I)=(RK(I)*XB)-((2*pi)*F(I)*TB)+dph(i)
        CONTINUE
25      c      THE SIGNAL DATA IS WRITTEN TO UNIT 5
c
c      write(*,*)fname ATE
c      read(*,*)fname
c      open(5,file=fname,status='new')
c      WRITE(5,1101)NPT,SEC,NFC,TB,XB
c
c      THE SIGNAL IS CALCULATED AND THE COMPONENTS SUMMED
c
c      DO 40 I=1,NPT
        X=(I-1)*sec
        ATE=0.0
        DO 35 JJ=1,NFC
            ATE=ATE+(a(JJ)*COS((-2.*pi*F(JJ)*X)-PHA(JJ)))
        CONTINUE
        ATE=IFIX(ATE*DVAL)+MINDLE
        ITE(I)=ATE
        CONTINUE
        WRITE(5,1200)(RK(I),J=1,NFC)
        WRITE(5,1200)(CG(K),K=1,NFC)
        write(5,1100)(ITE(I),I=1,NPT)
        ICHAN=0
        IGATE=0
40      c      THE SIGNAL IS SENT TO THE OSCILLOSCOPE FOR ANALYSIS
c
c      TO VISUALLY PICK THE WINDOW LIMITS
c
c      WRITE(*,*)PRESS RETURN TO MAKE WAVES
c      READ(*,*)XCI

```

```

310 CALL FOPEN
1000 CALL SETCLOCK(sec,lgate)
1100 DO 310 I=1,NPT
1101   CALL ATODTK(0.1,FAKE)
1200   CALL DTOA(ICHAN,ITE(I))
      CONTINUE
      format(f10.5)
      format(10i7)
      FORMAT(15,F10.5,15,2F10.5)
      FORMAT(4f10.5)
      STOP
      END

```

SENDM.FOR

Written by Mark Loewen

Functioning: This program uses the raw wave packet data from GENPACK2.FOR as input. It windows the data and smooths each end of the signal using a cosine function.

```

PROGRAM SENDM
CHARACTER FNAME*16
DIMENSION ITE(8000),CG(32),RK(32)

```

THE WINDOW LIMITS ARE INPUTTED INTERACTIVELY HERE

```

WRITE(*,*)'INPUT START POINT IPS AND END POINT IPE'
READ(*,*)IPS,IPE
NSAMP=(IPE-IPS)+1
PI=3.14159

```

THE NAME OF THE INPUT FILE PREVIOUSLY GENERATED BY
THE BREAK2 PROGRAM IS INPUTTED HERE

```

WRITE(*,*)'INPUT FNAME'
READ(*,*)FNAME
OPEN(3,FILE=FNAME,STATUS=OLD)
FORMAT(10i7)
READ(3,1001)NPT,SEC,NFC,TB,XB
FORMAT(15,F10.5,15,2F10.5)
READ(3,1100)(RK(I),I=1,NFC)

```

```

1100 READ(3,1100)(CG(K),K=1,NFC)
      FORMAT(4f10.5)
      DEK=ABS(RK(NFC)-RK(1))
      WDW=(4.*PI)/DEK
      TAU2=TB-(XB+WDW/2.)/CG(1))
      TAU1=TB-(XB-WDW/2.)/CG(NFC))
      ITEST=IPE-(TAU1-TAU2)/SEC
      IF(ITEST.GT.IPS)GO TO 33
      IPS=ITEST
      NSAMP=(IPE-IPS)
      CONTINUE
      WRITE(*,*)'IPS=',IPS,'ITEST=',ITEST
      WRITE(*,*)'NSAMP=',NSAMP
      FORMAT(15,F10.5)
      READ(3,1000)(ITE(I),I=1,NPT)
      DO 5 I=IPS,IPE
        J=(I-IPS)+1
        ITE(J)=ITE(I)
      CONTINUE
      EXPONENTIAL SMOOTHING OF EACH END OF THE WINDOW

      NPTT=NSAMP-50
      DO 99 I=NPTT,NSAMP
        FFC=COS((PI*I/100.)+(PI/2.)-(PI*NSAMP/100.))
        ITE(I)=INT(FFC*(ITE(I)-2048))+2048
      CONTINUE
      DO 98 I=1,50
        J=50-I
        ITE(I)=INT(COS((PI*I/100.)-(PI/2.))*(ITE(I)-2048))+2048
      CONTINUE
      THE SMOOTHED DATA IS WRITTEN TO UNIT 4 FOR USE AS INPUT
      FOR PROGRAM WAVGEN

      WRITE(*,*)'INPUT FNAME FOR SIGNAL'
      READ(*,*)FNAME
      OPEN(4,FILE=FNAME,STATUS=NEW)
      WRITE(4,1002)NSAMP,SEC
      WRITE(4,1000)(ITE(I),I=1,NSAMP)
      STOP
      END

```


543	CALL DTOA(ICHAN,MINDLE)
542	IF(1.EQ.NVAL1.OR.1.EQ.NVAL2)THEN
	CALL DIGOUT(0)
	ENDIF
	IF(1.EQ.NVP1.OR.1.EQ.NVP2)THEN
	CALL DIGOUT(15)
	ENDIF
310	CONTINUE
	DO 400 I=1,100
	CALL ATODTK(0.1,IFAKE)
	CALL DTOA(ICHAN,MINDLE)
400	CONTINUE
	WRITE(*,*) 'WAITING FOR TRIGGER'
	IFAKE=0
	CALL SETCLOCK(0.5,0)
	IF(1.CE.ICLIMIT)GOTO 1101
	DO 5000 I=1,5000
	CALL ATODTK(2.1,IFAKE)
	IF(IFAKE.GT.500)GO TO 6000
	IF(1.GT.1800)GO TO 5500
5000	CONTINUE
5500	WRITE(*,*) 'DELAY LONGER THAN 15 MINUTES'
	GO TO 1101
6000	WRITE(*,*) 'IFAKE=',IFAKE
C	
C	DELAY 60 SECONDS MORE HERE TO ALLOW
C	AMBIENT NOISE TO BE SAMPLED
C	
	DO 7000 I=1,120
	CALL ATODTK(2.1,IFAKE)
7000	CONTINUE
	GO TO 132
1100	FORMAT(15)
1101	STOP
	END

Appendix B: Chapter 3 Programs

PROGRAM	PROGRAM FUNCTION	2-D Experiments	3-D Experiments
ADDSK2.C	Used to sample acoustic data using the RC ISC-16 board, calls Spedding routines,	x	
SPLASH.FOR	Sends an analog wave packet signal to the wavemaker system using the DAS20 board.	x	
DIG20.FOR	Sets the digital ports on a DAS20 board.	x	
WAIT.FOR	Executes a dummy loop N times, to produce a delay.	x	
PACKET.FOR	Generates a packet of waves composed of 32 sinusoidal components, options available are constant slope, constant amplitude, transfer function implemented and transfer not implemented.	x	
MPOWL.P.F	Reads the time series produced by conv4.for and calculates the power spectrum, various options such as overlapping, averaging and smoothing are available, designed for use with data sampled during the 2-D experiments at MIT.	x	
SAMP.MAC	A macro file for use with SUPERKEY software for unattended sampling of data.	x	
AUTO4.FOR	Program which samples data using the RC ISC-16 board and the Spedding routines, waits for a trigger on the trig port then begins sampling, used at OTRC.		x
TXPOWL.P.F	Reads the time series produced by conv4.for and calculates the power spectrum, various options such as overlapping, averaging and smoothing are available, designed for use with data sampled at OTRC.		x
CONV4.FOR	Reads the data files produced when sampling data with the RC ISC-16 board and the Spedding drivers and separates 4 channels of data into 4 binary data files which can be read by NDP Fortran.	x	x
BANDPOW.F	Reads the power spectrum data files outputted by MPOWL.P.F and TXPOWL.P.F and calculates the power in a given set of frequency bands, reads data files with one or more spectra and writes the power in each band as a function of time.	x	x
BANDTOT.F	Reads the power spectrum data files outputted by MPOWL.P.F and TXPOWL.P.F and calculates the power in a given set of frequency bands, reads data files with one spectrum and writes the total power in each band.	x	x

Table B.1 Computer programs used in the experiments described in Chapter 3.

ADCDSK2 - take data in ISIZE word blocks and write it to disk for NBLOCKS. This program may be compiled with the Small model:
 • Program is compiled with Microsoft C
 cl -FPI87 -G2 -Ox adcdsk.c adc iver

v2.0 6.4.88

This program was modified from ADCDSK.C from ADC Routines for RC ISC-16 C Language by G. Spedding

The program waits for an external trigger on the trig port and then samples data to disk. For maximum speed a file on a ramdisk should be used.*/

```
#include <stdio.h>
#include <malloc.h>
#include <math.h>
#include <conio.h>
#include "adc.h"

#define MAXBLOCK 64

main0
{
    int err(MAXBLOCK);
    short int huge *ip;
    long nch, size, isize, iume, delay, idisk=1L;
    long n, nblock;
    int c, i, ierr;

    /* get ADC operating parameters from keyboard */
    do {
        cputs("\nnch [1,2,4,8,16]:");
        scanf("%ld",&nch);
        cputs("\niume [usec, 1-65536]:");
        scanf("%ld",&iume);
        cputs("\ndelay [usec, 0-65535]:");
        scanf("%ld",&delay);

        /* select RC buffer size */
        cputs("... select buffer size --\nvSIZE BUFFER");
    }
```

```
for(size=0; size<8; size++){
    isize=(long)pow(2.,(double)(size+8));
    printf("\n%1ld %5ld",size,isize);
}
cputs("\nenter SIZE:");
scanf("%ld",&size);
isize=(long)pow(2.,(double)(size+8));

/* allocate the ISIZE length memory buffer */

if((ip=(short huge *)halloc(isize,sizeof(short)))==NULL){
    cputs("\ninsufficient RAM\n");
    exit(1);
}

/* select number of blocks */

printf("\nblock [1-%d]:",MAXBLOCK);
scanf("%ld",&nblock);
n=isize*nblock;

/* open the ADC file and write the header block */

ierr=adfilo(n, nch, iume, delay);

/* set up ADCs and start after external trigger */

adc0(nch, iume, size);
cputs("\nstart on external trigger");
trig00;
cputs("\n\nrunning..");

/* nblocks of data into idat buffer and write buffer to disk */

for(i=0; i<nblock; i++)
    err[i]=rdbuf(ip, isize, idisk);

/* stop the ADCs and close the data file */

adhalt0;
ierr=adfilc0;

/* free the data buffer */
```



```

C
    hfree(ip);

/* check the error flags */

    cpustat("\n\n");
    for(i=0; i<nbblock; i++)
        printf("\nblock#%d ierr=%d", i, ierr[i]);

/* do it all again ? */

    } while(iver("\n\nrepeat?"));

C
C PROGRAM SPLASH
C
C PROGRAM TO SEND TO THE WA VEMAKER AWA VE PACKET GENERATED
C BY THE PROGRAM GENPACK
C THIS PROGRAM IS WRITTEN FOR DAS20 BOARD
C
C NOTE THAT THE D/A OUTPUT ON BOARD MUST BE SET TO +/- 10 C
C VOLTS

C
C INPUT: filename: packet filename (generated by genpack.for)
C gain: gain factor to be applied to signal
C dout0: time for digital output (100th sec)
C OUTPUT: to channel 0 for d/a and to the specified channel for dout?

C
C 08-21-90: FIRST WRITTEN BY ERIC LAMMARE
C 09-03-90: MODIFIED
C 09-09-90: MODIFIED FOR FALL 90 EXP.
C 90-12-12: Modified by Mark Loewen
C 91-01-15: MODIFIED BY MRL

C
C COMPILING AND LINKING NOTES: Microsoft Fortran and Metabyte library
C send20.obj: send20.for
C FL /c /AYdb /G0 /I2 /Fs send20.for
C
C send20.exe: send20.obj
C LINK $*, $@, NUL, c:\lib\libfor7+libc7+das20f /NOD /NOE
C
C program splash

```

```

C
integer base
integer*4 buffer, alloc
integer choice
integer das20
integer data(0:2499)
integer dmalev
integer dout0
integer i
integer inlev
integer junkint
integer*4 k
integer mode0, mode7, mode8, mode9, mode12, mode15, mode25
integer n1rate, n2rate
integer npt
integer param(5)
integer rcode
integer rcode
integer rcode
integer segpar, offadr
integer trig1, trig2, dig1, dig2

real dataat(0:2499)
real gain
real junkreal
real sumak

character*30 filename
character*15 junkname

data base/#300/
data dmalev/1/
data dout0/1/
data inlev/3/
data mode0/0/, mode7/1/, mode8/8/, mode9/9/
data mode12/12/, mode15/15/, mode25/25/
data n2rate/1000/, n1rate/50/
data rcode/1/
buffer = alloc(32766)

C
C INITIALIZE DAS16 A/D BOARD
C
param(1) = base
param(2) = inlev

```

```

param(3) = dmalev
rcode = das20(mode0, param)
if (rcode .ne. 0) print *, 'Error, rcode = ', rcode

C
C SET ANALOG CHANNEL 0 TO 0.0 VOLTS
C

param(1) = 0
param(2) = 0
rcode = das20(mode7, param)
if (rcode .ne. 0) print *, 'Error, rcode = ', rcode

C INPUT WAVE FILE
C
write(*, '(aV)') 'Enter wave data file: '
read(*, '(a)') filename
write(*, '(aV)') 'Enter Gain: '
read(*, *) gain
write(*, *) 'Enter 2 trigger times, 100ths of a sec='
read(*, *) trig1, trig2
write(*, *) 'Enter 2 digital trigger values, dig1 and dig2'
read(*, *) dig1, dig2

C LOAD DATA AND ADJUST FOR A/D AND ADJUST FOR GAIN
C
open(16, file = filename, status = 'old')
read(16, 4000) junkname, junkreal
read(16, 4000) junkname, junkreal
read(16, 4000) junkname, junkreal
read(16, 4000) junkname, junkreal
read(16, 3000) junkname, junkint
read(16, 4000) junkname, junkreal
read(16, 3000) junkname, npt
read(16, 4000) junkname, junkreal
read(16, 4000) junkname, junkreal
read(16, 4000) junkname, sumak
write(*, 6000) ' Slope of packet = ', gain * sumak
read(16, 4000) junkname
read(16, 4000) junkname
do 10 i = 0, npt-1
    read(16, 2000) data(i)
10 continue

param(3) = dmalev
rcode = das20(mode0, param)
if (rcode .ne. 0) print *, 'Error, rcode = ', rcode

C SET ANALOG CHANNEL 0 TO 0.0 VOLTS
C

param(1) = 0
param(2) = 0
rcode = das20(mode7, param)
if (rcode .ne. 0) print *, 'Error, rcode = ', rcode

C INPUT WAVE FILE
C
write(*, '(aV)') 'Enter wave data file: '
read(*, '(a)') filename
write(*, '(aV)') 'Enter Gain: '
read(*, *) gain
write(*, *) 'Enter 2 trigger times, 100ths of a sec='
read(*, *) trig1, trig2
write(*, *) 'Enter 2 digital trigger values, dig1 and dig2'
read(*, *) dig1, dig2

C LOAD DATA AND ADJUST FOR A/D AND ADJUST FOR GAIN
C
open(16, file = filename, status = 'old')
read(16, 4000) junkname, junkreal
read(16, 4000) junkname, junkreal
read(16, 4000) junkname, junkreal
read(16, 4000) junkname, junkreal
read(16, 3000) junkname, junkint
read(16, 4000) junkname, junkreal
read(16, 3000) junkname, npt
read(16, 4000) junkname, junkreal
read(16, 4000) junkname, junkreal
read(16, 4000) junkname, sumak
write(*, 6000) ' Slope of packet = ', gain * sumak
read(16, 4000) junkname
read(16, 4000) junkname
do 10 i = 0, npt-1
    read(16, 2000) data(i)
10 continue

1000 format(i10)
2000 format(f10.3)
3000 format(a15,i10)
4000 format(a15,f10.3)
5000 format(a15)
6000 format(a19,f6.3)
C
102 continue
if (gain .gt. 4.0) then
    print *, 'This gain is too high'
    stop
endif
do 15 i = 0, npt-1
    data(i) = int(gain * data(i) * (4095/20.0))
15 continue
C
C SET CLOCK RATE FOR DAS20 A/D BOARD
C
param(1) = n1rate
param(2) = n2rate
rcode = das20(mode25, param)
if (rcode .ne. 0) print *, 'Error, rcode = ', rcode
C
C LOAD DATA WITH MODE8 INTO buffer MEMORY SEGMENT
C
101 continue
param(1) = npt
param(2) = segptr(buffer)
param(3) = 0
param(4) = offadr(data(0))
rcode = das20(mode8, param)
if (rcode .ne. 0) print *, 'Error, rcode = ', rcode
C
C SEND DATA TO D/A CHANNEL 0
C
param(1) = npt
param(2) = segptr(buffer)
param(3) = 2
param(4) = rycyc
param(5) = 0
pause 'Press return to send signal now'
print *, 'Signal being send'
print *

```

```

    rocode = das20(mode9, param)
    if (rocode .ne. 0) print *, 'Error, rocode = ', rocode
C
C  C MONITOR DATA OUTPUT COUNT NUMBER AND OUTPUT DIGITAL DATA
C  C SET DIGITAL PORTS
C  C ON THE FIRST CONVERSION THIS TIME CODE IS TRIGGERED BY
C  C SWITCHING FROM HIGH TO LOW ON DIGOUTS I.E. DIG=7
C  C TRIGGER 1 IS SENT TO DIGITAL PORT AT CONVERSION TRIG1
C  C TRIGGER 2 IS SENT TO DIGITAL PORT AT CONVERSION TRIG2
103 continue
    rocode = das20(mode12, param)
    if (param(3) .eq. 1) then
        param(1) = 7
        rocode = das20(mode15, param)
        go to 104
    endif
104 if (param(3) .eq. trig1) then
    param(1) = dig1
    rocode = das20(mode15, param)
    go to 105
endif
105 if (param(3) .eq. trig2) then
    param(1) = dig2
    rocode = das20(mode15, param)
    go to 106
endif
if (param(3) .ge. npt) goto 106
go to 103
106 continue
    rocode = das20(mode12, param)
    if (param(3) .lt. npt) go to 106
C
C  C OPTION TO GENERATE 1) SAME WAVE, 2) CHANGE GAIN, 3) EXIT
C
109 print *, '1) Generate same wave'
print *, '2) Change gain and generate same wave'
print *, '3) Exit program'
write(*, '(aV)') 'Enter choice:'
read(*, *) choice
if (choice .eq. 1) go to 101
if (choice .eq. 2) then
    write(*, '(aV)') 'Enter new Gain:'
    read(*, *) gain
    write(*, '(aV)') 'Slope of packet = ', gain * sumak
    write(*, *) 'Enter trigger values, trig1 and trig2='
    read(*, *) trig1, trig2
    go to 102
endif
if (choice .eq. 3) stop
stop
end
C
C  C PROGRAM DIG20
C
C  C PROGRAM TO ACTIVATE THE DIGITAL PORTS ON DAS20 BOARD
C  C 1) ACTIVATE ON DIGITAL PORT HIGH OR LOW
C  C 2) SEND A PULSE AT THE DIGITAL PORT
C
C  C 08-31-90: FIRST WRITTEN BY ERIC LAMMARE
C
C  C COMPILING AND LINKING NOTES: Microsoft Fortran and Metabyte library
C  C dig20.obj: dig20.for
C  C FL /c /4 Ydb /GO /412 /fs dig20.for
C
C  C dig20.exe: dig20.obj
C  C LINK $*, $@, NUL, c:\lib\libfor7+libc7+das20f /NOD /NOE
C
C  C program dig20
C
integer base
integer choice
integer dmalcv
integer das20
integer digin
integer flag
integer*4 i
integer inlev
integer mode8, mode17, mode0, mode13, mode15, mode18
integer*4 length
integer param(5)
integer rocode
data base/#300/

```

```

data dmalev/1/
data inilev/3/
data mode17/17/, mode0/0/, mode8/8/
data mode13/13/, mode15/15/, mode18/18/
C
C INITIALIZE DAS16 A/D BOARD
C
    param(1) = base
    param(2) = inilev
    param(3) = dmalev
    rcode = das20(mode0, param)
    if (rcode .ne. 0) print *, 'Error, rcode = ', rcode
C
C INPUT PARAMETERS
C
100 continue
    print *, '1) Activate ports'
    print *, '2) Send pulse'
    print *, '3) Exit'
    write(*, '(aV)') 'Enter choice:'
    read (*, *) flag
    if (flag .eq. 3) stop
    write(*, '(aV)') 'Enter digital value:'
    read (*, *) digin
C
C OPTION 1) ACTIVATE PORTS
C
    if (flag .eq. 1) then
        param(1) = digin
        rcode = das20(mode15, param)
        if (rcode .ne. 0) print *, 'Error, rcode = ', rcode
    endif
C
C OPTION 2) SEND PULSE - RESETS AT LOW - GOES FROM LOW TO HIGH -
C
    if (flag .eq. 2) then
        write(*, '(aV)') 'Pulse length:'
        read (*, *) length
        param(1) = 0
        rcode = das20(mode15, param)
        if (rcode .ne. 0) print *, 'Error, rcode = ', rcode
        param(1) = digin
        rcode = das20(mode15, param)

```

```

    if (rcode .ne. 0) print *, 'Error, rcode = ', rcode
    do 10 i = 1, length
10    continue
        param(1) = 0
        rcode = das20(mode15, param)
        if (rcode .ne. 0) print *, 'Error, rcode = ', rcode
    endif
    go to 100
C
    stop
end
C
C PROGRAM WAIT
C
C PRODUCES A TIME DELAY BY EXECUTING A DUMMY LOOP N TIMES
C
C 09-09-90: FIRST WRITTEN BY ERIC LAMARRE
C
C COMPILING AND LINKING NOTES: Microsoft Fortran
C wait.obj: wait.for
C          FL/c /AYdb /GO /Fs wait.for
C
C wait.exe: wait.obj
C          LINK $** $@, NUL, c:\nb\libfor7+libc7 /NOD /NOE;
C
    program wait
C
    integer ihr(2), imin(2), isec(2), i100th(2)
    integer*4 i, n
C
C INPUT TIME DELAY
C
    write(*, '(aV)') 'Enter n, number of loops:'
    read (*, *) n
C
    call getum(ihr(1), imin(1), isec(1), i100th(1))
    write(*, '1000ihr(1), imin(1), isec(1)')
    print *, 'Waiting ...'
    do 10 i = 1, n
10    continue
        call getum(ihr(2), imin(2), isec(2), i100th(2))
        write(*, '1000ihr(2), imin(2), isec(2)')
1000 format('i2.2, ', i2.2, ', i2.2, ', i2.2)

```

```

C      stop
C      end

C PROGRAM PACKET
C
C PROGRAM TO GENERATE A PACKET OF WAVES COMPOSED
C OF 32 SINUSOIDAL COMPONENTS
C
C INPUT: fc: center frequency of packet (Hz)
C      bw: bandwidth of packet (Hz)
C      xb: breaking position (m)
C      tb: time to breaking (sec)
C      pd: period (sec) of entire signal (pd<25), npt=pd/(1/fout)
C      flag: if yes => slope (ak) is kept constant
C           if no => amplitude (aa) is kept constant
C      tf: if yes => transfer function is applied (ampl. & phase)
C           if no => no transfer function is applied
C DATA: nfc: number of frequency components evenly spaced (32)
C      ak: constant (non dimensional)
C      aa: constant (cm)
C      npt: number of points forming the packet (2000)
C      fout: output frequency of d/s board (100 Hz)
C      h: depth of water (0.6m)
C OUTPUT: data: array containing packet
C
C 08-25-90: FIRST WRITTEN BY ERIC LAMMARE
C 09-03-90: MODIFIED
C
C COMPILING AND LINKING NOTES: Microsoft Fortran and Metabyte library
C packet.obj: packetak.for
C FL /c /AYdb /G2 /M12 /F's packet.for
C
C packet.exe: packet.obj
C LINK $*.* $@, NUL, c:\lib\libfor7+libc7 /NOD /NOE
C
C program packet
C
C integer nfc, npt
C integer i, j, n
C
C real aa, ak, fc, bw, xb, tb, g, fout, pd

```

```

real f(32), a(32), pha(32), k(32), compha(32), data(16000)
real deltabw, pi, ko, time, signal, h, w2g
real a0, a1, a2, a3
real a0pha, a1pha
real sumak, nakc

C      character*30 filename
C      character*1 flag, tf

C      data nfc/32, fout/100.0f, aa/1.0f, ak/0.01f, g/9.81f, h/1.14f
C      data pi/3.14159f
C      data a0/-2.718f, a1/21.184f, a2/-17.125f, a3/4.055f
C      data a0pha/1.14f, a1pha/-1.13f

C INPUT DATA
C
C      write(*,'(aV)' Enter output filename: '
C      read(*,'(aV)' filename
C      write(*,'(aV)' Enter fc (Hz): '
C      read(*,*) fc
C      write(*,'(aV)' Enter bw (Hz): '
C      read(*,*) bw
C      write(*,'(aV)' Enter xb (m): '
C      read(*,*) xb
C      write(*,'(aV)' Enter tb(sec): '
C      read(*,*) tb
C      write(*,'(aV)' Enter pd(sec): '
C      read(*,*) pd
C      npt = pd / (1/fout)
C      write(*,'(aV)' Keep ak constant (y/n): '
C      read(*,'(aV)' flag
C      if (flag.eq. 'n'.or. flag.eq. 'N')
C      1 print *, 'Therefore amplitude is kept constant'
C      write(*,'(aV)' Apply transfer function (y/n): '
C      read(*,'(aV)' tf
C      print *, 'Computing ...'
C      if (tf.eq. 'n'.or. tf.eq. 'N') then
C      a0 = 1.0
C      a1 = 0.0
C      a2 = 0.0
C      a3 = 0.0
C      a1pha = 0.0
C      print *, 'No transfer function applied'

```

```

endif
C
C COMPUTE FREQUENCY COMPONENTS [EVENLY SPACED IN
C FREQ. DOMAIN]
C
    detabw = bw / (nfc-1)
    do 10 i = 0, nfc - 1
        f(i+1) = (fc - bw/2.0) + detabw * i
    10 continue
C
C COMPUTE WAVENUMBER FOR EACH FREQ. COMP. USING
C DISPERSION RELAT.
C
    do 20 i = 1, nfc
        w2g = ((2*pi*f(i))**2) / g
        ko = w2g
    25 k(i) = w2g / tanh(ko*h)
        if (abs(k(i)-ko) .lt. 0.0001) go to 20
        ko = k(i)
    go to 25
    20 continue
C
C COMPUTE PHASE OF EACH COMPONENT WITH CORRECTION C FOR
C TRANS. FUNCT.
C
    a0pha (rad), a1pha (rad/Hz)
C
    do 30 i = 1, nfc
        compha(i) = a0pha - a1pha*f(i)
    30 continue
C
C IF a1 CONSTANT OPTION IS CHOSEN THEN ADJUST a SUCH THAT a1
C IS CONSTANT AND THEN CORRECT FOR AMPLITUDE TRANSFER
C FUNCTION
C
C IF a CONSTANT OPTION IS CHOSEN THEN SIMPLY APPLY TRANSF.
C FUNCT. TO a
C
    a0, a1, a2, a3 ARE COEFF. TO THE AMPL. TRANSF. FUNCT.
C
    do 40 i = 1, nfc
        if (flag.eq. 'y' .or. flag.eq. 'Y') then
            a(i) = ak / (k(i)/100)
        else
            a(i) = aa
        endif
    40 continue
C
    a(i) = a(i) / (a0 + a1*f(i) + a2*f(i)**2 + a3*f(i)**3)
    40 continue
    sumak = 0.0
    nakc = 0.0
    if (flag.eq. 'y' .or. flag.eq. 'Y') then
        do 45 i = 1, nfc
            sumak = sumak + a(i) * (a0 + a1*f(i) + a2*f(i)**2 +
                1 a3*f(i)**3) * (k(i)/100)
        45 continue
    else
        do 46 i = 1, nfc
            nakc = nakc + a(i) * (a0 + a1*f(i) + a2*f(i)**2 +
                1 a3*f(i)**3)
        46 continue
        nakc = nakc * (k(16)/100)
    endif
C
C COMPUTE SIGNAL BY SUPERPOSING ALL NFC FREQUENCY
C COMPONENT
C
    do 50 j = 1, npt
        time = (j-1) * (1/fout)
        signal = 0.0
        do 60 i = 1, nfc
            signal = signal + a(i) * cos( - k(i)*xb
                - 2*pi*f(i)*(time - tb) - compha(i) )
        60 continue
        data(j) = signal
    50 continue
C
C SET EXPONENTIAL INCREASE AND DECAY USING 1.0 SEC
C (100 POINTS)
C
    n = 100
    do 55 i = 1, n
        data(i) = data(n) * exp((i - n)/20.0)
    55 continue
    do 57 i = npt-n, npt
        data(i) = data(npt-n) * exp(((npt-n) - i)/20.0)
    57 continue
C
C WRITE DATA TO DISK
C

```

```

open(16, file=filename, status = 'unknown')
write(16,4000) 'c (Hz) = 'fc
write(16,4000) 'bw (Hz) = 'bw
write(16,4000) 'xb (m) = 'xb
write(16,4000) 'tb (sec) = 'tb
write(16,3000) 'afc (H) = 'afc
write(16,4000) 'foua(Hz) = 'foua
write(16,3000) 'npt (H) = 'npt
write(16,4000) 'h (m) = 'h
C
if (flag.eq. 'y'.or. flag.eq. 'Y') then
  write(16,4000) 'ak (nd) = 'ak
  write(16,4000) 'sumak (nd)= 'sumak
  write(16,5000) 'const. ak '
  write(16,5000) 't.f. applied'
else
  write(16,4000) 'aa (cm) = 'aa
  write(16,4000) 'Nakc (nd) = 'Nakc
  write(16,5000) 'const. amp '
  write(16,5000) 'no t.f. '
endif
write(16,5000) '
do 70 j = 1, npt
  write(16,2000) data(j)
70 continue
1000 format(i10)
2000 format(f10.3)
3000 format(a15,i10)
4000 format(a15,f10.3)
5000 format(a15)
C
stop
end

```

MPOWL.P.F

- 900327 - MRL
- Program to read the data files outputted by
- the RC board using the Spedding drivers and compute
- the power spectrum.
- The DC is removed from the entire time series first.
- The data is then windowed and the spectrum calculated on
- data segments 2**pol2 long.
- Spectra are averaged over incr number of data segments.

Frames may be overlapped.
 Spectra are adjusted so that Parseval's theorem is satisfied.
 Loops through many files and reads filenames from MPOWLP.FLE
 Hydrophone and microphone response are accounted for.
 Program uses signal processing routines from NDP.FFT
 MPOWLP.MAK - make file for compiling and linking uses NDP Fortran
 mpowlp.obj: mpowlp.f
 f77 -c -u mpowlp.f
 mpowlp.exp: mpowlp.obj c:\nicexp\programs\cvar.obj
 386L.LNK @mpowlp.lnk
 MPOWLP.LNK - link file
 -twocase
 -pack
 CANDP20dos386.obj
 CANDP20A__co387.obj
 mpowlp.obj
 c:\nicexp\programs\cvar.obj
 c:\nicexp\programs\buave.obj
 -lib CANDP20LIBPndpfft
 -lib CANDP20LIBPlibf
 -lib CANDP20LIBPihm387
 -lib CANDP20LIBPibc
 -lib CANDP20LIBPibgrex
 -exe
 mpowlp.exp
 integer*2 idata(300000)
 real*4 data(300000)
 real*4 x(8194),wx(8194),psd(8194),sct(8300)
 complex*8 c(4097),zw(4097)
 integer i,ilim,type,npts,jc,je,nar,pol2,incr
 integer n2p,n24p,ilim,incnt,icount,norm,mode,ic
 integer cw,jpstart,ipstop,hpnum,nact
 real scale,sum,mean,fact,var,fact1,fact2
 real g(10),gain,freq,is
 real*4 sump,sumx2,fct

```

integer mpts,jmstart,jmstop,iover,jwin,irecl
integer io,jk,jm,rfiles,jsmooth,kwin
equivalence (c,x)
character filename*'9,filename2*10,path*29,file*40
open(1,file='mpowlp.in')
read(1,'(a29)')path
read(1,'*)npts
read(1,'*)iover
read(1,'*)pf2
read(1,'*)mode
read(1,'*)norm
read(1,'*)scale
read(1,'*)incr
read(1,'*)jwin
read(1,'*)ipstart
read(1,'*)ipstop
read(1,'*)(g(i),i=1,10)
read(1,'*)rfiles
read(1,'*)kwin
read(1,'*)smooth
call getndp(type)
nar = 2*'pf2
nact = nar-iover
n2p = (nar/2)+1
n24p = n2p*4+4
cw = 0
irecl = npts*2

Loop through files here
open(18,file='mpowlp.file')
do 7000 im = 1,nfiles
  read(18,'(a9)')fname
  read(18,'(a10)')fname2
  read(18,'*)gain
  read(18,'*)hprnum
  write(file,19)path,fname
  format(a29,a9)
  write(*,*) Opening file=',file
  open(2,file=file,form='unformatted',access='direct',
    & iorecl=status,'unknwnw',err=10,iostat=io)
integer mpts,jmstart,jmstop,iover,jwin,irecl
write(*,*) Error opening file, iostat=',jo
goto 6000
read(2,end=50,rec=1)(data(j),j=1,npts)
goto 60
write(*,*) Warning end-of-file encountered'

```

19

U U U


```

200      ic = ((i-1)*(nar-iover)) + j
      if(j.eq.1)then
        ts = (ic-1)/freq
      endif
      x(i) = data(ic)
      call cvar(x,nar,sumx2)
      if(iwin.eq.1)call btf92(x,w1,nar,mode)
      if(iwin.eq.2)call hamrn(x,w1,nar,mode)
      if(iwin.eq.3)call hamrn(x,w1,nar,mode)
      if(iwin.eq.0)then
        call rfft(x,pof2,norm,scale)
        do 1100 k = 1, n2p
          psd(k) = c(k) * conjg(c(k))
        continue
      else
        call rfft(w1,pof2,norm,scale)
        do 1200 k = 1, n2p
          psd(k) = zw(k) * conjg(zw(k))
        continue
      endif
1100      C
1200      C
      C      Smooth PSD here
      C
      C      if(smooth.eq.1)then
      C      call buave(psd,scrt,n2p,kwin)
      C      endif
      C
      C      Adjust spectrum here so that Parseval's theorem
      C      is satisfied
      C      Remember:  $PSD(f) = (2/N(dt))(X(f))^2$ 
      C      Therefore:
      C       $(1/N)sum(x^2) = (1/Ndt)sum(PSD(f))$ 
      C      or
      C       $dt sum(x^2) = sum(PSD(f))$ 
      C
      C      sump = 0.0
      C      do 1400 k = 1, n2p
      C      sump = psd(k)+sump
      C      fct = (sumx2/freq)/sump
      C      do 1500 k = 1, n2p
      C      psd(k) = psd(k)*fct
      C
      C
      C      Sum the spectra
      C
      C      do 1600 k = 1, n2p
      C      p(k) = p(k) + psd(k)
      C      continue
      C
      C      Average the spectra
      C
      C      if(incont.eq.incr)then
      C      cw = cw+1
      C      write(*,*) 'Writing to file',cw,'.frame2'
      C      do 1700 k = 1, n2p
      C      p(k) = p(k)/incr
      C      continue
      C      write(3,rec=cw)ts,(p(k),k=1,n2p)
      C      format(e12.6)
      C      incrt = 0
      C      icount = 0
      C
      C      Zero p(k) here
      C
      C      do 1800 k = 1, n2p
      C      p(k) = 0.0
      C      continue
      C      endif
      C      continue
      C      stop
      C      end
      C
      C      MPOWLP.IN - input parameters for mpowlp.f
      C      f:\mark4\vnice\p\data\910205\
      C      49152
      C      20000
      C      171
      C      9
      C      0
      C      2
      C      1.0
      C      3
      C      1
      C      1
      C
      C      npts
      C      freq-sampling freq.
      C      iover
      C      pof2
      C      mode
      C      norm
      C      scale
      C      incr
      C      iwin,1-BM,2-HAMM,3-HANN
      C      ipstian

```

```

144
-165.0,-211.4,-211.4,-211.4,-211.5,-211.5,-206.4,-211.3,-211.6,-152.4
10
9
0
nfiles
kwin
ismooth- 1 to smooth

```

```

*SAMP.MAC - macro file for use with superkey.com software to run batch
•
program to sample acoustic data.

```

```

<BEGDEF><A1S>
adcdsk2<ENTER>
4<ENTER>
50<ENTER>
0<ENTER>
7<ENTER>
6<ENTER>
d:01.dat<ENTER>
n
copy d:01.dat 0128_6.dat<ENTER>
conv4<ENTER>
0128_6.dat<ENTER>
0128_6<ENTER>
2<ENTER>
run386 tplot4<ENTER>
0128_6<ENTER>
<CMD>FR00:01:20.00<CMD>
hplpt<ENTER>
adcdsk2<ENTER>
4<ENTER>
50<ENTER>
0<ENTER>
7<ENTER>
6<ENTER>
d:01.dat<ENTER>
n
copy d:01.dat 0128_7.dat<ENTER>
conv4<ENTER>
0128_7.dat<ENTER>
0128_7<ENTER>
2<ENTER>
run386 tplot4<ENTER>
0128_7<ENTER>
<CMD>FR00:01:20.00<CMD>

```

```

hplpt<ENTER>
adcdsk2<ENTER>
4<ENTER>
50<ENTER>
0<ENTER>
7<ENTER>
6<ENTER>
d:01.dat<ENTER>
n
copy d:01.dat 0128_8.dat<ENTER>
conv4<ENTER>
0128_8.dat<ENTER>
0128_8<ENTER>
2<ENTER>
run386 tplot4<ENTER>
0128_8<ENTER>
<CMD>FR00:01:20.00<CMD>
hplpt<ENTER>
adcdsk2<ENTER>
4<ENTER>
50<ENTER>
0<ENTER>
7<ENTER>
6<ENTER>
d:01.dat<ENTER>
n
copy d:01.dat 0128_9.dat<ENTER>
conv4<ENTER>
0128_9.dat<ENTER>
0128_9<ENTER>
2<ENTER>
run386 tplot4<ENTER>
0128_9<ENTER>
<CMD>FR00:01:20.00<CMD>
hplpt<ENTER>
adcdsk2<ENTER>
4<ENTER>
50<ENTER>
0<ENTER>
7<ENTER>
6<ENTER>
d:01.dat<ENTER>
n

```

```

copy d:01.dat 012810.dat<ENTER>
conv4<ENTER>
012810.dat<ENTER>
012810<ENTER>
2<ENTER>
run386 tuplo4<ENTER>
012810<ENTER>
<CMD>FR00:01:20.00<CMD>
hplht<ENTER>
<ENDDDEF>

```

AUTO4 - written by Mark Loewen 910529

Purpose: To sample the acoustic data for the OTRC experiments.
 The program loops and gathers data to a ramdisk file and then converts it to binary format which NDP Fortran can read and writes it to a hard disk file. Sampling is started when a trigger pulse is received on the trig port. The RC ISC16 board is required.
 The program uses the Spedding routines listed below.

External routines required:

ADFLS, ADC0, ADC1, RDBUF, ADHALT & ADFLC, all in ADCLIB.

Compiling and linking info: uses NDP Fortran

AUTO4.MAK

auto4.obj: auto4.for

fl/c-Ox-FP187-G2-AL auto4.for

auto4.exe: auto4.obj ad110.obj ad10n.obj iver.obj

LINK /NOD /NOE \$**,\$@,NUL,c:\NIBLIB\for7 c:\NIBLIB\7 /se:1024;

program auto4

parameter (max=32768, maxblock=32)

character*7 prfile

character*9 flnam

character*4 pre

integer*2 idat(max), ierr(maxblock)

integer*4 n, nch,itime, size, isize, delay, idisk, jerr

integer*4 nloop, jsart, expnum

data idisk//

* get root filename and iteration count

```

1 write(*,92)
read(*,*)nloop
write(*,93)
read(*,*)jsart
write(*,94)
read(*,94)pre
* read the ADC input parameters

```

```

nch=4
itime=25
delay=0
size=7
nblock=32
isize=2*(size+8)
n=size*nblock

```

* go round in loop writing data to flnam each time

```

write(*,*)
do 1000 j=1,nloop
call fname(flnam)

```

* open data file, write file header, initialise RC board

```

call adfls(flnam, n, nch, itime, delay, jerr)
call adc0(nch, itime, size)
write(*,135)j
call trig00

```

* read NBLOCK blocks of data from RC A/D and write to file

```

10 do 10 i=1,nblock
call rdbuf(idat, isize, ierr(i), idisk)

```

* stop the ADCs, close the data file

```

call adhalt0
call adflc(jerr)

```

* inspect IERR array for error flags

```

do 500 i=1,nblock
if(ierr(i).ne.0)then

```

```

write(*,140); ierr(i)
stop 'overflow'
endif
continue

```

500

• Write the data to the hard disk

expnum=(j-1)*jstart

call fname2(pre,expnum,prefile)

call conv4(filnam,prefile,3)

close(2)

continue

1000

• formats

91 format(a)

92 format(nloop: \)

93 format(/ Enter starting experiment number: \)

94 format(/ Enter month and day i.e. 0601: \)

100 format(/ nch [1,2,4,8,16]: \)

110 format(/ time [usec, 1-65384]: \)

115 format(/ delay [usec, 0-65535]: \)

120 format(-- select buffer size -- / SIZE BUFFER /

* 0

256 / 1 512 / 2 1024 /

* 3

2048 / 4 4096 / 5 8192 /

* 6

16384 / 7 32768 / enter SIZE: \)

format(nblock: \)

format(+nloop: j3)

format('block# j3', ierr = 'j1)

end

• Sets name of ramdisk file to 001.dat

subroutine fname(s)

character*9 s

s='d:001.dat'

return

end

Subroutine to set the prefix of the files

written to the hard disk

subroutine fname2(s0,i,s)

character*4 s0

character*7 s

integer*4 i

format(a4,'_0',i1)

format(a4,'_j',i2)

if(i .le. 9)then

write(s,100)s0,i

endif

if(i .gt. 9)then

write(s,200)s0,i

endif

return

end

100

200

•

Subroutine to translate 4 channel Spedding routine data files into files which

NDP fortran can read

format, 1 channel of data per file

Note: nchwt is the number of channels of data to be written

to disk, nch equals 4 always.

910524 - MRL

•

subroutine conv4(ifile,prefix,nchwt)

integer*2 idata(32768), icdat(4,8192), idum

integer*4 n, nch, iume, delay, i,j,k,iocheck,nchwt

integer*4 i,j,irec,ilim,jc

character*32 prefix,ifile,jfile

• open the ADC data file and read the header

c open(unit=9,file=ifile,form='binary',access='direct',

c * recl=2, status='old')

open(unit=9,file=jfile,form='binary',status='old')

read(9)n,nch,iume,delay

format(a7,'_0',i1)

20

C

C

C

C

Loop through the number of channels in the

USC data file

do 100 i = 1 , nchwt

iu = i+10

```

      write(nfile,20)prefix,i
      open(unit=iw,file=nfile,form='unformatted',access='direct',
      rec=16384)
      continue
      do 5000 i = 1, 50
        write(*,*) Processes loop #=:i
        isrec = 9+((i-1)*32768)
        read(9,rec=isrec-1)idum
        if((i*32768).ge. n)then
          ilim=n-((i-1)*32768)
        else
          ilim=32768
        endif
        read(9,end=200,iostat=ioccheck)idata
        goto 250
      200 write(*,*) End-of-file encountered
        write(*,*) ioccheck=:ioccheck
        jc = j - 1
        ich = 8192
        do 1000 k = 1, nch
          do 1000 j = 1, ich
            ij = k + (nch*(j-1))
            icdat(k,j)=idata(ij)
          continue
        if(jc.lt. 32768)then
          do 1200 k = 1, nch
            do 1200 j = ich+1, 8192
              icdat(k,j) = 0
            continue
          endif
          do 2000 k = 1, nchwr
            write(unit=k+10)(icdat(k,j),j=1,ich)
          continue
          do 3000 k=1,4
            write(*,*)(icdat(k,j),j=1,5)
          format(5i12)
          if((i*32768).ge. n)goto 6000
        5000 continue
        6000 do 6100 i = 1, nch
          close(i)
        6100 continue
          close(9)
          return

```

```

end
TXPOWLP.F
910530 - Mark Loewen
Program to read the data files outputted by
the RC board using the Spedding drivers and compute
the power spectrum.
The DC is removed from the entire time series first.
The data is then windowed and the spectrum calculated on
data segments 2**pof2 long.
Spectra are averaged over incr number of data segments.
Frames may be overlapped.
Spectra are adjusted so that Parseval's theorem is satisfied.
Loops through many files and reads filenames from MPOWLP.FLE
Hydrophone and microphone response are accounted for.
Program uses the signal processing routines from NDP.FFT
Compiling and Linking info: uses NDP Fortran
TXPOWLP.MAK
txpowlp.obj: txpowlp.f
f77 -c -u txpowlp.f
txpowlp.exp: txpowlp.obj c:\nrcexp\programs\cvar.obj
386i.LNK @txpowlp.lnk
TXPOWLP.LNK
-twocase
-pack
CANDP20dos386.obj
CANDP20A_co387.obj
txpowlp.obj
cvar.obj
blave.obj
-lib CANDP20LIBPndpfft
-lib CANDP20LIBPnibf
-lib CANDP20LIBPnibm387
-lib CANDP20LIBPnibc
-lib CANDP20LIBPnibgrex
-exe
txpowlp.exp

```

```

integer*2 idata(270000)
real*4 data(270000)
real*4 x(16388),wx(16388),p(16388),psd(16388),scr(16600)
complex*8 c(8194),zw(8194)
integer i,j,lim,type,npts,jc,nar,pof2,incr
integer n2p,n24p,jlim,incr,jcount,norm,mode,ic
integer cw,ipstart,ipstop,hpnum,nact
real scale,sum,mean,fact,var,fact1,fact2
real g(3),gain,freq,fs,fcf
real*4 sump,sumx2
integer mpts,jmstart,jmstop,iover,jwin,irecl
integer io,j,k,im,nfiles,ismooth,kwin
equivalence (c,x)
character fname*10,fname2*10,path*15,ifile*25
open(1,file='tupowlp.in')
read(1,'(a15)')path
read(1,'*')npts
read(1,'*')freq
read(1,'*')iover
read(1,'*')pof2
read(1,'*')mode
read(1,'*')norm
read(1,'*')scale
read(1,'*')incr
read(1,'*')jwin
read(1,'*')ipstart
read(1,'*')ipstop
read(1,'*')(g(i),i=1,3)
read(1,'*')nfiles
read(1,'*')kwin
read(1,'*')ismooth
call getndp(type)
nar = 2**pof2
nact = nar-iover
n2p = (nar/2)+1
n24p = n2p*4+4
cw = 0
irecl = npts*2

C
C
C
Loop through files here
open(18,file='tupowlp.le')

do 7000 im = 1,nfiles
  read(18,'(a10)')fname
  read(18,'(a10)')fname2
  read(18,'*')gain
  read(18,'*')hpnum
  write(ifile,19)path,fname
  format(a15,a10)
  open(2,file=ifile,form='unformatted',access='direct',
    * recl=irecl,status='unknown',err=10,iostat=io)
  19
  *
  goto 20
  10
  write(*,*) 'Error opening file, iostat=',io
  goto 6000
  20
  read(2,end=50,rec=1)(data(j),j=1,npts)
  goto 60
  50
  write(*,*) 'Warning end-of-file encountered'
  *
  * Remove the DC, correct for hydrophone response
  * and gain, and convert to pressure in Pascals
  *
  * hpnum's 1 and 2 are for the 2 B&K hydrophones
  * gain means mV/unit out on 2635 amps.
  * hpnum 3 is the Shure microphone which has a
  * sensitivity of -165 dB re 1 microV/Pa
  *
  sum = 0.0
  if(hpnum .eq. 3)then
    fact1 = 1.0/(10.0***(gain/20.0))
    fact2 = 1.0/(10.0***(g(hpnum)/20.0))
    fact = (20.0/4096.0)*fact1*fact2*1.0e-6
  else
    fact1 = 1.0/g(hpnum)
    fact2 = 1.0/(10.0***(gain/20.0))
    fact = (20.0/4096.0)*fact1*fact2
  endif
  *
  * Note that the number of data points read is npts
  * and the variance is calculated over mpts points
  *
  * the number of data points over ipstart to ipstop segments
  * i.e. npts>fft length*ipstop
  *
  do 70 i = 1, npts
    data(i) = float(idata(i))*fact
  70

```



```

endif
5000 continue
7000 continue
6000 stop
end

```

• TXPOWLP.IN - input parameters for TXPOWLP.F

```

f:\audio\1\
path
npts
freq-sampling freq.
iover
pof2
mode
norm
scale
incr
iwin,1-BM,2-HAMM,3-HANN
ipstart
ipstop
V/unit out (1,2) and microphone sens.
nfiles
kwin
ismooth- 1 to smooth

```

• CONV4.FOR

Program to translate 4 channel USC data files into files which

NDP fortran can read

format, 1 channel of data per file

900328 - MRL

Compiling and Linking info: Microsoft Fortran

conv.obj: conv4.for

FL /c /4Ydb /ZI /G2 /F+ sp2dlp.for

conv4.exe: conv4.obj

LINK \$** \$@, NUL, /libfor7 libbc7 /SE:1024 /NOE /NOD

program conv4

integer*2 idata(32768), icdata(4,8192),idum

integer*4 n, nch,itime, delay,j,jk,ioccheck

integer*4 ij,irec,ilim,jc,rl

character*32 file,prefix,nfile

• open the ADC data file and read the header

```

10 write(*,*) 'Enter USC data filename'
read(*,*) file
open(unit=2,file=file,form='binary',access='direct',

```

*rec1=2,status='old',err=10)

read(2,n,nch,itime,delay

write(*,*) n='n', nch='nch', itime='itime', delay='delay

write(*,*) 'Enter the channel files prefix, 6 letters'

read(*,*) prefix

format(a6,'0',i1)

Loop through the number of channels in the

USC data file

write(*,*) 'Enter rec1='

read(*,*) rl

do 100 i = 1, nch

iu = i+10

write(nfile,20)prefix,i

open(unit=iu,file=nfile,form='unformatted',access='direct',

* rec1=16384)

100

continue

do 5000 i = 1, 50

write(*,*) '96 Kbyte loop=' ,i

isrec = 9+((i-1)*32768)

read(2,rec=isrec-1):idum

if((i*32768).ge. n)then

ilim=n-((i-1)*32768)

else

ilim=32768

endif

read(2,end=200,iostat=ioccheck)(idata(i),j=1,ilim)

goto 250

write(*,*) 'End-of-file encountered'

write(*,*) ioccheck='ioccheck

write(*,*) 'Number of data points read=' ,j-1

write(*,*) (idata(k),k=1,8)

jc = j - 1

ich = (j-1)/nch

write(*,*) 'ich =',ich

200

250


```

100      continue
      do 500 k = 1, n2p
        if (k .eq. 1) goto 510
        icj = icj+1
        f = (k-1) * dfreq
        if ((.gt. b(ib))) then
          ic(ib-1) = icj-1
          icj = 1
          ib = ib+1
        endif
        if (f .eq. b(ib)) then
          ic(ib-1) = icj
          icj = 0
          ib = ib+1
        endif
        sum(ib-1) = dat(k)+sum(ib-1)
        continue
      do 600 k = 1, nbands
        sum(k) = sum(k)/float(ic(k))
        continue
      Calculate PSL's here
      do 700 k = 1, nbands
        if (sum(k) .le. 1e-52) then
          ps(k) = -400.0 - 10*log10(b(k+1)-b(k))
        else
          ps(k) = 10*log10(sum(k)/1e-12) - 10*log10(b(k+1)-b(k))
        endif
        continue
      Write data to disk
      write(11,710)u,(ps(k),k=1,nbands)
      format(6e12.4)
      continue
      stop
      end
510
500
600
700
710
1000
5000

```

```

* BANDPOW.IN - input parameters for BANDPOW.F
c:\micexp\data\
nfiles
n2p
nbands
nspec
freq
b(i)
0.0,1000.,10000.,
69
1025
2
32
20000

```

```

* BANDTOT.F
* 910221 - MRL
* Program which reads the power spectrum data files
* outputted by mpowlp.f and calculates the total power
* in a given set of frequency bands.
*
* Compiling and Linking info - uses NDP Fortran
*
bandtot.obj: bandtot.f
f77 -u bandtot.f

```

```

program bandtot
real dat(8200),sum(10),b(10)
real ts,dfreq,freq,f,ap
integer i,j,k,ijspec,nfiles,ic(10)
integer nbands,n2p,irecl,ib,icj
character ifile1*10,ofile*10,path*25,ifile*35
open(1,file='bandtot.in')
open(2,file='bandtot.fie')
read(1,'(a25)')path
read(1,'(a10)')ofile
read(1,'*')nfiles
read(1,'*')n2p
read(1,'*')nbands
read(1,'*')nspec
read(1,'*')freq
read(1,'*')(b(i),i=1,nbands+1)
write(*,'*')nfiles
write(*,'*')n2p
write(*,'*')nbands
write(*,'*')nspec
write(*,'*')freq

```


Appendix C

The Effect of Noncircular Cylinder Shape

This appendix describes in detail the procedure used to estimate the effect of noncircular shape on the pulsation frequency of cylinders of air immersed in water. The analysis is based on the work of Strasberg (1953) who estimated the effect of nonspherical shape on the pulsation frequency of air bubbles in water. It is assumed that as the cylinder pulsates the undisturbed volume and pressure remain constant and that the stiffness is not affected by the shape. Therefore any change in the pulsation frequency must be associated with a change in the inertia or mass. Calculating the pulsation frequency of a noncircular cylinder is therefore reduced to the problem of determining the inertial constant of a cylinder of arbitrary shape but fixed volume.

The differential equation of a pulsating cylinder can be written in terms of the volume pulsation $\Delta V(t) = V(t) - V_0$ where V_0 is the undisturbed volume per unit length. If $\Delta V \ll V_0$ then the differential equation is the standard second order equation of a linear oscillator,

$$m \Delta \ddot{V}(t) + K \Delta V(t) = 0 \quad \text{C.1}$$

where m and K are the inertial and stiffness constants respectively, the dots denote differentiation with respect to time and the effects of damping have been neglected. The stiffness constant K equals minus the ratio of the change in pressure inside the cylinder to its change in volume,

$$K = - \frac{dP}{dV} . \quad \text{C.2}$$

For a spherical air bubble it can be shown that $dP = -3\gamma P_o (a/a_o - 1)$ and $dV = 4\pi a_o^3 (a/a_o - 1)$. Then, $K = \gamma P_o / V_o$ where a_o is the undisturbed bubble radius, P_o is the undisturbed pressure inside the bubble and γ is the ratio of the specific heats. The inertial constant represents the pressure required to give the surrounding fluid a volume acceleration,

$$m = \frac{dP}{\Delta \ddot{V}} \quad . \quad C.3$$

For a spherical air bubble it can be shown that $dP = -\rho \omega^2 a_o \delta$ and $\Delta \ddot{V} = -4\pi \omega^2 \delta a_o^2$ and therefore $m = \rho/4\pi a_o$ where ω is the radian frequency and δ is the amplitude of the bubble wall oscillations. Then the resonant frequency is given by,

$$f_o = \frac{1}{2\pi} \sqrt{\frac{K}{m}} = \frac{1}{2\pi} \left[\frac{\gamma P_o}{\frac{4}{3}\pi a_o^3} \right] \left[\frac{4\pi a_o}{\rho} \right] = \frac{1}{2\pi} \sqrt{\frac{3\gamma P_o}{\rho a_o^2}} \quad C.4$$

which is the well known Minnaert (1933) formula.

The work done on the fluid by the pulsating cylinder can be written as,

$$W = \int_{V_o}^V P(t) dV(t) dt = \int_0^{\Delta \dot{V}(t)} P(t) \Delta \dot{V}(t) dt \quad . \quad C.4$$

The work done on the fluid becomes kinetic energy of the fluid. Using equation C.3 to substitute for $P(t)$ in equation C.4 an expression relating the kinetic energy T to the inertial constant m is obtained,

$$T = \int_0^{\Delta \dot{V}(t)} m \Delta \dot{V}(t) \Delta \dot{V}(t) dt = \frac{1}{2} m (\Delta \dot{V}(t))^2 . \quad C.5$$

From equation C.5 the inertial constant can be seen to be the constant of proportionality between the kinetic energy of the fluid and half the square of the volume velocity. The kinetic energy of the fluid can be calculated by evaluating the following surface integral on the cylinder surface,

$$T = \frac{1}{2} \rho \int_A \Phi \nabla \Phi \cdot \mathbf{n} dA \quad C.6$$

where Φ is the velocity potential, A is the area per unit length of the cylinder, the gradient of the velocity potential, $\nabla \Phi = \mathbf{u}$ the velocity vector, ρ is the density of the fluid and \mathbf{n} is the unit vector normal to surface (Batchelor, 1967, p. 383). Combining equations C.5 and C.6 gives,

$$m = - \frac{\rho}{(\Delta \dot{V}(t))^2} \int_A \Phi \nabla \Phi \cdot \mathbf{n} dA . \quad C.7$$

If $ka_0 \ll 1$ then Φ will be essentially constant over the surface of the cylinder and equation C.7 becomes,

$$m = - \frac{\rho \Phi}{(\Delta \dot{V}(t))^2} \int_A \nabla \Phi \cdot \mathbf{n} dA = \frac{\rho \Phi}{\Delta \dot{V}(t)} . \quad C.8$$

Therefore the inertial constant is seen to be proportional to the ratio of the velocity potential to the volume velocity. The problem has now been reduced to determining the effect of shape on the ratio of the velocity potential to the volume velocity.

A mathematical analogy exists between electrostatics and fluid dynamics which simplifies the solution. The electrostatic potential of an electrostatic field is equivalent to the velocity potential of a hydrodynamic field. It can be shown that the dielectric flux Ψ is equivalent to the volume velocity $\Delta\dot{V}(t)$ (flow rate). The capacitance C is defined as,

$$C = \frac{\Psi}{(\Phi_1 - \Phi_2)} \quad \text{C.9}$$

where Ψ is the dielectric flux and in this equation Φ is the electrostatic potential. From equation C.9 it is evident that the capacitance is equivalent to the ratio of the volume velocity to the velocity potential, that is,

$$C \equiv \frac{\Delta\dot{V}(t)}{(\Phi_1 - \Phi_2)} = \frac{1}{m} \quad \text{C.10}$$

where Φ is the velocity potential. This analogy allows published results on the capacitance of conducting ellipsoids to be used to calculate the ratio of the inertial constant of a circular cylinder to that of a noncircular cylinder. The following relationships are valid,

$$\frac{f}{f_o} = \sqrt{\frac{m_o}{m}} \propto \sqrt{\frac{C}{C_o}} \quad \text{C.11}$$

where f_0 , m_0 and C_0 are the pulsation frequency, inertial constant and capacitance respectively of the circular cylinder and f , m and C are the corresponding values of the noncircular cylinder.

It can be shown that a set of equipotential surfaces is defined by the following formula,

$$1 = \frac{x^2}{a^2 + \beta} + \frac{y^2}{b^2 + \beta} + \frac{z^2}{c^2 + \beta} \quad 3.12$$

where x , y , and z are Cartesian coordinates, $c > b > a$ and $-a^2 < \beta < \infty$ (Smythe, 1939). When $\beta = 0$ an ellipsoid with axes lengths a , b and c is defined and when $\beta = \infty$ a sphere of infinite radius is defined. The potential on the surface of the ellipsoid is constant and if the potential at $\beta = \infty$ is taken to be zero the capacitance of the ellipsoid is given by,

$$C = 2 \left[\int_0^{\infty} \frac{d\beta}{\sqrt{(a^2 + \beta)(b^2 + \beta)(c^2 + \beta)}} \right]^{-1} \quad 3.13$$

(Smythe, 1939). The integral in equation 3.13 can be evaluated numerically by splitting it into two parts, integrating from 0 to some finite value γ and then from γ to ∞ . In the second integral the transformation $\theta = 1/\sqrt{\alpha}$ is made and the limits of integration become $1/\sqrt{\gamma}$ to 0. If $c \gg a$ or b then the shape of the ellipsoid approaches that of a two dimensional cylinder. Therefore with $c = 7.6$ m (10 times the wave channel width) and $(ab) = 0.02$ equation 3.13 was evaluated for various values of a/b the ratio of the major to minor axis length. These results are tabulated in table C.1.

a/b	C	f/f_0
1.0	2.764	1.0
2.0	2.824	1.011
4.0	3.006	1.043
8.0	3.318	1.095
16.0	3.783	1.170

Table C.1 Results from integrating equation 3.13 numerically, f/f_0 is the ratio of the calculated pulsation frequency to f_0 the pulsation frequency of an ellipsoid with a circular cross section.

The observed cylinders had a major to minor axis ratio of approximately 3. Therefore from table C.1 the frequency of the observed cylinders could be expected to be approximately 3% higher than that of a circular cylinder of equal volume. Clearly then, the effect of noncircular shape on the pulsation frequency is very small and can be neglected.

Appendix D: Chapter4 Programs

PROGRAM	FUNCTION	80386 PC	Sun Sparc
MODEL9.F	Generates a time series using bubble histogram data as input. Referred to as the Monte Carlo Method in chapter 4.	x	x
MODSPEC6.F	Generates the power density spectrum directly using bubble histogram data as input. Referred to as the Analytic Spectrum Model in chapter 4.	x	x
RPOWER4.F	Calculates the power spectrum level of the time series generated by MODEL9.F	x	
RANDOM.F	Outputs a random number between 0 and 1 given a seed number.	x	x
CVAR.F	Subroutine which computes the sum of $(x(t))^2$ given $x(t)$ as input.	x	

Table A.1 : Computer programs used in the modeling work of chapter 4. The programs were run on either an 80386 PC or a Sun Sparc Station or both as indicated.

MODEL9.FOR

Written by Mark Loewen 900924

Function: to read in a bubble histogram data (i.e. Medwin and Daniel's) file and use this information to generate a time series using damped sinusoids as the model bubble signatures.

Program is designed to replicate the bubble distribution as closely as possible given that an integer number of bubbles is required in each radius bin.

The input bubble histogram data is used to calculate how many bubbles occur in each radius bin. Then the program distributes them randomly across the bin.

The bubble depth and fractional amplitude of the bubble wall oscillations are varied randomly between a max and min.

Crowther's (1988) equation for the damping constant is implemented.

The full equation for the acoustic pressure is used to include near and far field effects.

Compiling and linking instructions: Using NDP FORTRAN

```
model9.mak:
    model9.obj; model9.f
    f77 -c -u model9.f
    model9.exp: model9.obj
    386LINK @model9.lnk
```

```
model9.lnk:
    -twocase
    NDP20\dos386.obj
    NDP20\co387.obj
    model9.obj
    random.obj
    -lib C:\NDP20\LIB\libf
    -lib C:\NDP20\LIB\libm387
    -lib C:\NDP20\LIB\libc
    -lib C:\NDP20\LIB\libgex
    -etc
```

```
model9.exp
-pack
```

```
seed - start # for random number generator
a(i) - histogram radii
ar(i) - bubble radius calculated by the program
br(i) - histogram amplitudes
nval - # points in histogram
r(i) - random ranges rmin - rmax
t(i) - random start times 0 - time
p(k) - pressure time series
el(i,j) - bubble depth
ec(i) - fractional amplitude of bubble oscillation
nb(i) - number of bubbles in a radius bin
dh - the damping constant
```

```
program model9
real p(150000),r(5000),a(1000),b(1000),ar(100,200)
real el(100,200),c(5000)
real fr,p1,p2,p3,pt,time,rmax,bsum
real dh,te,cps,pi,rmin,d,fract
real elmin,elmax,amax,amin,freq,z
real epamin,epamax,p4,kr
integer nb(100),i,j,k,jc,naum
integer nbub,nval,npts,seed,n24p
character histd*11,out*10
```

Open input file and read input parameters

```
histf - input bubble histogram data file
out - output data file
nbub - total number of modeled bubbles
epamin - minimum fractional amplitude
epamax - maximum fractional amplitude
d - receiver depth
rmax - maximum range
rmin - minimum range
elmax - twice the maximum bubble depth
elmin - twice the minimum bubble depth
seed - initial random number generator seed
time - length of time series
```

	- sampling frequency of time series	
	freq	
	open(1,file='mode19.in')	
	read(1,(a1))histf	
	read(1,(a10))out	
	read(1,*)nbub	
	read(1,*)epemin	
	read(1,*)epemax	
	read(1,*)d	
	read(1,*)rmax	
	read(1,*)rmin	
	read(1,*)elmax	
	read(1,*)elmin	
	read(1,*)seed	
	read(1,*)time	
	read(1,*)freq	
	pi = 3.14159	
	Open bubble histogram file and read the data	
	open(2,file=histf)	
	read(2,*end=5)(a(i),b(i),i=1,10000)	
	nval = i	
	writeln(*,*) nval=',nval'	
	format(2f10.5)	
	continue	
	Calculate the bubble radii based on the bubble histogram data	
	Sum the bubble histogram amplitudes	
	bsum = 0	
	do 150 i=1, nval	
	bsum = b(i) + bsum	
	continue	
	writeln(*,*) bsum=',bsum'	
	Calculate the number of bubbles in each bin	
	nb(i)=(nbub/bsum)*b(i)	
	nsum = 0	
	do 200 i = 1, nval	
	fact = b(i)*float(nbub)/bsum	
	nb(i) = anint(fact)	
	nsum = nb(i) + nsum	
	continue	
	write(*,*) Number of model bubbles=',nsum'	
	Pick nb(i) random numbers for each bin and use random numbers to spread them across the bin. Note that if nb(i)=1 the bubble is placed at the center of the bin at r(i). Also pick random numbers to use to scale el by.	
	do 250 i = 1, nval	
	if(i .eq. 1)then	
	amin = a(i)-((a(i+1)-a(i))/2.)	
	amax = (a(i)+a(i+1))/2.	
	elseif(i .eq. nval)then	
	amin = (a(i)+a(i-1))/2.0	
	amax = a(i)+(a(i)-a(i-1))/2.0)	
	else	
	amin = (a(i)+a(i-1))/2.0	
	amax = (a(i)+a(i+1))/2.0	
	endif	
	if(nb(i) .eq. 1)then	
	ar(i,1) = a(i)	
	goto 240	
	endif	
	do 225 j = 1, nb(i)	
	call random(seed,z)	
	ar(i,j) = z*(amax-amin)+amin	
	continue	
	do 245 j = 1, nb(i)	
	call random(seed,z)	
	el(i,j) = z*(elmax-elmin)+elmin	
	continue	
	continue	
	Pick nsum random numbers to specify the range and scale them by rmax	
	do 700 i = 1, nsum	

Line	Code	Comment
1	read(1,*)rmin	
2	read(1,*)el	
3	read(1,*)seed	
4	read(1,*)nspec	
5	read(1,*)fs	
6	read(1,*)para1f	
7	pi = 3.14159	
8	gm = 8.777e-5	
9	ja = (0,1)	
10	dω = (fs/2.0)*2*pi/(nspec-1)	
11	dτ = (fs/2.0)/(nspec-1)	
12	Open bubble histogram file and read the data	
13	open(2,file=histf)	
14	read(2,*,end=5)(a(i),b(i),i=1,10000)	
15	goto 6	
16	nval = i-1	
17	write(*,*) nval='nval'	
18	format(2f10.5)	
19	continue	
20	Calculate the bubble radii based on the bubble histogram data	
21	Sum the bubble histogram amplitudes	
22	baum = 0	
23	do 150 i=1, nval	
24	baum = b(i) + baum	
25	continue	
26	write(*,*) baum='baum'	
27	Calculate the number of bubbles in each bin	
28	nb(i)=(nbub/baum)*b(i)	
29	num = 0	
30	do 200 i = 1, nval	
31	fact = b(i)*float(nbub)/baum	
32	nb(i) = amin1(fact)	
33	num = num + nb(i)	
34	continue	
35	write(*,*) Number of model bubbles='num'	
36		
37		
38		
39		
40		
41		
42		
43		
44		
45		
46		
47		
48		
49		
50		
51		
52		
53		
54		
55		
56		
57		
58		
59		
60		
61		
62		
63		
64		
65		
66		
67		
68		
69		
70		
71		
72		
73		
74		
75		
76		
77		
78		
79		
80		
81		
82		
83		
84		
85		
86		
87		
88		
89		
90		
91		
92		
93		
94		
95		
96		
97		
98		
99		
100		
101		
102		
103		
104		
105		
106		
107		
108		
109		
110		
111		
112		
113		
114		
115		
116		
117		
118		
119		
120		
121		
122		
123		
124		
125		
126		
127		
128		
129		
130		
131		
132		
133		
134		
135		
136		
137		
138		
139		
140		
141		
142		
143		
144		
145		
146		
147		
148		

<pre> jc = 0 do 1000 i = 1, nval write(*,*) i = i do 950 j = 1, nb(i) ar(i,j) = ar(i,j)/1000.0 wb = 20.48/ar(i,j) fr = 3.26/ar(i,j) dth = (4.4e-4*sqrt(fr)*(1+(fr/2.5e5)))/2.0 d2 = dth*dth f1 = dth*wb f2=f1*f1 jc = jc+1 p1 = 5729.0*eps*el*d((jc)*r(jc)) p2 = p1*p1 kr = (wb/1500.0)*r(jc) </pre>	<pre> is satisfied Note: If it is not that is because the bubble spectrum was truncated or the resolution was inadequate write(*,*) MSS=,mass,' PSUM=',psum,' RATIO=',mass/psum Adjust the spectrum levels to enforce Parseval's theorem when parsif=1 if(parsif .eq. 1)then do 935 k = 1, nspec psd(k) = psd(k) * (mass/psum) continue endif </pre>
<pre> p1 = 5729.0*eps*el*d((jc)*r(jc)) p2 = p1*p1 kr = (wb/1500.0)*r(jc) </pre>	<pre> 935 </pre>
<pre> Calculate the mean square of the signal d1 = 1.0/(4*dth*wb*(d2+1)) d2 = (2*d2+1)/((kr*dth)*(4*dth*wb*(d2+1))) d3 = 2/((kr)*(4*wb*(d2+1))) mss = p2*(d1+d2-d3) </pre>	<pre> Sum the spectra next do 940 k = 1, nspec fpsd(k) = fpsd(k) + psd(k) continue continue continue </pre>
<pre> Calculate the spectrum here do 925 k = 1, nspec w = (k-1)*d*wb b1 = kr*dth*((f2+(wb-w)*(wb-w))*((f2+(wb+w)*(wb+w))) t1 = (wb*wb*(dth-kr)*(dth-kr))+(w*w) mphii = 2*t1/b1 psd(k) = p2*mpihii continue </pre>	<pre> Transform the data to dB and subtract 7.8 dB to account for average over 6 waves do 960 k = 1, nspec fpsd(k) = 10*log10(fpsd(k)/1e-12)-7.8 continue </pre>
<pre> Integrate under the calculated spectrum psum = 0.0 do 930 k = 1, nspec-1 psum = ((psd(k)+psd(k+1))*d(f2.0) + psum continue </pre>	<pre> Open the output file and write the data to it open(10,file=out) write(10,1400)(fpsd(i),i=1,nspec) format(e12.6,i8) format(e12.6) format(e12.6) format(e12.6,1x,e12.6) stop end </pre>
<pre> Check the spectrum levels to see if Parseval's theorem </pre>	<pre> 1200 1300 1400 1600 </pre>


```

10 read(1,'(a10)')fname
11 read(1,'(a10)')fname2
12 read(1,'*)npts
13 read(1,'*)frcq
14 read(1,'*)iover
15 read(1,'*)pof2
16 read(1,'*)mode
17 read(1,'*)norm
18 read(1,'*)scale
19 read(1,'*)incr
20 read(1,'*)iwin
21 read(1,'*)ipstart
22 read(1,'*)ipstop
23 call getndp(type)
24 nar = 2**pof2
25 dfrcq=frcq/nar
26 nact = nar-iover
27 n2p = (nar/2)+1
28 n4p = n2p*4+4
29 cw = 0
30 irecl = npts*4
31 open(2,file=fname,status='unknown',err=10,iostat=io)
32 goto 20
33 write(*,*) 'Error opening file, iostat=',io
34 goto 6000
35 read(2,5,end=50)(data(i),i=1,npts)
36 format(e12.6)
37 goto 60
38 write(*,*) 'Warning end-of-file encountered'
39
40 Remove the DC
41
42 sum = 0.0
43
44 Note that the number of data points read is npts
45 and the variance is calculated over npts points
46 the number of data points over ipstart to ipstop segments
47 i.e. npts>fft length*ipstop
48
49 do 70 i = 1,npts
50   sum = data(i) + sum
51   mean = sum/npts
52   write(*,*) 'mean=',mean
53
54 70
55
56 80 i = 1,npts
57 data(i) = data(i) - mean
58 incnt = 0
59 open(3,file=fname2)
60
61 Loop starts here for processing segments
62
63 do 5000 j = ipstart, ipstop
64   write(*,*) 'spectrum#:',j
65   incnt = incnt + 1
66
67 Fill real array x(i) with nar points of
68 data from the real array data(i)
69 Note that the frame overlap is given by - iover
70
71 do 200 j = 1, nar
72   ic = ((i-1)*(nar-iover)) + j
73   if(j.eq.1)then
74     is = (ic-1)/frcq
75   endif
76   x(j) = data(ic)
77   call cvar(x,nar,sumx2)
78   if(iwin.eq.1)call bh92(x,wx,nar,mode)
79   if(iwin.eq.2)call hammi(x,wx,nar,mode)
80   if(iwin.eq.3)call hann(x,wx,nar,mode)
81   if(iwin.eq.0)then
82     call rfft(x,pof2,norm,scal)
83     do 1100 k = 1, n2p
84       pad(k) = c(k) * conjg(c(k))
85     continue
86   else
87     call rfft(wx,pof2,norm,scal)
88     do 1200 k = 1, n2p
89       pad(k) = zw(k) * conjg(zw(k))
90     continue
91   endif
92
93 Adjust spectrum here so that Parseval's theorem
94 is satisfied
95 (1/N)*sum(x(n)^2)=sum(psd(k))
96
97 sump = 0.0
98 do 1400 k = 1, n2p

```

```

1400      sump = psd(k)+sump
      fact = (sums2/nas)/sump
do 1500 k = 1, n2p
      psd(k) = psd(k)*fact

```

Sum the spectra

```

do 1600 k = 1, n2p
      p(k) = p(k) + psd(k)
      continue

```

Average the spectra

```

if(incont .eq. incr)then
      cw = cw+1
      write(*,*) Writing to file,cw
do 1700 k = 1, n2p
      p(k) = p(k)/incr
      continue

```

Convert to dB and subtract 7.8 dB for averaging over 6 waves and subtract 10log(dfreq) to get PSL

```

do 1720 k = 1, n2p
      p(k) = 10*log10(p(k)/1e-12)-7.8-10*log10(dfreq)
      continue

```

```

write(3,131)(p(k),k=1,n2p)
format(e12.6)
incr = 0
icount = 0

```

Zero p(k) here

```

do 1800 k = 1, n2p
      p(k) = 0.0
      continue
endif
      continue
stop
end

```

Program which calculates the sum of the square

- of a given time series
- y - time series
- n - length of time series
- s2 - sum of y^2

- Note that the mean should have been removed from y already

```

subroutine cvar(y,n,s2)
      real*4 y(1),s2
      integer n,i
      s2 = 0.0
      do 100 i = 1, n
            s2 = y(i)*y(i)+s2
            continue
      return
end

```

100

Medwin and Daniel's (1990) Data

Radius (mm)	Number of Bubbles per wave
0.049793	1.077496
0.098775	5.843364
0.146066	9.543167
0.195942	6.155420
0.241447	3.727699
0.290967	3.075903
0.338176	2.068501
0.393046	0.927449
0.435092	0.971049
0.480297	1.010741
0.525057	0.946580
0.573988	0.575576
0.619666	0.201950
0.673652	0.734602
0.724229	0.569198
0.766772	0.619580
0.809555	0.290299
0.864299	0.095681
0.904934	0.188681
0.956758	0.492269
1.001740	0.172392
1.089012	0.355643
1.180596	0.145803
1.237824	0.581654
1.279882	0.186756
1.328908	0.141900
1.424710	0.136333
1.462899	0.346425
1.512605	0.096659
1.608160	0.457885
1.651267	0.087233
1.695529	0.091754
1.790135	0.227638
1.976126	0.668907
2.026273	0.224374
2.092206	0.089386
2.118586	0.083022
2.252422	0.452308
2.299955	0.276138
2.351762	0.198938
2.455483	0.205096
2.606970	0.262999
2.971469	0.189158
3.293926	0.184653
3.920059	0.181322
4.232015	0.194602
5.910966	0.103824
6.372480	0.098004
7.113351	0.097210

DOCUMENT LIBRARY

March 11, 1991

Distribution List for Technical Report Exchange

Attn: Stella Sanchez-Wade
Documents Section
Scripps Institution of Oceanography
Library, Mail Code C-075C
La Jolla, CA 92093

Hancock Library of Biology &
Oceanography
Alan Hancock Laboratory
University of Southern California
University Park
Los Angeles, CA 90089-0371

Gifts & Exchanges
Library
Bedford Institute of Oceanography
P.O. Box 1006
Dartmouth, NS, B2Y 4A2, CANADA

Office of the International
Ice Patrol
c/o Coast Guard R & D Center
Avery Point
Groton, CT 06340

NOAA/EDIS Miami Library Center
4301 Rickenbacker Causeway
Miami, FL 33149

Library
Skidaway Institute of Oceanography
P.O. Box 13687
Savannah, GA 31416

Institute of Geophysics
University of Hawaii
Library Room 252
2525 Correa Road
Honolulu, HI 96822

Marine Resources Information Center
Building E38-320
MIT
Cambridge, MA 02139

Library
Lamont-Doherty Geological
Observatory
Columbia University
Palisades, NY 10964

Library
Serials Department
Oregon State University
Corvallis, OR 97331

Pell Marine Science Library
University of Rhode Island
Narragansett Bay Campus
Narragansett, RI 02882

Working Collection
Texas A&M University
Dept. of Oceanography
College Station, TX 77843

Library
Virginia Institute of Marine Science
Gloucester Point, VA 23062

Fisheries-Oceanography Library
151 Oceanography Teaching Bldg.
University of Washington
Seattle, WA 98195

Library
R.S.M.A.S.
University of Miami
4600 Rickenbacker Causeway
Miami, FL 33149

Maury Oceanographic Library
Naval Oceanographic Office
Stennis Space Center
NSTL, MS 39522-5001

Marine Sciences Collection
Mayaguez Campus Library
University of Puerto Rico
Mayaguez, Puerto Rico 00708

Library
Institute of Oceanographic Sciences
Deacon Laboratory
Wormley, Godalming
Surrey GU8 5UB
UNITED KINGDOM

The Librarian
CSIRO Marine Laboratories
G.P.O. Box 1538
Hobart, Tasmania
AUSTRALIA 7001

Library
Proudman Oceanographic Laboratory
Bidston Observatory
Birkenhead
Merseyside L43 7 RA
UNITED KINGDOM

REPORT DOCUMENTATION PAGE	1. REPORT NO. WHOI-92-13	2.	3. Recipient's Accession No.
4. Title and Subtitle Laboratory Measurements of the Sound Generated by Breaking Waves		5. Report Date December 1991	
		6.	
7. Author(s) Mark R. Loewen		8. Performing Organization Rept. No.	
9. Performing Organization Name and Address Woods Hole Oceanographic Institution Woods Hole, Massachusetts 02543		10. Project/Task/Work Unit No. WHOI-92-13	
		11. Contract(C) or Grant(G) No. (C) (G)	
12. Sponsoring Organization Name and Address		13. Type of Report & Period Covered Ph.D. Thesis	
		14.	
15. Supplementary Notes This thesis should be cited as: Mark R. Loewen, 1992. Laboratory Measurements of the Sound Generated by Breaking Waves. Ph.D. Thesis. MIT/WHOI, WHOI-92-13.			
16. Abstract (Limit: 200 words) The primary motivation for this research was to determine whether measurements of the sound generated by breaking waves could be used to quantitatively study the dynamics of the breaking process. The sound beneath two and three-dimensional breaking waves was measured. It was determined that the mean square acoustic pressure correlates with the wave slope and dissipation for waves of moderate slope and that the amount of acoustic energy radiated by an individual breaking event scales with the amount of mechanical energy dissipated by breaking. Sound at frequencies as low as 10 Hz was observed and the mean square acoustic pressure, in the frequency bands below 1 kHz correlate strongly with the wave slope and dissipation. The correlations of the mean square acoustic pressure and the wave amplitude were found to be similar for the two and three-dimensional breakers. The spectra of the sound generated by the large scale three-dimensional breaking waves sloped at -5 to -6 dB per octave at frequencies greater than 1 KHz. Evidence is presented which supports the hypothesis that the low frequency signals observed beneath both the two and three-dimensional breaking waves were caused by the collective oscillation of bubble clouds. A model of the sound produced by breaking waves which uses the sound radiated by a single bubble oscillating at its linear resonant frequency and the bubble size distribution to estimate the sound spectrum is presented.			
17. Document Analysis a. Descriptors sound breaking waves b. Identifiers/Open-Ended Terms c. COSATI Field/Group			
18. Availability Statement Approved for publication; distribution unlimited.		19. Security Class (This Report) UNCLASSIFIED	21. No. of Pages 354
		20. Security Class (This Page)	22. Price